Permeability Estimation From Time-Lapse Seismic Data For Updating the Flow-Simulation Model

Mehdi Paydayesh

A Thesis Submitted for the Degree of Doctor of Philosophy,
Institute of Petroleum Engineering,
Heriot-Watt University, Edinburgh, United Kingdom.

April 2010

ABSTRACT

The key to increasing reservoir recovery is to provide accurate estimates of the permeable pathways (permeability, transmissibility) and the transmissibility of the barriers that control reservoir heterogeneity. The reservoir-engineering techniques (such as well testing, well logging and production data) supply the estimate of these properties in the reservoir region which is limited to well locations. Providing estimates of the permeability in the reservoir rocks located *between* the wells is the holy grail of reservoir engineering for history matching. Compared with all other engineering techniques, 4D seismic could play a unique role in providing the property of the reservoir at a good spatial coverage. In this thesis, the estimation of permeability, transmissibility, and the transmissibility multiplier, using 4D seismic, is addressed.

First, current methodologies for permeability estimation were applied in synthetic and field examples. Based on the investigations performed, the permeability-estimation method was modified and adjusted to produce an improved result. Consequently, the estimates of permeability provided an introduction to the fast-track history-matching method. The proposed history-matching technique implies a simple and practical approach for quickly updating the simulation to improve the history-matching in the model. In following, the assessment of the uncertainties associated with the permeability estimation that involves using a variety of different attributes, using different time-lapse surveys, tuning effects and method assumptions, were performed. The uncertainties were tackled by addressing these issues; thus, the permeability result was further enhanced, and the uncertainty associated with the estimates was quantified. Next, the relationships between the quantitative estimates of connectivity and the 4D seismic signal were established. Two types of connectivity assessments using 4D seismic (hydraulic sand connectivity and barrier connectivity) were proposed, depending on the fact that 4D-seismic information is either pressure- or saturation-dominant. Accordingly, two types of attributes were introduced, the seismic connectivity attribute (SCA) and the Laplacian attribute. When applied to the Schiehallion field data, an interpretation approach is used to interpret pressure- and saturation-anomalies in frequent time-lapse seismic, using all available sources of data. Following this, a pressure-anomaly map is utilized for locating faults and compartments

(using the Laplacian attribute), and a saturation-anomaly map is used to calculate the SCA. New approaches were chosen for estimating transmissibility and transmissibility multipliers, based on proposed attributes extracted from 4D seismic.

To my dear family and my beloved wife

ACADEMIC REGISTRY
Research Thesis Submission

Name:	Mehdi Paydayesh		
School/PGI:	Inistitute Of Petroleum Engineering		
Version: *(i.e. First, Resubmission, Final)*	Final	Degree Sought (Award **and** Subject area)	PhD in Petroleum Engineering

Declaration

In accordance with the appropriate regulations I hereby submit my thesis and I declare that:

1) the thesis embodies the results of my own work and has been composed by myself
2) where appropriate, I have made acknowledgement of the work of others and have made reference to work carried out in collaboration with other persons
3) the thesis is the correct version of the thesis for submission and is the same version as any electronic versions submitted*.
4) my thesis for the award referred to, deposited in the Heriot-Watt University Library, should be made available for loan or photocopying and be available via the Institutional Repository, subject to such conditions as the Librarian may require
5) I understand that as a student of the University I am required to abide by the Regulations of the University and to conform to its discipline.

* *Please note that it is the responsibility of the candidate to ensure that the correct version of the thesis is submitted.*

Signature of Candidate:	Mehdi Paydayesh	Date:	06/04/2010

Submission

Submitted By *(name in capitals):*	Mehdi Paydayesh
Signature of Individual Submitting:	Mehdi Paydayesh
Date Submitted:	06/04/2010

For Completion in Academic Registry

Received in the Academic Registry by *(name in capitals):*			
Method of Submission *(Handed in to Academic Registry; posted through internal/external mail):*			
E-thesis Submitted (mandatory for final theses from January 2009)			
Signature:		Date:	

ACKNOWLEDGMENTS

Part of my journey is coming to an end. These have been the best and most challenging years of my life so far. I am indebted to the many people who have been instrumental in the successful completion of my research. To begin, I will thank God for having made everything possible – by giving me the strength and courage to accomplish this work.

I would like to express my heartfelt thanks to my supervisor, Professor Colin MacBeth, for the extensive time that he spent guiding my research. He was always accessible, and constantly provided insightful reviews and timely responses throughout the various stages of this work.

Special thanks should go to Dr Xuri Huang and Dr Asghar Shams for investing their time in reading and evaluating my thesis. I am grateful that, despite their many other commitments, they agreed to become members of the examining committee.

I would like to thank Dr Rossmary Villegas for her collaboration on the history-matching part of this thesis. I also acknowledge the Schiehallion field partners (BP, Shell, Hess, Statoil (UK) Ltd, Murphy Petroleum Ltd, and OMV) for providing the data, and for giving me permission to publish them. I am also grateful to the sponsors of the Edinburgh Time-Lapse Project, Phase III (BG, BP, Chevron, ConocoPhillips, EnCana, ExxonMobil, Hess, Ikon Science, Landmark, Maersk, Marathon, NORSAR, Petrobras, Shell, Statoil (UK) Ltd, Total, and Woodside) for their financial support of this research.

As a recipient of the BP/Ian Jack Scholarship, I would like to express my sincere thanks to the SEG Foundation Scholarship Program, and especially to Ian Jack for his encouraging and motivating comments on my work.

I am indebted to my fellow office-mates, Hamed Amini, Amran Benguigui, Nuri Edriz, Yesser Hajnasser, Dr Weisheng He, Nader Kooli and Valeriy Rukavishnikov, for providing an inspiring and enjoyable environment in which to learn and grow. During these memorable years, we spent most of our time together, like a family, sharing our knowledge, joy, happiness and sadness. I am also grateful to all the members of the Reservoir Geophysics group: Fabian Domes, Reza Falahat, Ilya Fursov, Alejandro

Garcia, Yi Huang and Karl Stephen. I am thankful to all the staff at the Institute of Petroleum Engineering, in particular the computer-support staff, for their continuous support.

For my parents' continued love and encouragement I can never thank them enough. They have been my inspiration throughout this endeavour. Mere words fail to express my appreciation to my wife, Raheel, for her endless patience, love and encouragement that buoyed me up throughout my PhD. This thesis would not have been possible without her invaluable, constant support. I also wish to acknowledge my sisters and family-in-law for their prayers and support.

TABLE OF CONTENTS

LIST OF TABLES

LIST OF FIGURES

CHAPTER 1: INTRODUCTION

Overview

This chapter provides an introductory description of the various geophysical and engineering tools used for permeability estimation, and their advantages and disadvantages, and identifies the need for a time-lapse seismic method in permeability estimation. First, the various possible permeability-inversion approaches are described. Next, the use of permeability estimates in updating the reservoir simulation model is discussed. Finally, the main contributions of this thesis are addressed.

1.1 Introduction

New high-resolution time-lapse seismic data have led to the delivery of accurate quantitative interpretations. This has satisfied many reservoir-engineering objectives in reservoir management and monitoring. Time-lapse seismic interpretations have successfully contributed to the attainment of maximum hydrocarbon recovery at a minimum cost. The key concept in achieving maximum recovery is the role of time-lapse seismic in the development of the science of reservoir characterization.

Reservoir characterization involves building a reservoir model that incorporates the characteristics of the reservoir that are pertinent to storing and producing hydrocarbons. In reservoir characterization, a two-fold problem is considered: (1) the distribution of hydrocarbons through the reservoir, and (2) the likely fluid pathways towards the producing wells.

The reservoir model must provide a description of the reservoir that correctly accounts for the spatial variation and continuity of the porosity, permeability and fluid saturation that are essential for storing hydrocarbons and transforming hydrocarbons. The reservoir property that provides the necessary pathways for hydrocarbon flow towards the production wells is permeability. In reservoir characterization, after the Initial Oil In Place (IOIP) and aquifer properties, it is important to determine the permeability. An accurate estimate of permeability is crucial, because, in most fields, it is the most important parameter that affects the reservoir performance (Yoon *et al.*, 1999). It controls the behaviour of the simulation model designed as the basis for well-completion strategies, production, and reservoir management. Most of the sensitivity analysis prior to history matching in reservoir simulation has shown that, generally, permeability values, fault multipliers, and transmissibilities are among the parameters to be adjusted for achieving an optimal match in the reservoir-simulation model (Harpole and Hearn, 1982). For example, Jian *et al.* (2004) built 50 reservoir models, varying the combinations of parameters using experimental design technique. They ran the simulation for these models, and they showed that there are large differences (some greater than 200%) in water-cut, breakthrough time, water production and oil recovery. These differences in the model predictions were found to be due to changes in the horizontal permeability between the models.

The accuracy of reservoir management and strategies for future prediction of the reservoir are tied to the accurate and reliable permeability measurements based initially on the simulation model. Despite the crucial importance of accurate permeability estimation, the generation of permeability models that best describe the reservoir heterogeneity sometimes seems to be a difficult target to achieve. The conventional capabilities of permeability estimation, such as well logging, cores and well testing, suffer from unreliability beyond the wells, because their evaluation is limited to the borehole region. Permeability estimation between the wells is vital in constraining the reservoir model. Hence, there is a critical need for a new technology that can provide this type of information.

Recently, the number of new techniques of delivering high-resolution dynamic information using time-lapse seismic has increased. This has led the industry to examine the practice of evaluation of reservoir properties, such as the location of sealing faults, flow barriers or high-permeability pathways, and general field-wide pressure- and saturation-changes (MacBeth *et al.*, 2005). Now an important question in a reservoir-engineering context is: how far can time-lapse seismic go in the refinement of the reservoir-simulation model. Based on this philosophy, current work has concentrated on efforts to establish a new role for time-lapse seismic in the prediction of the most challenging reservoir property: permeability. In fact, it would be an outstanding achievement for time-lapse seismic to extract permeability across the field with a reasonable resolution. Further, to fulfil such an intention, an algorithm has to be designed to update the simulation model using the predicted results from the 4D seismic. The overall aim is to validate whether the 4D permeability product brings value to the history-matching process. The procedure proposed by the latter step addresses several challenging issues in simulation updating using seismic-scale products. Figure 1.1 is an illustration of the general workflow that gives an overview of the framework of the present work.

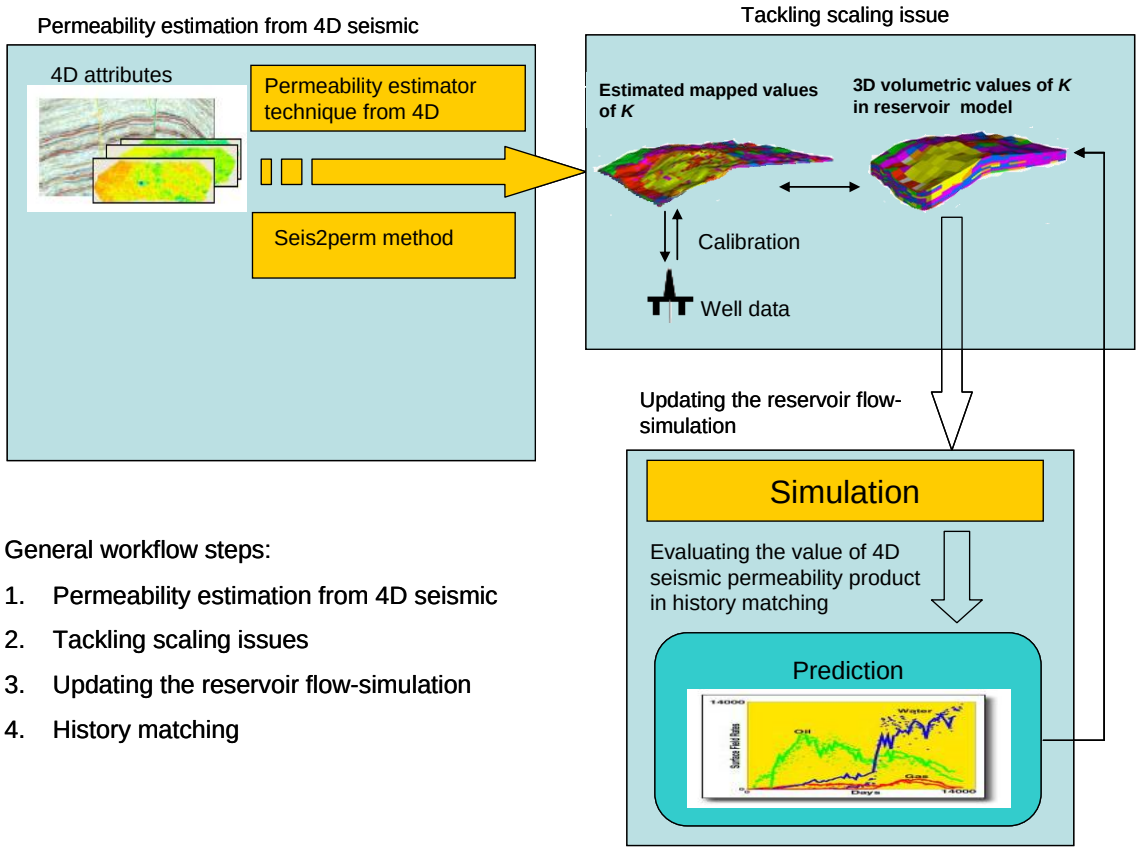

Figure 1.1: *4D-seismic-derived horizontal permeability is used to update the simulation model.*

1.2 Permeability measurement

Although permeability is an important rock property (Ahmed *et al.*, 1989), it is one of the most difficult of all petrophysical properties to determine (Johnson, 1994). The conventional sources for permeability determination provide a formation permeability that represents different averaging volumes. Core analysis, well-test analysis and well logs are conventional tools used to measure the permeability. 3D seismic is also a new potential tool introduced to infer permeability. However, it is still highly controversial and not yet entirely proven as described in section 1.2.5. The following section gives a brief review of the range of permeability-estimation methods, describing how they measure the permeability and listing the shortcomings attached to their measurement.

1.2.1 Core-determined permeability

Permeability is usually determined from core analysis. Permeability determination using core analysis is considered as a standard measurement such that the permeability derived from all other methods is usually compared with the core permeability. The procedure to establish the permeability starts with cutting core plugs from the whole core, and then cleaning and drying the core plugs; then flow is induced at several rates. For each flow rate, the inlet and outlet pressures are measured. Finally, the permeability is calculated using the slope of the graph in which the flow rate is plotted versus the pressure function across the faces of the sample.

Conventionally, core permeability is then populated through the geological facies, using geostatistical methods, and this is utilized as the initial permeability model for future flow-simulations. The procedure involves establishing a relationship between plug permeability, porosity and facies. The facies in the reservoir volume are delineated by conditioning to 3D seismic and wireline logs. Once porosity is assigned using the facies model, the permeability can be established, based on the porosity–permeability relationship derived from core plugs.

Although the practice of measuring the permeability using cores provides high resolution estimation, in reality high-quality core-based permeability data are difficult to achieve, either because of the borehole conditions or due to the high cost of coring. For these reasons, over the years attempts have been made to estimate permeability using alternative methods. One of the comparatively inexpensive and readily available sources of inferring permeability is well-logging information.

1.2.2 Using wireline logs to determine permeability

Various models have been used to estimate permeability using correlations from well logs (Wyllie and Rose, 1950; Timur, 1969; Coates and Dumanoir, 1974). Most of these correlations are established directly from core-plugs, attempting to relate a commonly logged property such as porosity (φ) and/or V_{clay} to permeability (K). These correlations are generally semi-log in nature (such as $\varphi = aLn(K) + b$). The second type of correlation incorporates information from water saturation estimated from resistivity

logs combined with Archie's equation (1949). For example, Wyllie and Rose (1950) proposed the following equation for determining permeability:

$$K = A\left(\frac{1}{P_c^2 F^{\left(2-\frac{1}{m}\right)} S_w}\right) \tag{1.1}$$

where F is the resistivity factor; S_w is connate water saturation; P_c is capillary pressure; A is a constant value, which varies for different lithologies; and m is the cementation factor. Recently, NMR (nuclear magnetic resonance) log technology has been used in inferring permeability. This is a relatively new technique (Coates *et al.*, 1999). NMR uses hydrogen protons as an indicator of the presence of fluids in the pore space of porous media.

All methods of permeability determination from well logs use an indirect relationship via various physical properties of the rock and fluid. The relationship is not often well defined. Moreover, the correlations of permeability with porosity and water saturation are limited because the portions of the porous medium that dominate permeability, porosity and water saturation are different (see Figure 1.2). Permeability is dominated by the pore throats, while porosity and water saturation are dominated by the volume within the pore bodies. Hence, correlations for permeability are inherently limited when correlating to porosity and water saturation or any other rock property that is strongly influenced by any part of the porous media other than the pore throat. Even in NMR technology, as Kenyon (1997) points out, while the objective is to measure the throat size (the dominant effect on permeability), the NMR logs provide information about pore size. Although they are related to each other, this may not be very realistic in a quantitative model as expressed in Kenyon's equations. In conclusion, there is no direct method to determine permeability using well logs.

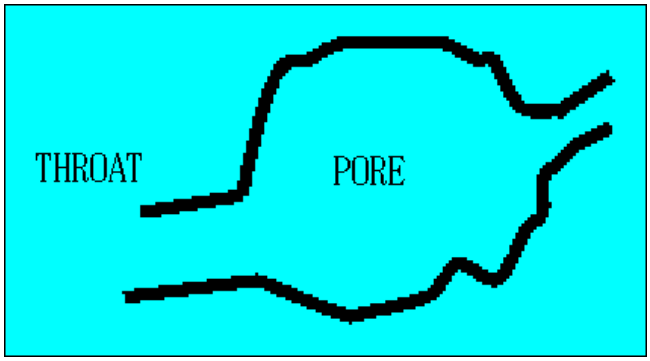

Figure 1.2: *Schematic picture defining a throat and a pore in the pore space of a porous material. Permeability is related to the throat size of a porous medium, whereas porosity and saturation are related to pore-size distribution.*

1.2.3 Well-test permeability estimation

The calculation of the so-called effective well-test-derived permeability is based on the interpretation of a pressure-transient well test. Usually, such a well test consists of generating some flow-rate impulses in the reservoir by build-up and drawdown and then observing the resultant pressure response. A number of techniques are available to perform pressure-transient analysis (Sabet, 1991). Generally, in most of these techniques, the following diffusivity equation is solved:

$$\frac{\partial^2 P}{\partial r^2} + \frac{1}{r}\frac{\partial P}{\partial r} = \frac{\varphi \mu c_t}{K}\frac{\partial P}{\partial t} \tag{1.2}$$

where $P(r,t)$ is pressure, r is the radial distance from the well-bore, t is time, φ is the porosity, μ is the viscosity, c_t is the total compressibility, and K is the absolute permeability. The use of Equation 1.2 implies the following assumptions: (1) flow is radial; (2) the well is open over the entire vertical thickness of the reservoir; (3) the reservoir is homogeneous and isotropic; (4) the fluid has constant properties and slight compressibility; and (5) the pressure gradients are small and gravitational forces are negligible. For the transient period (the period in which the pressure disturbance has not reached the boundary of reservoir), the following boundary and initial conditions apply:

$$P(r, t=0) = P_i, P(r=\infty, t) = P_i, \frac{\partial P}{\partial r}\Big|_{r=\infty} = 0 \tag{1.3}$$

where P_i is the initial reservoir pressure. The solution for the transient flow period to Equation 1.2 is given by:

$$P(r,t) = P_{\mathrm{i}} - \frac{qB\mu}{2\pi Kh}\left[-\frac{1}{2}E_{\mathrm{i}}\left(-\frac{\varphi\mu c_t r^2}{4Kt}\right)\right] \tag{1.4}$$

where $P(r,t)$ is the pressure at a given radius r and time t; P_{i} is the initial reservoir pressure; h is the reservoir thickness; q is flow rate; B is the formation volume factor; K is absolute permeability; and E_{i} is the exponential integral function that is defined as:

$$-E(-x) = \int_x^{\infty} \frac{\mathrm{e}^{-u}}{u}\mathrm{d}u \tag{1.5}$$

For all but very early times, the E_{i} function can be approximated by a logarithmic function, and Equation 1.4 can be rewritten as:

$$P(r,t) = P_{\mathrm{i}} - \frac{qB\mu}{4\pi kh}\left[\ln\frac{Kt}{\varphi\mu c r^2} + 0.80907\right] \tag{1.6}$$

Using Equation 1.6, a semi-log plot of pressure versus time should produce a straight line for the early linear response, from which the effective well-test permeability can be determined by this equation:

$$K = -162.6\frac{qB\mu}{mh} \tag{1.7}$$

where m is the slope of the semi-log straight line. The permeability K represents an effective average of the absolute permeability within the reservoir volume drained by the well test. In fact, the solution of the diffusivity equation (Equation 1.2) is based on the assumption that the reservoir is homogeneous; however, no reservoir is homogeneous, and the degree of heterogeneity is a function of the lithology, depositional and post-depositional environment of the reservoir. For practical purposes, it is assumed that the permeability determined by well-test analysis is an effective permeability representing some average within a radius of investigation or drainage radius, which is influenced by the producing well. In other words, the well-test result is insensitive to small-scale heterogeneities. Grader and Horne (1988) showed that it is possible to have a sizeable 'hole' in the reservoir without making any discernible difference to an interference test. The definition of radius of drainage is questionable in the presence of heterogeneities (Matthews and Russell, 1967). Many attempts have been

made to estimate the effective response of the heterogeneous model without recourse to numerical simulation (Beggs and King, 1985; King, 1989; Duquerroix *et al*., 1993; Vega, 1995). However, no analytical solution has been found that accounts for all parameters affecting fluid flow. To overcome the limitations of conventional well test that is indicative of near wellbore homogenous permeability, the well interference test is introduced as an alternative that provides regional permeability trend and conveys permeability anisotropy. The well interference test involves a cyclic injection of fluid into the source well (that is associated with changes in rates), and measurement of the pressure pulse in a neighbouring well (known as observation well). Type curves are utilized for interpreting pulse interference tests and provide detailed hydraulic characterization including permeability evaluation between wells. Although this technique is usually have more precision than conventional well testing methods, it usually takes considerable time for production at one well to measurably affect the pressure at an adjacent well. Consequently, interference testing is more expensive and there is a difficulty in maintaining fixed flow rates over an extended time period (Dyer, 2007).

1.2.4 History matching for updating permeability

Generally, it is possible to improve the permeability field in the history-matching process (Fasanino and Molinard, 1986; Ouenes, 1992; Grimstad *et al.*, 2004). In this process, the production data are used to infer permeability/transmissibility values so that the model prediction matches the observed data. For example, Fasanino and Molinard (1986) defined an objective function based on a measured pressure distribution. The transmissibility values are iteratively modified until the gradient descends to the smallest value of the objective function. Ouenes (1992) also presented an automatic history-matching algorithm that simultaneously estimates relative permeability and capillary pressures for core floods using the optimization method of simulated annealing. Grimstad *et al.* (2004) also showed how unknown large-scale permeability structures such as channels or barriers can be identified by history matching, using adaptive multi-scale estimation (AME) (Figure 1.3). They assumed that the true permeability field is known. Then they used this reference permeability in a ‘field-scale synthetic model’ to generate bottom-hole pressures and fluid well rates. These production data were then used as the information for the permeability identification.

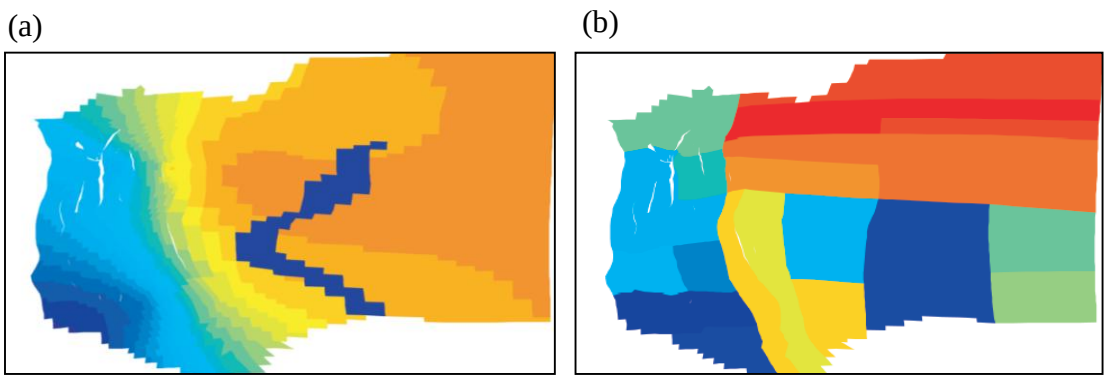

Figure 1.3: *History matching for estimation of permeability: (a) reference permeability, and (b) final permeability result using AME (after Grimstad et al., 2004).*

The studies mentioned show the promise of using optimization techniques to estimate reservoir properties. However, such applications are computationally expensive and time-consuming. Moreover, they can provide no more than the general trend or large-scale variation of the property. The final resolution of an optimized model depends on the cell size, and usually produces a very coarse-scale view of the permeability field.

1.2.5 Using 3D seismic for permeability estimation

One of the first attempts to address the problem of estimating permeability from seismic data was done by Maurice Biot (1956). Biot recognized a frequency-dependent analytical relationship between permeability and seismic attenuation. However, laboratory, sonic log, cross-well, VSP (Vertical Seismic Profile), and surface seismic have all demonstrated that Biot's predictions often greatly underestimate the measured levels of attenuation. In 2001, the Department of Energy at Berkeley University brought together 15 participants from industry, national laboratories, and universities to concentrate on whether permeability can be determined from the seismic data (Pride *et al.*, 2003). They investigated whether the permeability of the rock in which the seismic wave propagates influences the amplitudes versus distance. They considered attenuation mechanisms as a controlling issue to address this question. They concluded that there is a hope that the structure of permeability for a geological formation may be resolved at a specific degree of resolution. However, they found their calculation to be beyond the capabilities of the computers at that time, and they are hopeful that future technological developments and further research will be able to solve the problem. Other researchers, such as Klimentos and McCann (1990) and Shapiro and Müller (1999) used almost the

same concept to infer permeability from 3D seismic. Klimentos and McCann (1990) used the relationship between attenuation and porosity, and then inferred the permeability map indirectly (if a core-based porosity–permeability relationship could be established). Shapiro and Müller (1999) investigated the link between permeability and attenuation for heterogeneous media. They noticed that in such structures, two effects are of importance for seismic attenuation: interlayer flow or the process of diffusion and elastic scattering of seismic waves. They showed that the frequency dependence of the P-wave attenuation coefficient and its anisotropy are sensitive to the permeability, especially at lower frequencies. They also concluded that the permeability that controls the seismic attenuation can differ very strongly from the hydraulic permeability. In summary, a survey of the literature shows that, as yet, investigations have shown that there is no clear and direct relationship between the 3D seismic signal and permeability.

1.3 Why estimate permeability from 4D seismic?

When considering conventional methods of permeability estimation, it seems that the requirements of the reservoir engineer cannot be fulfilled by the methodologies that are currently available. A brief overview of these methodologies is listed in Table 1.1, in which a comparison has been made between the various methods of permeability determination. Permeability data taken from cores have an excellent vertical resolution and no lateral resolution. Usually only a small percentage of the field is cored, which gives only a poor aerial coverage. Well-test permeability does not have the required vertical resolution, as it is an average for the interval from which the well is drained. However, it has a good lateral resolution (with a variable radius of influence). Although well-test information provides aerial coverage of the field, especially for well-developed reservoirs, the medium-scale formation heterogeneity cannot usually be resolved by conventional well-test data. Log-derived permeability data have both the required vertical resolution and a slightly better lateral resolution. But this is not a direct method of permeability measurement, as it is usually calculated through correlations with other properties. Moreover, its aerial coverage (lateral resolution) is limited to the areas close to the well-bore. Generally there are some inherent uncertainties in the above-mentioned methods. Furthermore, each of these methods is unreliable beyond a few sample locations of the well. The permeability evaluation in the regions away from the wells remains crucial in constraining the simulation model and predicting the accurate future

behaviour of the reservoir. An alternative tool is required to provide the permeability values between wells. The domain of seismic data is the only suitable source of information that provides spatial coverage over the entire field. As discussed, 3D-seismic data cannot be easily converted to permeability estimates. However, the permeability derived from time-lapse seismic is a promising tool that can enhance the permeability estimation in inter-well space. In fact, the new tool can fill the gap in conventional techniques in terms of lateral coverage, aerial resolution and also providing sufficient information on connective pathways and barriers.

Table 1.1: *Comparison of the different tools used for the measurement of permeability*

Data	Resolution	Aerial coverage	Comments	Timing
Cores	Excellent vertical resolution (0.05–0.1 m)	Poor – sparse in 1D	High level of uncertainty on the inferred trends	Included in geological model
Wireline logs	Very good vertical and horizontal (0.1–1 m)	1D	Indirect conversion to permeability	Included during initial geological model
Well tests (conventional and Well Interference Test)	WT: Poor vertical and moderate horizontal (e.g. 30 m by 30 m by 10 m) WIT: Good horizontal resolution between wells (depends on distance between wells)	Extends partly into 2D – variable radius of influence	WT: are done throughout the life of the field in order to refine the estimates WIT: is expensive to run	WT: carried out over a few days or weeks. WIT: takes more time compared with conventional WT.
History match on rates/water-cuts and pressures	Poor to moderate vertical and horizontal (e.g. 100 m by 100 m by 3 m)	Coarse 2D scale, as based on well data	History-match resolution depends on the cell size and the flow regime	Time-consuming task
3D seismic	Good horizontal and poor vertical (e.g. 12.5 m by 12.5 m by 12 m)	Potentially excellent	Use of attenuation, or porosity, still highly debatable	Static information only
4D seismic	Good horizontal and poor vertical (e.g. 12.5 m by 12.5 m by 12 m)	Potentially excellent	Overall, has the highest potential to deliver value	Over a few years, depending on the survey frequency

1.4 Different methods of estimating permeability from 4D seismic

Most of the methods in the literature propose a history-matching approach using time-lapse seismic as an indirect permeability estimator. 4D seismic is part of the process known as 'seismic history-matching' that aims to model production information plus 4D seismic data, using the conventional principles of history matching (Landa and Horne, 1997; Kretz *et al.*, 2004; Stephen and MacBeth, 2006; Dadashpour *et al.*, 2007). Here, the 4D seismic is integrated with production data into an objective function that measures the mismatch between the computed and observed data. In this type of technique, 4D seismic is also treated as dynamic data, and matched with synthetic data calculated from the simulation model via petro-elastic and seismic modelling. If the match is insufficient, then the reservoir model parameters such as the permeability, transmissibility and the transmissibility multiplier will be perturbed by a parameterization technique in an iterative loop until an optimal match is achieved. For example, Landa and Horne (1997) introduced a history-matching method that uses the estimated saturation from 4D seismic in an objective function. They worked with areas of the reservoir where changes in the saturation are known to infer the permeability (Figure 1.4). Another example is from Kretz *et al.* (2004), who used a streamline simulation approach to match fluid-front data (Figure 1.5). In this method, the fluid-flow simulation is run and the permeability is adjusted along the streamlines so that the computed fluid-fronts coincide with the observed fluid-fronts derived from 4D seismic. The information is matched by varying the permeability multipliers iteratively and updating the permeability multipliers model at each step, and finally inverting for the individual grid block permeabilities (Figure 1.6). In the seismic history-matching approach, it is hoped that permeability is extracted with a better resolution than traditional production-only history matching.

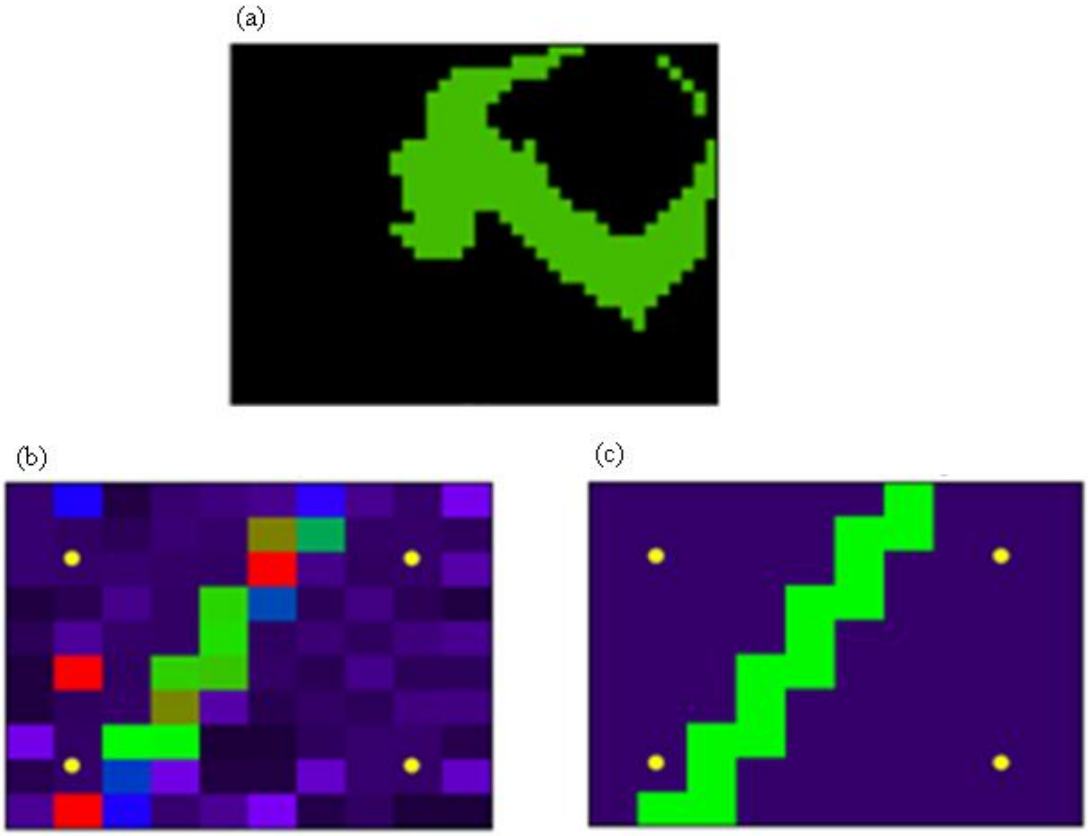

Figure 1.4: *(a) 4D-seismic saturation anomaly in binary format; (b) calculated reservoir permeability using 4D seismic; and (c) true reservoir permeability (Landa and Horne, 1997).*

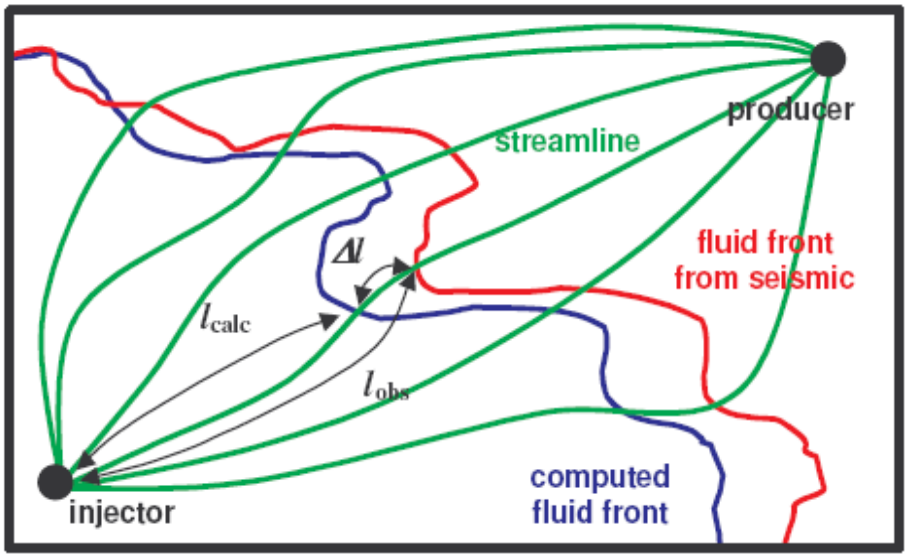

Figure 1.5: *Fluid-front history-matching to estimate permeability (Kretz et al., 2004).*

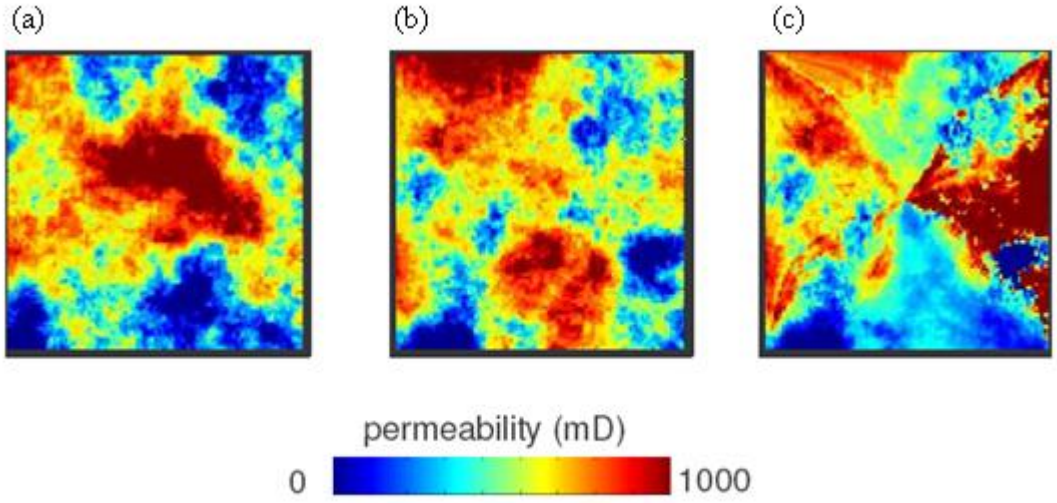

Figure 1.6: *Five-spot synthetic case in which the fluid front has been matched: (a) reference, (b) initial and (c) updated permeability fields (Kretz et al., 2004).*

The second and main category of the permeability-estimation method involves utilizing inversion for pressure- or saturation change derived via 4D seismic (de Haan *et al.*, 2001; Vasco, 2004; Vasco *et al.*, 2004; MacBeth and Al-Maskeri, 2006).

de Haan *et al.* (2001) developed a permeability inversion method using streamlines. 4D seismic is used to provide the position of the saturation fronts in time. Then the 4D seismic is contoured, and the streamlines are traced from this. The flow velocity is estimated at each grid block between injector and producer. This velocity (u_x, u_y), depends on the permeability, K, viscosity, μ, and the pressure gradient, ∇P, via Darcy's law ($\vec{u} = -\frac{K}{\mu}\nabla P$). Therefore, the permeability at all grid blocks within the outer contour can be calculated using:

$$K = -\frac{\mu\sqrt{\left(u_x^2 + u_y^2\right)}}{\sqrt{\left(\frac{\delta P}{\delta x}\right)^2 + \left(\frac{\delta P}{\delta y}\right)^2}} \tag{1.8}$$

Assuming a known and constant viscosity and starting from a homogeneous permeability field as an initial guess, the pressure gradient is determined at each grid block. The new pressure is subsequently fed in to estimate permeability in an iterative approach. Figure 1.7 shows the results of this method when applied to a synthetic

model. The true pressure field provides the best permeability estimate; however, in practice the pressure field is unknown. Moreover, using this method, permeability cannot be predicted outside the last contour, as the saturation front has not reached this point.

Vasco *et al.* (2004) also used a streamline (trajectory)-based approach to relate perturbations in reservoir permeability to perturbations in time-lapse-seismic amplitude changes. Using a petro-elastic transformation, they calculated seismic amplitude (A) for each column of cells in the reservoir model, as a function of pressure, saturation and porosity, $A(P_{ij}, S_{ij}, \varphi_{ij})$, where the vectors S_{ij}, P_{ij} and φ_{ij} denote the vertical average of the saturations, pressures, and porosities for all vertical cells in the ijth column. By neglecting the pressure- and porosity-change for the reservoir, a perturbation in the time-lapse amplitude response is:

$$\delta A^1\left(S_{ij},\phi_{ij}\right)-\delta A^0\left(S_{ij},\varphi_{ij}\right)=\sum_k \frac{\partial A^1}{\partial S_{ijk}}\delta S^1{}_{ijk}-\sum_k \frac{\partial A^0}{\partial S_{ijk}}\delta S^0{}_{ijk} \tag{1.9}$$

The quantities $\delta S^1{}_{ijk}$ and $\delta S^0{}_{ijk}$ are determined by a semi-analytical expression for the saturation history at a point on the trajectory:

$$S(t,\sigma)=S\left(\frac{\sigma}{t}\right) \tag{1.10}$$

where (σ) is an analytical expression for the travel time of the two-phase front along a trajectory, $\sum$, based on Darcy's law:

$$\sigma=\int_{\sum}\frac{\varphi(r)}{\lambda K(r)\left|\nabla P\right|}\mathrm{d}r \tag{1.11}$$

where $\varphi(r)$ is the porosity; $K(r)$ is the absolute permeability; P is the pore pressure; r is the distance along the trajectory $\sum$; and the variable λ is the total mobility. A perturbation in σ is related to a perturbation in saturation S by:

$$\delta S\left(\frac{\sigma}{t}\right)=\frac{1}{t}S'\left(\frac{\sigma}{t}\right)\delta\sigma \tag{1.12}$$

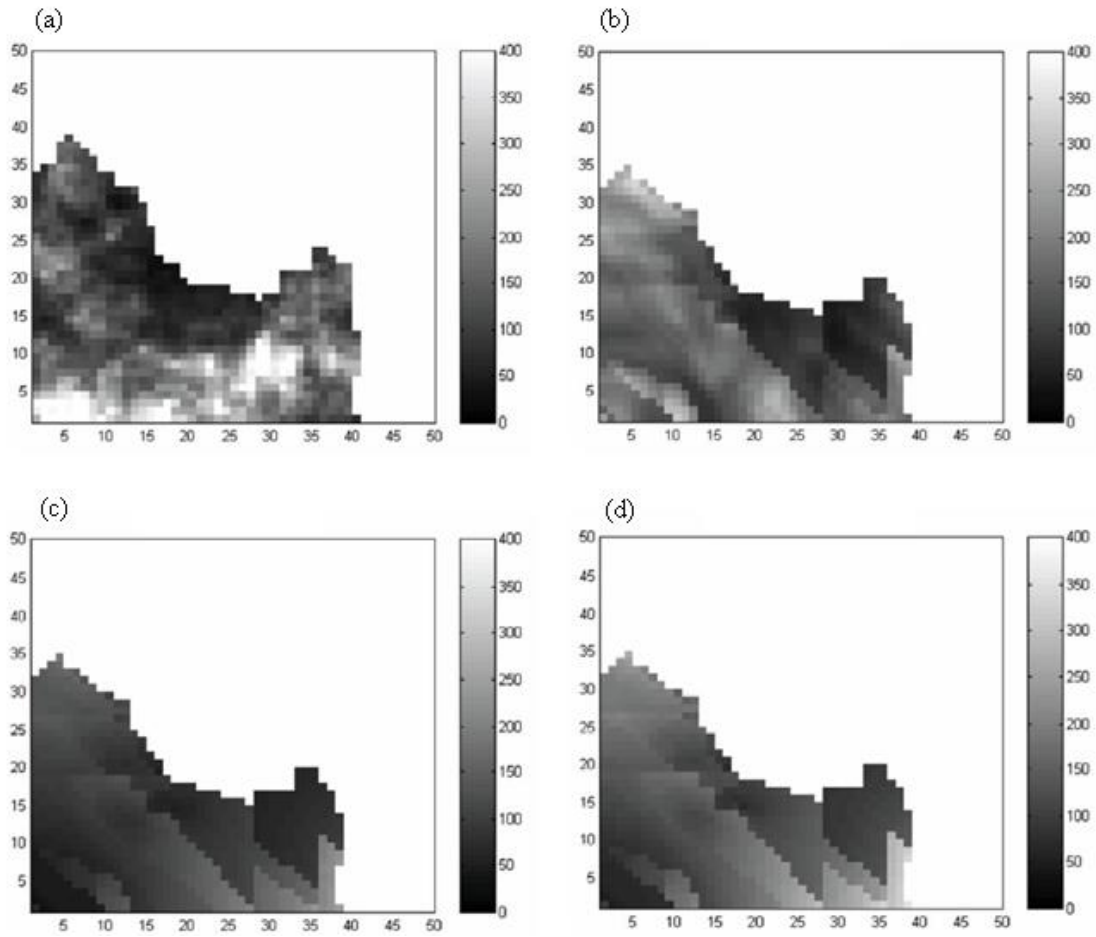

Figure 1.7: *(a) Actual permeability field; (b) inverted permeability field from true underlying pressure field; (c) inverted permeability field using a "homogeneous pressure field"; and (d) inverted permeability field using an iterated homogeneous pressure field (after de Haan et al., 2001).*

The quantity $\delta\sigma$ comes from a perturbation of the integral in Equation 1.11. The combination of Equation 1.9 and Equation 1.12 results in a linearized expression relating perturbations in time-lapse amplitude changes to perturbations in reservoir flow properties. This is a basis for a procedure in which the permeabilities are modified to obtain a match to the observed data. The process is started with an initial reservoir model, and it iteratively updates the permeabilities in order to better fit the observed time-lapse amplitude changes. For each iteration of the algorithm, a reservoir simulation is run to re-compute the trajectories and redefine the pressure- and saturation-histories in each grid block. To test this methodology, Vasco *et al*. (2004) performed a synthetic test with a reference permeability, as shown in Figure 1.8(a). The starting model is a homogeneous layer with an initial permeability of 100 mD. Through the iterative

algorithm, the final permeability map is obtained, and this is shown in Figure 1.8(b). The final model contains some large-scale features of the reference model. The permeability cannot be resolved beyond the edge of the final location of the water-front, where saturation is not reached. In addition, the resolution of the heterogeneity is limited to the trajectories shown in Figure 1.8(c).

As Calvert (2005) remarked: "Most of the methods which have been introduced to infer the permeability from 4D seismic based on the saturation change concept are based on the streamline logic" (de Haan, 2001; Kretz *et al.*, 2004; Vasco *et al.*, 2004). Because streamlines do not cross, they partition 3D flow problems into a series of 1D problems. These problems would be very easy to deal with if such streamlines did not change with the pressure field over time'. In contrast to the streamlines used to recover permeability, finite-difference simulation is the main simulation modelling tool. Also, using a saturation approach to infer permeability has some shortcomings. Its applications have revealed the fact that using a pressure solution could be more useful, due to the fast diffusion of the pressure disturbance across the field, as compared with the saturation profile which is often spread over a particular region of the field. Based on this heuristic, two important developments for determining permeability have been proposed by Vasco (2004) and MacBeth and Al-Maskeri (2006). Vasco (2004) described a technique that uses pressure change estimated from 4D seismic to infer the reservoir permeability using the finite-difference approach. His methodology starts from the governing simulation equation for a two-phase, compressible fluid, neglecting the gravity term:

$$\nabla.(K\lambda\nabla P) = Q \tag{1.13}$$

where K is the absolute permeability; λ is the total mobility; P is the reservoir pressure; and Q is the flow rate. By considering the pressure field for this equation at T_0 and T_1 corresponding with seismic survey times, and then subtracting, the difference equation is:

$$\nabla.(K\lambda_1\nabla P_1 - K\lambda_0\nabla P_0) = Q_1 - Q_0 \tag{1.14}$$

Then, by his rearranging, the final formula is:

$$\nabla.(KG) = Q_\Delta, \; G = \left[\bar{\lambda}\nabla P_\Delta + \lambda_\delta(2\nabla P_0 + \nabla P_\Delta)\right] \tag{1.15}$$

where P_Δ and Q_Δ denote the change in reservoir pressure and flow rate between T_0 and T_1. $\bar{\lambda}$ and λ_δ are the average total mobility and change in total mobility respectively:

$$\bar{\lambda} = \frac{\lambda_1 + \lambda_2}{2} \tag{1.16}$$

$$\lambda_\delta = \frac{\lambda_1 - \lambda_0}{2} \tag{1.17}$$

The system of linear equations formed by the discretization of Equation 1.15 can be solved using a numerical linear solver. The system of equations is solved for permeability. The result of the synthetic test for this methodology is shown in Figure 1.9; some main features of reference permeability are captured in the final permeability map.

MacBeth and Al-Maskeri (2006) have proposed an approach which can be either saturation- or pressure-based. However, pressure solution was preferred for the optimal illumination of the reservoir. They started from the governing equation for flow of a single-phase, compressible fluid, neglecting the gravity term, and they proved the following formula for the reservoirs, in which pressure has a dominant effect on 4D seismic signatures:

$$K(x, y) = \frac{c_f \mu}{\Delta T} \varphi(x, y) \left\{ \frac{|\Delta A(x, y)|}{\left\| \left[\frac{\partial^2 \Delta A(x, y)}{\partial x^2} + \frac{\partial^2 \Delta A(x, y)}{\partial y^2} \right] \right\|} \right\} \tag{1.18}$$

where ΔA is the 4D seismic signature, φ is effective porosity (NTG multiplied by sand porosity); ΔT is the time between the two seismic surveys; μ is the fluid viscosity; and c_f is the fluid compressibility. In this equation, fluid compressibility and viscosity are assumed to be constant. However, these two parameters vary mainly with pressure (viscosity varies with pressure to a lesser extent and varies mainly with temperature; note that this thesis is primarily focused on iso-thermal water flooding process). As the result, pressure variation may introduce instabilities in permeability result, particularly around injection and production wells where production activities are occurred. In this

thesis, the error due to this assumption is minimized via compressibility compensation factor introduced in Chapter 2 and well calibration performed in Chapter 4.

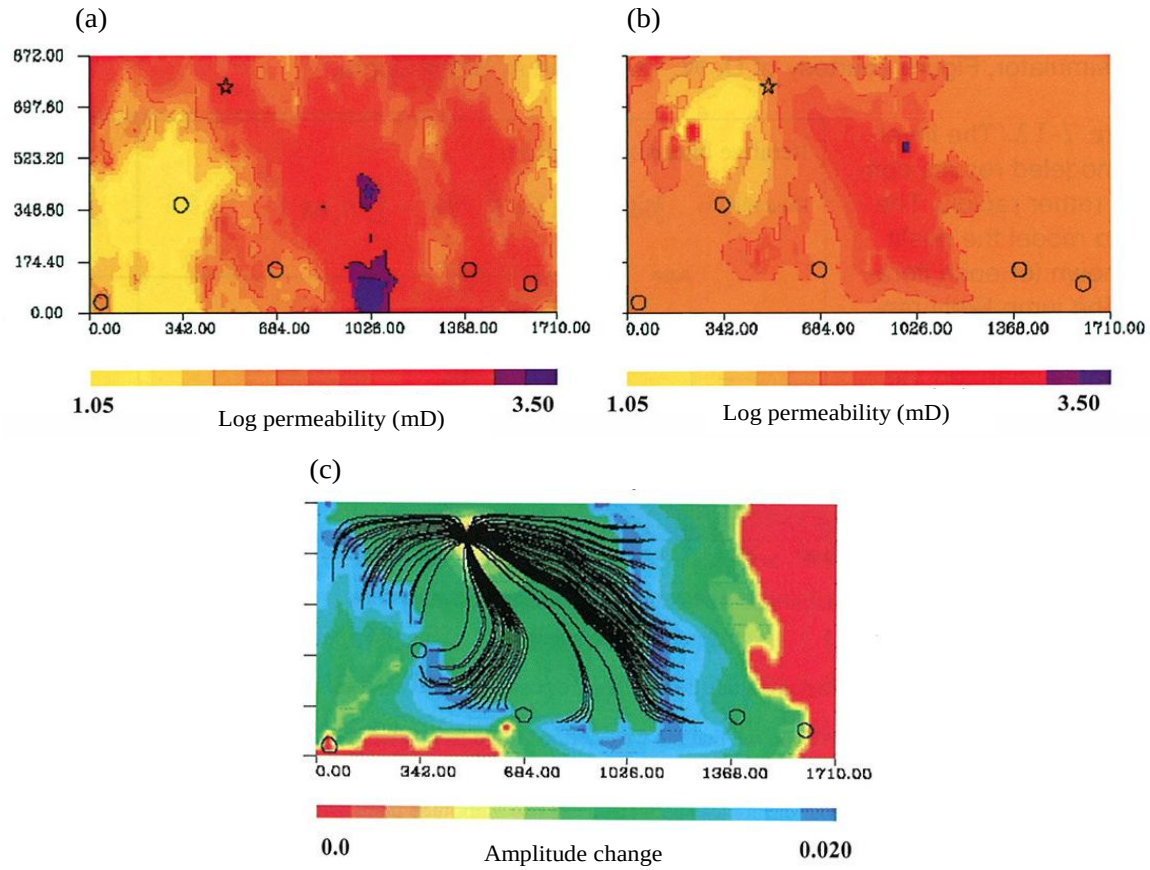

Figure 1.8: *(a) The reference permeability model; (b) the final permeability model; and (c) amplitude changes between 180 and 670 days (after Vasco et al., 2004).*

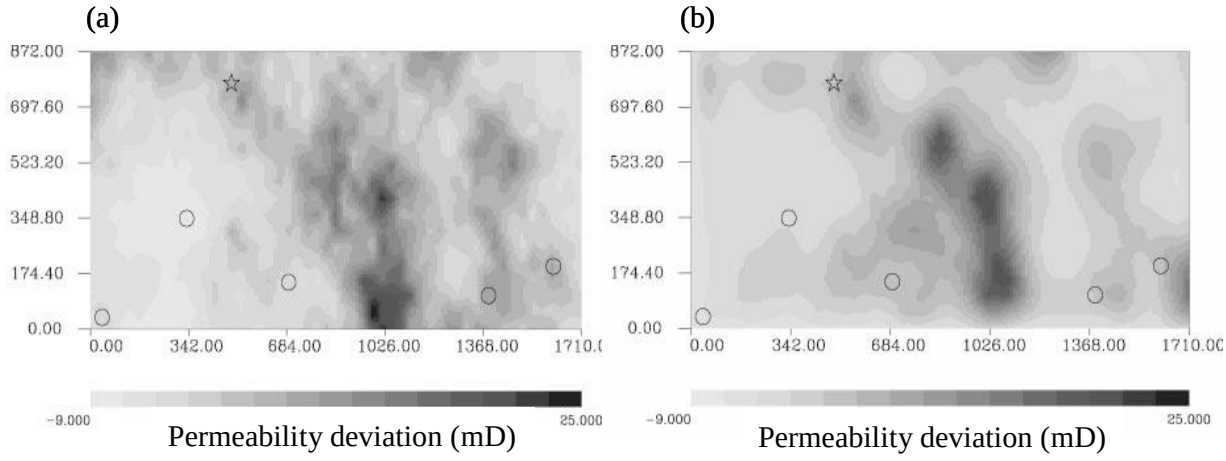

Figure 1.9: *(a) Reference permeability model, and (b) recovered permeability model (after Vasco, 2004).*

The result of this technique is tested both on synthetic and field data. Figure 1.10 shows a very good agreement between the recovered permeability map derived using this technique and the reference model of permeability. Figure 1.11 demonstrates the permeability estimated using the proposed technique applied to segment 4 of the Schiehallion field, located to the west of the Shetland Islands, UK. In comparison with the existing vertically averaged permeability from the simulation model, the recovered permeability looked promising for imaging the outline permeability structure of the simulation model.

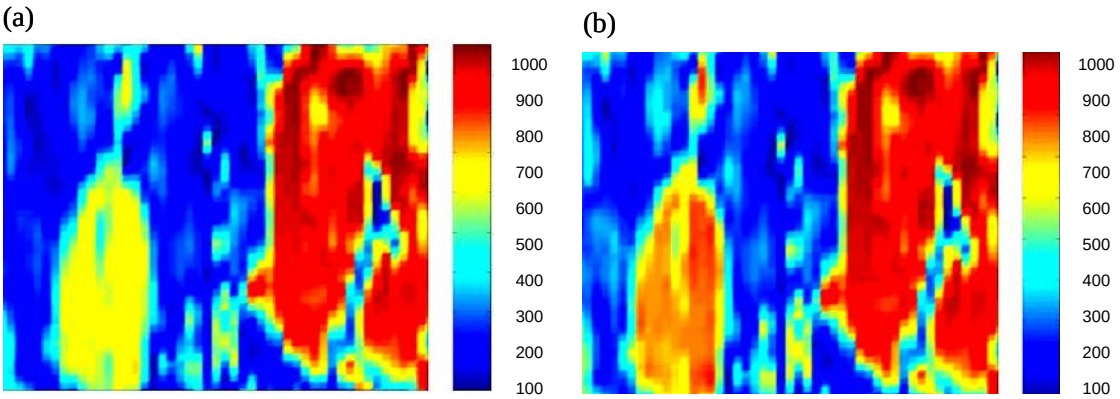

Figure 1.10: *Synthetic test: (a) reference permeability, and (b) the recovered permeability map (after MacBeth and Al-Maskeri, 2006).*

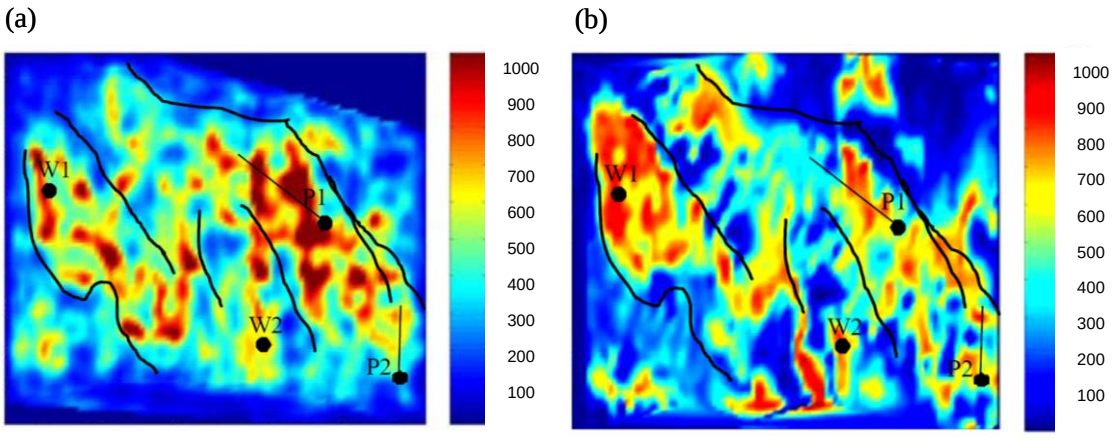

Figure 1.11: *Field application of the technique proposed by MacBeth and Al-Maskeri (2006): (a) vertically averaged permeability from the existing simulation model, and (b) resolved permeability for the same section of the field.*

1.5 Updating simulation model

"It is fair to say that the practice of updating reservoir models by using 4D seismic data is a young but growing technology that teaches and contributes a great deal" (Calvert, 2005).

Bearing in mind that permeability has a great impact on management decisions for the future prediction of the reservoir behaviour, updating the reservoir simulation is the final piece of the puzzle. Updating the simulation-model permeability is a challenging practice, which involves tackling crucial problems such as the lack of vertical resolution of the seismic data compared with the simulation model; up-scaling of the 4D seismic in the lateral sense; and adjusting the geometry of the simulation model with that of the Cartesian geometry of the 4D-seismic product.

Conventional 4D-seismic interpretation satisfies the main needs of the reservoir engineer to a large extent. This has led to a large number of cited business successes. It is now widely agreed that time-lapse seismic data, if interpreted appropriately, can provide invaluable information with which to optimize hydrocarbon recovery. This information includes, for example, the location of hydraulically conductive faults, no-flow barriers or high-permeability pathways; the identification of isolated compartments possibly containing bypassed oil; the position of injected fluid fronts or contacts; and general field-wide pressure- and saturation-changes. For example, Koster *et al.* (2000) showed how 4D seismic can provide information on the location of a water-front. This information was used to update a simulation model in the field. As a result, the uncertainties in the forecast production profile were reduced. In addition, undrained blocks were identified and one infill well was planned to target the larger of these blocks.

To date, most of these features are commonly inferred by visual inspection of brightening or dimming on time-lapse seismic difference sections or maps, and are thus essentially semi-quantitative and can provide subjective interpretations (Figure 1.12). In fact, visual adjustment is working well, but lacks uniqueness and accuracy. However, it is satisfactory for simple, clear-cut cases. The possible quantitative approaches to updating the reservoir-flow simulation using time-lapse information are as follows.

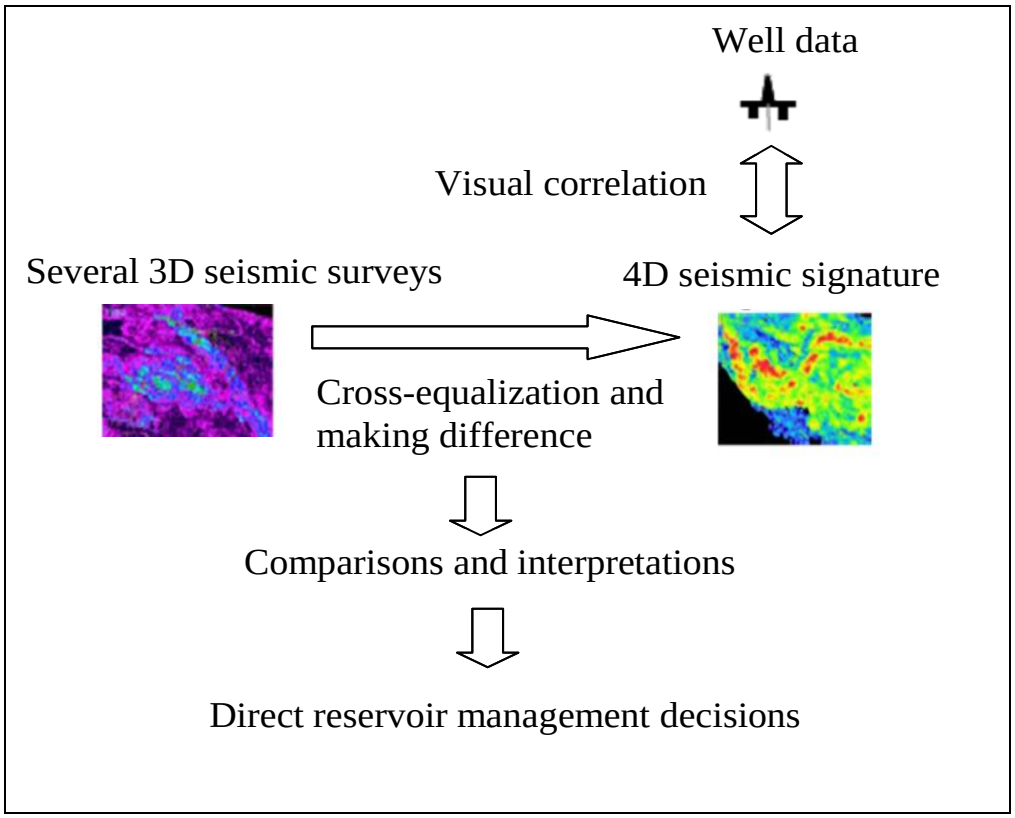

Figure 1.12: *Qualitative interpretation for updating a reservoir-flow simulation.*

1.5.1 Approach 1 – update of the simulation model, using 4D seismic as a dynamic property (seismic history-matching)

The basic idea is to use time-lapse seismic as dynamic data similar to production data, but with added aerial resolution. Seismic history-matching updates the simulation model to jointly honour both production- and seismic-data. In this approach, the time-varying property estimates from 4D seismic, such as pressure-, saturation-, amplitude- or impedance-change are used to match the simulated properties. Hence, there are a number of choices to be matched, as illustrated in Figure 1.13. The comparison could be made on pressure/saturation changes, elastic inverted parameters, or the seismic amplitude signal. Among these choices, selecting inverted elastic parameters is the most common approach in the literature (Stephen and MacBeth, 2006). The reason for this is that it avoids CPU-time-consuming forward seismic modelling. In addition, it takes into account both saturation- and pressure-effects and avoids the difficulty of pressure and saturation separation (Gosselin *et al.*, 2003).

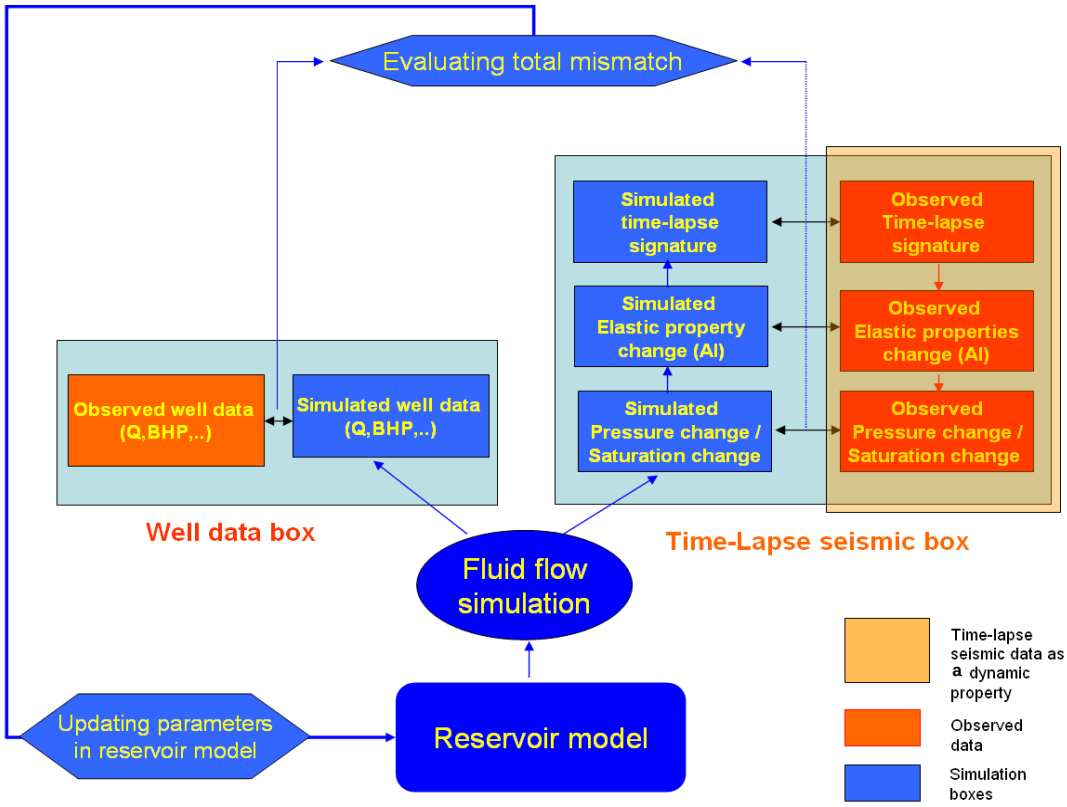

Figure 1.13: *General workflow of the seismic history-matching workflow and data-match possibilities*

1.5.2 Approach 2 – update of the simulation model, using 4D seismic as a reservoir-property estimator

History matching using time-lapse seismic data is a time-consuming process that requires high-powered computers. A faster alternative is to update the model using properties fed in directly from the 4D seismic, to jump-start the history matching. Thus, permeability estimates from 4D seismic can lead to a direct update of the flow simulation model and jump-start the history-matching process, reducing the time and cost of conventional seismic history-matching. The permeability estimates from time-lapse seismic provide a further constraint on the reservoir model, using information from between the wells to overcome the problem of non-uniqueness. A conventional approach for history matching is then pursued, which involves reducing the misfit between observed data and simulated data until the optimal match is achieved (see Figure 1.14).

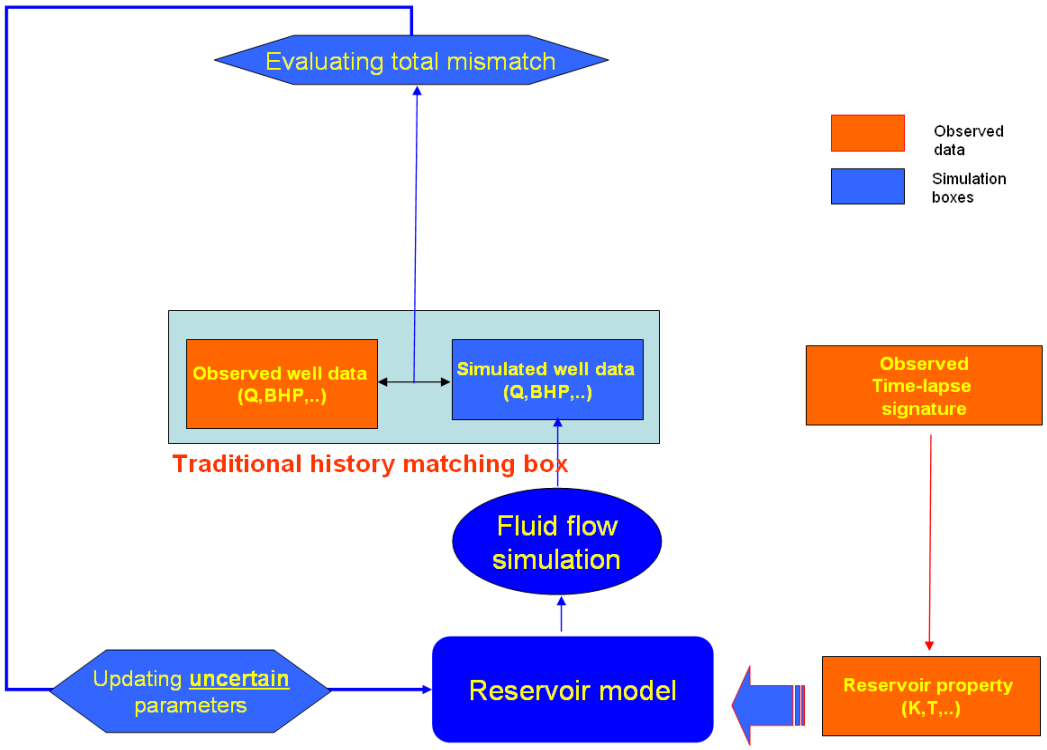

***Figure 1.14**: Update of the simulation model, using 4D seismic as a reservoir property estimator.*

1.6 Scope of the following chapters

Now that I have discussed the reasons for utilizing 4D seismic to infer permeability, the remainder of this thesis is organized as follows. The focus in Chapter 2 will be the analysis and enhancement of the Seis2perm technique proposed by MacBeth and Al-Maskeri (2006). Then, in Chapter 3, I will deal with updating of the simulation model using the permeability product of 4D seismic. In Chapter 4, the errors involved in the practical implementation of the method will be verified. Chapter 5 and Chapter 6 will link the permeability-estimation method with an effective connectivity-estimation technique. Connectivity-estimation techniques are utilized to update the transmissibility and transmissibility multipliers of the reservoir. Finally, Chapter 7 presents conclusions for this work. In addition, recommendations are suggested for future development of the techniques described in this thesis.

CHAPTER 2: INVESTIGATIONS ON THE 4D-SEISMIC-DRIVEN PERMEABILITY-ESTIMATION METHOD

Overview

This chapter critically examines the method introduced by MacBeth and Al-Maskeri (2006) for estimating permeability from 4D seismic. The theoretical and practical aspects are investigated using synthetic and field applications. This study looks at the challenges and potentials of the current method and suggests some modifications in order to enhance the final permeability product.

2.1 Introduction

Updating permeability in the history-matching process with and without including 4D seismic in the objective function is an established method, as discussed in Chapter 1. It is an indirect estimation method, and produces smoothed and coarse-scale permeability variation across the field. However, inversion of 4D-seismic data directly to permeability information can lead to additional constraints on some of the non-uniqueness inherent in the simulation model. As described in Chapter 1, a few researchers have addressed the use of the inversion of 4D seismic data for estimating permeability. These techniques involve separating the saturation change and pressure change from the 4D seismic signatures. The extracted saturation/pressure change is then utilized as the input for permeability estimation, by employing a governing simulation equation (de Haan *et al.*, 2001; Vasco, 2004; Vasco *et al.*, 2004; MacBeth and Al-Maskeri, 2006).

Depending on the fact that seismic data is pressure controlled or saturation controlled, every method has a different strategy to estimate the permeability. Saturation-based methods generally relate the permeability to time-lapse saturation variation via streamline concepts. Streamline-based techniques provide an analytical relationship between permeability and saturation changes (Vasco *et al.*, 2004). However, pressure methods involve the inversion of permeability values via a numerical solution for the simulation governing equation.

Modelling and field applications suggest that the saturation- dominant seismic solution is restrictive because of the compact areal ‘image’ of the resultant permeability structure. In other words, permeability cannot be imaged in locations that the saturation front has not covered. However, pressure-dominant 4D seismic is more suited for optimal permeability estimation. This is due to the relative fast speed of diffusion of the pressure front (see Figure 2.1). In fact, the size of the ‘image’ area at a specific time is large for pressure as compared with saturation. Furthermore, it is pressure that sets up the streamlines along which the changes of saturation are guided at a velocity determined by the pressure gradients. These are two major factors in favour of the pressure solution option in the proposed permeability-estimation techniques.

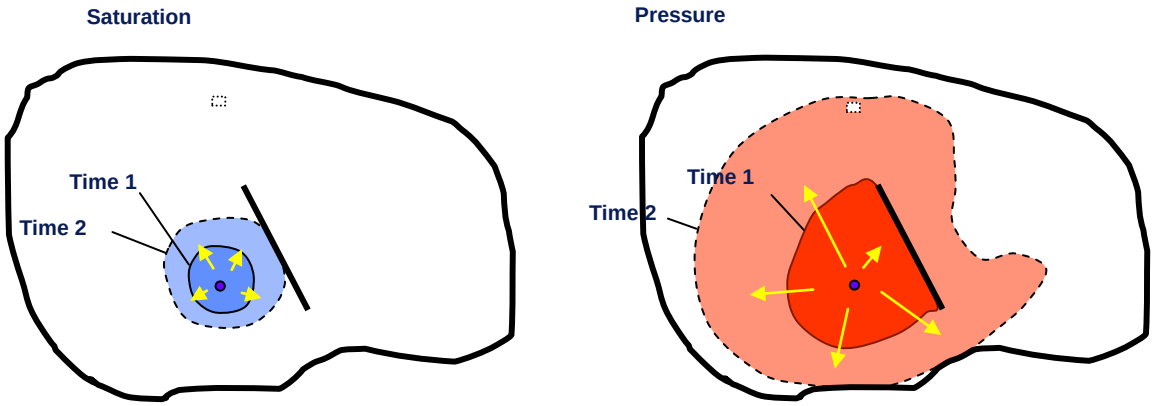

Figure 2.1: *The saturation front arrives after the pressure profile is established.*

Two methods have been proposed for estimating permeability from pressure-dominant 4D seismic. These are a numerical approach developed by Vasco (2004), and a direct transform derived by MacBeth and Al-Maskeri (2006). Investigation and implementation of the method introduced by MacBeth and Al-Maskeri (2006), and its application to synthetic and observed data, are the focus of this study.

In this thesis, the method suggested by MacBeth and Al-Maskeri (2006) is referred to as the Seis2perm method, as it is a direct transform from the 4D response to permeability values. This name is chosen to simplify referencing and also to be consistent with the other products in the Edinburgh Time-Lapse project, such as Sim2seis and Log2seis. All of these submodules fit together in a loop connecting simulation modelling and seismic data.

In this chapter, first the theoretical background of the permeability inversion methods is investigated. Then the method is implemented and studied on synthetic and field applications separately. The potential and pitfalls of the method are addressed at the end.

2.2 Detecting the effect of permeability in the pressure response

Methods developed for permeability estimation using time-lapse pressure data are based on the governing equation of fluid flow in reservoir simulation. The governing equation comes from mathematical modelling of the fluid flow in porous media (see Appendix A). Starting from the simulation governing equation, the permeability-estimation

relationships are eventually derived and simplified to link the time-lapse pressure data to the permeability estimates (see Appendix B).

Time-lapse pressure is the main type of data input used to infer permeability in 4D-seismic-based methods. This essentially means that the pressure behaviour is affected by permeability variation in the reservoir. In order to address the validity of this assumption, in this section a test is performed to investigate the detection of permeability in the pressure response.

As a demonstration, a simulation model consisting of 100 by 100 cells horizontally and only one cell thick is considered. Each cell has horizontal dimensions of 500 ft by 500 ft and 250 ft thickness. The reference permeability models used to generate the reservoir pressure- and saturation-changes are shown in Figure 2.2(a). Three cases are considered: a homogeneous model, a low-permeability patch, and a high-permeability patch. For heterogeneous models, two different regions of permeability and porosity values have been considered. The NTG is held constant, but porosity has been considered to vary with permeability. The values of the high- and low-permeability regions are chosen to be 1000 mD and 100 mD respectively. The permeability value for the homogeneous model is 500 mD. Porosity values are also selected accordingly, in order to be consistent with the permeability regions. High-porosity values of 0.25 and low-porosity values of 0.15 are assigned to the corresponding permeability regions.

A single producer is positioned in the bottom left-hand corner of the model to control the model mainly by pressure rather than saturation. This is imitating the case of primary production in which only a negligible percentage of saturation is changing and the hydrocarbon is mainly recovered by drawdown pressure. The production is set at a liquid rate of 20,000 bbl/day, and the bottom-hole pressure (BHP) limit is set to be 2000 psi. This gives a drawdown pressure of up to 530 psi near the production well, from the initial 4514 psi.

A simulation is run to calculate the time-lapse changes in pressure. The result for each case is demonstrated in Figure 2.2(b). At first glance, the first effect observed involves the flow directions or streamlines calculated based on the pressure gradients (Figure 2.2). Streamlines basically show inter-well connections. As the flow paths are directly

related to the underlying permeability, investigating these flow paths could help us to understand the relationship between pressure and permeability. Streamlines depend upon the flow velocity field, which in turn is a function of the pressure distribution in the reservoir according to Darcy's equation. As has been illustrated by the streamlines in Figure 2.2(c), the preferential flow path is along the high-permeability zones. The effect of permeability on pressure change is more noticeable in Figure 2.2(d), where the pressure change is cross-plotted along the diagonal line of the model from the production well to the other corner of the model. For example, once the flow hits the low-permeability patch, the patch behaves like a barrier and the flow 'prefers' to find a direction *around* the patch, where the permeability values are ten times higher than the permeability within the patch. Conversely, the streamlines calculated based on the pressure profile highlight the high-permeability region, indicating the high density of the streamlines in that region.

This fundamental simple test reveals that the pressure change is affected by the permeability features. Therefore, recovering the permeability from pressure data via inversion techniques is a feasible practice.

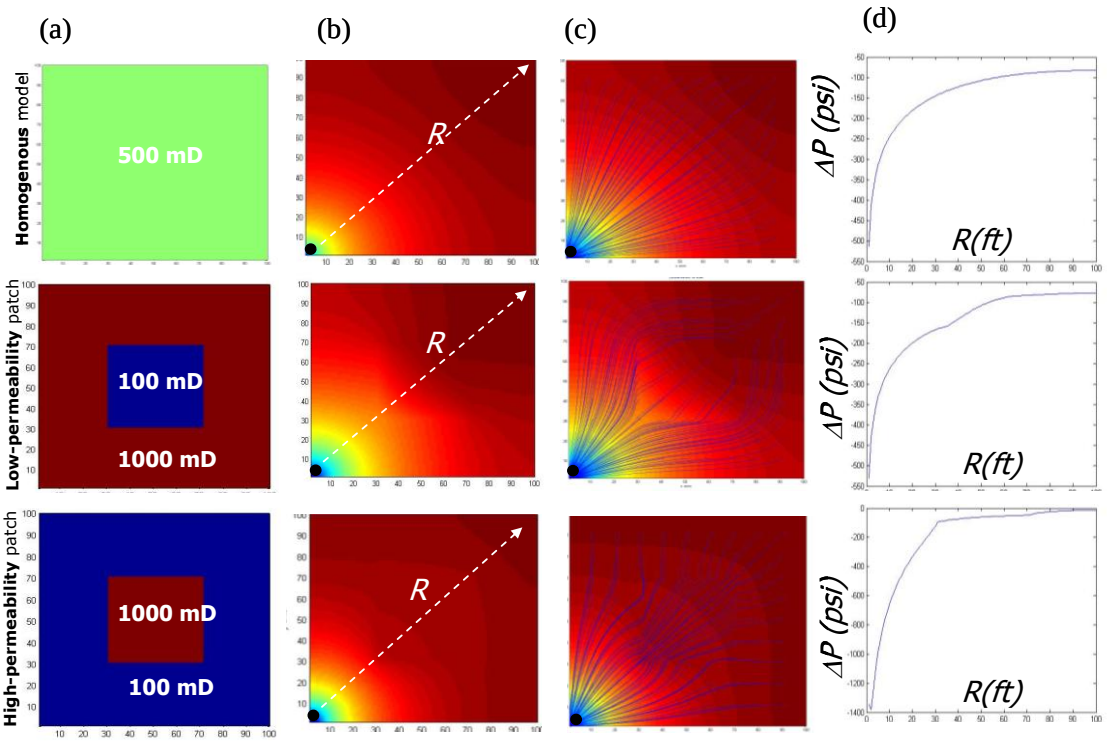

Figure 2.2: *The effect of permeability on the pressure-change response: (a) synthetic cases for high permeability, low permeability, and the homogeneous model; (b) the time-lapse change in pressure for each of the permeability cases; (c) the streamlines of flow; and (d) identification of the permeability signature in time-lapse pressure change in the cross-sectional profile along the diagonal of the model (R).*

2.3 Laplacian calculation

The formula of the Seis2perm transform is derived from the single-phase diffusivity equation (see Appendix B). It is used to estimate the mapped 2D permeability distribution, *K*, using the time-lapse seismic data:

$$K = \frac{c_f(\bar{p}).\mu(\bar{p})}{T_2 - T_1}.\varphi(x,y)\left[\frac{|\Delta A(x,y)|}{\left|\frac{\partial^2(\Delta A(x,y))}{\partial x^2} + \frac{\partial^2(\Delta A(x,y))}{\partial y^2}\right|}\right] \tag{2.1}$$

where c_f is the total compressibility, μ is the fluid viscosity and φ is the effective porosity (porosity × net to gross). ΔA is the seismic attribute difference between the two

seismic measurements, and it is assumed to be dominated by the pressure changes. Note that the permeability is defined where 4D seismic signature is observed ($\Delta A \neq 0$). In other words, if no change of seismic amplitude is captured in 4D seismic responses in a certain area, the resultant permeability map would not provide permeability estimates in that specific region. In addition, The change of compressibility with pressure above the bubble point can be compensated using compressibility compensation factor addressed in section 2.7.2. However, At pressures below the bubble point, a shift in the value of compressibility is occurred (McCain, 1993), particularly around the well locations where main changes in pressure are taken place. This issue is addressed in Chapter 4 where permeability values are calibrated with well information.

Interestingly, in the Seis2perm transform, the 4D seismic appears to provide the permeability solution by itself, by effectively normalizing the conventional 4D signature by a Laplacian term similar to that used in evaluating seismic curvature. Using this technique, the permeability is a derived 'attribute' of the 4D seismic. The solution is dependent on the seismic attribute utilized, although a precondition is clearly an attribute sensitivity analysis for the underlying reservoir pressure. The investigation of the Laplacian functionality demonstrates the response of the second derivatives to the pressure behaviour. The Laplacian calculated for the high-/low-permeability patches in the synthetic model of the previous section is displayed in Figure 2.3. Streamlines are calculated based on the gradient of the pressure change in the *x* and *y* directions, in order to illustrate the flow direction (the gradient of pressure is also called the velocity field over the pressure profile). The direction of the streamlines is the direction of the velocity field. The divergence of the gradient field (Laplacian) has a positive value when the gradient field is expanding (see the streamlines). Conversely, if the gradient field is contracting, then the divergence will be negative.

The numerical stability and accuracy of the permeability values are linked mainly to the denominator of Equation 2.1, and, in particular, the evaluation of the Laplacian and the strength of the second derivative of pressure across the field. The robustness and resolution of the estimate are determined by adjusting the size of the window and the choice of algorithm for calculating the Laplacian (see Appendix C for a description of the various algorithms). Several techniques are used to test the stability of the Laplacian calculation. Figure 2.4 shows the result of the Laplacian calculation for the pressure

response of the high-permeability patch model for each algorithm. It is found that the numerical central difference-based approach and the divergence of the gradient give the most satisfactory and stable result. They show a reasonably good accuracy in detecting the edge of the permeability block. However, a polynomial solution is only an approximation of Laplacian, as it serves as a curve-fitting method to a series of pressure functions in the *x* or *y* directions separately, while the pressure has to be considered as a function of *x* and *y* at the same time, over a surface fitted to the data. In the Laplacian of Gaussian (LOG) method, the smoothness of the Gaussian on the second derivatives prevents the detection of the edges of the permeability block. However, a simple three-term numerical difference approximation and the divergence of the gradient equally provide a result of satisfactory accuracy.

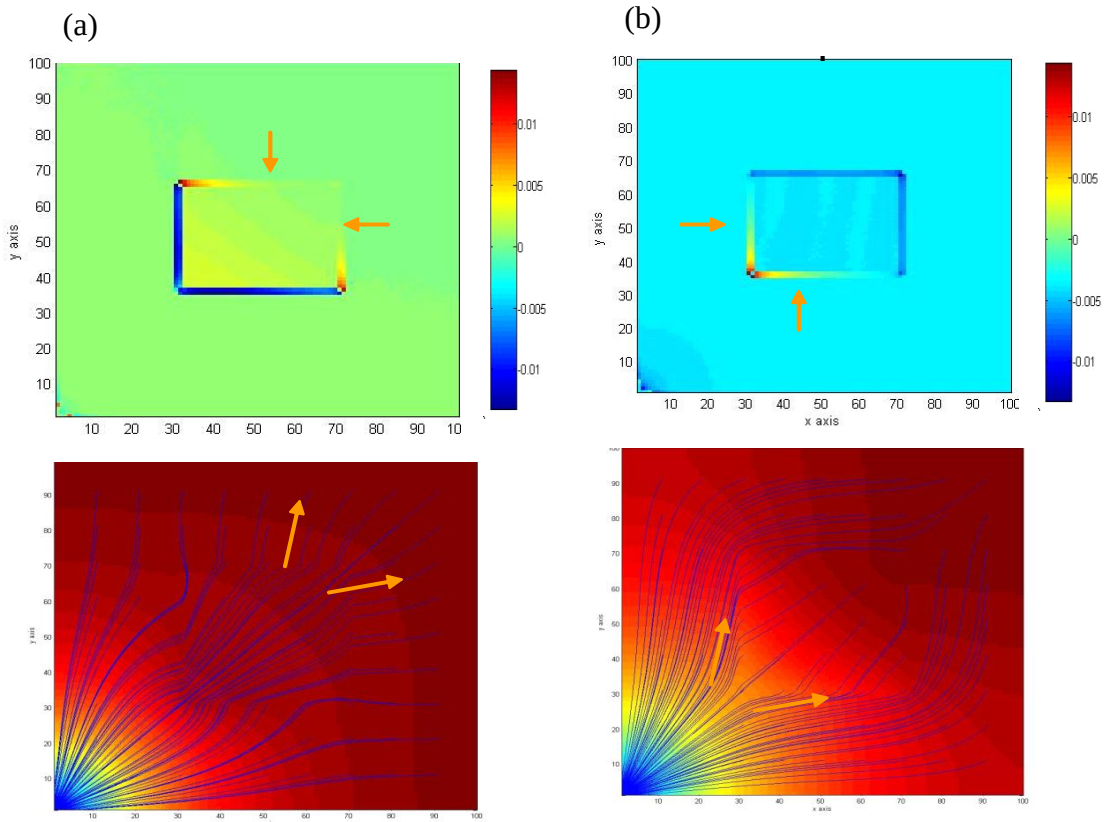

Figure 2.3: *Calculated Laplacian and streamlines demonstrating the gradient fields for the cases of: (a) high-permeability, and (b) low-permeability patches.*

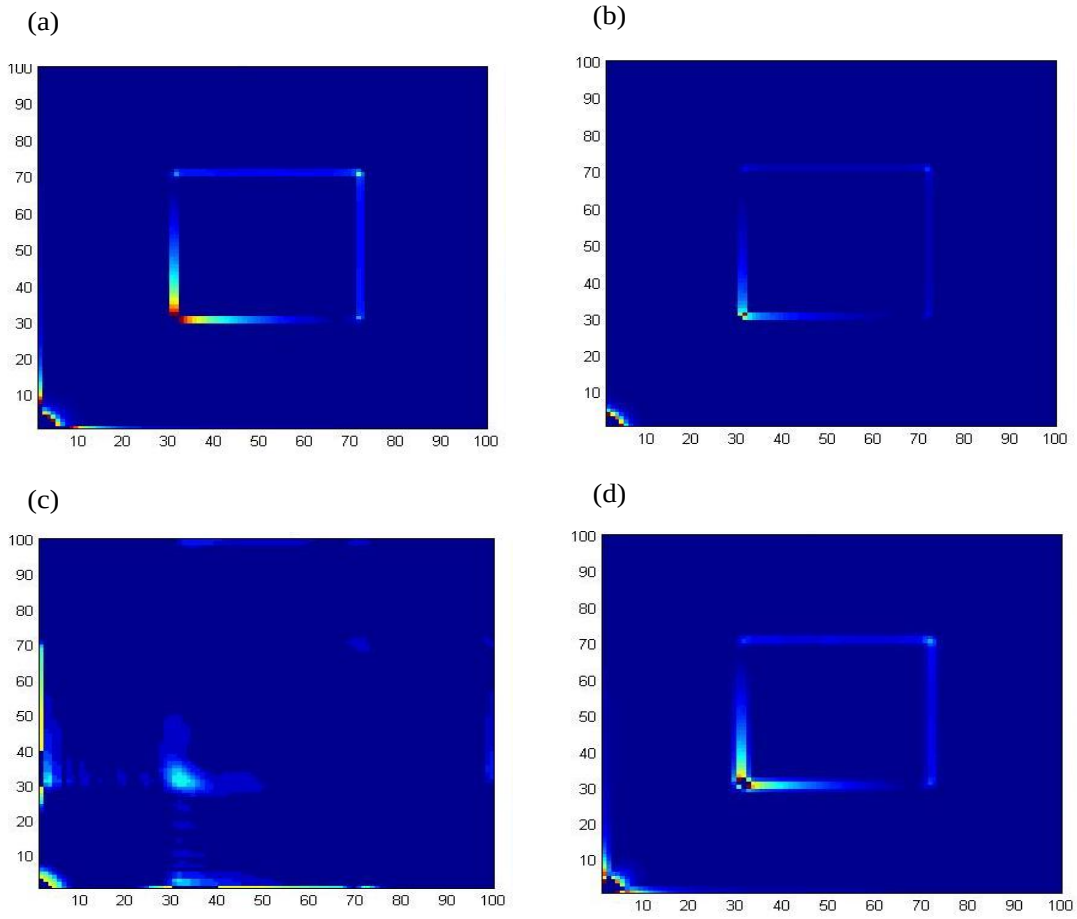

Figure 2.4: *Absolute value of the calculated Laplacian for the pressure response of the high-permeability patch model, using (a) the numerical central difference; (b) the Laplacian of the Gaussian; (c) the polynomial; and (d) the divergence of the gradient.*

2.4 The detection capability of the Seis2perm method (i.e. permeability-signature identification using the Seis2perm method)

In order to test the feasibility and effectiveness of the Laplacian-based method at detecting permeability regions, the permeability signature is modelled using this technique. A variety of models with sequences of low- and high-permeability areas of different sizes are now generated. The simulation is run for these models in order to calculate the pressure changes. Subsequently, the Laplacian of the pressure response is computed. Figure 2.5 illustrates an example of these permeability models, and demonstrates how the Laplacian is calculated from the pressure response of the model.

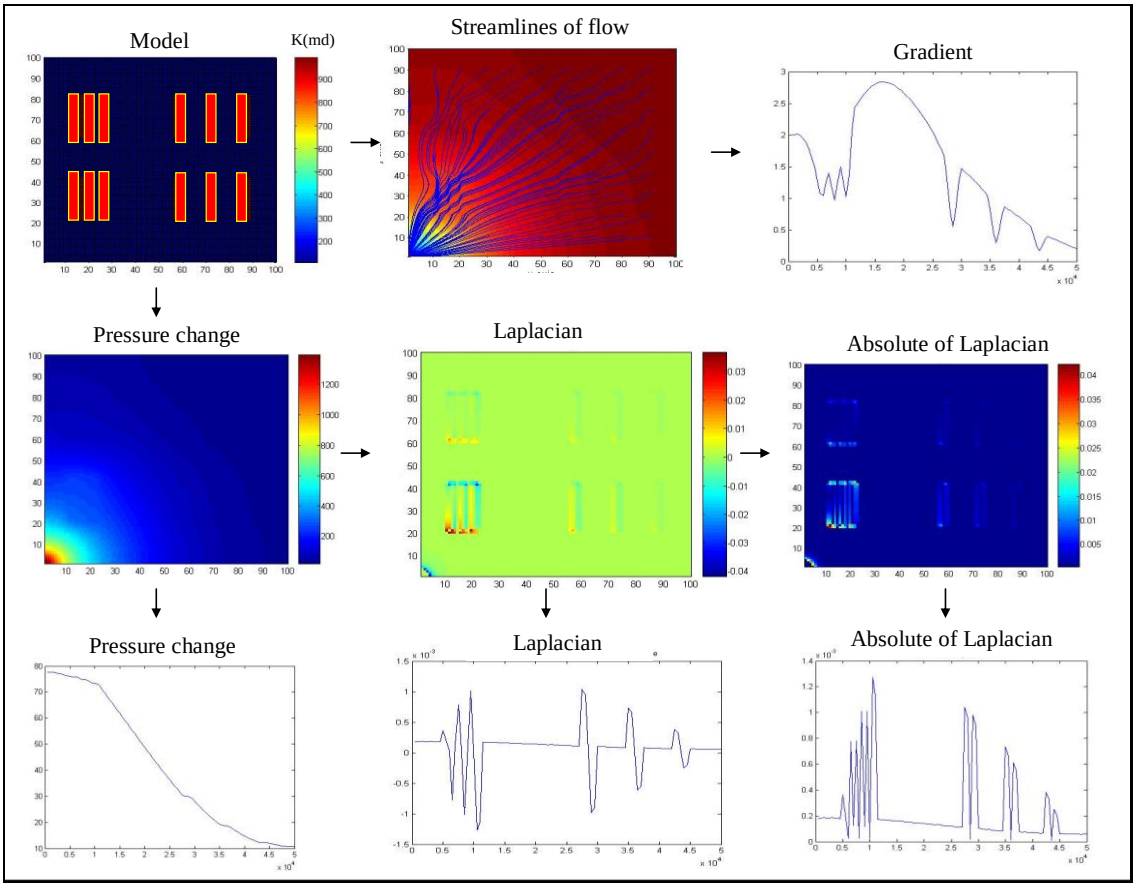

Figure 2.5: *The pressure change, gradient and the Laplacian of the pressure change are computed for the various permeability models. The bottom row shows the horizontal cross-sectional profile of the pressure change in row 30, the Laplacian, and the absolute value of the Laplacian.*

Various types of modelling are performed in order to provide the permeability signatures captured in the absolute value of the Laplacian. It is found that signatures can be categorized in terms of the magnitude of the permeability and the size of the permeability region. The resultant signatures are summarized in Table 2.1.

The categorized signatures enable us to identify the high permeability channels and structures captured in the Seis2perm method. To investigate this, it was decided to examine the absolute Laplacian for the various models. Figure 2.6 shows a cross-sectional profile of the absolute values of the Laplacian for the model shown in Figure 2.5, selected at cell 75 in the *y* direction. In this figure, by referring to Table 2.1 for a narrow block of high-permeability signature, three of this type in the western part Figure 2.6 are distinguishable next to each other, and three further apart in the eastern

part. For the low-permeability narrow block, two related signatures can be identified in the eastern part, between high narrow blocks. For the high-permeability thick block, three features are recognized to the right, between the high-permeability narrow blocks. Finally, for the low-permeability thick block, no related signature is found in this example. To validate this approach to permeability extraction, the recognized permeability features are compared with a reference permeability model. The comparison confirms a good agreement between the captured features, using this method and the reference model of permeability.

Table 2.1: *Captured signatures of permeability in absolute values of Laplacian used in the Seis2perm method, based on modelling for the various generated permeabilities.*

	Thick block	**Narrow block**
High permeability block	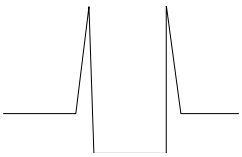	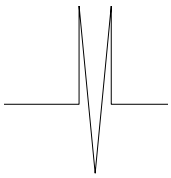
Low permeability block	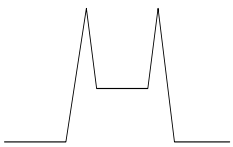	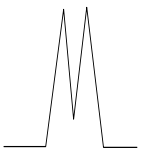

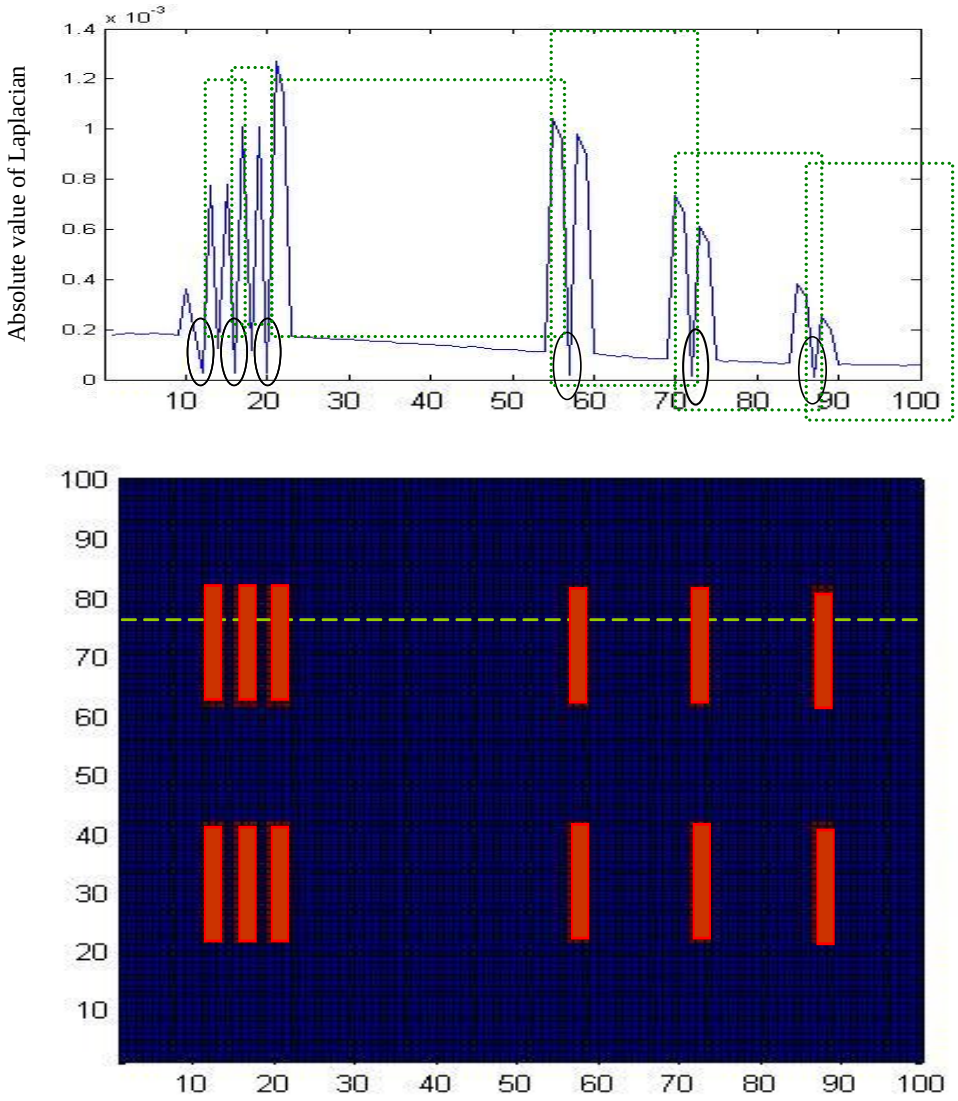

Figure 2.6: *Permeability signature identification using the Seis2perm and recovering the permeability from pressure-change data using the Laplacian.*

2.5 The stability of the permeability calculation (the edge problem in the Laplacian calculation)

In signal processing, the Laplacian operator is a second derivative operator often used in image edge detection (Lindeberg, 1993, 1994, 1998; Ziou and Tabbone, 1998). Similarly, in reservoir geophysics, edge-sensitive attributes, such as curvature and coherence, are used to underline faults and compartments (Roberts, 2001). Coherence attribute computes the trace-to-trace similarity and therefore produces interpretable changes. Similar traces are mapped with high coherence coefficients and discontinuities have low coefficients. Regions of seismic traces cut by faults for example, result in sharp discontinuities in trace-to-trace coherence, producing delineation of low

coherence along fault planes. Curvature attribute is defined by the radius of a circle tangent to a curve and measures the lateral changes in dip magnitude and dip azimuth, and are thus allows to map folds, collapse features, and fault discontinuities (Chopra and Murfurt, 2007). Equally, the Laplacian in the denominator of Equation 2.1 is capable of detecting the edges of channels and discontinuities related to compartmentalization (high values of second-derivaties). However, very high or very low values in the denominator of Equation 2.20 can bias the permeability estimation. This is what is called as an edge problem here. Edge problem involves very high values of the Laplacian at the boundaries of high- and low-permeability patches (synthetic applications) or channels and compartments (real applications) where a rapid change in pressure has occurred. The focus of the current investigation is to understand the behaviour of the Laplacian in high- and low-permeability regions, in order to adjust the calculated Laplacian to compute a stable estimation of permeability.

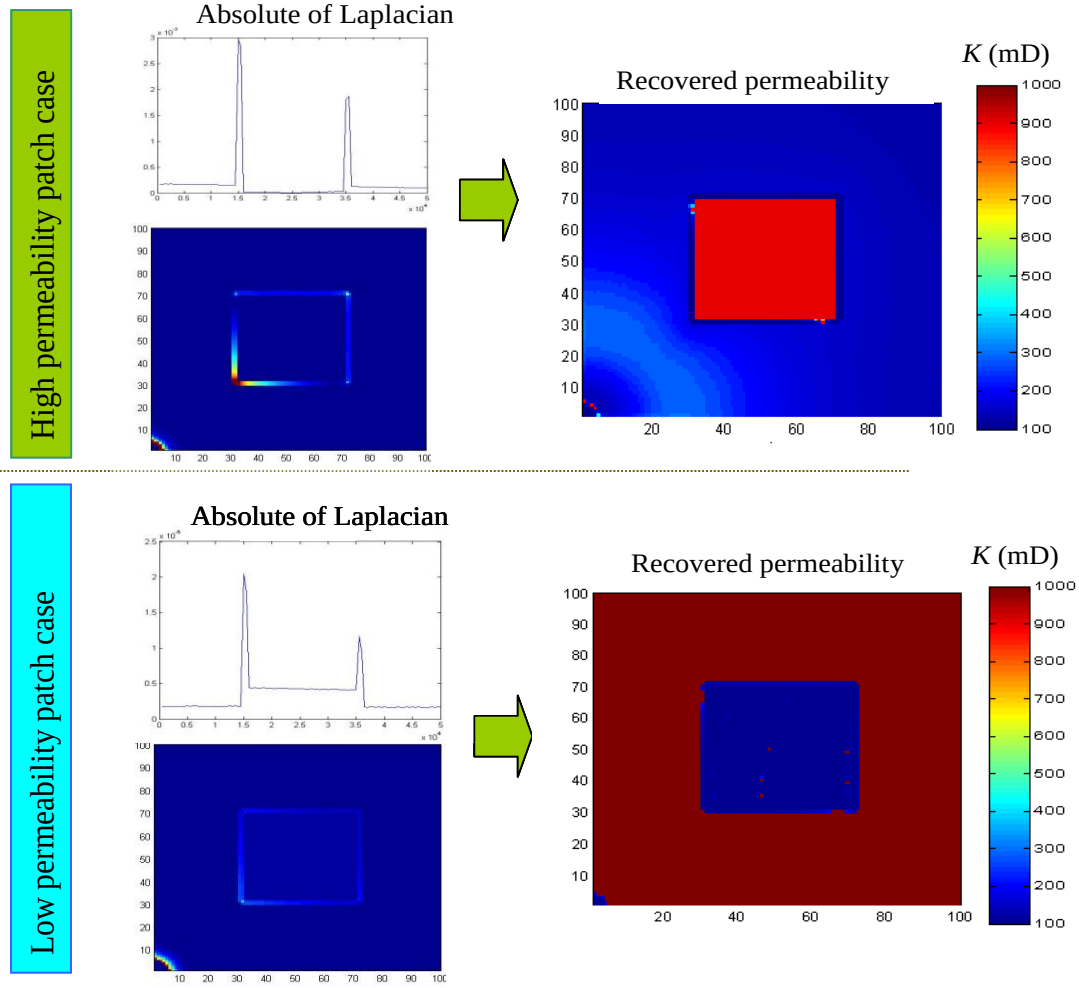

Figure 2.7: *Laplacian versus permeability calculation (the edge problem).*

Clearly, the edge problem has an effect on the recovered permeability for both low-permeability and high-permeability regions. For example, with increasing permeability in a channel, the Laplacian has to decrease in the denominator of the permeability formula. Conversely, this is applicable for the low-permeability area, in which high values of Laplacian are correlated with low permeability. The calculated permeability shown in Figure 2.7 matches this expectation, except at the boundaries of the high-/low-permeability regions. At the edges, high values of the Laplacian for both high- and low-permeability regions alter the permeability result. Edge values in the Laplacian are the direct effect of sudden changes in pressure at the edges of the permeability region. The consequence of changes in pressure will increase first in the gradient and then in the Laplacian calculation, as demonstrated in Figure 2.8.

As the width of the pressure anomaly tends to be shorter, the boundaries of the compartment or channel become closer to each other (see the permeability signature of the narrow block in Table 2.1). As a result, the high values at the edges will be the dominant features in the Laplacian maps. Figure 2.9 illustrates how this may lead to our observing high Laplacian values in the region where, based on the other data available in field, one may expect high permeability. This occurs due to a dominating edge-values effect. To treat the instability in the permeability estimation, several filters are examined in order to control and smooth the sharpness caused by the Laplacian edge values.

By applying different filters, it is revealed that the Gaussian low-pass filter and moving average filter applied at the edges could successfully de-spike the contrasts around the edges (see Figure 2.10). However, the intention is not to flatten of the edge effect. Instead, the idea is to de-spike the pulse at the boundaries, so that the final permeability map will have an appropriate stability. On the other hand, sustaining the boundaries of the compartments in the final permeability is of interest. In fact, this is an interesting effect that is captured by the seismic-derived permeability estimates, and it contains the influence of barriers and sealed faults. If the computation window for the permeability straddles a barrier, then the effective permeability must be diminished. The exact drop in permeability depends on the size of the window and the way in which the Laplacian in the denominator of Equation 2.1 is calculated. This information is identified at the lower end of the permeability spectrum, and may be useful in assessing the

transmissibility of the barriers, but it requires more interpretation and analysis to bring out the details.

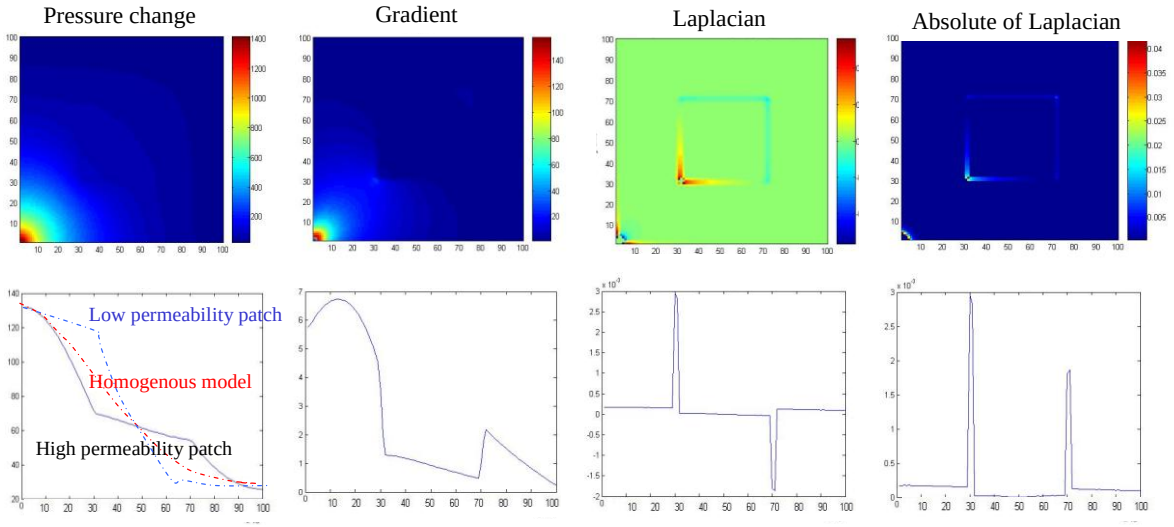

Figure 2.8: *High Laplacian magnitudes at the edges of the permeability region are a direct effect of the sudden change in pressure. This change increases in the gradient terms, and then in the Laplacian calculation.*

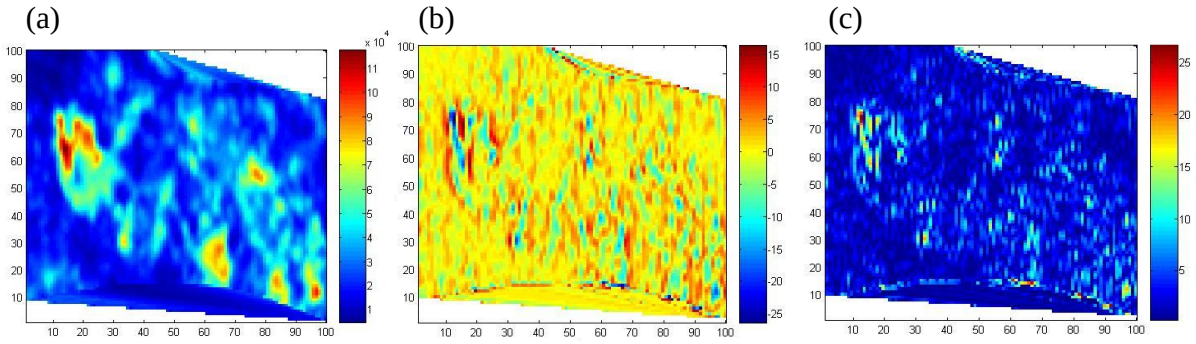

Figure 2.9: *(a) Time-lapse signature between 1993 and 1999 in the Schiehallion field; (b) the Laplacian of pressure-dominated time-lapse amplitudes; and (c) the absolute value of the Laplacian indicates edge problems in a field application: i.e. due to dominating edge effects, a high Laplacian is observed where a high-permeability region is expected based on the other available permeability data in the field.*

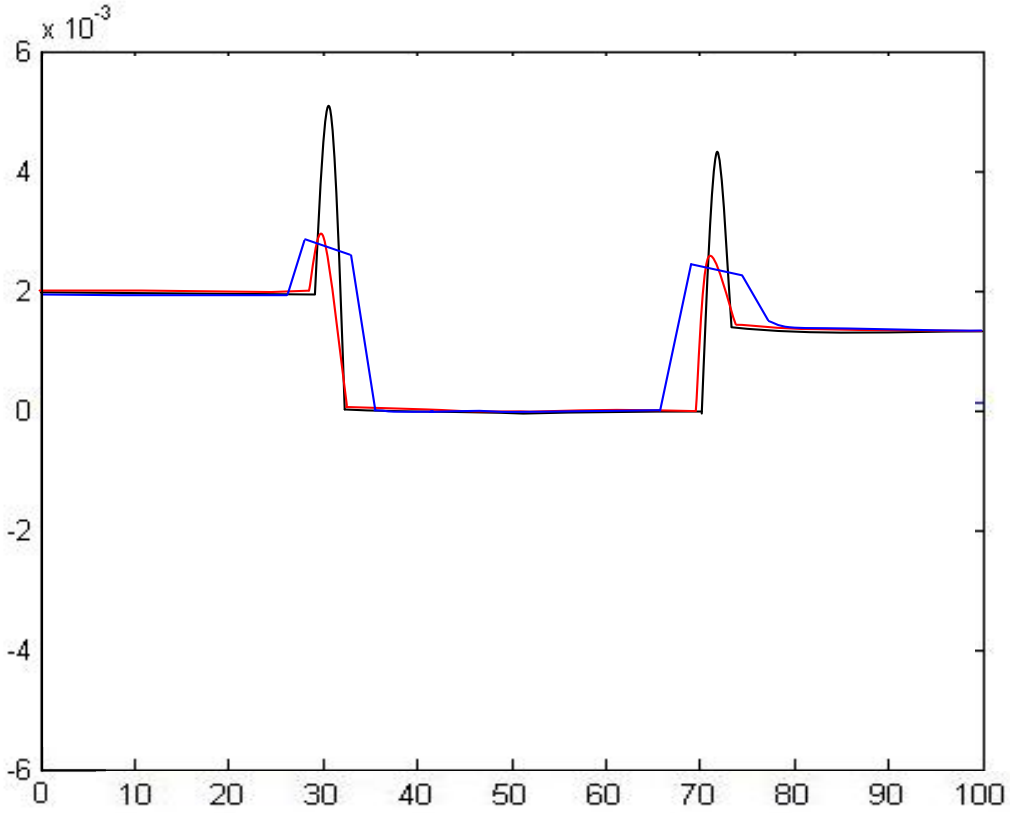

Figure 2.10: *The smoothing on the calculated Laplacian needs to be applied in order to control and smooth the edge values. The black curve was originally calculated for the Laplacian of a high-permeability blocky model; the red curve is a Gaussian loss-pass filter applied to the Laplacian; and the blue curve is a moving average for a window defined around the boundaries applied to the Laplacian at the edges.*

2.6 Permeability estimation from different time-lapse surveys

Pressure as a dynamic property evolving over time could be different from the same static model. It is a function of time and distance from the well, $P(r,t)$, and varies once the injection/production rate or bottom-hole pressure in the wells changes due to production activities. Hence, recovering the permeability as a static property from dynamic pressure is challenging.

A test is performed to investigate this issue using the Seis2perm transform. The simulation is run for the high-permeability patch model for 700 days, and time-lapse pressures are calculated for 100, 200, 400 and 700 days after production, to see how

considering the different time-lapses may affect the final permeability calculation. Figure 2.11 illustrates how pressure disturbance moves across the reservoir within the reservoir production time period. The outer boundaries are treated as no-flow boundaries, meaning that the model is surrounded by completely impermeable rock.

Sensitivity analysis using different pressure scenarios shows that the stable result for permeability estimation is obtained when the stabilized pressure profile (after an early time of simulation) is established. At this stage, the permeability can be calculated more accurately from the pressures. Figure 2.12 shows that, as the time-span of the simulation increases, the pressure gradients (and second derivatives) become stronger. The time-lapse signature developed after 100 days cannot deliver an accurate estimate of permeability. In comparison, at later times the errors drop to a fairly manageable level and the permeability structure is recovered more accurately.

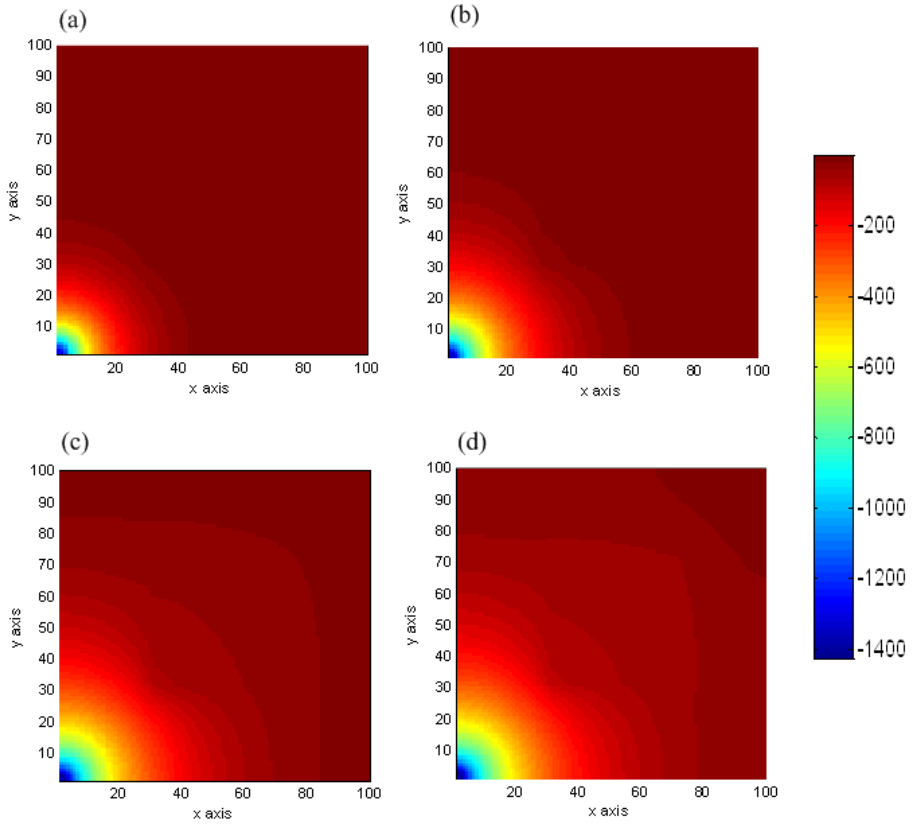

Figure 2.11: *Pressure change (a) 100 days after production; (b) 200 days after production; (c) 400 days after production; and (d) 700 days after production. Due to pressure diffusion, the pressure disturbance is moving with time.*

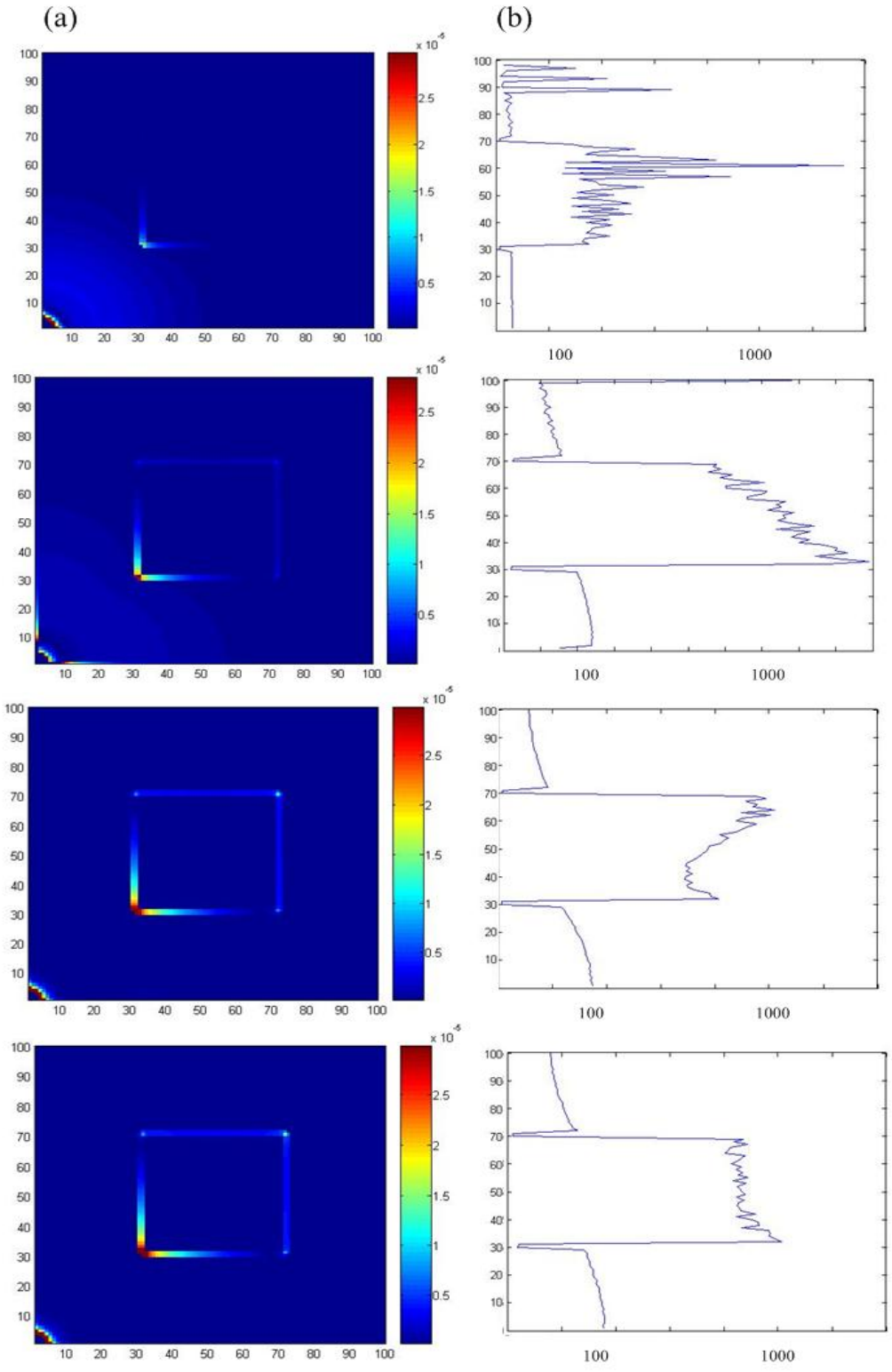

Figure 2.12: *(a) Absolute value of Laplacian for the high-permeability patch model after 100, 200, 300 and 700 days' production (top to bottom), and (b) a cross-section of the corresponding calculated permeabilities at row 50.*

2.7 Application to the Schiehallion field

The Seis2perm is implemented on a dataset from the UK continental shelf. More details of this field and the relevance of seismic interpretation and integration are presented in Parr and Marsh (2000). For the current investigation, post-stack migrated 3D-seismic volumes from 1999 (monitor survey, time T_1) and 1993 (base survey, time T_0) are available. Prior to our study, the seismic data are cross-equalized and the results are found to be sufficiently good to enable further accurate studies. The producing interval of specific interest in our study is the T31a sand, in which compartments and faults are noticeable. The southernmost sector of the field is chosen, separated from the other sectors by a sealing normal fault. In this sector there are four active wells, two vertical water injectors and two active horizontal producers, in the time period between the base (time T_0) and monitor (time T_1) surveys. Water-flooding has been applied in order to maintain the pressure and to sweep the remaining oil. The initial reservoir pressure is close to the bubble-point pressure, but the gas does not exsolve from solution during the time period of interest. Figure 2.13(a) shows the changes in the seismic signature between times T_0 and T_1.

The seismic attribute used is the 'sum of negative values', as it is believed to have the 4D attribute that which has an adequate response from pressure, according to past experience in this field (Floricich, 2006). The 4D signatures show an obvious general brightening around the two injector wells, with injector C_{12} giving a smaller response, as its injection rates are generally lower. In contrast, the main producer, P_4, brightens slightly. The calculated Laplacian for the 4D-seismic attribute is displayed in Figure 2.13(b).

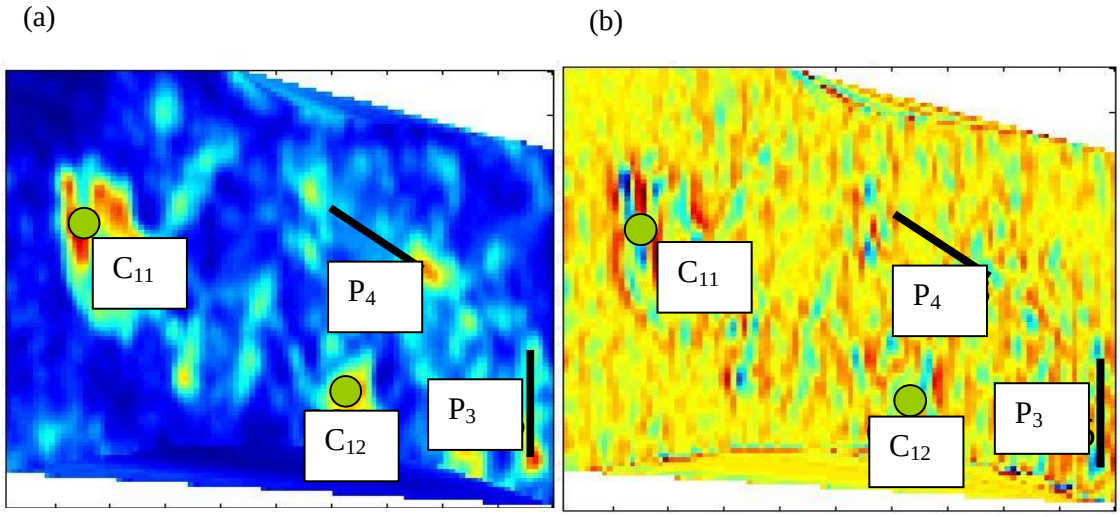

Figure 2.13: *(a) Time-lapse seismic signatures between 1993 and 1999, and (b) the calculated Laplacian in west-east direction (x direction).*

In practice, the difference attribute $\Delta A(x,y)$ might be either a point measurement or a localized average, depending on the numerical accuracy, while the Laplacian terms are by necessity estimated using several cells surrounding the central (x,y) location, and are thus more global estimates. In implementation, estimates are obtained using Equation 2.1 for each position of a moving 2D window, in order to obtain a spatially dependent permeability (K) –with the robustness and resolution of the estimate being determined by adjusting high values of edges in the Laplacian using the appropriate filter.

2.7.1 Effective porosity calculation

The information on the effective porosity must be supplied prior to the permeability calculation. Equation 2.1 takes into account a macroscopic porosity–permeability relationship, with the constant linking of the two parameters being controlled by the 4D response of the reservoir. In Equation 2.1, the permeability is assumed to be proportional to the porosity field; however, it is not linearly correlated, as the relationship is modified by the 4D-seismic term, involving the strength of the 4D seismic signature and its spatial variation expressed via the Laplacian in the denominator. The general prediction is that the horizontal permeability is best when porosity is highest, or when the 4D-seismic signature is most intense.

The most convenient estimate of porosity comes from the base-line seismic amplitude, because all of the other main elements in the formula, such as the Laplacian and the 4D signatures, are defined at the seismic scale. If the base-line seismic attributes could be scaled appropriately, then they would be transformed into an effective porosity product. The value of the threshold is set by inspection of the histograms of the base-line seismic amplitudes. A reservoir-specific transformation was applied to convert the seismic amplitudes to effective porosity. The mean and variance are controlling parameters which are determined by inspecting the data from the simulation model, yielding a mean of 0.25 and a standard deviation of 0.045. It is recognized that the approach for evaluating effective porosity is likely to vary from field to field:

$$\phi_{\text{eff}} = \phi_0 + \delta\phi\left(\frac{A_{\text{bl}} - \overline{A_{\text{bl}}}}{A^{\max}{}_{\text{bl}} - \overline{A_{\text{bl}}}}\right) \tag{2.2}$$

where ϕ_{eff} is the effective porosity; $A_{\text{bl}}^{\max}$ is the maximum value of amplitude in the base-line survey; $\overline{A}_{\text{bl}}$ is the mean value of amplitude of the base-line survey, A_{bl} is the amplitude of the base-line survey; $\delta\phi$ is the variance of the simulation model porosity; and ϕ_0 is the mean value of the simulation model porosity. The estimated porosity is shown in Figure 2.14.

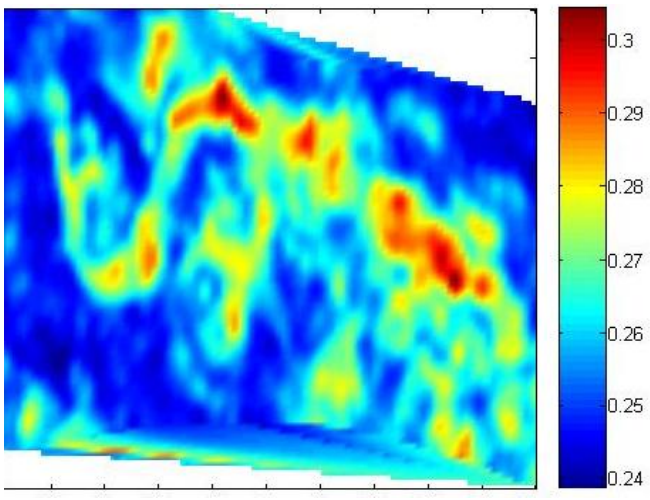

Figure 2.14: *Estimated porosity from the 1993 base-line seismic.*

2.7.2 Compressibility calculation

Reservoir pressure tells us how much potential energy the reservoir contains (or has left) and enables us to forecast how long the reservoir production can be sustained. However, pressures in the vicinity of the well-bore are affected by production activities, and may be much more or much less than the pressure of the reservoir at large. The effect of well activities on permeability estimation becomes important when the pressure at the well locations differs significantly from that of the reservoir. The over-pressured area around the wells does not necessarily allow geological features to be indicated. This implies that the method is mainly applicable to regions away from wells, as excessive pressure gradients caused by neglecting the source terms in Equation A.13 (in Appendix A) tend to invalidate the assumptions upon which Equation 2.1 is based. Therefore, calculating fluid compressibility appears to be necessary to estimate stable permeability results in the vicinity of the over-pressure area at well locations. Since compressibility is a pressure-dependent property, the 4D-seismic-dominated pressure can be directly linked to the compressibility calculation. The oil compressibility above the bubble point is given by the following equation:

$$C_{\mathrm{o}} = -\frac{1}{B_{\mathrm{oi}}}\left(\frac{\partial B_{\mathrm{o}}}{\partial P}\right)_{T} \tag{2.3}$$

where B_{oi} is the initial oil-formation volume factor, and the term in brackets is the fractional change in the oil-formation volume factor (B_{o}) as the pressure (P) is changed at a constant temperature (T). In addition, the pressure change is considered to be varying approximately linearly; hence, it is assumed that:

$$\overline{P} = P_1 + \frac{1}{2}\Delta P \tag{2.4}$$

where $\overline{P}$ is the average pressure between P at time T_0 and T_1; ΔP is the change in pressure between T_0 and T_1, and P_1 is the initial pressure. The graph in Figure 2.15 shows the validation of the linear approximation of pressure variation in this reservoir. The red curves correspond with a cell between two injectors but away from most of the producers, while the black curves correspond with a cell in the vicinity of a producer. The linear approximation (dashed line) is used to evaluate Equation 2.4, and is based on approximating the areas under the pressure curves, between the production start-up and the survey date, by the area under the straight line drawn between the two survey

pressures. This approximation appears to be reasonably well justified in these two examples. On the other hand, the 4D-seismic signature, ΔA, is assumed to be directly proportional to the reservoir pressure change, ΔP, for this reservoir (see MacBeth and Al-Maskeri, 2006 and Floricich, 2006). Therefore, the pressure change can be expressed by:

$$\Delta P = \left(\frac{\Delta P_{max}}{\Delta A_{max}}\right).\Delta A \tag{2.5}$$

where ΔP_{max} is the maximum pressure change in the reservoir and ΔA_{max} is the maximum time-lapse signature. Thus, substituting Equation 2.4 and Equation 2.5 in Equation 2.3, yields:

$$C_o = \frac{1}{B_{oi}} \frac{B_o\left(\overline{P}\right) - B_{oi}}{\frac{1}{2}\left(\frac{\Delta P_{max}}{\Delta A_{max}}\right)\Delta A} \tag{2.6}$$

As a result, the compressibility calculation is linked to the 4D seismic, and can be calculated using the 4D signature at the seismic scale.

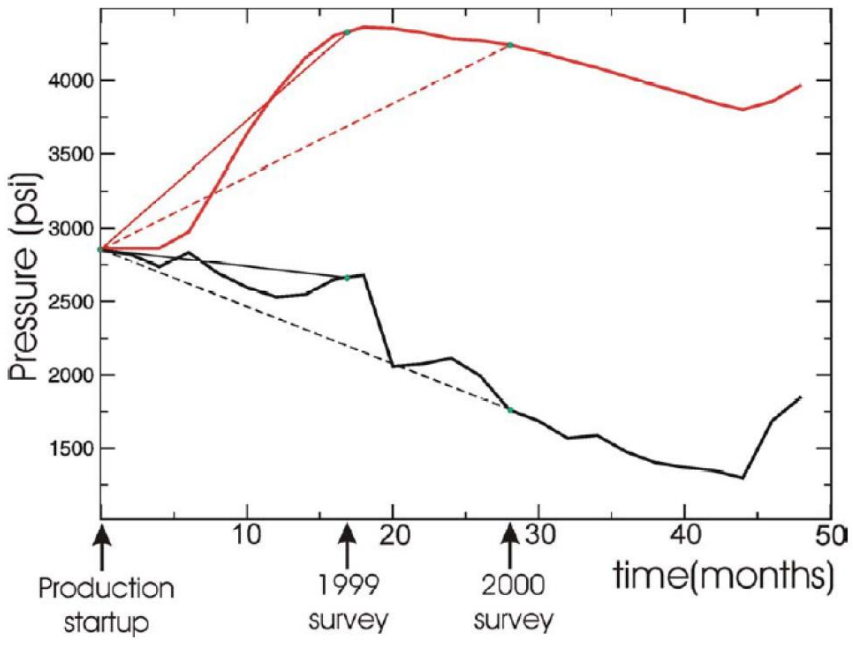

Figure 2.15: *Validation of the linear approximation of pressure variation in this reservoir: the red curves correspond with a cell between two injectors but away from most of the producers, while the black curves correspond with a cell in the vicinity of a producer (after MacBeth and Al-Maskeri, 2006).*

2.7.3 Estimated permeability in the Schiehallion field

The permeability result of Seis2perm calculated for the Schiehallion field is shown in Figure 2.16. Sequences of narrow channels of permeability are imaged by the seismic permeability solution, where zones of high permeability are mostly bounded by the picked fault segments. The permeability results are found to be of satisfactory quality when checked and validated with other available data such as a compartmentalization map, geological settings, a connectivity map, and the porosity–permeability relationship within channels in the model (see Figure 2.17). Comparison in terms of the compartmentalization point of view shows a degree of agreement between very compartmentalized segments proposed for Schiehallion and the sparse pattern of high-permeability regions in the solution of the permeability transform. In fact, the presence of segmentations and compartments explains the discontinuities and sparse pattern of calculated permeability. In addition, comparison with the facies map indicates the major channels that are imaged by the Seis2perm transform. Tracing channels and compartments through the porosity–permeability relationship is another comparison that can be made on the permeability result. It appears that the outline structure of the high-permeability pathways is similar with the porosity structure in some locations.

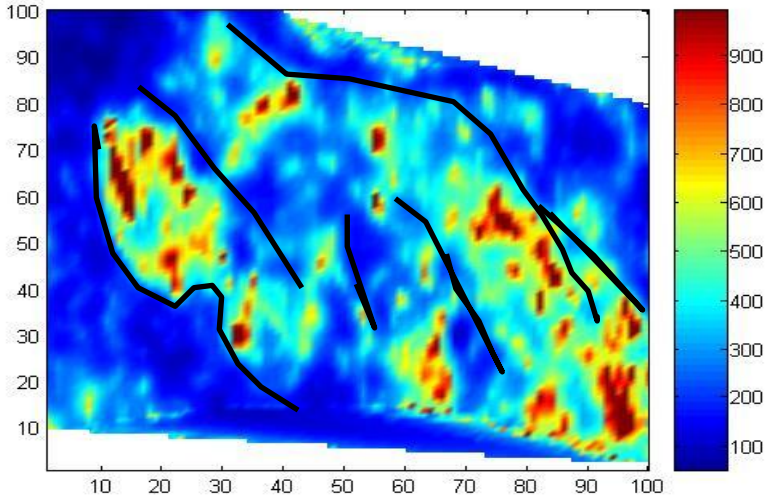

Figure 2.16: *Estimated permeability using the Seis2perm method.*

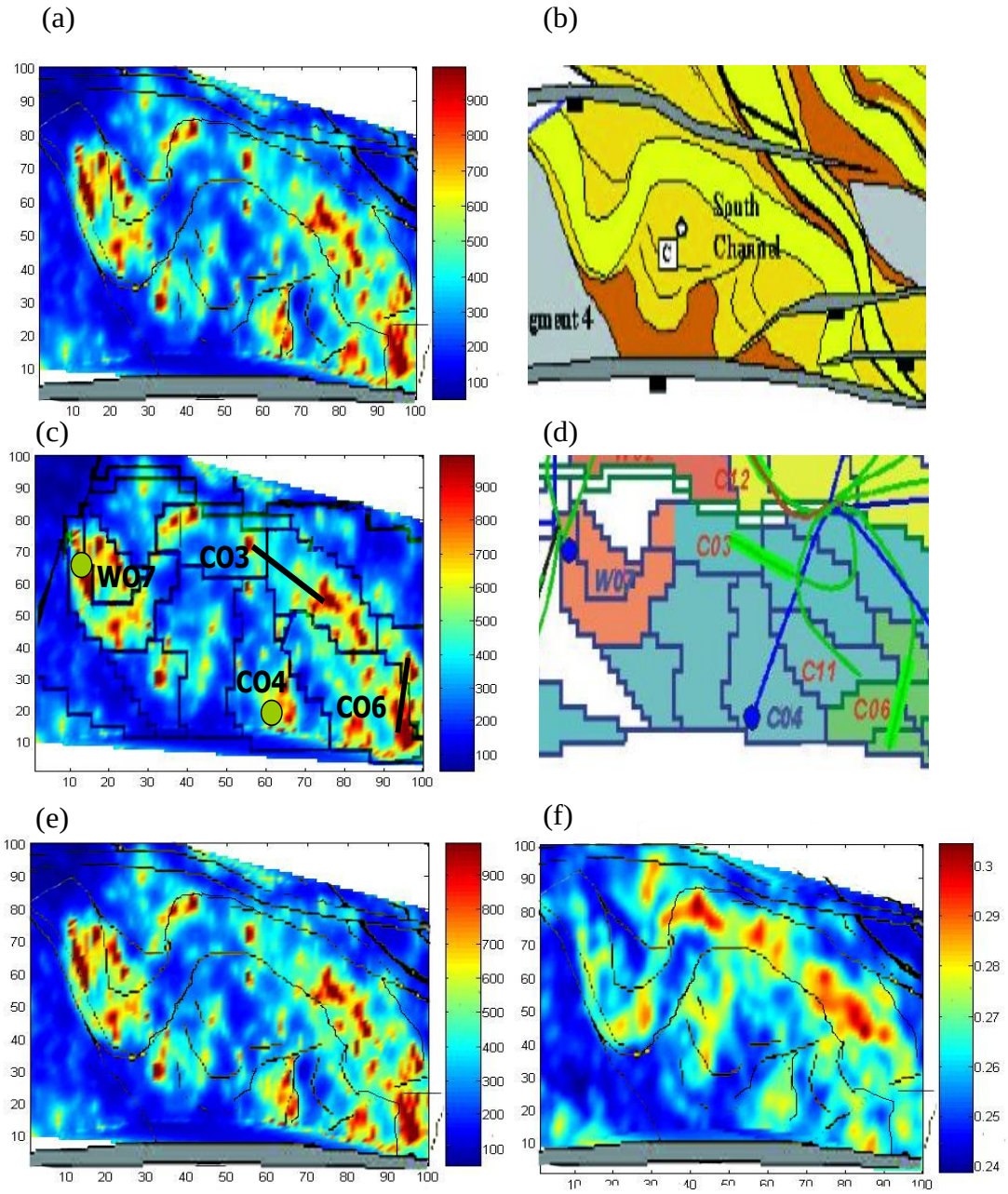

Figure 2.17: *(a) and (b) A comparison of the estimated permeability pathways with the Schiehallion facies map (after Leach et al., 1999) shows a fair agreement between the calculated permeability pathways and the major and minor channels of the T31a sand; (c) and (d) show that the sparse pattern of permeability is consistent with Schiehallion compartmentalization (after Dobbyn and Marsh, 2001); and (e) and (f) comparison of the estimated permeability with the effective porosity shows similarity through the channel orientations.*

2.8 Application to the Girassol field

Girassol is a field located in the Gulf of Guinea, Angola, and was discovered in 1996. It is a deep-water (1250–1400 m) reservoir, consisting of large, vertically stacked turbidite channels with high porosity and permeability (up to 40% and *c*.8 Darcy). Pre-production high-resolution seismic was acquired in 1999 and the first monitor seismic was run after one year of production had started in late 2002. The second monitor was run in 2004. In the current study, the time-lapse seismic attribute calculated between 1999 and 2002 was used for permeability extraction.

The permeability transform that was applied to the 4D attribute for part of field data is displayed in Figure 2.18. This figure shows that the permeability in the simulation model agrees with the estimated permeability, i.e. the patterns look the same. However, there are some differences in the details: clearly there is no connection with the lower permeability, even though there are sands present. This shows that the 4D attribute has not imaged the sands, because it is in a no-data area. The simulation model has larger permeabilities than the estimated permeabilities. However, the estimated permeabilities appear to suggest a more continuous distribution.

In another example, the pressure change extracted from 4D seismic in the central part of field is used to calculate the permeability. Applying the Seis2perm transform, the permeability distribution is displayed in Figure 2.19. The estimated permeability shows more continuity in the reservoir relative to the simulation-model permeability, especially in the eastern and western parts where the continuity of the channels can be traced. It also indicates an increase in permeability close to the fault in the south. Moreover, lateral connections in the estimated maps are noticeable. So, generally, one may suggest that the estimated permeability shows an enhanced image of permeability relative to the simulation-model permeability.

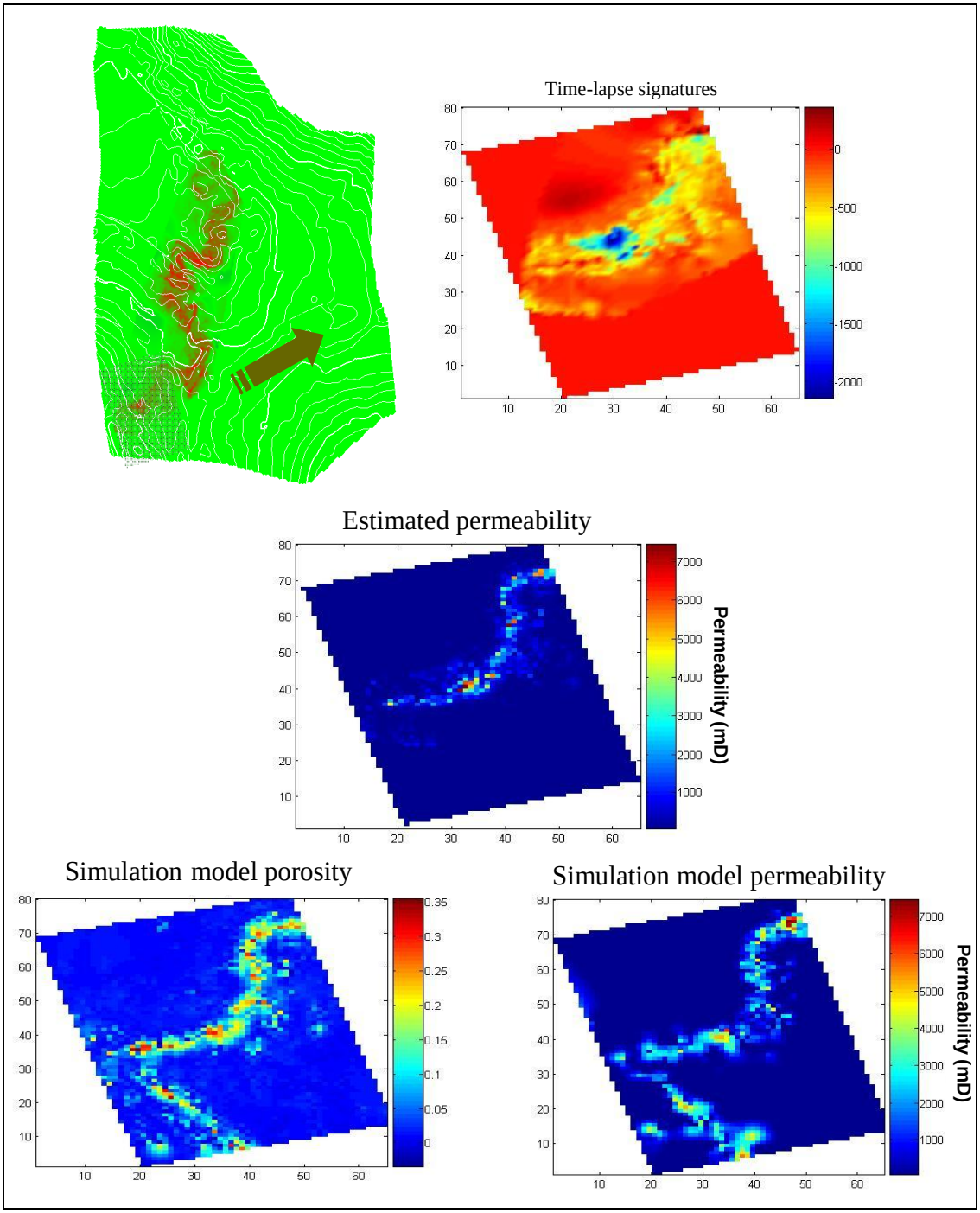

Figure 2.18: *The Seis2perm transform is applied to the southern part of the Girassol field. Comparing the estimated permeability with the simulation model, the solution appears to be in fair overall agreement with the depth-averaged permeability, although the locations of the main highs and lows are somewhat different.*

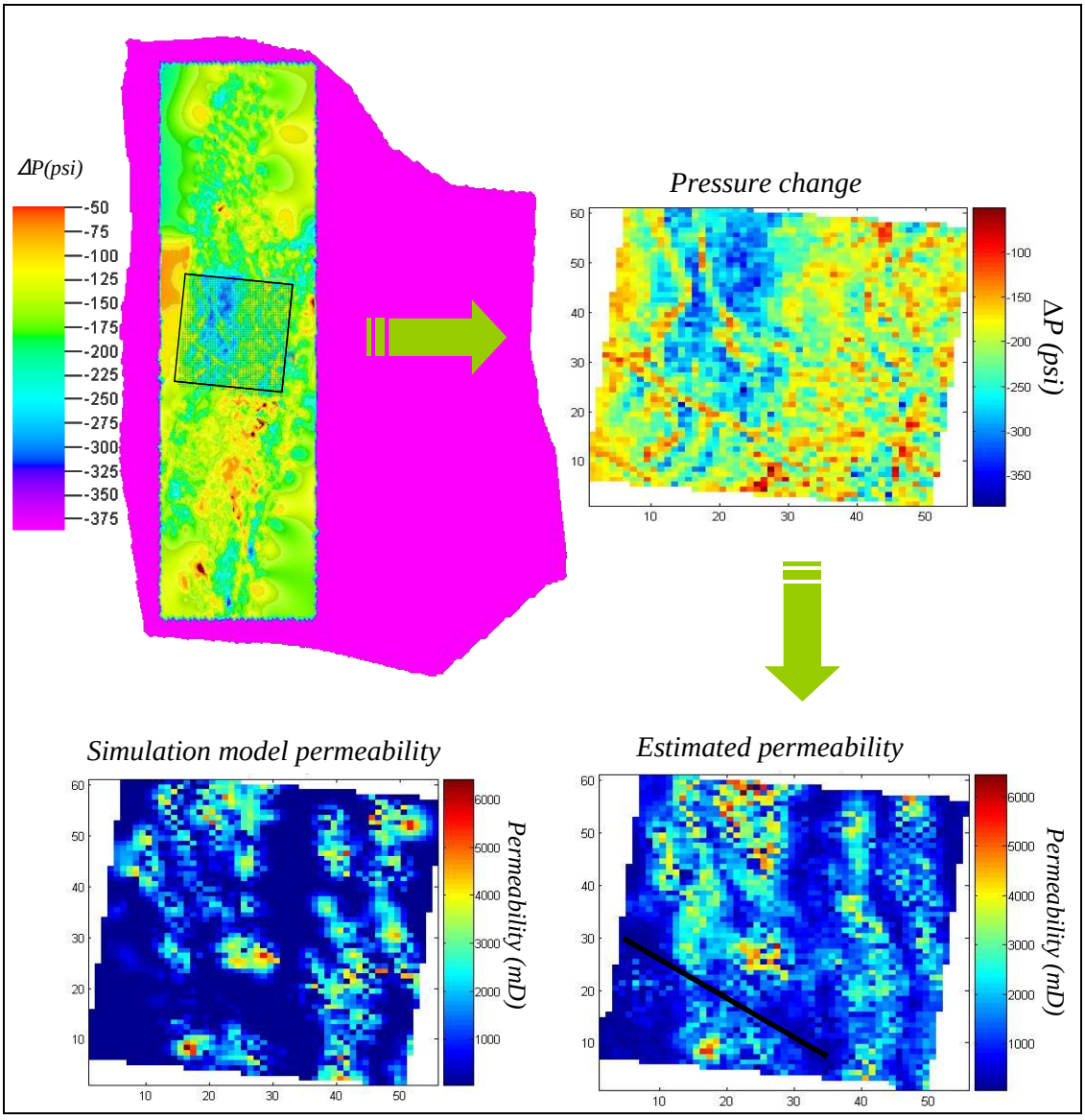

Figure 2.19: *The Seis2perm transform is applied to pressure changes in the central part of the Girassol field. Compared with the simulation model, the outline structure of the permeability is very similar to the simulation model.*

2.9 Summary and conclusions

Tests on synthetic models have shown that the Seis2perm method can recover accurate permeability features if the Laplacian can be calculated precisely. Application to real data examples (e.g. the Schiehallion and Girassol fields) has further demonstrated the robustness and the potential value in providing permeability at a seismic-scale resolution. In this approach, the 4D-seismic amplitudes can be directly converted into permeability, with only a few additional constraints from the engineering domain. The porosity field, however, does need to be known, and must be obtained from the base-line seismic data or the geological model. In fact, this methodology suggests the introduction of a new attribute, which can be termed a 'permeability attribute', using a simple transform that is proven to show permeability features. This attribute can serve as a quick and practical assessment of aerial connectivity in the field.

The outcome of 4D-seismic permeability estimation is a permeability map that can be utilized as an initial impetus to improve history matching in the simulation model. The next step would be to feed the simulation model with the estimated permeability between the wells, in order to limit the problem of non-uniqueness in the traditional history-matching process. This step is addressed in Chapter 3. Another aspect of the permeability calculation is the uncertainty in the measurements and how these might propagate into the simulation model update. This is discussed in Chapter 4.

CHAPTER 3: UPDATING THE SIMULATION MODEL USING 4D-SEISMIC-DRIVEN PERMEABILITY

Overview

In this chapter, a new methodology is presented for updating the simulation model by incorporating 4D-seismic-estimated permeability. Using the proposed method, it is possible to build an improved 3D permeability model by integrating the pre-existing 3D simulation model of the reservoir and the time-lapse seismic results. History matching is then carried out using the 3D permeability model that has been generated. The history-matching method used here is a gradient-based history-matching approach, which uses production data to update the simulation model.

The new proposed ‘bump-update’ history-matching approach is then analysed and compared with conventional history-matching, in an application to the same dataset. This examination is performed in terms of the resultant permeability models and matching with the history data (the objective function). In conclusion, this study discusses the effectiveness of 4D-seismic-directed updating.

3.1 Introduction

The traditional practice of reservoir modelling starts by creating a high-resolution 3D geo-cellular model using static data, and then up-scaling this model to build simulation-model static data. This model honours the static data, but does not match the production data; therefore, a history-matching procedure is applied to match the model with the production data. Having reservoir static properties such as permeability, porosity and NTG, the flow simulation is run to model the pressure diffusion and saturation transmission in the reservoir. Hence, dynamic parameters (properties that are changing over time) such as water-cut, bottom-hole pressure, and flow rates at the well locations, are modelled. These modelled data are compared with history data gathered from the field. This process is called *history matching*.

In history matching, an optimization algorithm is chosen in order to find the minimum misfit or objective function between the observed data and the adjusted modelled data. However, due to the non-uniqueness problem, there could always be other models that produce a similar reservoir-production response. To obtain a model that matches the true reservoir behaviour as closely as possible, the effect of every single parameter must be reviewed by the multidisciplinary team conducting the study. When the parameters for optimized history matching are properly selected, the optimum value of the reservoir parameter is found in a way that produces the lowest mismatch between the observed and predicted values for reservoir production. Once the model has been set up and then verified through history matching, it can be used to predict the future reservoir behaviour that would arise from different development scenarios, such as different production rates, infill drilling of development wells, and depletion drive versus water- or gas-injection.

The conventional methods involve the use of only sparse well data as dynamic data, which may result in the matching of too many possible models. However, a novel technique recently practised in the oil industry is to use the 4D seismic as additional dynamic data in the history matching. The advantage of this additional component in the history-matching process is that it can use the spatial constraints offered by the 4D seismic, which extensively limits the problem of non-uniqueness (Gosselin *et al.*, 2003; Stephen and MacBeth, 2006).

In both these types of approaches, a perturbation technique is performed (manually or automatically) on the reservoir static model until a satisfactory production-data match is achieved. Also, usually the static data are forced and altered in order to obtain a good dynamic match that may not eventually represent the geological features. This means that, despite the fact that a good match in the optimization problem is achieved, the model mainly matches the production history; hence it precludes the reliable prediction of future performance.

In order to overcome the shortcomings associated with conventional history-matching schemes, in this study an alternative approach is proposed: utilizing 4D-seismic-estimated permeability. The 4D-seismic permeability inversion techniques are used to provide a geologically constrained permeability model for updating the simulation. This facilitates the simulation and perturbation of the reservoir model, while simultaneously honouring both the static and the dynamic data. The goal of this study is to supply a fast and effective method of updating the simulation, using the 4D-generated information as a direct and bump updating method. This can serve as an alternative to other methods that indirectly produce history-matched permeability through minimizing the objective function in an optimization process.

The workflow of the procedure proposed in this chapter covers steps 2 to 4 of the whole general workflow of this thesis. The former is illustrated in Figure 3.1. In the first part of the study, the permeability is estimated from the 4D seismic. In previous chapters, a direct transform of the time-lapse seismic signatures into a permeability map was investigated. Then the results of this method are further enhanced in order to become suitable for feeding into the reservoir-simulation model. In the next step, the permeability map thus produced is used to update the 3D reservoir-simulation model. The seismic-resolution problem is tackled in the process of integrating the 2D permeability map (derived from the 4D seismic) with the 3D reservoir permeability model.

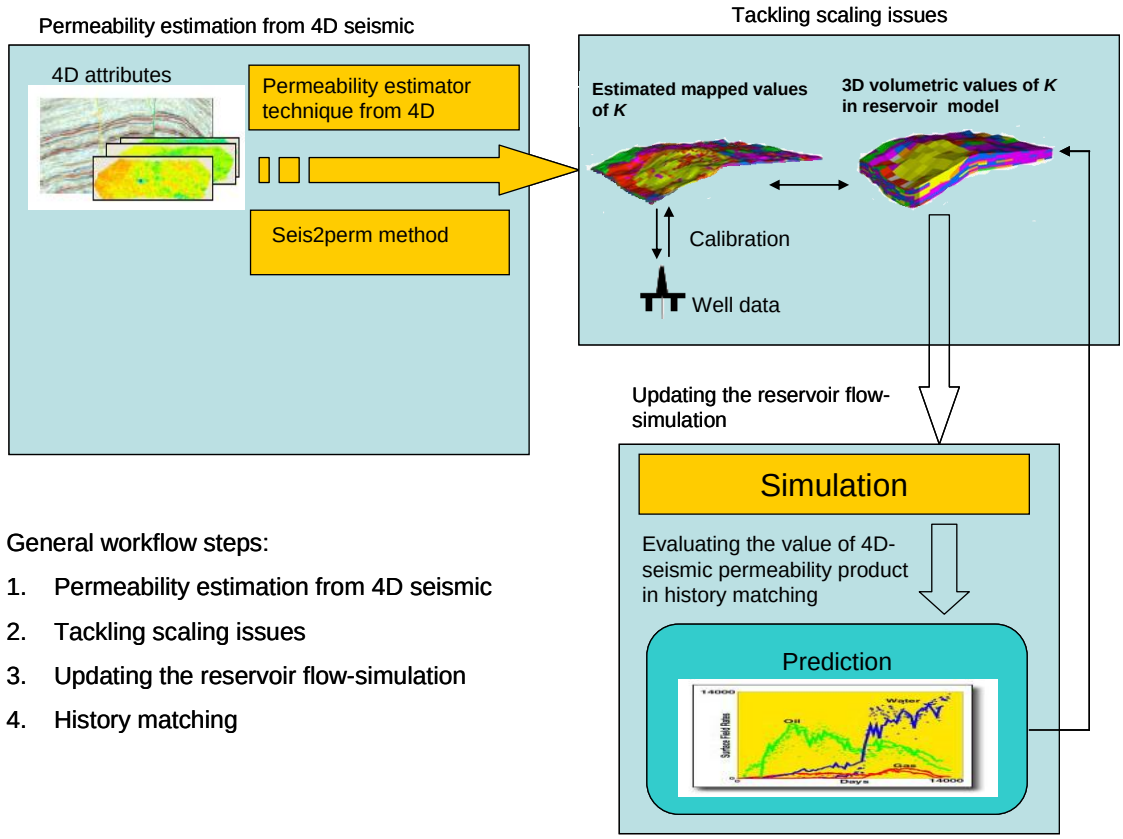

Figure 3.1: *Workflow of the direct updating of the simulation model using the 4D-seismic-produced permeability.*

3.2 Incorporating the 2D permeability map into the 3D permeability model

In the past few years, considerable attention has been paid to the problem of integrating data measured at different scales in Earth models (Doyen, 1997; Behrens and Tran, 1998; Tran *et al.*, 1999). The focus of the current study is to provide a solution to allow permeability results at the seismic scale to be integrated at the scale of a simulation model. The information content of the time-lapse seismic data is naturally limited by the bandwidth of the seismic signal. As a result, the seismic data generally have a lower vertical resolution than the thickness of individual cells in 3D reservoir models. Typically, the sampling interval of the seismic data with regard to depth is coarser (e.g. 3 m to 12 m) than the thickness of the reservoir grid blocks (e.g. 1 m to 6 m). Laterally, a completely opposite situation applies. The lateral dimensions of the individual grid cells (e.g. 50 m or 100 m) in the simulation model are typically larger than the seismic CMP (Common Midpoint) spacing (e.g. 12.5 m or 25 m). As the result, up-scaling horizontally and down-scaling vertically have to be done to transfer the property from the seismic to the reservoir grid. Figure 3.2 illustrates the resampling of the seismic

properties from the seismic grid to the simulation grid. In the lateral dimension, several seismic samples from the original regularly sampled seismic domain are averaged into one cell of the reservoir grid. Various up-scaling approaches can be applied here to transfer the properties between the two domains of scale. However, in the vertical dimension, the scale problem is more crucial, as there is a lack of vertical information in the seismic cube or map values.

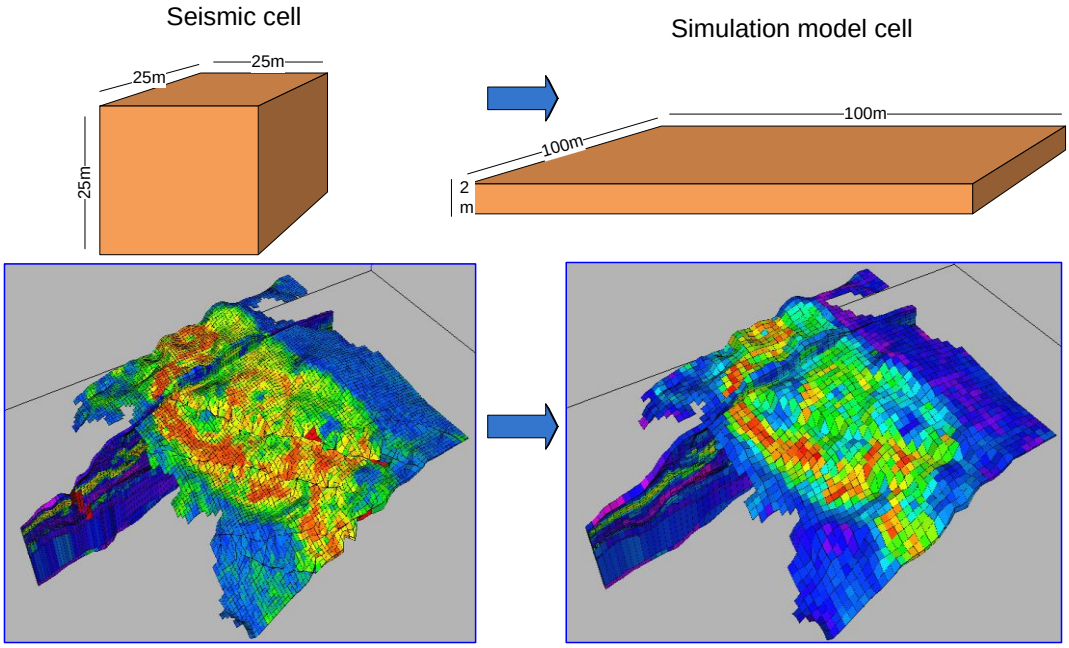

Figure 3.2: *Resampling of seismic properties to the reservoir-simulation grid.*

Due to the limited resolution in the vertical sense, the presence of a high-permeability or low-permeability zone can be observed within the averaged seismic response. Hence, the exact location of the zone is not detected directly in the interval in which the 4D seismic has performed some kind of averaging.

The average amplitude map is computed by vertical averaging between the surfaces defining the top and base of the reservoir. This serves as an input for the permeability-estimation method. Since, in the seismic domain, the amplitudes are averaged vertically for the map attributes, the final permeability is in the form of a 2D map. The derived 2D permeability map is useful for some applications such as areal connectivity assessment. However, the lack of vertical resolution of the 4D-seismic permeability result compared

with the simulation model is challenging when the intention is to update the reservoir model with this type of averaged permeability. Therefore, the question is how this vertically averaged information can be used to constrain a fine-scale 3D reservoir model.

The method proposed here attempts to solve this problem by integration of the 2D permeability map with other sources of vertical information on permeability. The reservoir-simulation model is considered to be the up-scaled version of all the data included in the geological model. Therefore, the permeability information included in this model is used for the purposes of integration with the 2D map of permeability. It is assumed that the 4D-seismic-derived permeability at one point represents a uniformly weighted vertical average over a column of cells in the 3D reservoir model. This assumption is more accurate when the seismic data are high-resolution, the reservoir interval is thick, and the simulation model has relatively coarse grid cells. Any deviation from these assumptions may introduce further uncertainty and noise related to the proposed methodology.

In this approach, first, the arithmetic average of permeability is computed from the reservoir-simulation model. The arithmetic averaging is chosen to be consistent with reservoir flow behaviour in Schiehallion. In this field, reservoir units are separated by shale intervals, so the flow is more parallel to layers than crossing the layers. The general practice for calculating effective permeability in these circumstances is using arithmetic averaging of permeability in layers (see Appendix D).

Next, a column-dependent rescaling factor to all the cells in one column is applied to ensure that the rescaled permeability values match the local 4D-seismic average map (see Figure 3.3). The scaled resultant permeability is calculated using the following formula:

$$K_{\mathrm{i}}^{\mathrm{scaled}} = K_{\mathrm{i}} \frac{\overline{K_{4\mathrm{D}}}}{\overline{K_{H\,\mathrm{sim}}}} \tag{3.1}$$

where K_{i} is the initial permeability value in the reservoir grid, $\overline{K}_{4\mathrm{D}}$ is the average 4D-seismic permeability; $\overline{K}_{H\,\mathrm{sim}}$ is the averaged permeability along each column of the

reservoir; and K_i^{scaled} is the scaled local permeability value in the reservoir grid. The resulting 3D model incorporates the fine-scale permeability values and reproduces the 4D-seismic-derived permeability values.

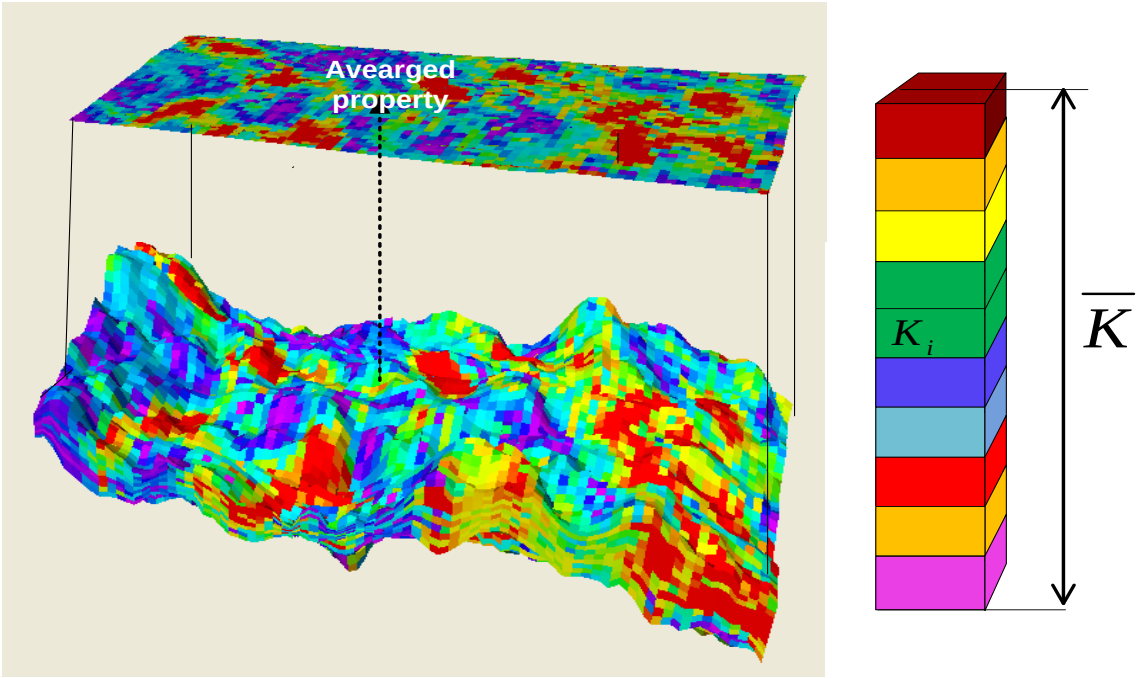

Figure 3.3: *Rescaling cell values to match the column average.*

3.3 Bump-update of the simulation model using the Seis2perm method (application to the Schiehallion field)

The proposed updating procedure is implemented on a seismic and simulation dataset from the Schiehallion field. The focus of study is the southernmost part of the field, known as segment 4, separated from the adjacent segments by a normal fault. The permeability is estimated for this section in Chapter 2. The simulation model for this segment consists of 88 × 27 × 55 grid blocks with average cell sizes of 100 × 100 × 6 m. The producing interval of the specific area of interest in our study is the T31a sand, corresponding with the first four layers of the simulation model. In this section, there are four active wells in the time period from base survey to monitor survey of this particular 4D seismic (1999–1993): two injection wells (C11 and C12) and two horizontal production wells (P3 and P4). Water-flooding has been applied to maintain the pressure and optimally sweep the remaining oil.

In order to generate the new 3D permeability model, 2D average permeability maps from seismic and simulation were calculated. The average permeability map of the reservoir from the simulation model is displayed in Figure 3.4(a). This map is the result of averaging the values over four layers of the numerical simulation model corresponding with the T31a reservoir. Note that seismic amplitudes are also averaged between the top and base of the T31a reservoir prior to permeability estimation. Multipliers are defined as the average permeability from time-lapse seismic data, over the average permeability from the simulation model. To apply the multipliers in each layer of the 3D reservoir-simulation model, it is necessary to convert the areal seismic gridding to a simulation corner-point grid. This is done by averaging the 4D-seismic permeability values located in the simulation cell of the corner-point grid. Calculated multipliers are shown in Figure 3.4(b). The multipliers map indicates that most of the dissimilarities between the simulation permeability model and the 4D-seismic-produced permeability are around the channel boundaries. This is where the locations of the compartments and barriers are uncertain in the model. It is hoped that using permeability from 4D seismic will correct the uncertain connectivities and disconnectivities in the simulation-model content. Notice that the majority of the multipliers are between 1 and 2.5, signifying that, for the majority of the segment, the values in the two maps are not far from each other. The calculated multipliers are applied throughout each layer of the reservoir-simulation model as the perturbing factors. These factors adjust the permeability value in each individual cell, taking into account the predicted permeability value from the 4D seismic.

By incorporating the time-lapse seismic result, a new 3D permeability model of the reservoir is generated. Figure 3.5 shows the comparison between the pre-existing 3D permeability model (Figure 3.5(a)) and the improved 3D permeability model (Figure 3.5(b)). In this figure, the permeability values for four layers of the simulation model prior to and after updating are demonstrated. In the updated permeability model, it is interesting to observe that including the time-lapse seismic information has highlighted channels marked by higher values of permeability. In the 4D-seismic-produced permeability, the connectivity of the channels is more emphasized compared with the model prior to integration. However, there are some very high and low values derived from the numerical instability in the result, due to the calculated Laplacian.

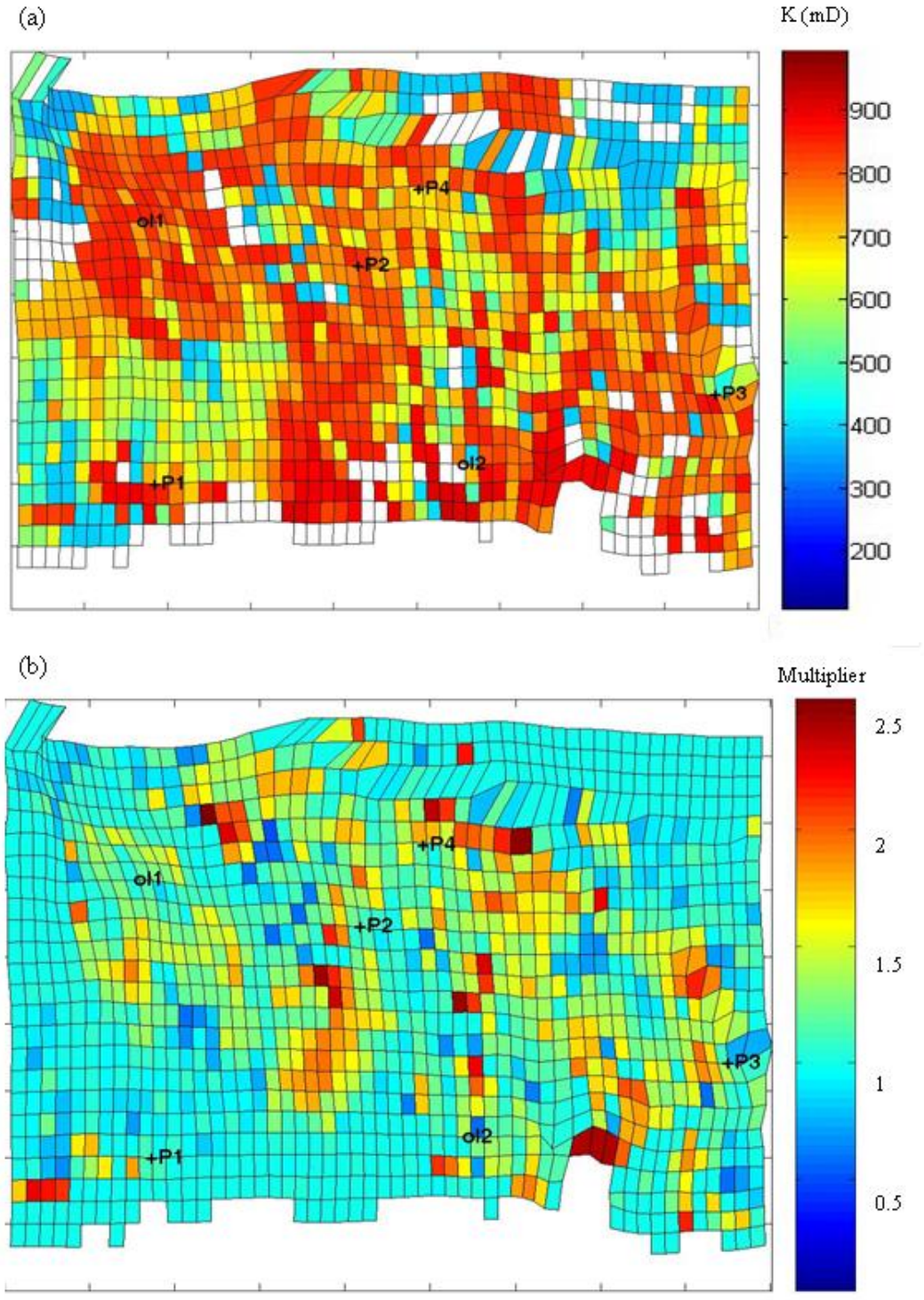

Figure 3.4: *(a) Average permeability from the simulation model, and (b) multipliers values. In this section, there were four active wells in the time period of this particular 4D seismic (1999–1993): two injection wells (C11 and C12), and two horizontal production wells (P3 and P4).*

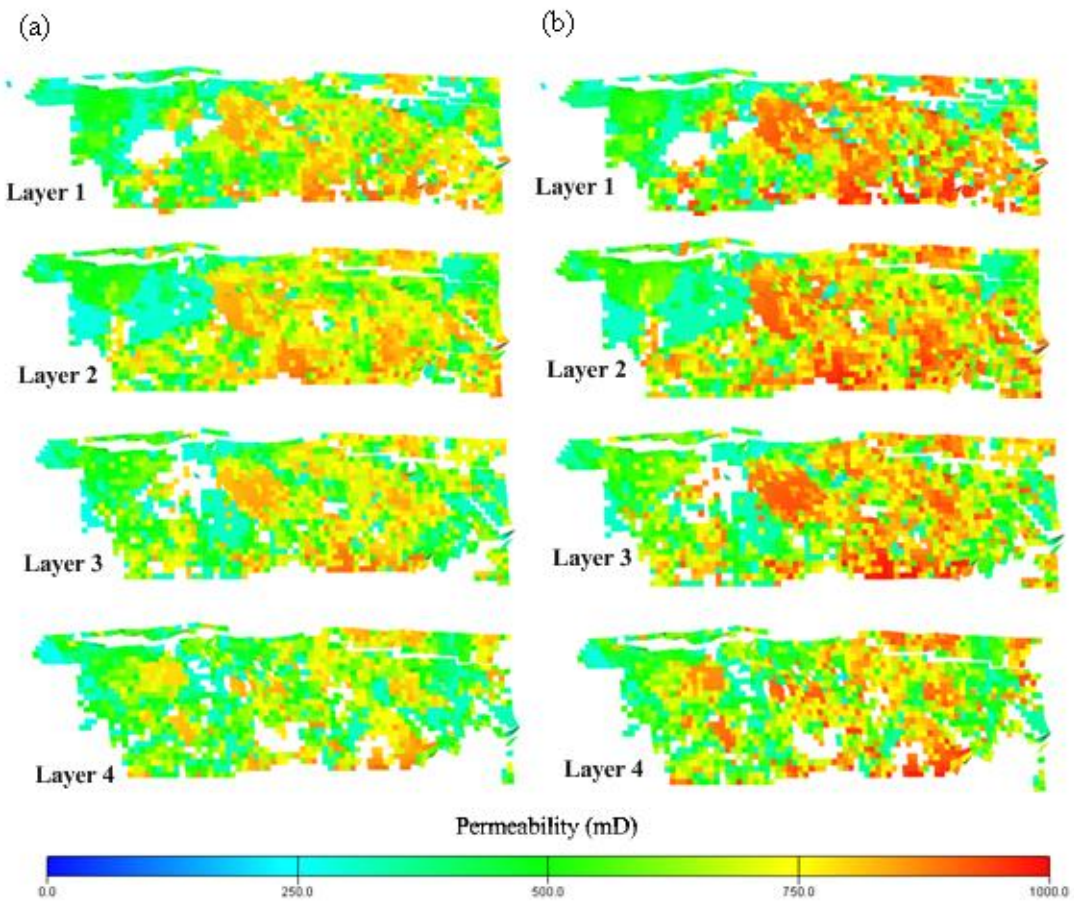

Figure 3.5: *(a) Simulation permeability model prior to integrating the 4D-seismic permeability, and (b) updated simulation permeability model after including the 4D-seismic permeability using the Seis2perm scheme.*

3.4 Fast-track history-matching and conventional history-matching

For the two models of permeability presented in the previous section, a history matching is performed. The history matching starting from the 4D-derived permeability model is called fast-track updating, in which the initial model is updated using a direct transform from the 4D seismic (Seis2perm). This is in contrast to applying conventional history-matching, in which altering the initial model (prior to 4D updating) is merely due to applied mathematical optimization. However, the objective function and history-matching algorithms used for history matching are kept identical in both approaches, in order to provide the basis for a fair comparison. The objective function and the history-matching algorithm are described in the following section.

3.4.1 Objective function

The misfit or objective function allows the ranking of different model realizations. Several types of objective function exist in the literature, but the most commonly used is the least-squares objective function. It calculates the sum of the squares of the differences between modelled and observed data. Here, the objective function is defined in the form of the residual operator (J) as a vector in the data space that contains the differences between the real and the simulated water-production rate, the bottom-hole pressure and the gas–oil ratio (GOR). Therefore, the objective function is defined as the least-squares data misfit, as shown below:

$$J = \sum_{N} \frac{\left(Q_{\mathrm{w}} - Q_{\mathrm{w_{OBS}}}\right)^2}{\sigma_{Q\mathrm{w}}^2} + \frac{\left(P_{\mathrm{w}} - P_{\mathrm{w_{OBS}}}\right)^2}{\sigma_{\mathrm{P}}^2} + \frac{\left(\mathrm{GOR} - \mathrm{GOR}_{\mathrm{OBS}}\right)^2}{\sigma_{\mathrm{GOR}}^2} \tag{3.2}$$

where Q_{wOBS}, P_{wOBS}, and $\mathrm{GOR_{OBS}}$ are the water-production rate, the bottom-hole pressure and the GOR from the history data; and Q_{w}, P_{w} and GOR are the simulated data resulting from running the forward simulation with a specified 3D permeability. The $\sigma^2_{Q\mathrm{w}}$ is the standard deviation of the water-production-rate measurements; σ^2_{P} is the standard deviation for the pressure measurements; and σ^2_{GOR} is the standard deviation for the GOR measurements. Note that the different σ's are calculated from the spread of the data to imply the normalization factor expressing the data accuracy for the information content of a given observable variable.

3.4.2 The gradient-based method

Traditionally, there are several approaches to performing history matching (McLaughlin and Townley 1996; Reynolds *et al.* 2004). The main difficulty in honouring the dynamic production data is the global and non-linear relationship between the dynamic data and the reservoir's petrophysical properties, e.g. porosity and permeability, through the flow equations. Matching dynamic production data in reservoir models is an inverse parameter-estimation problem in which flow equations must be solved to establish the relationship between data and model parameters (Tarantola, 2005).

The gradient-based method typically is used to solve the optimization problem and requires the calculation of the sensitivity coefficients of the reservoir responses, e.g.

pressure, saturation and fractional flow-rate, with respect to the model parameters, e.g. permeability. Gradient-driven searching uses the derivative of an objective function to change the property, e.g. the permeability field (Brun *et al.*, 2004). Computing the sensitivity coefficients of reservoir responses to the reservoir petrophysical properties has been an active research topic for decades, and many sophisticated methods have been developed in the literature. In this study, an automatic gradient-based history-matching approach is implemented, using a commercial tool from Schlumberger (SimOpt). The gradient, estimated by using SimOpt, is defined as the adjoint of the Frechet derivative applied to the residuals (an objective function). A Frechet derivative is a derivative defined for mapping from one vector space to another. Here, the Frechet derivative is applied as an operator to relate the resulting objective residuals to change in permeability:

$$\delta K = -R'[K] * R(K) \tag{3.3}$$

where δK is the gradient, $R'[K]$ is the adjoint of the Frechet derivative, and $R(K)$ is the norm of the residual operator defined previously. The relationship between change in permeability and permeability is established by the following equation:

$$K^{(n+1)} = K^{(n)} + \omega \delta K^{(n)} \tag{3.4}$$

where ω is a step-length that should be chosen properly (in the current case it is a line-search criterion). Using Equation 3.4, the permeability being perturbed iteratively until $R(K)$ becomes a satisfactory minimum. After applying automatic gradient-based history-matching, the optimized model of permeability is generated.

3.5 Resultant permeability and resultant history-matching for different methods

Based on the procedure described earlier, two history-matching approaches were performed: i.e. fast-track history-matching using the 4D-adjusted permeability model, and conventional history-matching initiated from the original permeability model. In this section, I will analyse the resultant permeability model after history matching, and the matching outcomes for different approaches.

3.5.1 Resultant permeability models after history matching

The resulting permeability models are displayed in Figure 3.6. This figure shows the permeability values of layers 1 to 4 respectively. It is observed that the permeabilities resulting from different methods are not similar. Figure 3.6(a) shows the results using the conventional history-matching approach. The final property distribution derived using this method gives a smoothed rectangular region, which does not seem to be related to the quality of the channel features and their orientation. In the Figure 3.6(b), the permeability model derived from fast-track history-matching is displayed. In the fast-track method, geological features such as the shapes of the channels are more noticeable. However, these do not all need to be relied to the updated model for future prediction of the reservoir. The degree of reliability also depends on the match of the model with the observed dynamic data. This issue is examined in this section by comparing the methods presented here in terms of the match with observed dynamic information.

3.5.2 Matching with observed data

The objective function evaluations using these new models, prior to the history-matching processes, are 1.66 for the base case and 1.67 for the 3D model updated using the 4D-seismic information; and, after 10 iterations in history matching, they are 1.53 for the history-matched base case using SimOpt, and 1.34 for history matching in SimOpt using the updated model. Thus, although the 4D-seismic update did not change the misfit significantly, it has changed the rate of convergence and the final history-matched model misfit.

Individual fits to water-cut, total-field gas production, and bottom-hole pressure, are shown in Figures 3.7 and 3.8. Figure 3.7 shows the result of history matching in a production well in the centre of the model (P_1) and in the group of production wells. This shows a considerable improvement in the fast-track history-matched model for the fit to the water-cut at individual wells. It is important to notice that water-cut prediction in this field is critical for forecasting the reservoir behaviour. A high level of water production in the field has been observed due to poor connectivity estimation in the field, and the management decisions are shifted towards water management. Therefore,

a reliable, matched model, with a production history that is firmly constrained with the geology, is vital for management of this field.

Figure 3.8 shows the history-matched results for field gas production and bottom-hole pressure for different models. The bottom-hole pressure is equally well matched by both models, showing a slight improvement in both cases. However, the fast-track history-match improvement in gas production has been significant.

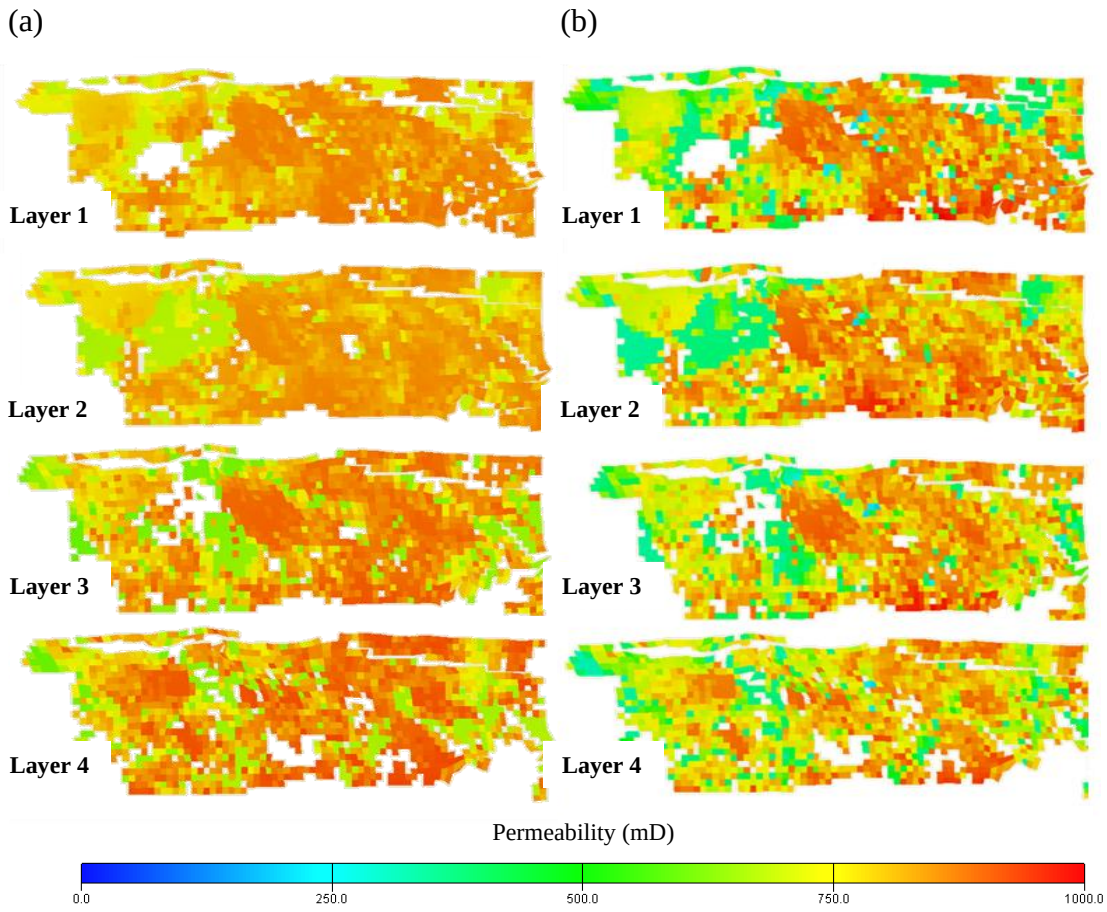

Figure 3.6: *Comparison of models after the history-matching process: (a) initiated from the operator model, and (b) initiated from the model with integrated 4D-seismic permeability.*

(a)

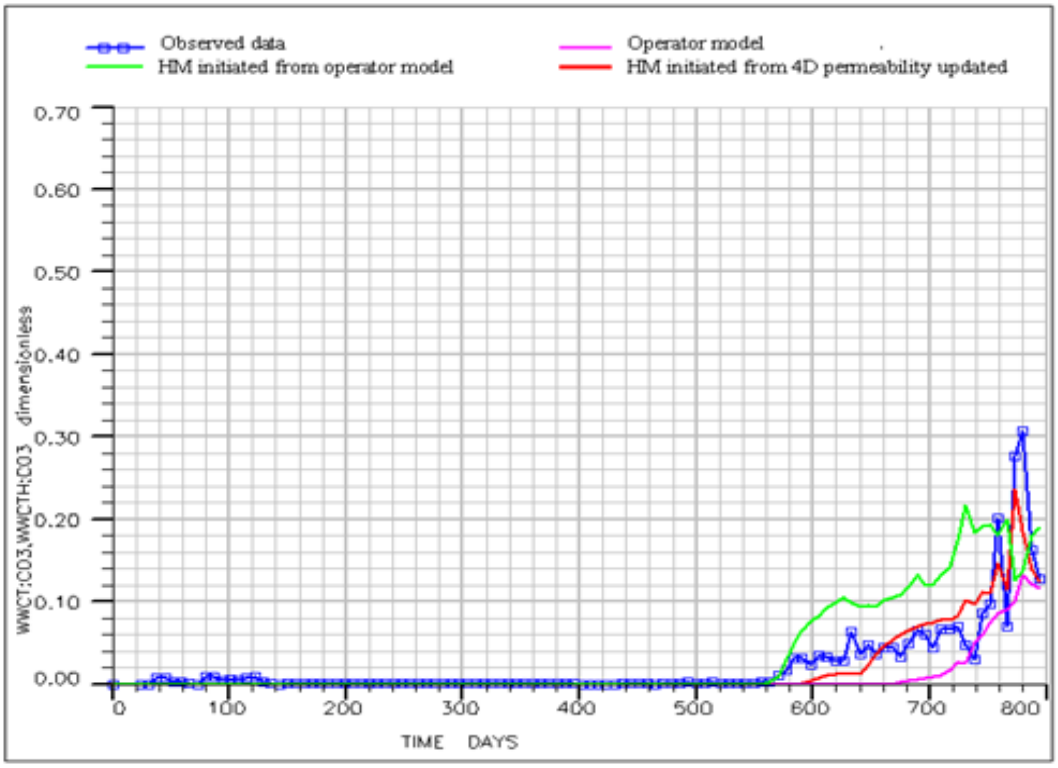

(b)

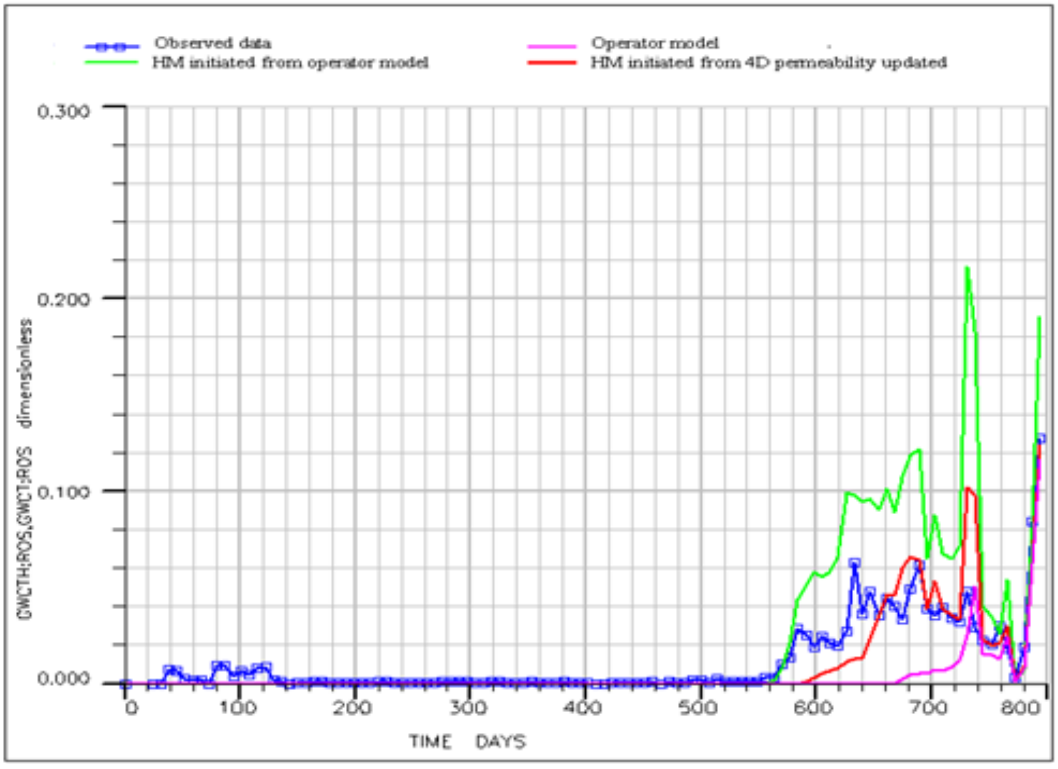

Figure 3.7: *(a) Water-cut in the production well P1, and (b) in a group of production wells (P1 and P2), after history matching (HM) the base case and the 4D-seismic-updated model.*

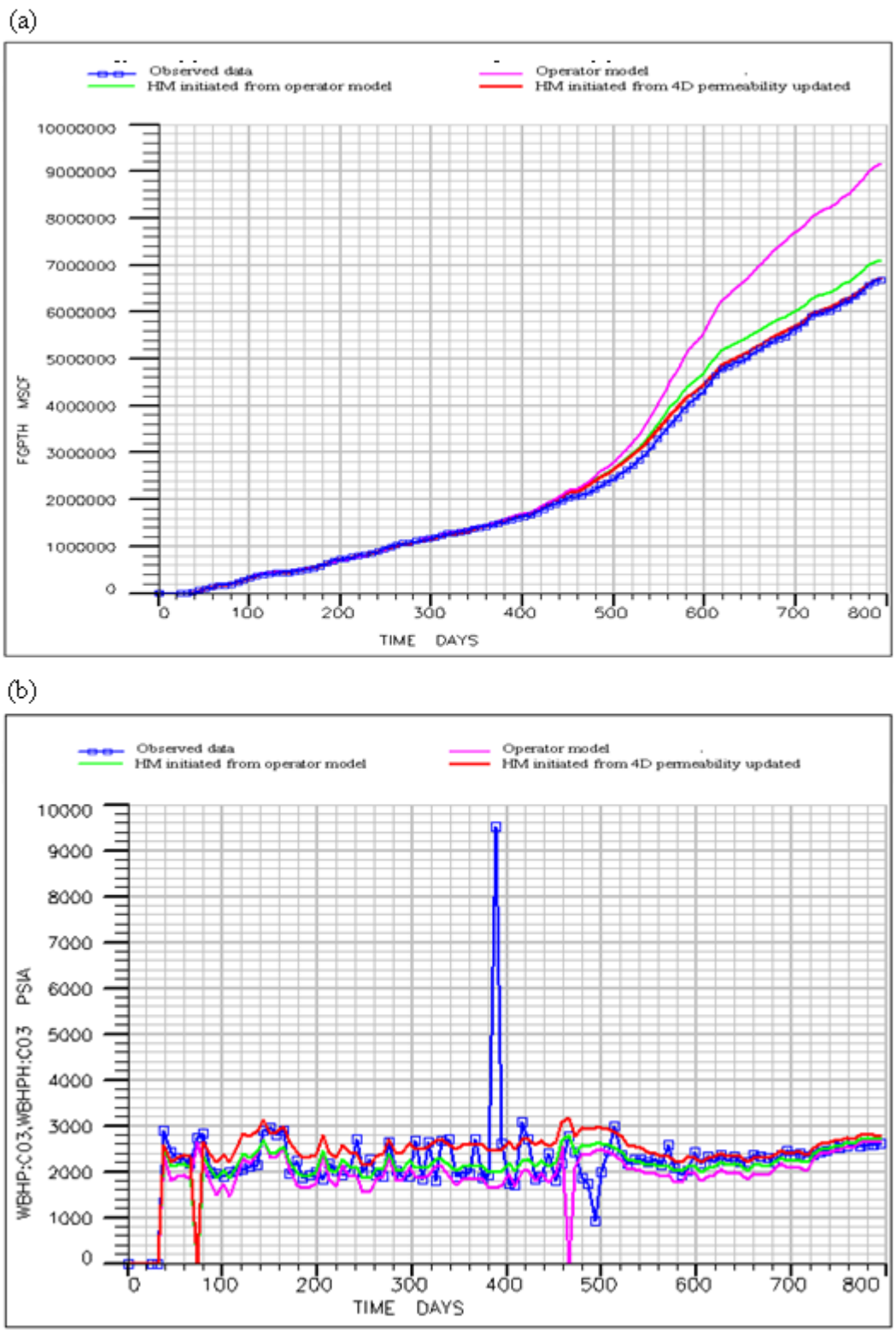

Figure 3.8: *(a) Comparison of the fit between observed total-field gas production and the simulated one in different models, and (b) comparison of the fit between observed bottom-hole pressure for well P1 and the simulated resulted one in different models.*

3.6 Discussion and analysis

3.6.1 Pros and cons of integrating the 2D permeability map in a 3D reservoir model

In the proposed technique for incorporating the 2D map of permeability in the 3D simulation model, it is assumed that seismic-derived permeability at one point represents a vertical average over a column of cells in the 3D model. This is a fast and practical approach, and in this chapter it has been proven to be of value for improving history-matching results. This technique is accurate for high-resolution seismic data, thick reservoir intervals and relatively coarse grid cells. However, there are situations where the vertical seismic resolution is too limited, so that its resolution is not comparable with that for the simulation. However, there are several techniques that can improve this framework. For example, the technique proposed here can be adapted to cells with variable thickness by considering thickness-weighted or cell-volume-weighted column averages instead of arithmetic averages. However, the application of a constant rescaling factor in each column of cells changes the histogram of permeability values and may give rise to vertical banding artefacts in the final model. Also, any deterministic way of rescaling the individual cell values to reproduce the column averages has the disadvantage of uncertainty, due to the non-uniqueness because there are many possible fine-scale permeability models that match the vertical average values. Therefore, an alternative method can be to use a stochastic approach such as the sequential Gaussian simulation (SGS) method conditioned to average the permeability over column cells equal to 4D-seismic permeability.

Another attempt to increase the accuracy of overcoming the scaling issue from the seismic to the simulation domain is using the cube of the acoustic impedance values instead of the map values. Inverted acoustic impedance has several advantages. It is a layer-based property as compared with amplitudes, which are interface properties. A layer-based property such as acoustic impedance is a suitable seismic attribute to be transformed to a reservoir property (such as permeability) that is also a layered reservoir property. Moreover, the acoustic impedance attribute has a higher resolution vertically, and it is usually validated and calibrated with well-logging data. As a result, the mismatch of resolution between the simulation and the seismic domain is decreased, and therefore the result of any applied technique will be more accurate. Although, the

non-uniqueness problem in the inversion process from amplitudes to acoustic impedance remains controversial.

3.6.2 How effective is fast-track history-matching compared with the conventional approach?

The history-matching process is a standard procedure in reservoir engineering, and it is necessary in order to make a sensible prediction with the simulator. In general, there are a large number of parameters defining the simulation model of each grid cell. These have the highest associated uncertainty during the early stages of production, where data are scarce. Reservoir permeability is a reservoir property that directly controls the flow and recovery factor (Corbett, 2009). Hence, permeability is a key parameter that a reservoir engineer can use to optimize the history matching.

Estimating permeability directly from time-lapse data is a possible alternative method using attribute analysis transformed from the seismic signature. It is a rapid and straightforward manipulation of the flow equations to yield permeability. Clearly, by using a permeability map, much more spatial permeability information is available for history matching than the data that are conventionally available from sparsely separated wells. This is a direct method of history matching (here called fast-track history-matching) in which permeability has been directly incorporated in the model in order to lead to a better history match.

In comparison with the conventional history-matching techniques, the fast-track technique has the power to quickly generate multiple scenarios that are conditioned to the observed data (for example, permeability estimated from different attributes) and allow for an independent assessment of how the geological input has been honoured. In this way, the dynamic data are always honoured, while the static data are incorporated at the geologist's discretion. Unlike the proposed method of updating, in history-matching methods, the final model may not be firmly constrained by geology, instead it is more to do with mathematical calculation to minimize the misfit in an optimization problem.

3.6.3 Fast-track history-matching versus seismic history-matching (SHM)

Seismic history-matching (SHM) is a joint history-matching scheme for estimating petrophysical properties by integrating both well data and 4D seismic data. It is expected that simultaneous history matching of well data and 4D seismic will lead to a better prediction of petrophysical reservoir properties and an improved production forecast. In recent years, much research has been devoted to the development of seismic history-matching in order to estimate the permeability in an iterative scheme. Most of the studies have used time-lapse seismic as an indirect spatial permeability estimator, using the conventional principles of history matching (Landa and Horne, 1997; Kretz *et al.*, 2004; Stephen and MacBeth, 2006; Dadashpour *et al.*, 2007). Here, the 4D seismic is integrated with production data in the objective function. The 4D seismic is treated as dynamic data, and is matched with synthetic data calculated from the simulation model. The flow simulator is coupled with a petro-elastic model in order to convert the simulator output and static rock properties into simulated elastic properties.

In the seismic history-matching process, after choosing the inversion parameters for adjustment, an objective function is estimated in order to incorporate the misfit of both the seismic and the production data. An optimization technique is applied to change the parameters during the history-matching process. In the optimization application, the misfit function works as a tuning factor that controls the adjustment between the observed behaviour of the field and the predictions. Neighbourhood algorithm optimization is a stochastic approach recently adapted to the seismic history-matching technique (Stephen and MacBeth, 2006), and has shown a successful outcome. A schematic of this history matching is shown in Figure 3.9. The observed values are obtained by inversion of the seismic signal to acoustic impedance estimates. The permeability is estimated after history-matching using the pilot-point method with kriging. Selected pilot points are where a permeability multiplier is applied as a parameter in the stochastic neighbourhood algorithm (NA) inversion. In the rest of the reservoir, the pilot points are where the multipliers are fixed to 1.0.The multipliers for the remaining cells are determined by kriging, in order to produce a horizontal multiplier map. As a consequence of using this method, the parameter space is reduced considerably and the optimization approach is faster. The pilot points that were chosen involved horizontal permeability measured at an arbitrary location.

By incorporating time-lapse data and production data and using the automated procedure, the computational-time and user-intervention associated with the history-matching process are reduced. In addition, seismic history-matching provides a basis for tackling the non-uniqueness problem, where the 4D-seismic information is included in the areas between the wells – an area where there is a lack of data. However, it needs to involve petro-elastic modelling, which is associated with uncertainty.

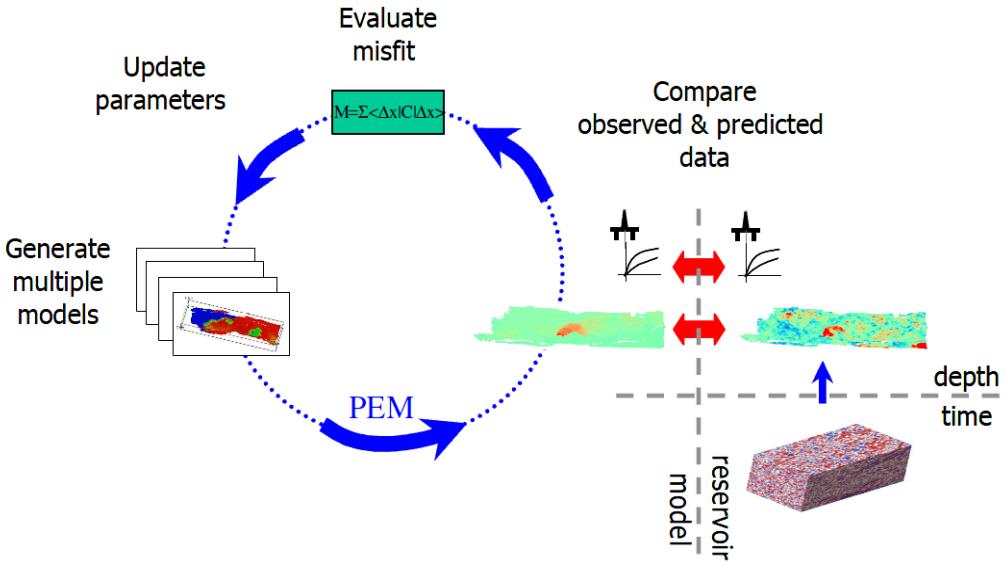

Figure 3.9: *Schematic of history matching using 4D seismic (Stephen and MacBeth, 2006).*

In seismic history-matching, the pilot-point method uses kriging to determine most of the grid-cell permeabilities, and kriging has the tendency to produce smoothed permeability fields. Moreover, the pilot-point method does not detect all the heterogeneities in the reservoir. It is possible that certain heterogeneities are not detected because no wells or pilot points are located sufficiently close to them. Since permeability is dependent on well locations (fixed permeability) and pilot points (where it can be adjusted), it is always difficult to capture all the heterogeneities in the final history match. However, the history-matching process will conserve the average field permeability close to that of the real case. This makes small patches of high- or low-heterogeneities undetectable even with pilot points. This procedure requires many iterative steps, and a number of flow simulations are run during the updating process. However, more frequent time-lapse seismic measurements give an improved resolution to the calibration of the flow properties.

In contrast to seismic history-matching, in this chapter an alternative solution (fast-track) is proposed for using 4D seismic in history-matching. The fast-track approach provides a fast, practical and effective history-matching method. Table 3.1 gives a comparison between the fast-track and seismic history-matching methods.

Table 3.1: *Comparison between the seismic history-matching and the fast-track history-matching approaches*

	Seismic history-matching	**Fast-track history-matching**
Complexity of workflow	• Intensive user-interaction	• Less user-interaction
Overall project time	• Of the order of weeks	• Relatively rapid, of the order of days
Data requirement	•Requires production data, and 4D-seismic data	• Requires permeability from the logs, 3D-seismic, 4D-seismic and production data
Resolution and accuracy	•Small-scale features may not be detected	• Fine-scale with the seismic bin-size resolution
Robustness	• Inherently stable	• Some instabilities due to 4D-seismic Laplacian and numerical instability
Cost	•Overall the cost is greater	• Inexpensive

3.6.4 The gradient-based method and other history-matching methods

There are several methods of optimization described in the literature. These methods are concerned with issues such as non-uniqueness in the history-matching problem, and the risk of trapping in local minima, requiring many iterations. Adjoint methods are gradient-driven methods in which the speed has been greatly increased by implementing derivatives calculated internally in the simulator (Valstar, 2001). However, they have the risk of being trapped in local minima and often require many iterations. A gradient-based method is employed in this study; however, it is suggested that the methods of history matching should be enhanced in order to achieve better results. Below, a brief

overview is provided of the potential of history matching as compared with the gradient-based method.

More global optimization techniques such as genetic algorithms and simulated annealing have the advantage that the risk of trapping in local minima is smaller; however, even more iterations are required to obtain a reasonable history match (Zhang *et al.*, 2005). As a result, it is difficult to obtain a suite of matched models. The ensemble Kalman filtering technique (Naevdal *et al.*, 2002; Evensen, 2007) is different in the sense that the suite of realizations is a key element from the outset. It has the advantage that iterations of the forward model for each realization are not required, and that the assimilation can be performed in a sequential sense. An update can be made after every time-step, without the need to run a complete simulation from the beginning.

3.7 Summary and conclusions

In this chapter the reservoir-simulation model was updated using a new methodology to build 3D permeability distributions of the reservoir, by combining time-lapse seismic data with the pre-existing 3D reservoir simulation model of the field. A new history-matching approach, known as fast-track history-matching, is introduced in this chapter in order to history match the simulation model using a 4D-driven permeability model. Implementing this approach pursued a multi-fold purpose. Initially, it is examined in order to investigate whether the method is able to provide a fast and effective history-matching procedure as compared with the other existing methods. In order to do so, a commonly used method of optimization of the simulation model, known as the gradient-based method, is implemented on both the original dataset and the model updated by 4D-seismic permeability. In this history-matching process, only production data are used in the objective function. Comparisons of the final results for these methods are performed in terms of estimated permeability models; the ability to achieve a minimum misfit function in an efficient time period; and well-data matching such as bottom-hole pressure and flow rates. By utilizing the fast-track methodology, the gas–oil ratio (GOR) and water-cut data misfit in the Schiehallion field were significantly reduced when the estimated permeability map was fed directly into the simulation model. Inclusion of 4D results and interpretation provides a more reliable representation of the distribution of geological properties in the reservoir static model. The permeability

distribution after the history matching initiated from the 4D seismic data preserves the representation of the possible channel connections. Such a methodology is easy to implement, and it was shown that it was possible to reduce the dynamic data misfit by incorporating the time-lapse seismic information into our 3D permeability models without including the petro-elastic model during the history-matching process.

Moreover, estimating the flow response of permeability from Seis2perm provides a basis for evaluating the value of the resulting permeability 4D seismic. This is the supplementary purpose of the previous studies in analysing the effectiveness of the Seis2perm estimation. It was shown that the total objective function was rapidly reduced after a number of iterations. Also, the convergence of the optimization procedure improved when the fast-track technique was used.

CHAPTER 4: ERROR QUANTIFICATION IN THE SEIS2PERM TECHNIQUE

Overview

This chapter addresses the potential uncertainty, challenges and quality of permeability estimation from 4D seismic, and investigates how errors may propagate through the updating of a reservoir-flow simulation. Various tests on how to select the different attributes for permeability estimation, in addition to how to select the different time-lapse surveys, will be considered. A test will be performed to validate the assumption of linear proportionality between 4D signatures and pressure change in order to infer permeability. Resolving the tuning effect and calibrating the estimated permeability with the well data are also addressed. Finally, I will discuss how to treat Laplacian evaluation in a practical way.

4.1 Introduction

The value of using 4D-seismic permeability results in a reservoir model depends strongly on their overall accuracy and resolution. This is directly linked to the quality of the data; the ability of the selected attribute to 'sense' the reservoir state; and the reliability of the method used to extract the permeability.

Relating time-lapse seismic to permeability, and then updating the reservoir-flow simulation using this product, is a long process. Here, one may imagine three main stages in which uncertainty could be introduced. The first comes from the nature of the seismic. For most reservoirs, the seismic data provide information on a depth-averaged response within the zone of interest. The vertical features are not well resolved. It is a limitation of the seismic that the permeability is only an average. Also the selection of the seismic attribute is important, as not all attributes sense the reservoir state in the same way. Another uncertainty arises from the assumptions of the method that is trying to infer permeability from saturation- or pressure-changes. The validity of the assumptions of the method in a specific field needs to be examined. In addition, the tuning effect in the seismic response can add further ambiguities. Finally, special care has to be taken in dealing with the numerical error inherently associated with the method chosen for solving the equation.

In this chapter, the three above-mentioned various sources of errors associated with the final permeability product have been studied to assess the quality of the estimated permeability. This study is carried out using a number of distinct tests, ranging from uncertainty in attribute selection; to the tuning effect; to the validity of the assumptions within the method; and to the numerical error attached to the solution. In the following section, I will examine several techniques that can be used to control the error attached to the permeability transform and to increase the reliability of the result.

4.2 Analysis of errors in permeability calculations using multiple attributes and sequence of time-lapse surveys

Segment 1 of the Schiehallion field is considered as the main focus of this study. A range of mapped attributes defined by the fixed picks for the top and base of the T31a reservoir are generated for the Schiehallion field. These attributes are also evaluated for

four separate time-lapse surveys shot during the production life of the reservoir. This is possible because two pre-production baselines and four repeated surveys were available for this field. For each case, the overlap of reservoir information and its robustness are evaluated. Subsequently, the horizontal permeability is estimated using the Seis2perm technique from attribute analysis. The results provide an indication of the stability and associated error in the permeability product determined by this method.

4.2.1 Data from repeated surveys and attributes

The attributes used in this study are listed in Table 4.1. The range of selected attributes are extended to all available options so that the error associated with attribute selection can be captured. Note that since the intention here is to pursue an uncertainty quantification procedure which includes all available options, no test is performed to select physically meaningful attributes whereas this is the main concern in a multi-attribute studies. Each attribute is calculated by transforming the seismic trace between the top and base of T31a. These attributes are extracted by making difference-attribute maps generated from two surveys, and as such they reveal a change in polarity. In addition to using information from different attributes, supplementary information is provided by repeated surveys over the same region of the field at different calendar times. Different time-lapse surveys are taken into account, with the hope of enhancing the signal due to permeability.

Table 4.1: *The range of attributes and their descriptions*

Attribute	Window size	Description
RMS(T2)–RMS(T1)	Top to base	Root of the mean square of the amplitudes in the selected window time interval
Arithmetic average (T2)–arithmetic average(T1)	Top to base	Arithmetic average of all the amplitudes in the selected window time interval
Minimum(T2)–minimum(T1)	Top to base	The smallest amplitude, regardless of sign in the selected window time interval
Maximum(T2)–maximum(T1)	Top to base	The largest amplitude, regardless of the sign in the selected window time interval
Most(T2)–most(T1)	Top to base	The amplitude with the lowest standard deviation in the selected window time interval
Median(T2)–median(T2)	Top to base	The centred amplitude value in the selected window time interval

The field being considered started production in 1998. Seismic surveys were acquired in 1999 and 2000, and were processed together with the 1993 pre-production seismic survey. The seismic surveys acquired in 2002, 2004 and 2006 were then processed together with the pre-production base-line 1996 seismic survey. Thus, in this study, the following four different seismic snapshots will be considered: 1999–1993, 2000–1993, 2002–1996 and 2004–1996. The channels that are potentially capable of registering a 4D signature will manifest themselves differently in the various time-lapsed seismic snapshots, due to production effects and noise. Variations in production activity will therefore help to build up an understanding of the potential flow pathways. Capturing these contributions requires a full evaluation of the uncertainties, including non-repeatability noise and imperfect picking. Here, it is considered that only the former exists, and I will attempt to minimize the noise content by overlapping many different data sources imaging a common underlying permeability structure.

Prior to calculating difference maps for time-lapse surveys, it is necessary to statistically balance the amplitudes of the surveys. The mapped attributes are statistically normalized by setting the mean value to zero and the standard deviation of the amplitude distribution to unity. Amplitude scaling is accomplished using the following equation:

$$Y_{\mathrm{i}} = \frac{y_{\mathrm{i}} - \mu_{\mathrm{y}}}{\delta_{\mathrm{y}}} \tag{4.1}$$

where Y_{i} is the statistically normalized amplitude; y_{i} is the original amplitude value; μ_{y} is the mean value of the amplitude; and δ_{y} is the standard deviation of the amplitude. The shape of the data is preserved in this linear transform, as is shown in the histograms of Figure 4.1(a) and (b). The mean and standard deviation are converted to become zero and one for all the surveys, so that the amplitudes of the different normalized surveys can be compared directly.

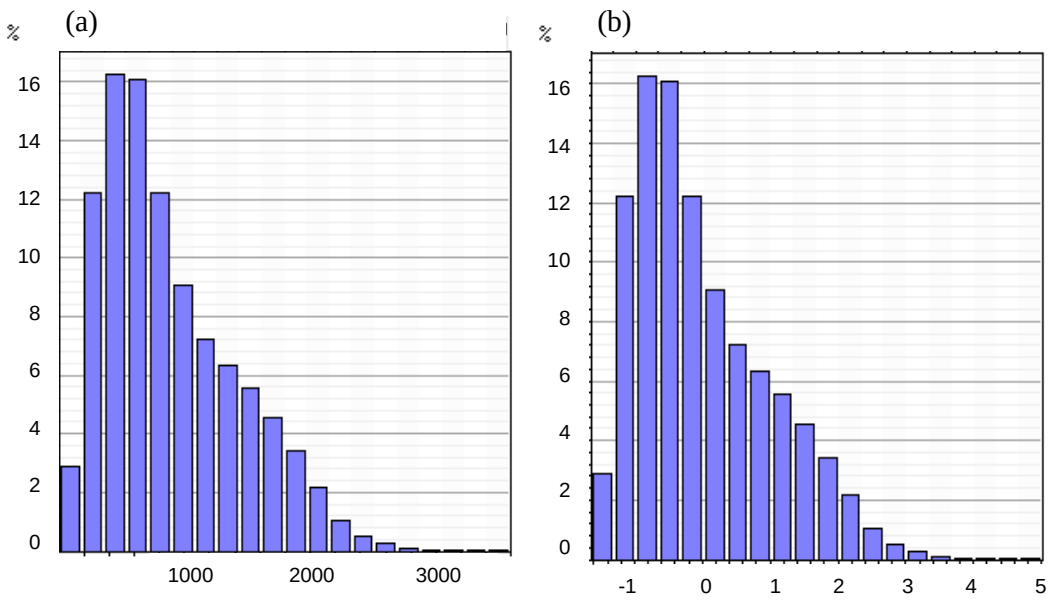

Figure 4.1: *The shape of the data is preserved by applying statistical normalization from (a) the 1996 RMS attribute, to (b) the normalized 1996 RMS attribute with a mean equal to zero and a standard deviation equal to one.*

The selected attributes and the range of 4D signatures allow many different realizations of the permeability to be calculated for the same reservoir. These are shown in Figures 4.2 and 4.3. Inspection of the maps reveals differences, but also many coarse-scale similarities and some common fine-scale features. There is very little visual distinction between the data taken from different attributes and those taken across different time-lapse surveys. This appears to suggest that all the maps are indicating some common features of the underlying dynamic reservoir behaviour, but also that there is little need to treat the different data snapshots across attribute-space any differently from those across the calendar-time space. Although it is expected that different attributes will sense the reservoir properties differently, the range of values chosen have been defined over the same interval and are similarly related mathematical operations, and thus do not show a high diversity. Furthermore, the changes with respect to production are quite large and are detected for most attributes to some degree. Given this, it is thought best to pursue the statistical analysis of the data by treating over attributes space and calendar times space together.

1999-1993 2000-1993

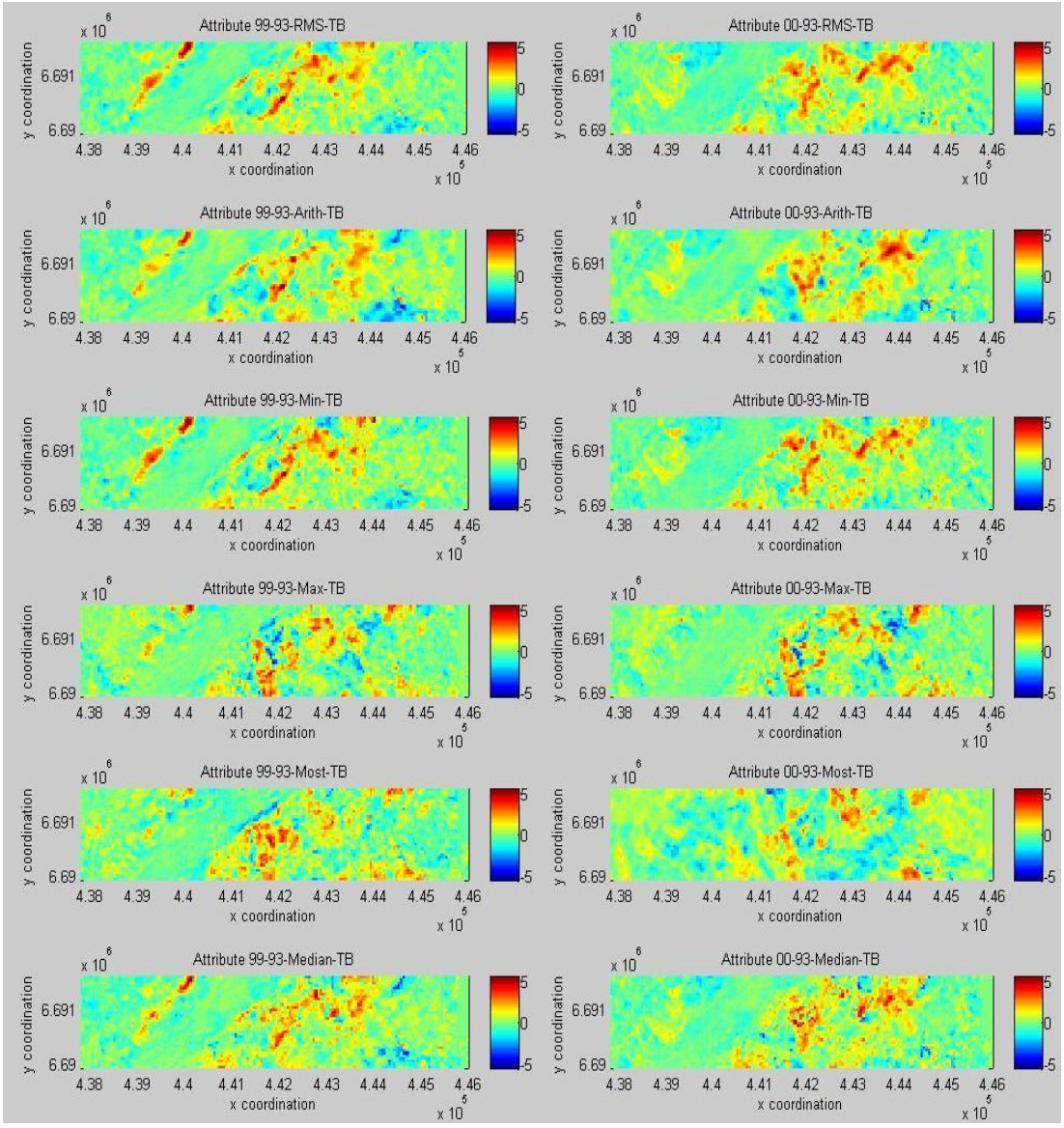

Figure 4.2: *Various attributes for the 1999–1993 and 2000–1993 time-lapse surveys.*

2002-1996 2004-1996

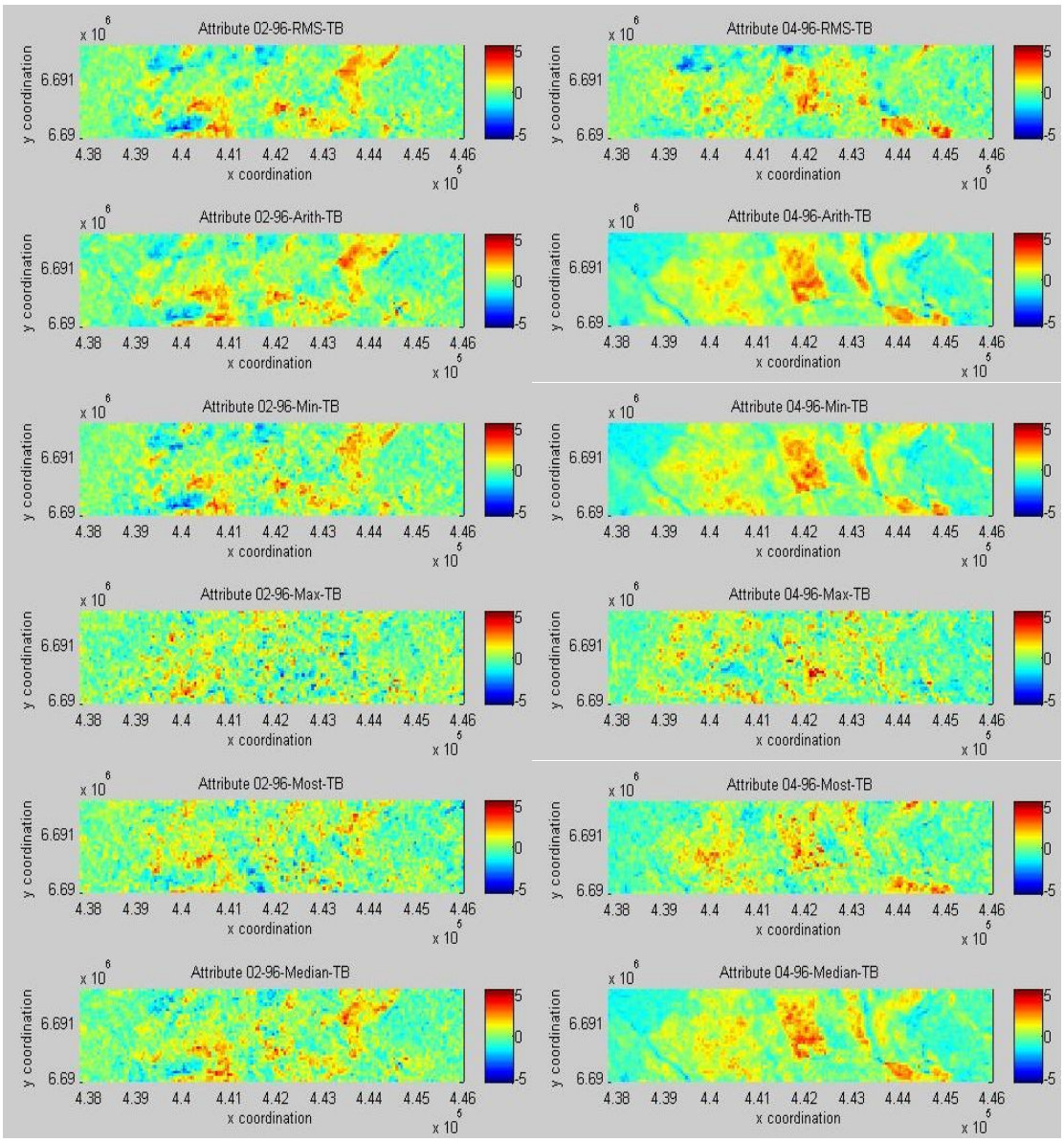

Figure 4.3: *Various attributes for the 2002–1996 and 2004–1996 time-lapse surveys.*

4.2.2 Analysis of the information content from the mapped amplitudes

Figure 4.4 shows the distribution of the means and the spreads for each 4D signature in Figure 4.2 and Figure 4.3. As illustrated in Figure 4.4(a), the last three attributes (maximum, most and median) in the different time-lapse surveys are more diverse, especially for the data include the 1993 base-line seismic. This is more noticeable in Figure 4.4(b). Changes of reservoir condition, different base-lines, and different noise content are all factors that can cause these differences. Another possible reason is the

presence of gas exsolving from solution, which occurred between 2000 and 2003. Inspection of the various attributes based on Figure 4.4(c) and (d) show that the variations do not change significantly between the 2002–1996 4D signature and the 2004–1996 4D signature. The reason for this is that the production activity did not change significantly between 2002 and 2004. The analysis above also suggests that the datasets with the 1993 base-lined are overall less stable and noisier.

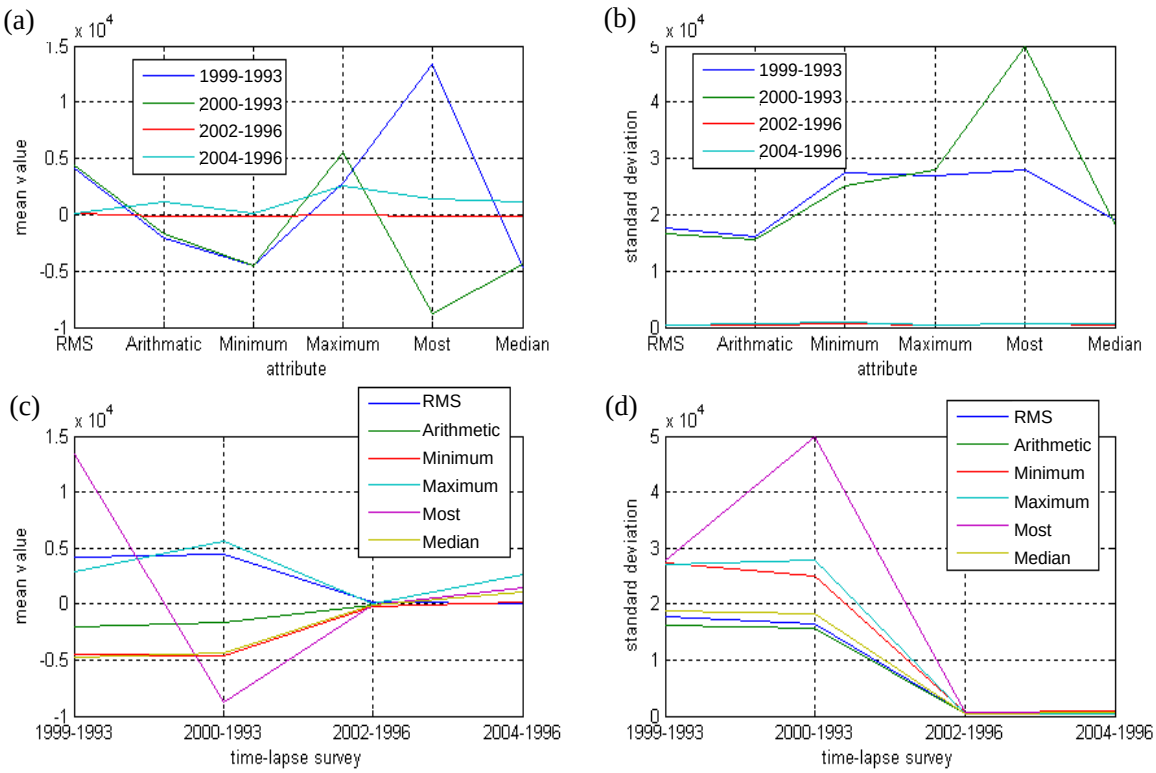

Figure 4.4: *Uncertainty analysis for time-lapse surveys and attributes: (a) mean value of different attributes, (b) standard deviation of different attributes, (c) mean value of different 4D-seismic surveys, and (d) standard deviation of different 4D-seimic surveys.*

Each set of mapped data in this study is treated as a normal distribution, correlated in some way to the other datasets. The correlation between the individually normalized 4D signatures was observed visually, but is also illustrated by cross-plotting in Figure 4.5. This shows that correlation is more significant between the various attributes (a lesser degree of correlation between some of the attributes such as Most and Median could be due to uncertainty of choosing irrelevant attribute), as compared with a specific attribute at different calendar times. This is normal, because the 4D signatures are controlled by a high level of production activity from time to time. In the early stages of reservoir life,

the response is mainly controlled by gas coming out of solution. As a result, several water infill injectors were utilized to recover the reservoir pressure and decrease the GOR (gas-oil-ratio) in the field. As the Schiehallion field has matured, water production has increased, and the focus of reservoir management has shifted from managing gas to managing sweep and water-cut. The high level of production activity over the time periods under consideration here justifies the need for selecting the attribute and averaging the results from this over calendar time. This helps to capture the different channels manifested by different production strategies over time.

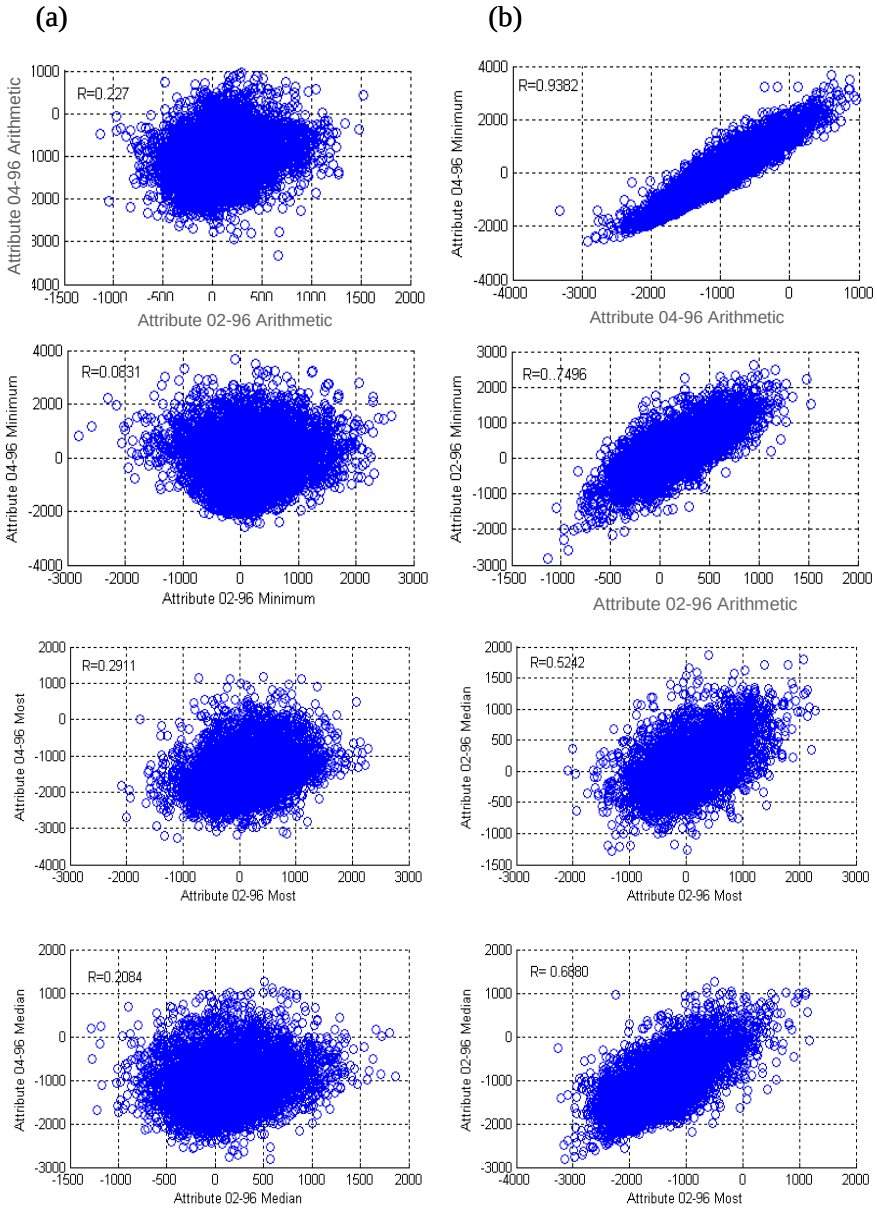

Figure 4.5: *(a) Correlation between the attributes, and (b) correlation between a specific attribute at different times. The correlation is higher between the different attributes, due to the high production activity over a reservoir's lifetime.*

4.2.3 Defining an optimal attribute for permeability calculation

Each 4D signature in Figures 4.2 and 4.3 gives some information on the true reservoir changes. The problem here is how to best combine the different 4D signatures in a sensible way that reveals an optimum attribute to detect the permeability pathways using all the available data, taking into account the uncertainty. There are a number of multi-attribute approaches to define an optimal attribute for a specific interpretation. Most of these techniques are pattern-recognition-based methods such as neural networks and principal-component analysis, in which a common-part of the maps is extracted and the remainder is treated as noise (de Groot *et al*., 2004). However, the main focus here is to keep the permeability transform as simple as possible in order to increase the practicality and facilitate implementation. Hence, it was decided simply to add the attributes that imaged the same reservoir differently, and to examine this method. The method is actually analogous to stacking the traces in seismic processing. This essentially implies the functionality of pattern-recognition methods in manifesting the common parts, while the random trend and noise are reducing in sum.

Figure 4.6(a) shows the result of summation. By firstly summing all the maps, a distribution is produced that has its mean as the sum of the individual map means:

$$\mu\left(\sum_{i=1}^{n} X_i\right) = \mu_{X1} + \mu_{X2} + \cdots \mu_{Xn} \tag{4.2}$$

where X_i is an attribute map and μ is the mean value of specified attribute map. The spread of the sum of the normally distributed but correlated (dependent) random variables is given by:

$$\sigma^2\left(\sum_{i=1}^{n} X_i\right) = \sum_{i}^{n}\sum_{j}^{n} \mathrm{Cov}\left(X_i, X_j\right) \tag{4.3}$$

where σ^2 is the variance and Cov is the covariance of each attribute map with all of other attribute maps. The covariance is zero for the independent random variables (if it exists). The formula states that the variance of a sum is equal to the sum of all elements in the covariance matrix of the components. An estimate of the uncertainty can also be examined by calculating the spread of the data for each bin location, and for all mapped 4D signatures (Figure 4.6(b)). In addition, the stacked attribute can be considered as the optimal attribute. However, it appears that map values are biased by the noise and very low values pattern, affected by some of the 93 base-lined attributes shown in Figure 4.2.

This is noticeable in the western part of the summed map, where an obvious thick strip following a NE–SW direction is observed, or in the flat anomaly in the northeast of this map.

To analyse this further, it is considered that the permeability result for each dataset consists of an underlying truth plus some normally distributed noise. Thus, the result of taking the mean of all data should provide a more robust measure of the data. It is decided to normalize maps (mean = 0 and variance = 1) prior to calculating the average, in order to avoid a biased result. Based on the Spearman–Brown (Brown 1910; Spearman, 1910) prediction formula of the classical test theory, if the variables have unit variance, then the variance of their mean is:

$$\sigma^2\left(\overline{X}\right)=\frac{1}{n}+\frac{n-1}{n}\rho \tag{4.4}$$

If the variables have equal variance (σ^2) and the average correlation of distinct variables (n is the number of variables) is ρ, then this implies that the variance of the mean increases with the average of the correlations. It is applicable for the normalized maps in which variables have unit variances and zero means. The mean of the normalized maps is shown in Figure 4.7. Comparison of the summation attribute and the mean of normalized maps shows that in the summed map each map does not have an equal influence on the result. Hence, very high or low values in non-normalized maps may end up biasing the summed map. In fact, by normalization of each map over its standard deviation, values are weighted according to their spatial variation. Standard deviation used for normalizing maps is a factor that scales the data according to accuracy or information content of a given observable variable. Therefore, it is suggested to use average of normalized values to eliminate the artefact observed in the summation of the data.

In the optimal average map calculated here, most of the coherent energy, which consists of a major signal, is captured; random noise, acquisition footprint, and non-repeatable noise response are reduced. It is also cost-effective compared with other methods such as principal component analysis (PCA) and the neural network method. Employing an optimal attribute while carefully measuring the uncertainty due to attribute selection

will enhance the permeability result of Seis2perm transform and provides the evaluated error attached to the final permeability map.

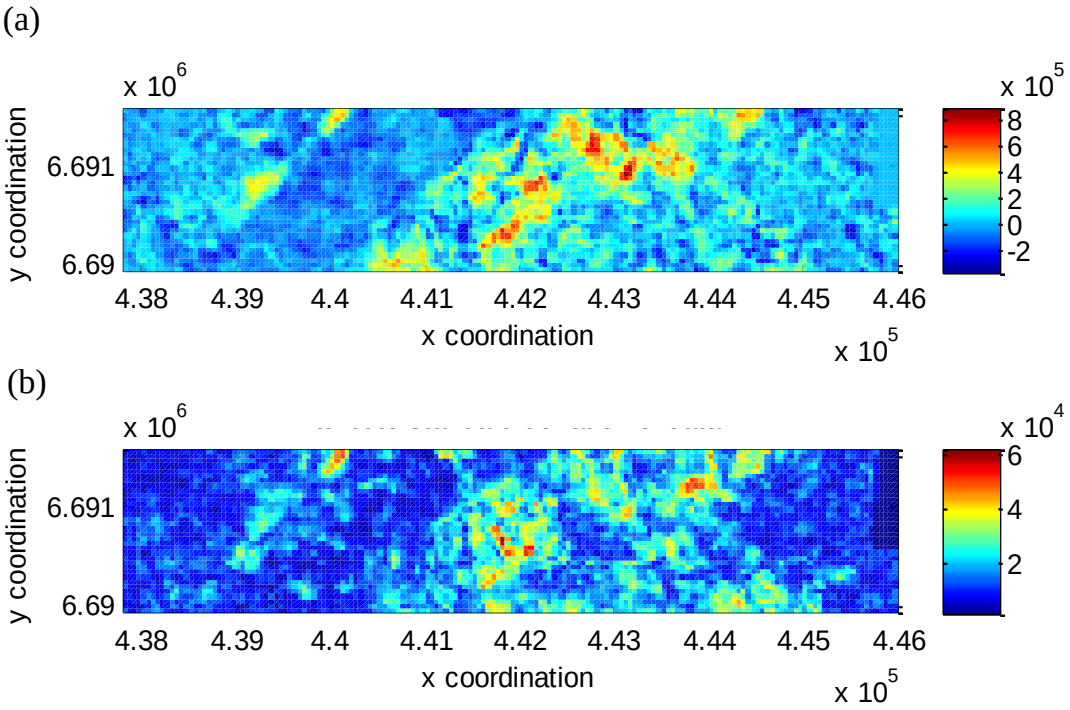

Figure 4.6: *(a) Summation of data for each bin over all the maps, and (b) standard deviation of the data for each bin over all the mapped 4D signatures.*

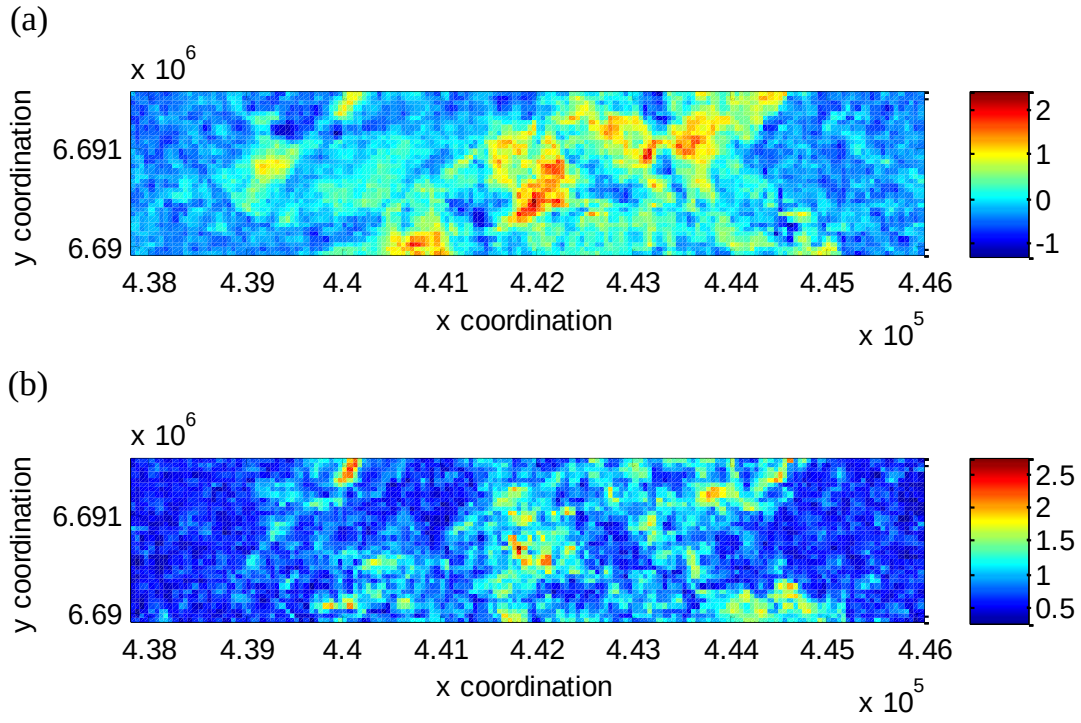

Figure 4.7: *(a) The mean of normalized data for each bin over all the maps, and (b) the standard deviation of the data for each bin, over all the mapped 4D signatures.*

4.3 Errors due to the tuning effect in calculating NTG for the Seis2perm transform

Another important aspect of the permeability-estimation transform (Equation 2.1) is calculating the effective porosity. The process of permeability assessment is a practice in which the 4D seismic is used to filter the active sands (sand-bodies responding to production activities). These sand-bodies are defined by the base-line seismic through the effective porosity estimation in the Seis2perm technique. This means that the channels are indicated by the effective porosity, and that the 4D-seismic signature manifests the active channels over time. Effective porosity is the product of sand porosity by net-to-gross (NTG). In the Schiehallion field, the variation of porosity is very small (for example, in segment 1 it is 0.27 to 0.29), so that it is generally considered as a constant value. Thus, the NTG effect is the influential parameter determining the shape of the channels and affecting the permeability result.

The conventional NTG calculation in this field has been using the arithmetic average or RMS average of amplitudes extracted from the coloured inversion volume (pre-production 1996 seismic survey), which is considered to be a good indicator of channels. For example, Soldo (2004) proposed a linear transform to scale the seismic-attribute range to NTG range for this field:

$$\overline{\mathrm{NTG}(x,y)} = \mathrm{NTG}_{\min} + \frac{\mathrm{RMS}(x,y) - \mathrm{RMS}_{\min}}{\mathrm{RMS}_{\max} - \mathrm{RMS}_{\min}} \left(\mathrm{NTG}_{\max} - \mathrm{NTG}_{\min}\right) \tag{4.5}$$

where $\overline{\mathrm{NTG}(x,y)}$ is the vertically averaged NTG map; RMS(x,y) is the average seismic attribute; and $\mathrm{NTG}_{\max}$ and $\mathrm{NTG}_{\min}$ are the maximum and minimum of vertically averaged NTG obtained from the operator's reservoir model. This transform could provide a good approximation when the appropriate attribute discriminating sand channels from shale is selected for NTG calculation. However, discounting the tuning effect may play an important role in introducing errors into the calculation.

The modelling performed for the Schiehallion field revealed that the RMS attribute used for calculating the NTG shows a tuning effect and cannot be directly transformed to NTG estimates (see Appendix E for more details). Therefore, the method proposed by Connolly (2007) is employed to calculate the detuned net pay for Schiehallion (refer to Appendix E). This net pay calculation is further processed here to calculate NTG.

Therefore, the estimated net pay is divided by the reservoir thickness extracted from the reservoir-simulation model. The final estimated NTG is shown in Figure 4.8(a). In fact, the NTG calculated based on the described procedure is a detuned and calibrated revision of the seismic attribute in Figure 4.8(c). The result appears to be more consistent with the NTG of the simulation model (Figure 4.8(b)). However, the NTG calculated from seismic data may preferentially reveal the reservoir reality between the wells, in contrast to the interpolated NTG values from the simulation model.

Measuring the uncertainty attached to the algorithm used for NTG estimation is also a desirable objective here. Connolly's algorithm is accurate for arbitrarily small true thicknesses (although the signal-to-noise will decrease for thin reservoirs). The rule-of-thumb is that the separation between picks should not be greater than the half-cycle of the lowest frequency component of the wavelet. Results for greater thicknesses should be used with caution. The reservoir must be isolated, in other words the wedge model must apply. The degree of reliability of the algorithm applied depends on the validity of the assumptions, thus, the uncertainties attached to the assumptions have to be measured. The main assumption of this net pay estimation procedure is that, for the band-limited data, the average of the band-limited data over the apparent thickness between zero crossings is proportional to the seismic net-to-gross. However, the accuracy of this relationship decreases as the gross interval increases. Departures from proportionality are largely caused by variations of the internal layering within the reservoir. The details of the uncertainty quantification for NTG calculation using the specific algorithm described above were addressed by Connolly and Kemper (2007). In their method, layering patterns are simulated using power-law exponentials for sand and shale bed-thickness distributions. Thousands of pseudo well-logs are generated to synthesize the average band-limited impedance responses between zero crossings. This is performed for a range of gross thicknesses and net-to-gross in order to span a wide range of net-to-gross. Total net from the V_{shale} log is measured and divided by apparent thickness to yield seismic net-to-gross. Average band-limited impedance is cross-plotted against seismic net-to-gross. From these cross-plots, maps of apparent thickness, and seismic net-to-gross, a seismic net-to-gross standard-deviation map is generated. (For details of this procedure, refer to Connolly and Kemper, 2007.) The calculated standard deviation is displayed in Figure 4.9.

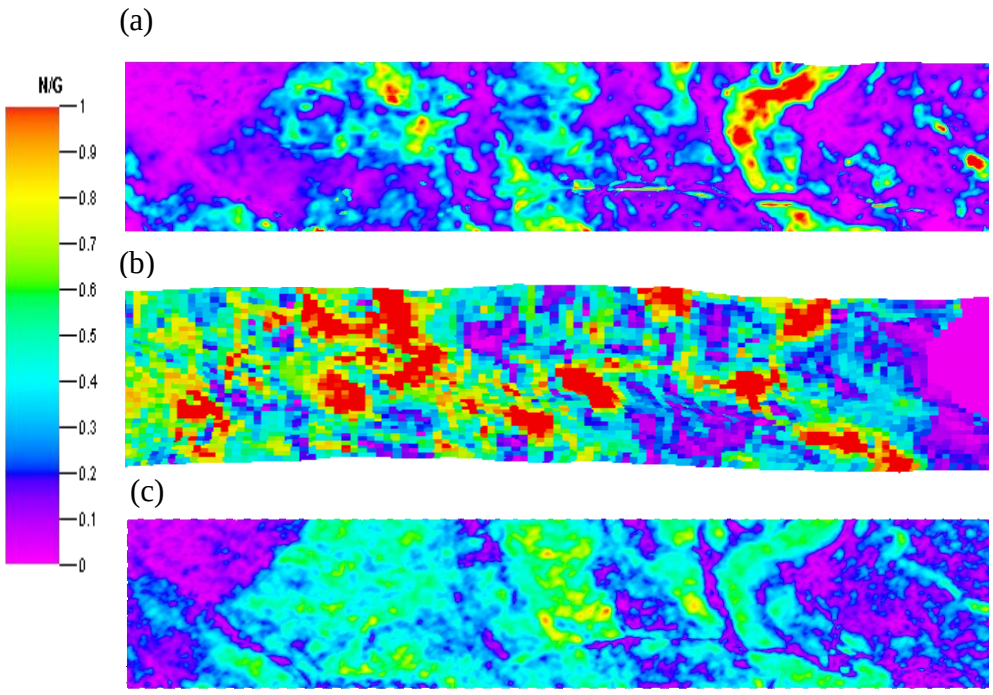

Figure 4.8: *(a) The NTG calculated from the coloured inversion base-line seismic (1996 seismic data), using a model adapted from Connolly's method; (b) the NTG from the simulation model; (c) the NTG estimated from the base-line seismic attribute without removing the tuning effect.*

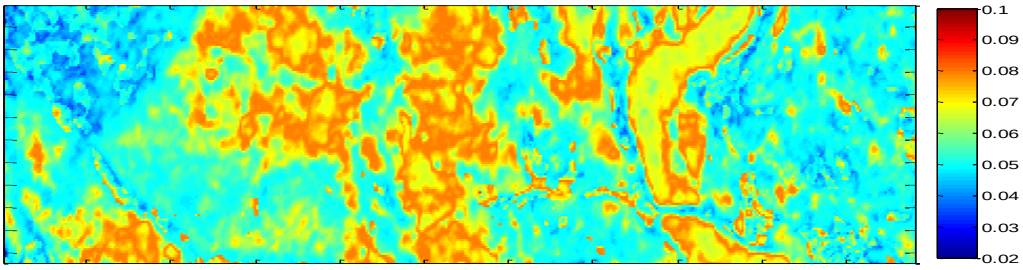

Figure 4.9: *Map of the standard deviations, indicating the spatial uncertainty of the seismic net-to-gross estimates.*

Removing the tuning effect also appears to be essential for calculating difference maps. The tuning effect may not be cancelled out in making difference maps, as it is not a linear event. The non-linearity is caused because the effect of fluid replacement changes the amplitude. As a result, the tuning thickness may shift as the top and base picks come together at a different location. Also, fluid contacts (the oil–water contact, the gas–oil contact and the water–gas contact) may show a tuning effect. The issue of a changing

tuning effect over time requires a technique to overcome the various challenges described above. In fact, this technique is very sensitive, as applying a method which does not consider all of these influencing artefacts may end up with added uncertainties instead of removing the uncertainty.

4.4 Validation of the assumptions of pressure-controlled seismic, and the uncertainty due to its inaccuracy

A further range of uncertainties are due to assumptions in the method estimating permeability. Here, uncertainty in the Seis2Perm transform method is due to inherent assumptions in the method, related to the pressure-only solution and the single-phase derivation of the method.

In an analytical comparison, the optimal 4D signature calculated in section 4.2 is compared with modelled dynamic change in the reservoir-simulation model. Since the 4D signal is a mixture of pressure- and saturation-change, the pressure change and saturation change are modelled from simulation data to compare with the optimal attribute (Figure 4.10). It appears that pressure change shows more spatial variation for this reservoir, in contrast to saturation change. Saturation change is mostly limited to well locations, while pressure change shows a high level of frequency change due to major segmentation in the reservoir. This may cause the pressure change to play a central role in affecting the 4D signature, although, in the regions close to the well, saturation change is also contributing to influencing the 4D seismic response. Interestingly, the optimal attribute appeared to be fairly dominant, with pressure change occurring as the result of various types of production activity over time. Hence, this confirms the assumption of pressure-controlled 4D signatures in the permeability-estimation technique for this specific field. However, this assumption may not always be true, as most of the reservoirs are dominated by both pressure and saturation, or mostly saturation. To analyse this further, the synthetic blocky model described in Chapter 2 is considered. Two scenarios are examined to investigate assumptions in the Seis2perm technique. Case 1 is the depletion due to production. In this case, pressure change is the main component, and saturation change is negligible as there is no upwards movement of the oil–water contact. Case 2 is a producer–injector pair involving both pressure- and saturation-changes. The reservoir model has 100 by 100

cells in which there is a patch of permeability. That background matrix has 100 mD permeability, and the patch permeability is 1000 mD. The objective is to evaluate the accuracy of recovering the permeability patch in both scenarios. The simulation model is run for the models in order to calculate pressure- and saturation-changes over time. The pressure- and saturation-changes can be utilized in the method of Floricich *et al.* (2005) to model the 4D signal without the need for rock and fluid physics:

$$\frac{\Delta A}{\overline{A}} = \mathrm{Cp}\frac{\Delta P}{\overline{P}} + \mathrm{Cs}\frac{\Delta S}{\overline{S}} \tag{4.6}$$

where C_p and C_s are weighting constants that adjust the influence of pressure and saturation on the 4D-seismic response. Table 4.2 shows the estimates of C_p and C_s from implementing the pressure-saturation inversion method on two field examples. This table shows that in the Schiehallion field the influence of pressure is almost three times more than saturation. The Marlim field appears to show a similar behaviour.

In the synthetic models, the impact of tuning C_p and C_s constants reveals how the pressure assumptions of the Seis2perm transform may tend to be invalid. The 4D-seismic signature (ΔA) is calculated for different scenarios with various weights on pressure and saturation terms. In a production-depletion scenario, the saturation change is negligible, so ignoring the saturation term (C_s) does not significantly influence the recovered permeability (see Figure 4.11). For different C_p and C_s in the production-depletion scenario, the overall match between reference- and recovered-permeability is reasonable. However, there is a 5% mean error between the model and the predictions, mainly due to a mismatch in the permeability values close to the producer. On the other hand, in an injection–production pair, the overlapping saturation change in the 4D signature results in resolving the permeability patch to a lesser extent. The errors rise when the method ignores the fact that the saturation plays a foreground role in the 4D seismic response. Thus, inaccuracies are introduced into the recovered permeability.

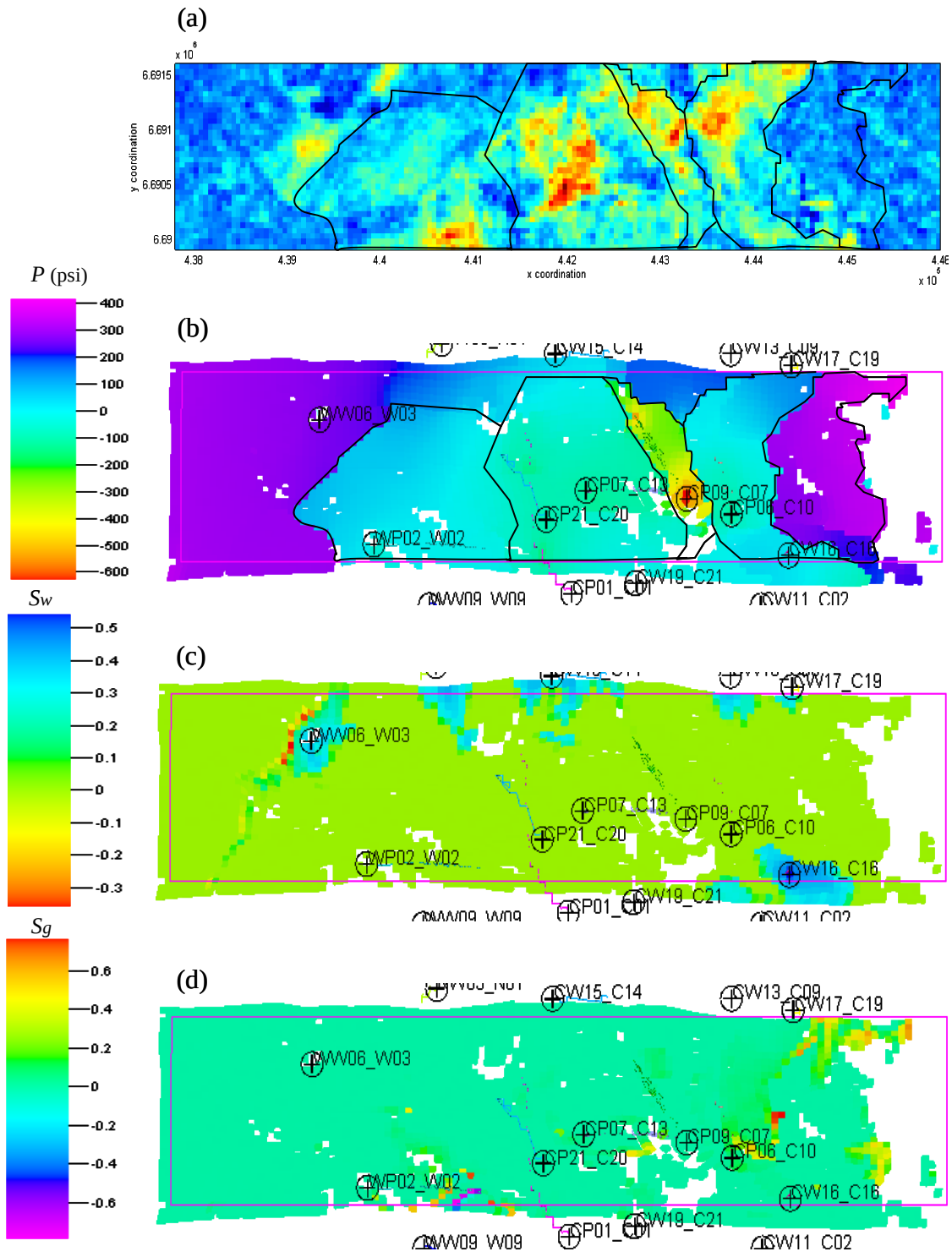

Figure 4.10: *(a) Multi-4D attributes response; (b) pressure change between 1998 and 2004 from the simulation model; (c) water-saturation change between 1998 and 2004 modelled from the simulation model; and (d) gas-saturation change between 1998 and 2004 modelled from the simulation model.*

The error involved with the result of permeability when the saturation involved in the 4D seismic signature lies within 30%, suggesting that the solution cannot be determined precisely. The imprint of the saturation flood front is noticeable in recovered permeability when the impact of saturation on the 4D signature is high (see Figure 4.11). In fact, the Laplacian function in the method may detect the water-front as a flow barrier with low permeability. These errors are caused by the simplicity of the method, in which saturation change is not considered in an appropriate way. The reason for this is that the Seis2perm equation is derived based on a single-phase assumption. Using a single-phase formulation which does not consider the saturation change will produce significant errors. Hence, a two-phase formula has to be examined in order to consider the trade-off between pressure- and saturation-change. Involving relative permeability is the key parameter to bring the saturation change in the two-phase pressure equation. A mathematical development is presented in Appendix F in order to address this issue. An equation is proposed for permeability estimation in which both pressure- and saturation-changes and their trade-off are incorporated in a single formula.

Table 4.2: *C_p and C_s constants for the Schiehallion and Marlim fields*

Schiehallion field			**Marlim field**		
Attribute	C_p	C_s	**Attribute**	C_p	C_s
RMS	1.63	–0.49	Near offset	2.04	–0.17
Sum of negatives	1.48	0.58	Mid offset	1.41	–0.20

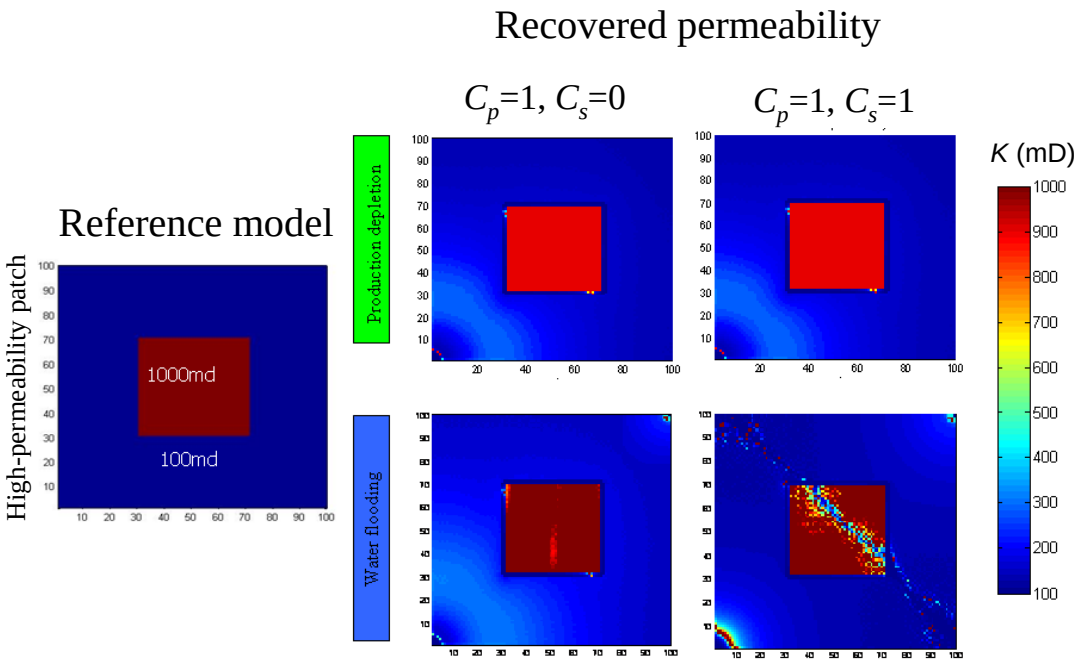

Figure 4.11: *Recovering permeability for the synthetic blocky model with 1000 mD permeability; two scenarios are considered: the production-depletion and the production-injection pair for water-flooding. The C_p and C_s terms in the Floricich et al. technique (2005) are used to weight the pressure/saturation impact on the 4D-seismic signature and to predict the consequence of pressure assumptions in the Seis2perm technique for recovering permeability.*

4.5 Calibration of the Seis2perm product with well data

Another source of error comes from assumption of the fixed viscosity and compressibility factor in Equation 2.1. In an isothermal process, compressibility and viscosity are pressure-dependent properties. For oils with a higher API factor (live oil), the compressibility is higher and the viscosity is lower. For oil with high compressibility factor, a certain amount of change in pressure would result in a significant change in compressibility. However, the viscosity varies with pressure to a lesser extent, and can still be considered as a constant.

Close to the injector, the pressures are high and the compressibility diminishes. On the other hand, close to the production well, the pressure is low and the compressibility increases. As a result, in the vicinity of wells the method tends to alter the permeability results. Thus, the chosen pre-selected constant value underestimates or overestimates

compressibility near to the well. This problem is addressed in Chapter 2 by introducing a pressure-dependent compressibility in which the pressure variation is linked directly to the 4D signature.

In order to further improve the accuracy of the permeability result around the wells, it is decided to calibrate the resultant permeability map with permeability values at the well locations. The calibration will partially compensate for the effect of compressibility variation described above. The procedure starts by extracting permeability values from the simulation model at well locations, in the form of pseudo well-logs. Well-log data are up-scaled vertically between the top and the base of the reservoir (Figure 4.12). Selected wells in the particular area of interest (segment 1 of the Schiehallion field), and the depth range in which they have been up-scaled, are listed in Table 4.3. In order to calibrate 4D-seismic-derived values to well data, the calibration factor, α, is determined in an optimization procedure. The calibration process is preceded by verifying α, so that the objective function (F) defined between 4D-seismic-driven permeability at well locations (K_{4D}) and well-log permeability (K_{well}) would be minimized:

$$F = \sum_{j}^{Ny} \sum_{i}^{Nx} \left(\alpha K_{i,j}^{4D} - K_{i,j}^{well} \right)^2 \rightarrow \min_{\alpha} \left| \alpha K_{4D} - K_{well} \right|^2 \tag{4.7}$$

$$K_{calibrated} = \alpha . K_{4D} \left(C_p, \text{NTG}, \Delta A, \text{Laplacian}(\Delta A) \right) \tag{4.8}$$

In practice, calibration remains a somewhat delicate process that should ensure consistency with well data and provide sensible permeability values transformed from the arbitrary seismic-attribute values (or optimal attribute values).

Table 4.3: *The list of the wells used in calibration, indicating the type of well, the trajectories, and the depth range in which they have been up-scaled.*

Well ID	Well type	Trajectory	Depth range (ft)
WW06_W03	Injection	Vertical	6708.876 to 6983.397
WP02_W02	Production	Horizontal	6504.114 to 6582.368
CP07_C13	Production	Horizontal	6533.655 to 6834.272
CP21_C20	Production	Horizontal	6425.047 to 6679.259
CP09_C07	Production	Horizontal	6422. 221 to 6579.343
CP06_C10	Production	Horizontal	6419. 324 to 6606. 765
CW16_C16	Injection	Vertical	6417.153 to 6551.659

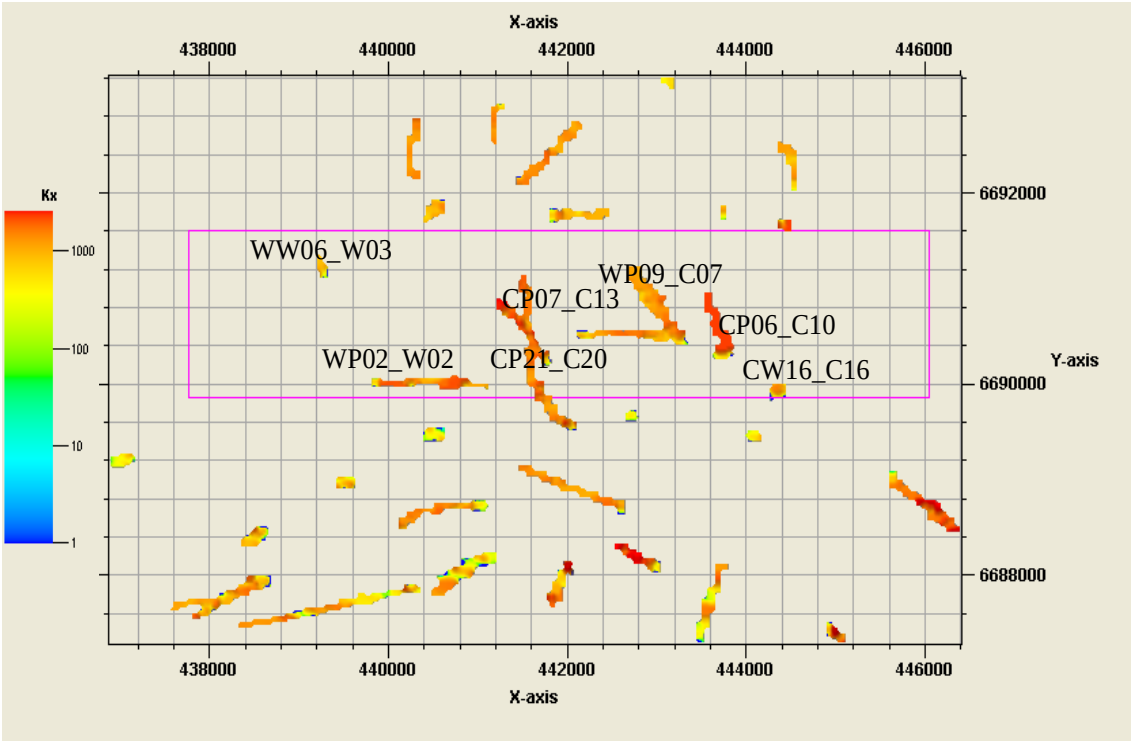

Figure 4.12: *The permeability is up-scaled between corresponding horizons to the top and base of reservoir T31a in Schiehallion. The map shows the up-scaled permeability values at the well locations. These are used for the calibration of 4D-seismic-estimated permeability.*

4.6 Analysis of the nature of the Seis2perm method and the influence of the Laplacian

Basically, the Seis2perm transform has two major components:

- component 1 = 1/Laplacian,
- component 2 = NTG (3D seismic attribute) × 4D seismic attribute.

The product of these two is equal to the effective permeability. The second component suggests that if 3D-seismic-imaged channels (scaled into NTG or effective porosity in the Seis2perm technique) are multiplied by 4D-seismic-highlighted channels responding to production activity over time, then the result will be an approximate indicator of the permeability pathways. This concept is used in the approach by Shams *et al.* (2007) to indicate the permeance connections in the reservoir. In this technique, in 3D seismic the sand-bodies are distinguished from shale by clustering (analogous to the NTG evaluated from 3D seismic in the Seis2perm transform) and then the 4D signatures within the recognized sand-bodies are multiplied to estimate the connectivity. Subsequently, this is

calibrated with evaluated connectivity from interference well testing (see Figure 4.13). Computing effective permeability from the product of 3D-seismic-distinguished sand-bodies by 4D-seismic signatures (component 2 of the Seis2perm transform) essentially implies the proportionality of the estimated permeability with the 4D response. Oliveira *et al.* (2007) employed this proportionality concept to guide permeability estimation in the reservoir, using kriging with external drift to the 4D-seismic attribute. In fact, they only used 4D seismic in component 2 of Seis2perm to populate the permeability values according to the 4D-seismic-attribute trend. They found the result very useful when they fed the predicted permeability into a simulation and reduced the duration of the history-matching process (see Figure 4.14). Huang and Ling (2006) also used a 4D-seismic difference map as an indication of inter-well connectivity. Based on the proportionality assumption, they translated the 4D-seismic difference map into a quantitative expression of connectivity using the stochastic hill-climbing approach.

While component 2 of the permeability transform identifies matrix permeability, the first component of the Seis2perm equation indicates fault permeability, in which the Laplacian is used to detect connectivity barriers in a similar way to coherency and curvature attributes. Many researchers have addressed the success of second derivative attributes for assessing fault permeance in the reservoir. For example, Floricich *et al*. (2008) used the coherency of the 4D attributes from different surveys to evaluate the connectivities of the flow barriers. Therefore, calculating what is called effective connectivity or permeability in Seis2perm transform as the product of two components appears to be a feasible approach proved over the course of various studies. However, in evaluating effective permeability by integrating two components, high Laplacian values at boundaries of compartments in the denominator of Equation 2.1 alter the result and introduce instability. Usually, it is not easy to control this effect (the issue of the Laplacian effect in permeability estimation and how to handle this are discussed in Chapter 2). However, an alternative method proposed in Chapter 5 can evaluate matrix permeability and fault permeability separately.

In addition, the Seis2perm transform would result in different estimate of permeability when a different 4D seismic surveys is used. This is due to change in saturation and to pressure anomalies caused by various production activities over time. Therefore, it is necessary to take into account successive 4D-seismic surveys in permeability

estimation, using an effective approach. In the next two chapters, an alternative approach will be used to assess connectivity and disconnectivity, by decomposing the two components of Seis2perm. This approach is a two-stage procedure, where fault connectivity and connectivity between the cells are calculated separately. The sequence of interpreted time-lapse-saturation- and pressure-anomalies from frequent surveys are used to evaluate transmissibility and transmissibility multipliers respectively. For transmissibility multiplier calculation, the Laplacian anomalies (instead of Laplacian values in Seis2perm) in time-lapse pressure are integrated with a material-balance calculation to estimate the fault transmissibility. Also, integration of channels imaged by 3D seismic that are also responsive in successive time-lapse saturation within the channels is used to assess transmissibility between cells. This is performed via a geostatistical approach in order to ensure that the transmissibility extracted from hard data at well locations is sustained.

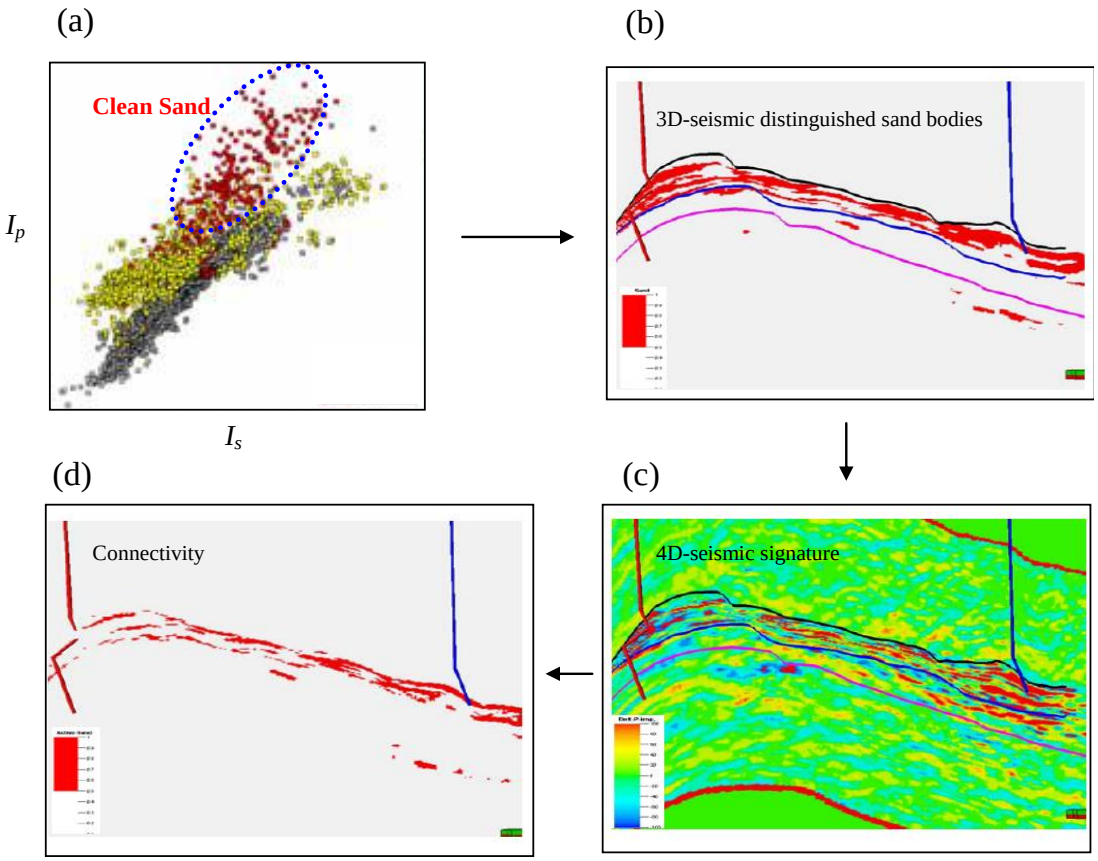

Figure 4.13: *Connectivity assessment procedure by Shams et al. (2007) applied to the Girassol field located in the Gulf of Guinea, Angola.*

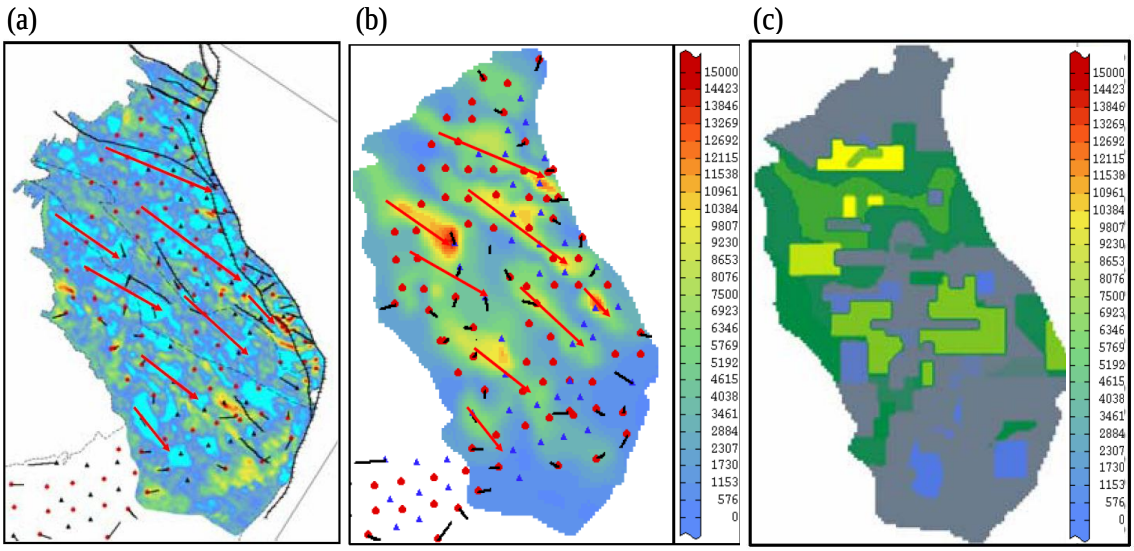

Figure 4.14: *Permeability estimation in the Marlim field, Brazil: (a) 4D difference map for 2005–1997, where light blue indicates heavy oil replaced by water; (b) introducing a 4D anisotropy map into permeability by kriging with external drift; and (c) permeability of a simulation model after the history-matching process (after Oliveira et al., 2007).*

4.7 Enhanced resulting permeability

In order to provide an enhanced permeability result and simultaneously provide the associated error attached to the estimation, the stages discussed in this chapter for treating the input parameters of the Seis2perm calculation have to be performed carefully. The optimal attribute calculated here is tested for pressure-only assumption and is found to be a satisfactory assumption for this field. The optimal attribute with a measured uncertainty is then multiplied by the detuned estimated NTG, for which its own uncertainty has been calculated. The result is calibrated at the well locations, using an optimization technique. Eventually, the resulting permeability map is displayed in Figure 4.15(b). In comparison with the vertically averaged permeability from the simulation model, there are some general agreements between estimated permeability derived from different attributes and the simulation-model permeability. However, in many regions there are significant differences between the estimated averaged permeability and the simulation model. This comparison is examined in greater detail in Figure 4.16, where cross-plots of values in the *x* and *y* directions are shown.

The error in the estimated permeability is calculated by taking into account the contributing uncertainties in the main inputs of the Seis2perm technique (3D-seismic and 4D-seismic attributes) using the following setting. The parameters of Seis2perm formula are either a function of the 4D-seismic attribute (ΔA) or the 3D seismic attribute (A_0):

$$K = \left(C_p(\Delta A) \times \frac{\Delta A}{Laplacian(\Delta A)} \right) \times \left(NTG(A_0) \right) \tag{4.9}$$

Therefore two types of functions (f and g) with different inputs can be identified:

$$K = f(\Delta A) \times g(A_0) \tag{4.10}$$

The standard deviation for this setting is calculated by (see Goodman, 1960):

$$\delta(K) = f_m g_m \sqrt{\left(\frac{\delta(f)}{f_m} \right)^2 + \left(\frac{\delta(g)}{g_m} \right)^2} \tag{4.11}$$

where $\delta(K)$, $\delta(f)$ and $\delta(g)$ are standard deviations of permeability, functions f and function g, respectively and f_m and g_m are mean values of function f and function g. The standard-deviation map ($\delta(K)$) shown in Figure 4.15(a) is an indication of the error attached to the permeability estimation, due to selecting different attributes and to the method used to estimate the NTG from 3D seismic. For the sake of interpretation, the resulting standard deviations are displayed for each point of the 4D-seismic-estimated permeability value in Figure 4.16. Clearly, in vertical cross-section, there are some rough similarities in the general trends of both maps. However, in horizontal cross-section the 4D product has imaged the permeability differently in certain areas. For example in the western and central parts of the maps, there are some agreements for both trends, although there is strong disagreement in the eastern part of the cross-section. In areas of disagreement, the standard-deviation value indicates the reliability of the 4D-seismic product. This is even applicable for areas of agreement. For example, in the western part of the horizontal cross-section up to cell 36, the trends are similar, and the standard deviation is also low, indicating that most of the attributes show the same pattern and that the NTG estimation method is less uncertain. Since this area is far from the well location (thus, the simulation model is less trustworthy), one may trust the Seis2perm-imaged permeability. From cell 111 to 121, high standard deviations (from

±210 mD to ±300 mD) imply that the attributes show different signatures in this region, or that the NTG uncertainty is greater. This is where the deviation of the simulation permeability map from the mean of the 4D-predicted permeability map is very large. Therefore, the 4D results should be used with caution. From cell 121 to 157, although the D-extracted permeability is different from the simulation permeability, the standard deviation is small enough (from ±80 mD to ±180 mD) to trust the 4D-seismic estimate.

Overall, the errors in the permeability estimation are moderate to high, but can still be used to adequately constrain the simulation model for history-matching purposes.

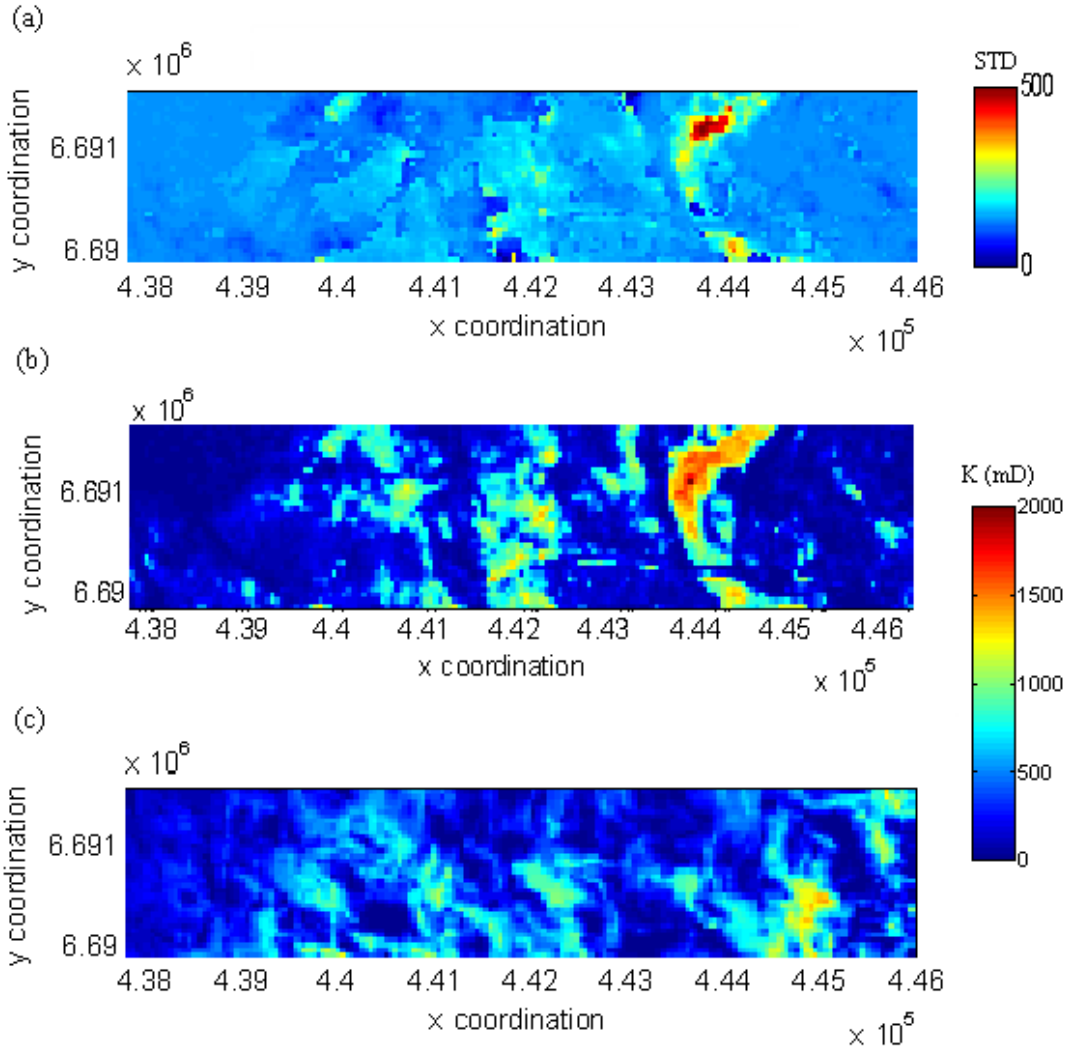

Figure 4.15: *(a) Standard deviation for the resulting permeability; (b) enhanced estimated permeability; and (c) vertically averaged permeability from the simulation model.*

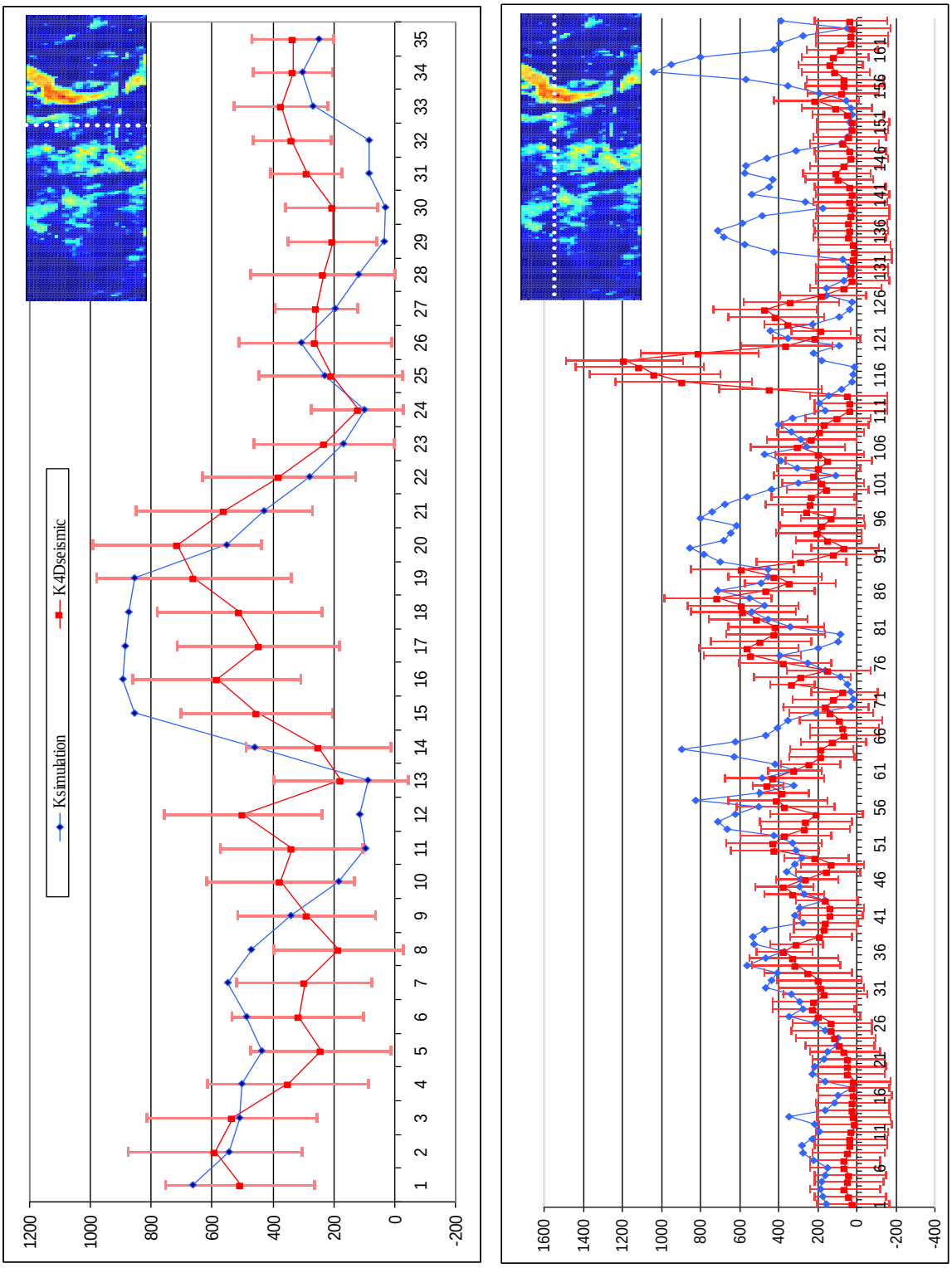

Figure 4.16: *Mean permeabilities derived from different attributes, compared with reservoir-simulation permeability using cross-sections in the x and y directions. The calculated error for the estimated permeabilities is specified.*

4.8 Summary and conclusions

Errors in permeability estimation can arise from many sources: seismic noise, picking error, the choice of the different attributes, calibration error, and invalidity of the assumptions of the proposed algorithm. The uncertainties in the input data can be quantified in order to measure the impact on the final estimated permeability. Also, certain techniques can be applied to make the Seis2perm technique a more robust algorithm; permeability can be calculated from the optimal attribute by combining a range of attributes and a sequence of multiple time-lapse surveys. Taking the mean of the statistically normalized maps is an effective strategy – fundamentally similar to pattern-recognition methods. However, compared with the pattern-recognition method, this technique is simple and practical, i.e. consistent with the objective of the current study to derive the permeability attribute from the 4D signature using a simple and rapid technique. The effect of diversity over different attributes in permeability prediction is investigated in terms of the uncertainty attached to the method. Furthermore, detuning the seismic NTG estimation helps to provide a more reliable result. Applying detuning makes the map attribute more consistent with the reservoir property. The assumption of pressure-dominated 4D seismic in the Seis2perm technique could be seen as a potential drawback of this approach. The validity of the pressure-controlled assumption in the Schiehallion field is tested and proved to be satisfactory when it is compared with the optimal attribute used. However, the application of the Seis2perm method to saturation-dominated 4D seismic has to be performed with special care. In an ideal case, pressure and saturation have to be separated prior to the permeability estimation. This has to be done in order to reduce the uncertainty caused by using a mixture of both pressure and saturation in a permeability-estimation scheme. The accuracy of permeability estimation can be improved further around the well locations, using a calibration procedure. As a result of carefully treating the input parameters in the Seis2perm transform, permeability estimation can be enhanced and the errors attached to the estimation can be calculated. The variability of the inputs will impact on the permeability result, and the errors are just about acceptable. Further errors may be added while transferring data between the seismic maps and the 3D volumetric information of the simulator. However, it was proved in Chapter 3 that, despite this, the method can serve as a reasonable approximation of permeability that will improve the history match in an effective way.

CHAPTER 5: CONNECTIVITY EVALUATION USING 4D SEISMIC

Overview

This chapter investigates connectivity in the context of the permeability estimation discussed in previous chapters, and examines the means by which this property can be estimated using 4D seismic. The study is performed together with a number of different tests to track exactly how connectivity might be related to the 4D-seismic response. It is found that connectivity has a variable imprint in 4D seismic, depending on whether it is dominated by pressure- or saturation-signals. Based on the understandings derived from this study, various inversion techniques are proposed in order to extract connectivity from the 4D-seismic signal.

5.1 Introduction

Two points in a system are said to be connective if there is an unhindered path from one point to the other. In the context of reservoir engineering, if a fluid is able to flow from one point to another, or if pressure communication can be established between two points, then these points are connected. (This is a very generic definition of connectivity, since one should also consider the recovery process involved.) This type of connectivity is also known as dynamic connectivity, due to the fact that in a porous medium the flow is advancing over time and is said to exhibit dynamic behaviour within the reservoir.

Effective pressure maintenance in a water-flooding process relies upon the existence of good dynamic connectivity between injectors and producers. Dynamic connectivity directly influences the recovery factor. Compared with permeability estimation, it is usually easier and more practical to estimate connectivity, as it is referred to as a larger-scale property. However, it will be shown that the physics of the Seis2perm equation are inextricably linked to the connectivity assessment proposed here.

The main challenge for connectivity modelling is the generation of a simple and general formula for reservoir connectivity to capture it quantitatively. As such, introducing a reasonably accurate formula relating the key measurable subsurface parameters is an essential element for every connectivity study. A review of previous attempts to evaluate connectivity both in the reservoir-engineering domain and the 3D/4D-seismic domain indicates that, generally, there are two main recognizable categories: local and global connectivity. If the connectivity of the porous medium is considered between two wells, it is referred as global connectivity (or well-to-well connectivity) and if it is between two local points (for example, grid blocks in reservoir model), it is referred as local connectivity (or cell-to-cell connectivity) (see Figure 5.1). The examples of global connectivity are the studies pioneered by Albertoni and Lake (2003), who presented connectivity as the regression coefficient between the wells in a multivariate linear-regression model (see Figure 5.1(a)). Huang and Ling (2006) utilized this approach to employ a 4D-seismic difference map. Yousef *et al.* (2006) also followed a similar concept for their proposed capacitance model (CM) to estimate well-to-well connectivity. Local connectivity is rarely investigated in the literature; however, Shams

et al. (2007) used a facies-analyses approach in 3D/4D seismic to distinguish 'active sands' responding to production activities. The active sands are assumed to reflect the local connectivity that was further calibrated with well-test information.

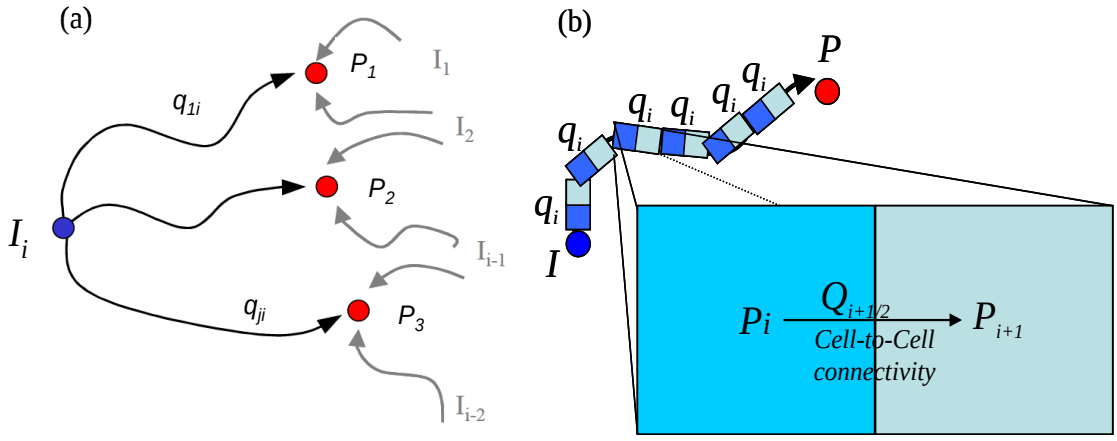

Figure 5.1: *(a) Global connectivity between wells (after Gentil, 2005), and (b) local connectivity from cell to cell.*

The focus of the current study is to examine how local connectivity can be estimated from seismic domain. Traditionally, static connectivity is estimated from 3D-seismic data. In this context, static connectivity is considered as the spatial continuity of the sand geobodies. This type of connectivity has been identified as the most important attribute to model in order to optimize the development of any oil reservoir. However, from the reservoir-engineering point of view, the central decision-making parameters, such as the recovery factor and the productivity index, are direct functions of dynamic connectivity (Tang and Wang, 2007). Dynamic connectivity discusses fluid movement paths and the degree of connectivity as a function of geological heterogeneity, capillary pressure, gravity force, fluid mobility and production/injection rate. Therefore, integrating 4D seismic as a tracking tool in monitoring flow-path directions within sand-bodies can add valuable observations to dynamic connections. Here, it will be investigated to see how 4D seismic is able to provide information on this property over time.

5.2 Evaluating connectivity using the Seis2perm method

The starting point for estimating connectivity from 4D seismic is linked to the Seis2perm philosophy of effective permeability calculation. It is important to note that connectivity is a consistent term with permeability, as on a large-scale the fluid will mainly flow through the highly permeable channels (Goloshubin *et al.*, 2008). For instance, high connectivity between a well pair could provide evidence for a highly permeable channel or a fracture between the wells. Conversely, a low connectivity value between two adjacent wells could be a sign of a low-permeability zone or barrier in the inter-well region. To investigate this concept further, the Seis2perm equation is rewritten as follows:

$$K_{\text{eff}} = a \times \phi_{\text{eff}}(A_0) \times \frac{|\Delta A|}{|\text{Laplacian}(\Delta A)|} \tag{5.1}$$

where a is a calibration or compensation factor, correcting for the effect of compressibility changes due to a high pressure change at the well location; φ_{eff} is the NTG-weighted porosity from 3D seismic (A_0); ΔA is the time-lapse seismic difference signature; and K_{eff} is the effective permeability. This equation consists of two connectivity-related terms, as shown in Equation 5.2. Hence, the effective connectivity can be decomposed into a continuity term (α) and a discontinuity term (β) respectively:

$$\text{Effective connectivity} \propto [A_0 \times \Delta A] \times \left[\frac{1}{|\text{Laplacian}(\Delta A)|}\right] \tag{5.2}$$

$$\alpha = [A_0 \times \Delta A] \tag{5.3}$$

$$\beta = \left[\frac{1}{|\text{Laplacian}(\Delta A)|}\right] \tag{5.4}$$

As was tested and described in the previous chapters, the existence of very high or low values of the Laplacian in the denominator of this formula tends to produce instability in the final permeability result. In addition, the two decomposed terms described above seem to indicate different types of continuity, such that in this thesis, the α term is referred to as the hydraulic connectivity and the β term is referred to as barrier connectivity. Therefore, it was decided to process these two types of connectivity separately and to combine them in the reservoir model for history-matching purposes.

Further tests in this chapter have proved the validity and consistency of the suggested decomposition with regard to the time-lapse response behaviour.

A diagram of the connectivity terms used in this study is shown in Figure 5.2, and illustrates how each definition is related to the others.

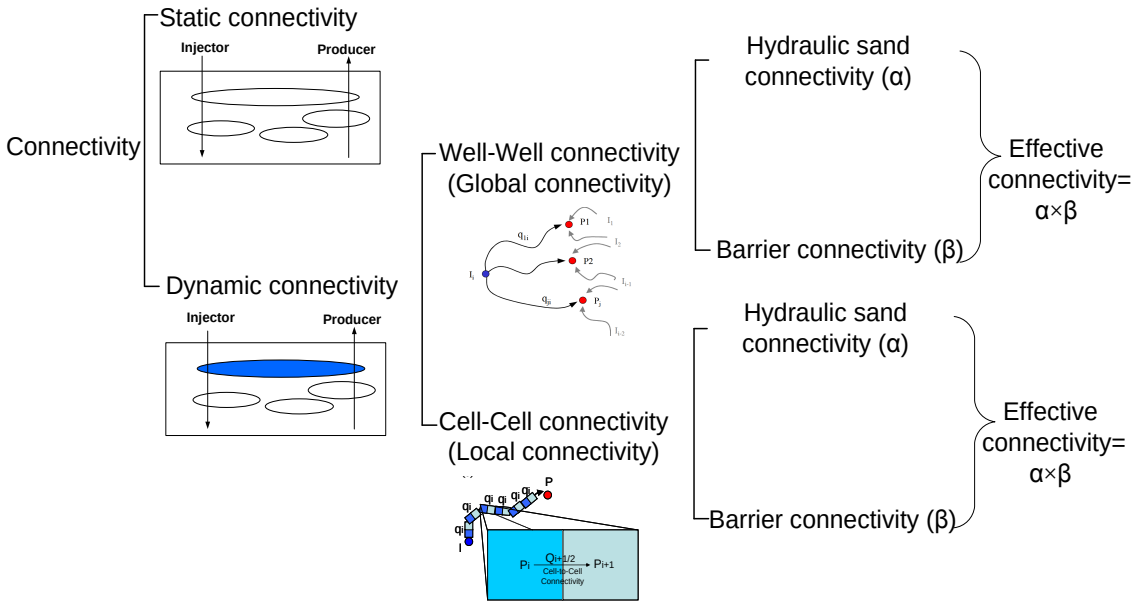

Figure 5.2: *How connectivity terms used in this study are fitted and related to each other.*

5.3 Hydraulic sand connectivity (α)

The α term introduced previously consists of two components of connectivity illumination: the 3D-seismic response and the 4D-seismic response. The functionality of each of these in estimating the hydraulic sand connectivity is described in this section. Subsequently, the consistency of this definition with the reservoir-engineering requirement for connectivity evaluation is tested.

5.3.1 Hydraulic-sand-connectivity assessment in the seismic domain

(a) 3D-seismic estimates of static connectivity: static connectivity is considered as the continuity of the sand geobodies, which is a function of the shale volume or NTG and describes a sand distribution. Apart from NTG, the transport properties in the initial

reservoir model are usually described in terms of permeability (porosity is a storability property). Unlike the NTG estimated from 3D seismic, estimating permeability from 3D seismic is a challenging task. Introducing a new attribute to infer permeability has been the focus of a number of studies (Nissen *et al.*, 2004; Goloshubin *et al.*, 2008; Kozlov *et al*., 2009). Although some of these attributes were used to detect fracture permeability in naturally fractured reservoirs (see Nissen *et al.*, 2004; Kozlov *et al.*, 2009), their workflow might be amenable to using attributes for assessing permeability. In some other attempts pioneered by Pride *et al.* (2003), using the Biot theory (1956), a frequency-dependent relationship between permeability and attenuation is proposed. In these studies, the general conclusion was that permeability information is concealed in the low-frequency content of the seismic data. Generally, the ultimate goal in most of these studies has been to try to relate the measurable seismic properties – such as acoustic impedance, and P-wave velocity variation and attenuation – to permeability. However, these methods are still ambiguous and debatable. Therefore, I have decided to consider NTG as a feasible parameter that can be estimated from 3D seismic as an indicator of static sand connectivity.

(b) 4D-seismic estimates of dynamic connectivity: monitoring the movement of fluid from the injection well towards the producers has been a very successful application proved during various secondary recovery operations (Parr and Marsh, 2000; McInally *et al.*, 2003). Assuming that fluid flow occurs in high-permeability sand-channels within the reservoir, 4D seismic can be utilized as an indication of the connectivity pathways within the reservoir (Andersen *et al.*, 2006; Huang and Ling, 2006; Oliveira *et al.*, 2007).

(c) Integration of 3D- and 4D-seismic estimates of connectivity: the two independent illuminations of connectivity from 3D seismic (NTG product) and 4D seismic are merged into the product defined as hydraulic sand connectivity. This is in fact a very useful product, in which the 3D-seismic NTG depicts the structure of the sand channels existing in the reservoir. Moreover, the 4D seismic illuminates the reservoir connection in areas within sand channels in which the flow sweep has occurred. Therefore, the final product indicates the regions of the reservoir that are hydraulically active. Thus, the estimated property is termed hydraulic sand connectivity.

On the other hand, this product boosts the channel presence and also filters the 4D-related noise, as described by Shams *et al.* (2007) and illustrated in Figure 5.3. The 4D seismic was always contaminated with repeatability issues and processing artefacts. The impact of this noise is more significant when one tries to quantitatively interpret a 4D-seismic difference map. In particular, if the 4D-seismic signal is transformed directly in order to estimate a reservoir property such as the permeability/transmissibility, special care should be taken not to transfer the 4D noise. Sand channels are highlighted in 4D seismic as the result of production activity (i.e. they are active sands). Assuming that the 4D-seismic response is the response of an active channel, the 3D seismic has to show a consistent recognized channel-sand body as well. In other words, where there is no sand (no signal in 3D seismic) there should not be a signal in the 4D response. However, the 4D signal may still be noisy and show a signature that can be interpreted as a sand responding to production. The 3D-seismic high-NTG helps to filter 4D-seismic-related artefacts when it is multiplied by the 4D-seismic signal. In addition, where there is a signal in both 3D seismic and 4D seismic attributed to a sand channel, the multiplication of the two signals boosts the presence of the channel in the reservoir.

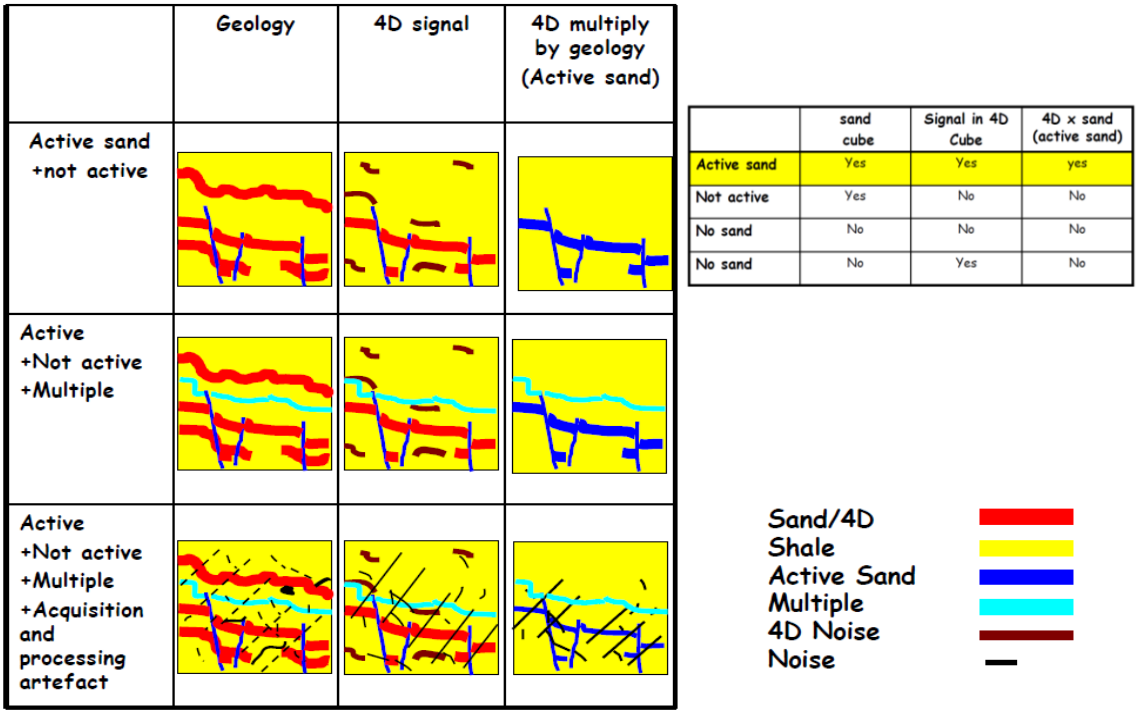

	sand cube	Signal in 4D Cube	4D x sand (active sand)
Active sand	Yes	Yes	yes
Not active	Yes	No	No
No sand	No	No	No
No sand	No	Yes	No

Figure 5.3: *The hydraulic sand connectivity is calculated in the α product. The α product is a useful estimate in which channel presence is boosted and 4D-related noise is filtered (after Shams et al., 2007).*

5.3.2 Hydraulic sand connectivity in the reservoir-engineering domain

It is crucial to establish a consistent understanding of the engineering parameters governing the reservoir dynamic connectivity in both the seismic- and reservoir-engineering domains. As a result, the attempts are to derive a relationship for connectivity in a step-by-step procedure, in order to take into account both the dynamic and static properties impacting the reservoir dynamic connectivity. The derivation of the connectivity relationship is initiated based on an analogy between Darcy's law for a linear, single-phase fluid flow:

$$Q = \frac{KA}{\mu L}\Delta P \tag{5.5}$$

and Ohm's law for a linear electric current:

$$I = \frac{1}{R}\Delta E \tag{5.6}$$

where I is the electrical current, ΔE is the voltage drop, and R is the electrical resistance. Inspection of these two equations shows that the permeance of the fluid system, $kA/\mu L$, is analogous to the reciprocal of the electrical resistance known as conductivity. The electrical conductivities are measured from electrical flow-rates (currents) under the influence of electrical potential differences. However, reservoir connectivities are determined from measured rates of fluid flow under the influence of differences in pressure or hydraulic potential. This analogy helps us to understand the connectivity in physical terms. In fact, permeability is part of the proportionality constant in Darcy's law, which relates the discharge (flow rate) and the fluid's physical properties (e.g. viscosity), to a pressure gradient applied to the porous media.

To investigate local connectivity, the cell volume is considered here. Thus, cell-to-cell connectivity can be defined as the measure of how easily fluids flow between the cells. According to this definition, Darcy's equation can be defined by the following formula:

$$Q_{i+1/2} = \eta(P_{i+1} - P_i) \tag{5.7}$$

where P_i and P_{i+1} are pressure or hydraulic potentials in the centres of grid blocks (see Figure 5.1(b)), and connectivity (η) is defined as:

$$\eta = \frac{(KA)_{i+\frac{1}{2}}}{\mu \Delta L} \tag{5.8}$$

This definition can be extended for the expression of two-phase flow between grid blocks *i* and *i*+1:

$$\eta_{\mathrm{w}} = \frac{\left(K_{i+\frac{1}{2}} A_{i+\frac{1}{2}}\right)}{\Delta L}\left(\frac{K_{\mathrm{rw}}}{\mu_{\mathrm{w}}}\right)_{i+\frac{1}{2}} \tag{5.9}$$

where η_{w} is the water connectivity index between grid block *i* and *i*+1; ΔL is the distance between the centres of adjacent grid blocks; $K_{\mathrm{i+1/2}}$ is the harmonic average of absolute permeability between the two adjacent grid blocks; and $(\mu_{\mathrm{w}})_{\mathrm{i+1/2}}$ is the arithmetic average of the viscosities between the two cells. K_{rw} is the relative permeability to water in the upstream-value grid-blocks between the two grids, and *A* is the cross-sectional area between the two grid blocks. Bearing in mind that transmissibility and water mobility are defined by the following formulae respectively:

$$T_{i+1/2} = \frac{(KA)_{i+1/2}}{\Delta L} \tag{5.10}$$

$$\lambda_{\mathrm{w}} = \left(\frac{K_{\mathrm{rw}}}{\mu_{\mathrm{w}}}\right) \tag{5.11}$$

Equation 5.9 can be rewritten as:

$$\eta_{\mathrm{w}} = T_{i+\frac{1}{2}} \lambda_{\mathrm{w}i+\frac{1}{2}} \tag{5.12}$$

Therefore, the total connectivity (η_{t}) is calculated according to the total mobility (λ_{t}):

$$\eta_{\mathrm{t}} = T_{i+\frac{1}{2}} \lambda_{\mathrm{t}\,i+\frac{1}{2}} \tag{5.13}$$

where total mobility and transmissibility are calculated using the following:

$$\lambda_{\mathrm{t}} = \frac{k_{\mathrm{rw}}(S_{\mathrm{w}})}{\mu_{\mathrm{w}}(P_{\mathrm{w}})} + \frac{k_{\mathrm{ro}}(S_{\mathrm{o}})}{\mu_{\mathrm{o}}(P_{\mathrm{o}})} + \frac{k_{\mathrm{rg}}(S_{\mathrm{g}})}{\mu_{\mathrm{g}}(P_{\mathrm{g}})} \tag{5.14}$$

$$T_{i+1/2} = \frac{(KA)_{i+1/2}}{\Delta L} = \frac{DX_i + DX_{i+1}}{\frac{DX_i}{(K \times A \times \mathrm{NTG})_i} + \frac{DX_{i+1}}{(K \times A \times \mathrm{NTG})_{i+1}}} \times \frac{1}{\frac{DX_i}{2} + \frac{DX_{i+1}}{2}} \quad (5.15)$$

The derived formula for connectivity can be written at t_n and t_{n+1} time steps corresponding to seismic survey times, as follows:

$$\eta_n = T \times \lambda_n \quad (5.16)$$

$$\eta_{n+1} = T \times \lambda_{n+1} \quad (5.17)$$

where λ_n is the total mobility at the time of the base-line seismic, and λ_{n+1} is the total mobility at the time of the monitor survey (t_{n+1}). Subtracting Equation 5.17 from Equation 5.16 yields the difference-form equation in which change of connectivity over time is described by:

$$\Delta\eta_n = T \times \Delta\lambda_n \quad (5.18)$$

Equation 5.18 indicates that Darcy-derived connectivity is the product of static transport properties captured in transmissibility (which involves NTG and permeability) multiplied by a change of mobility that controls the advancement of the fluid through the porous medium. This is a consistent concept with regard to hydraulic sand connectivity introduced in the seismic domain. The relationship between the hydraulic sand connectivity and the Darcy-derived connectivity is examined further in synthetic tests, which are described in the following section.

5.4 A simplified Schiehallion model (SSM)

A simple yet realistic model of a reservoir is modelled based on data extracted from the Schiehallion model. The eastern part of segment 1 is selected, and the geological information, including NTG, permeability and porosity, is extracted from this model. Next, these properties are assigned to building a reservoir-simulation model that presents a single-layer reservoir with reservoir properties from the vertically up-scaled T31a reservoir in the Schiehallion field. The cell sizes are chosen to be the same, and the permeability is assumed to be isotropic. This removes some of the non-essential

parameters for the purpose of study, such as the geometry effect and gravity, which add complications and may detract from the final objective.

Table 5.1 shows the various properties used to generate the model. A 33 × 41 × 1 cellular grid is used to describe the structure of the reservoir model. The cells of the reservoir model are 75.9 m (east–west) by 54.6 m (north–south) by 5.2 m (vertical) in extent. Figure 5.4 displays the permeability-, porosity- and NTG-distribution in the reservoir model. This single-layer model is characterized by higher permeabilities in the southern and eastern portions of the reservoir. Overall, the lower permeabilities are found to the northwest in this structure. The variation of porosity is less in the reservoir; however, the trend of variation is consistent with permeability. The NTG pattern also appears to show the orientation of the sand channels within the reservoir.

In the next stage, saturation and pressure are simulated for this reservoir in order to set up the petro-elastic model and calculate the seismic signatures. The details of the petro-elastic model used here are given in Appendices G and H.

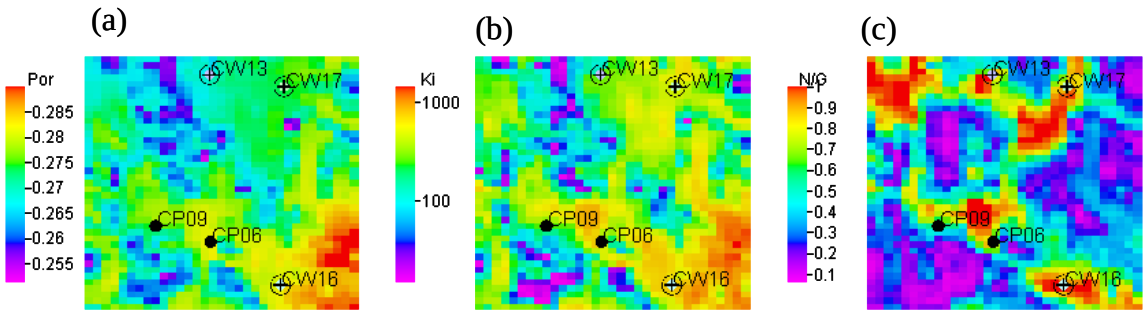

Figure 5.4: *(a) Porosity; (b) permeability; and (c) NTG for models used to compute synthetic time-lapse saturation- and pressure-changes. The three water injectors are indicated by open circles, and the two producing wells are denoted by black circles.*

Table 5.1: *Properties of the simplified Schiehallion model (SSM)*

Parameters	Range
Fluid contacts	Gas–oil contact: 6200 ft, and oil–water contact: 6317 ft
Relative permeability curves	Relative permeability curves and initial reservoir conditions assigned from Schiehallion PVT data
Fluid properties	Water viscosity is constant and equal to 0.50, but oil viscosity is assigned as a function of pressure
Permeability/NTG/porosity	Variable taken from the up-scaled model of the Schiehallion T31a reservoir
Faults and compartments	No fault or compartments
Injection wells/production wells	Three vertical injection wells (CW13, CW16, CW17) and two vertical production wells (CP06, CP09) are considered
Production/injection flow constraints	Reservoir volume rate/surface rate
Model extensions	X = 2414 m by 22,369 m by 5.2 m
Cell numbers	33 × 41 × 1
Cell size	249 ft × 179 ft × 17 ft (assigned based on the median values of dx, dy and dz sizes in segment 1 of the Schiehallion field)
Top and bottom of the reservoir	Constant top horizon 6300 ft, to base horizon 6317 ft
Date of base-line seismic survey	1998
Dates of monitor surveys	1999, 2000, 2001, 2002 and 2003

5.5 Static connectivity estimates in α

Forward modelling is performed for the SSM in order to investigate the ability of seismic signatures to identify static connectivity properties including NTG and permeability. Figure 5.5 shows the cross-plot of P-impedance versus NTG and permeability. These graphs indicate that impedance is a direct linear function of NTG and a weaker linear function of permeability. This reveals that permeability is concealed in the low-frequency content of the 3D seismic, and that NTG is in the higher spatial frequencies.

Inspection reveals that P-impedance is a function of both NTG and permeability. However, dependency of P-impedance on permeability could be due to a common secondary parameter, which is porosity. Permeability and NTG are combined in calculating transmissibility, which is recognized as the indicator of the static connectivity term in Equation 5.18. Figure 5.6(a) shows the calculated transmissibility model for SSM, in which the NTG impact is substantial. In this model, the high values of NTG in the upper part of map are smoothed by the low values of permeability in that area (cf. Figure 5.4(b) and Figure 5.4(c) with Figure 5.6(a)). As shown in Figure 5.6(b), the NTG is also playing a major impact in the final acoustic-impedance map. The acoustic-impedance is the static connectivity term in hydraulic sand connectivity (the α term) defined in the seismic domain. Therefore, the static-connectivity term of the hydraulic sand connectivity defined in the seismic domain is fairly consistent with the one in the reservoir-engineering domain.

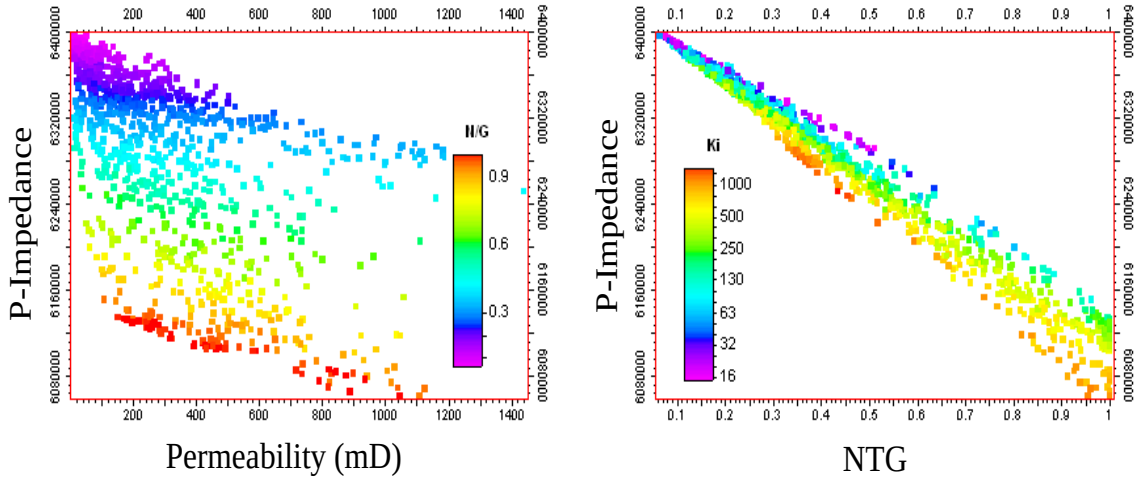

Figure 5.5: *P-impedance versus NTG and permeability in forward modelling. The P-impedance appeared to be a direct function of NTG and the weaker function of permeability.*

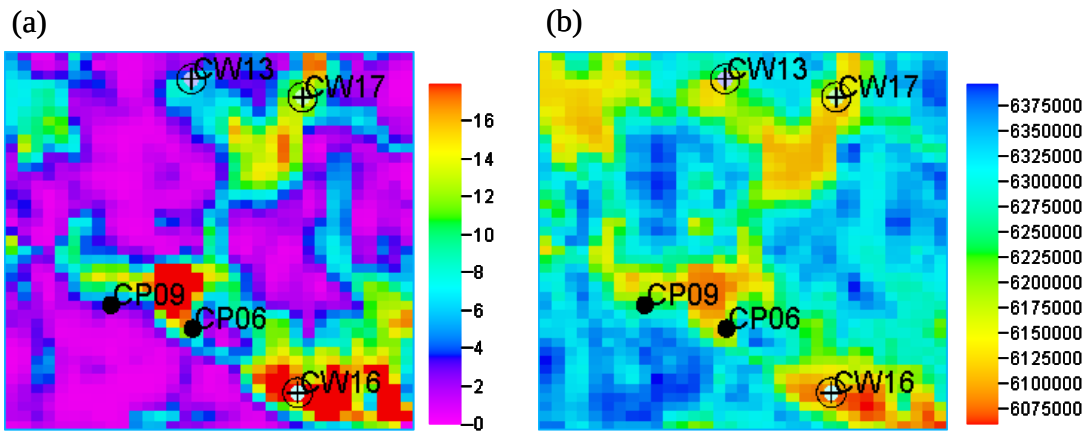

Figure 5.6: *(a) Transmissibility is a mixture effect of the permeability and NTG- see Figure 5.4(b) and Figure 5.4(c) respectively for comparison purpose, (b) P-impedance is affected substantially by NTG.*

5.6 Dynamic connectivity estimates (4D seismic) in α

In order to model the time-lapse seismic response, the saturation and pressure associated with five years of production for SSM are simulated. The time-steps for the simulation are set for a base-line pre-production seismic (1998) and five seismic-monitor survey times (1999, 2000, 2001, 2002 and 2003). Two producing wells, indicated by black circles in Figure 5.7, are located in the central part of the model. The two producing wells are constrained to maintain an oil-flow rate of 500 bbl/day for CP06, and 1000 bbl/day for CP09. Water injectors, denoted by open circles in Figure 5.7, are located near the southern and northern boundaries of the model. Water is injected into the reservoir interval at a surface rate of 300 bbl/day. No-flow boundary conditions are maintained at the edges of the model. Also, no flow is allowed across the top and bottom boundaries of the layer. The initial reservoir pressure is a uniform 2900 psi, and the initial oil saturation is 80% (20% water). Figure 5.7 shows simulated saturation and pressure after 365 days. The saturation sweep pattern seems to follow the NTG profile. Conversely, the pressure profile is affected only by pressure gradients assigned from the well differential pressure due to bottom-hole pressure (BHP) at the wells. After 365 days of production, the reservoir pressure near the producers has decreased from 2900 psi to values approaching 700 psi. The pressure is highest, approximately 2800 psi, surrounding the water injector to the north and southeast.

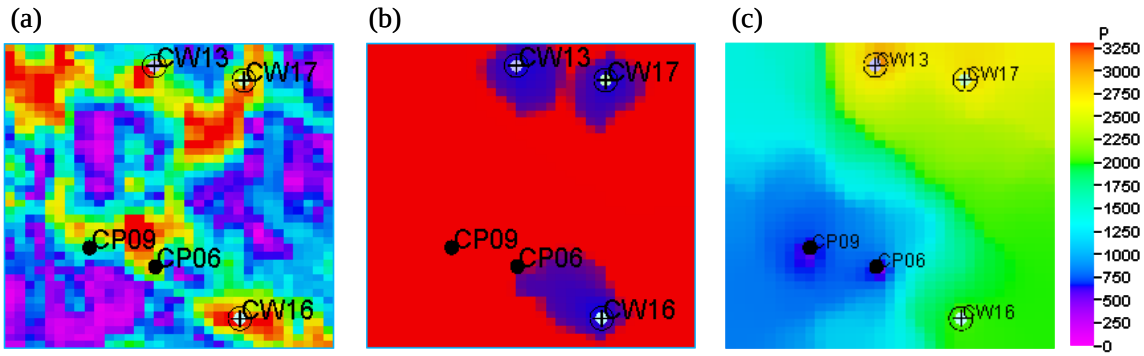

Figure 5.7: *(a) NTG; (b) saturation profile after 365 days' production; and (c) the pressure profile simulated after 365 days' production.*

The water saturation changes after every year, as shown in Figure 5.8. The inspection of pressure- and saturation-profiles over time shows that the influence of the heterogeneity is more visible in the saturations profile, where its orientation is skewed by the higher NTG in the centre of the model. For the most part, the water migrates along the central high-NTG channel from the northern and southern injectors to the central producers (Figure 5.8). In addition, the orientation of the sweep pattern is assigned by the pressure gradient between wells in the system, so that the water front has a tendency towards the lowest pressure direction (here the CP09 production well has the lowest pressure).

(a) Evaluation of Darcy-derived connectivity: in order to calculate connectivity in the reservoir model, Equation 5.18 is employed. Relative permeability and viscosity curves are used to calculate total mobility from saturation and pressure. Maps of K_{rw}, K_{ro} and μ_o, calculated mobility and time-lapse change in acoustic impedance and after 365 days (monitor time 1; 1999), are shown in Figure 5.9. Inspection of calculated mobility shows that total mobility is affected by both saturation and pressure, although the saturation effect is substantial here. The significant change in total mobility is concentrated near the water injector, as it is early injection. Conversely, the time-lapse seismic signal is also a function of saturation and pressure, which is more affected by saturation here. Hence, this can provide a basis for interrelating the dynamic connectivity term of hydraulic-sand connectivity (the 4D-seismic response) to the corresponding one in Darcy-derived connectivity (the mobility change).

The calculated Darcy-derived connectivity between surveys in the sequence of survey times ($\Delta\eta_n$) is mapped in Figure 5.10(a) to Figure 5.10(e). This figure shows how the

evolving saturation profile over time in a background of channels highlights the connection between cells. At the last time-steps, the connectivity path is completely imaged. Thus, in order to capture the entire connectivity path shown in Figure 5.10(f), all of the individual Darcy-derived connectivities are stacked together to produce the total reservoir connectivity (η_{total}):

$$\eta_{\text{total}} = \sum_{n=1}^{N} \Delta \eta_n \tag{5.19}$$

where N = the number of time-lapse surveys.

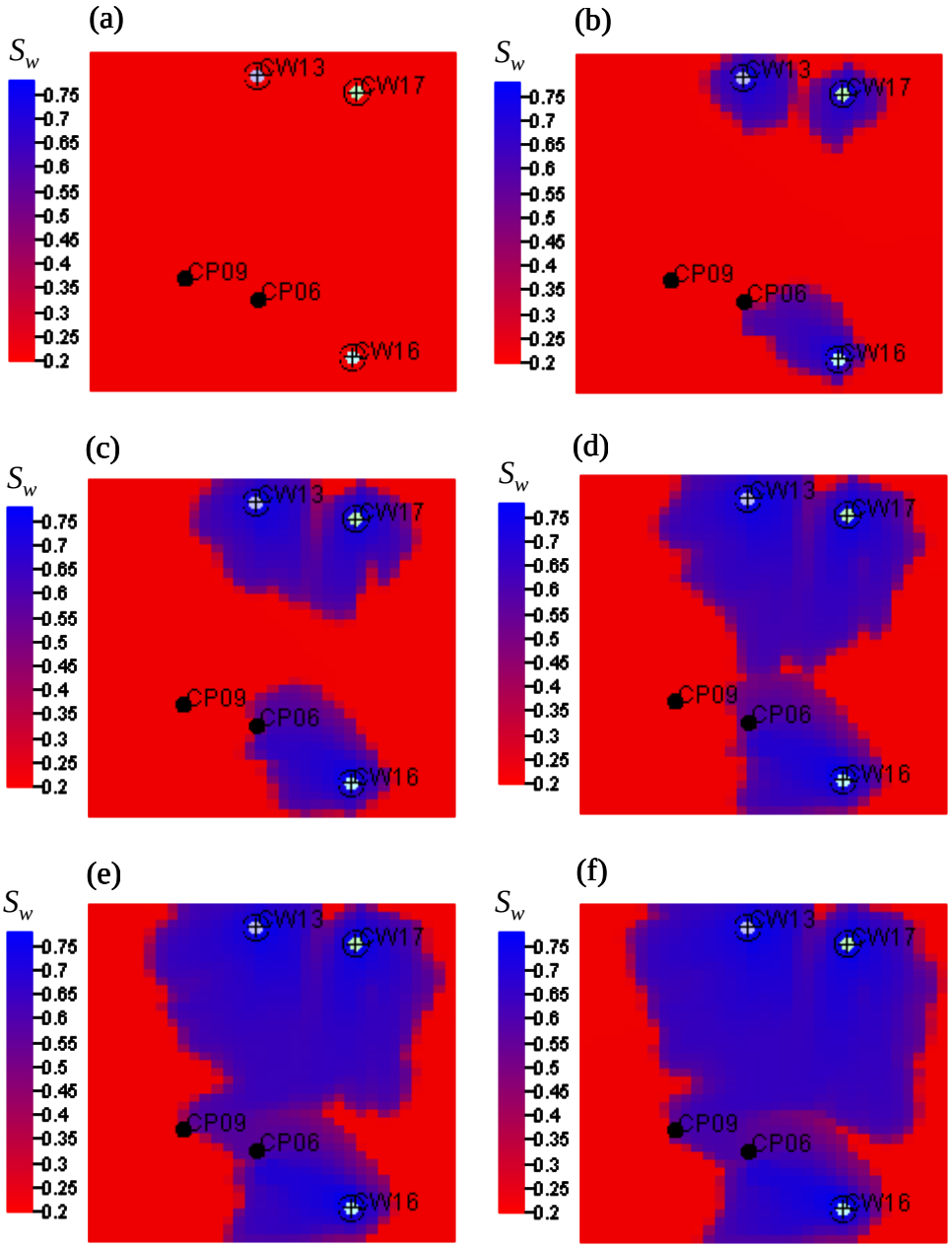

Figure 5.8: *Saturation distribution at different times: (a) 1998; (b) 1999; (c) 2000; (d) 2001; (e) 2002; and (f) 2003.*

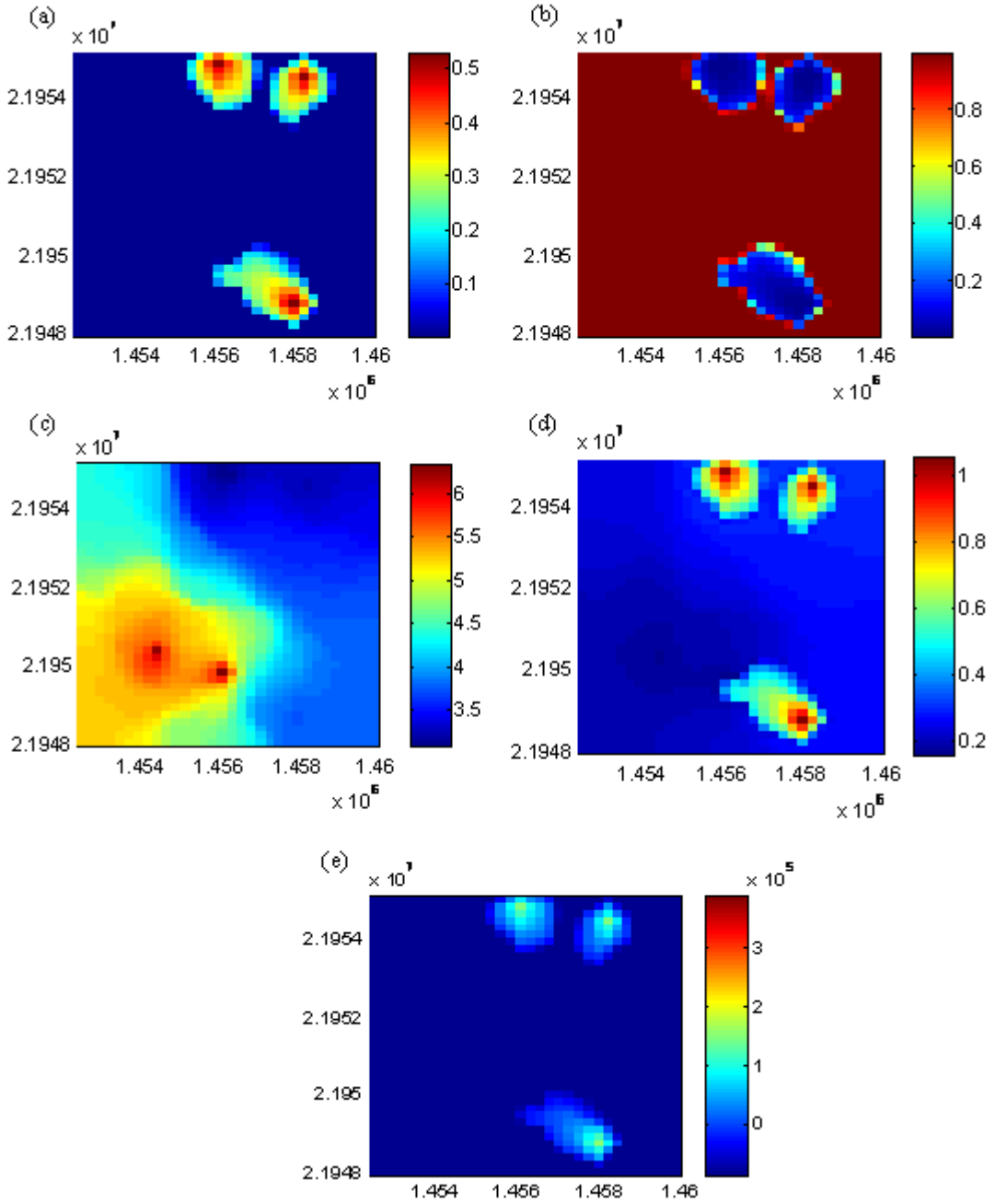

Figure 5.9: *(a) Relative water permeability as a function of water saturation, K_{rw}; (b) relative oil permeability as a function of oil saturation, K_{ro}; (c) oil viscosity (cP) as a function of pressure. (Note that water viscosity is considered to be a constant value of 0.50 cP.) (d) total mobility distributions within the reservoir after 365 days of production (monitor survey 1). Total mobility is a function of saturation and pressure (however, the impact of saturation is substantial here); and (e) the modelled time-lapse change in acoustic impedance.*

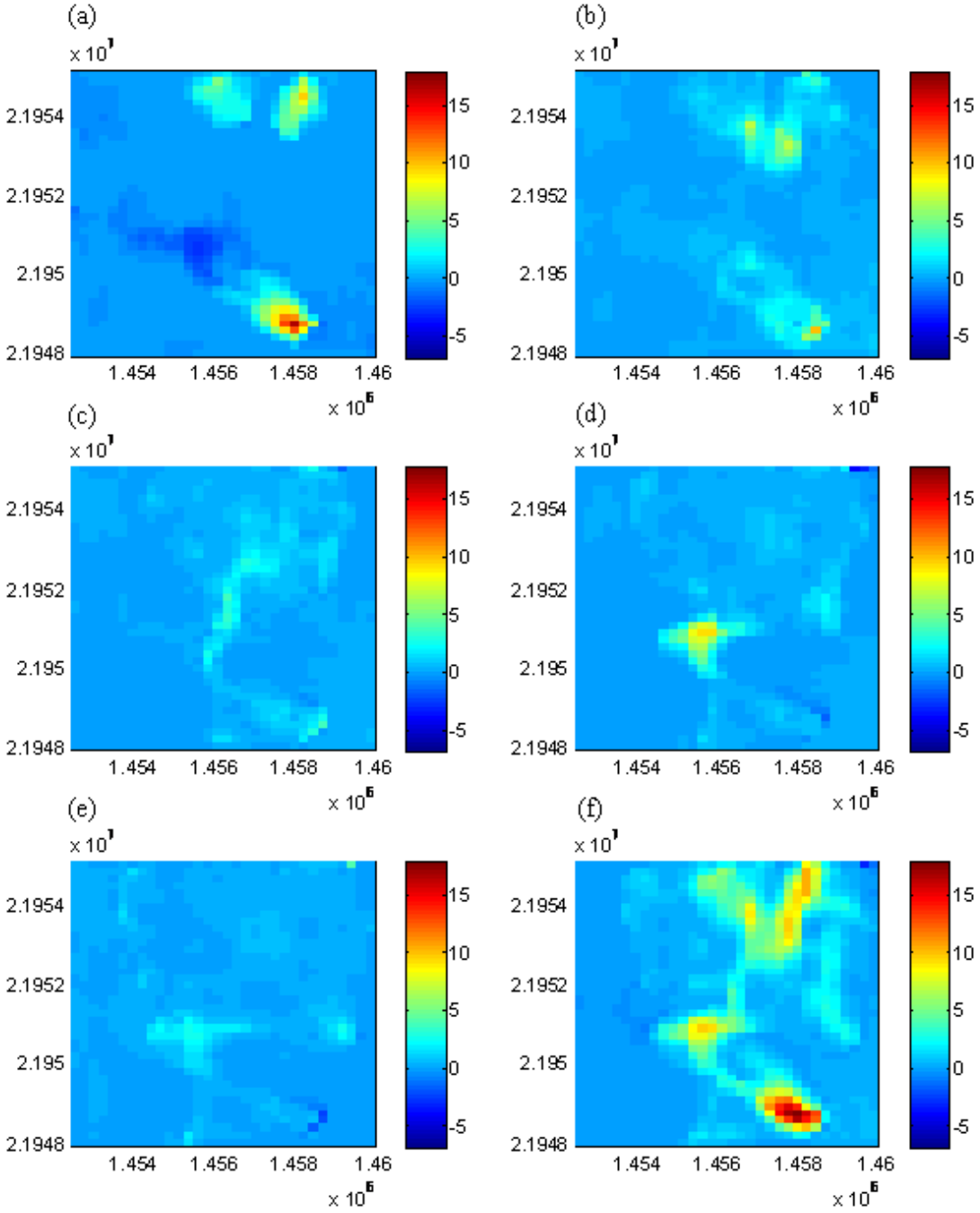

Figure 5.10: *Darcy-derived connectivity in the sequence of survey times: (a) 1999–1998; (b) 2000–1999; (c) 2001–2000; (d) 2002–2001; (e) 2003–2002; and (f) the sum of all difference maps, which is equal to total reservoir connectivity.*

(b) The relationship between total reservoir-connectivity and hydraulic sand connectivity: given the total reservoir connectivity calculated in the previous section, the investigation of the relationship between the resulting total reservoir-connectivity map and the hydraulic sand connectivity is of interest. The individual hydraulic sand connectivity maps for different time-lapse surveys are shown in Figure 5.11. The complete image of the total reservoir connectivity (calculated in Equation 5.19 and shown in Figure 5.12(a)) is the summation of all the individual time-lapse images. Therefore, to capture the corresponding connectivity image in the seismic domain, a new attribute is defined as the sum of hydraulic sand connectivities:

$$\mathrm{SCA}=A_0\times\sum_{i=1}^{N}\Delta A_i \tag{5.20}$$

where A_0 is the base-line seismic and ΔA_n is the time-lapse response for survey *n*. All of these attributes are stacked together and finally normalized between zero and one. The result is defined as the seismic-connectivity attribute (SCA), which is displayed in Figure 5.12(b). Note that if injection/production activities are continuous (similar to the example shown here), the last difference map is comparable with sum of differences. However, in real case application, the production activities might include shut-down of certain wells before the last 4D survey. As the result, the last 4D difference cannot capture any change around those particular wellbore regions. Instead the advantage of using sum of successive differences helps to convey all the possible channels highlighted in individual 4D differences due to various production activities over reservoir life. Comparing the proposed attribute with the calculated total reservoir connectivity shows that there is an obvious proportionality between the reservoir connectivity and the introduced seismic attribute (see Figure 5.12(a) and Figure 5.12(b)). In the cross-plot shown in Figure 5.12(c), the clear linear proportionality observed between these two properties indicates that the new introduced attribute is a suitable candidate for assessing reservoir connectivity defined in the reservoir-engineering context. In addition, a cross-comparison of formulations of both parameters shown below indicates that there is an analogy between individual components:

$$\mathrm{SCA}=A_0\times\sum_{i}^{N}\Delta A_i \quad\approx\quad \eta_t=T\times\sum_{i}^{N}\Delta\lambda_i \tag{5.21}$$

It is important to note that the connectivity analysis performed above is mainly due to the saturation-controlled time-lapse seismic signal in which the flow path is clearly traceable on the 4D-seismic response. Fortunately, there are many examples of reservoirs in which the 4D signature is almost completely dominated by saturation changes (for example, the Nelson field, McInally et al., 2003; the Gannet field, Staples et al., 2005). However, time-lapse seismic signals that are mainly pressure-controlled can be employed to assess barrier connectivities. This subject is investigated further in the next section, in which SSM is utilized to simulate a pressure-controlled signal in 4D-seismic response.

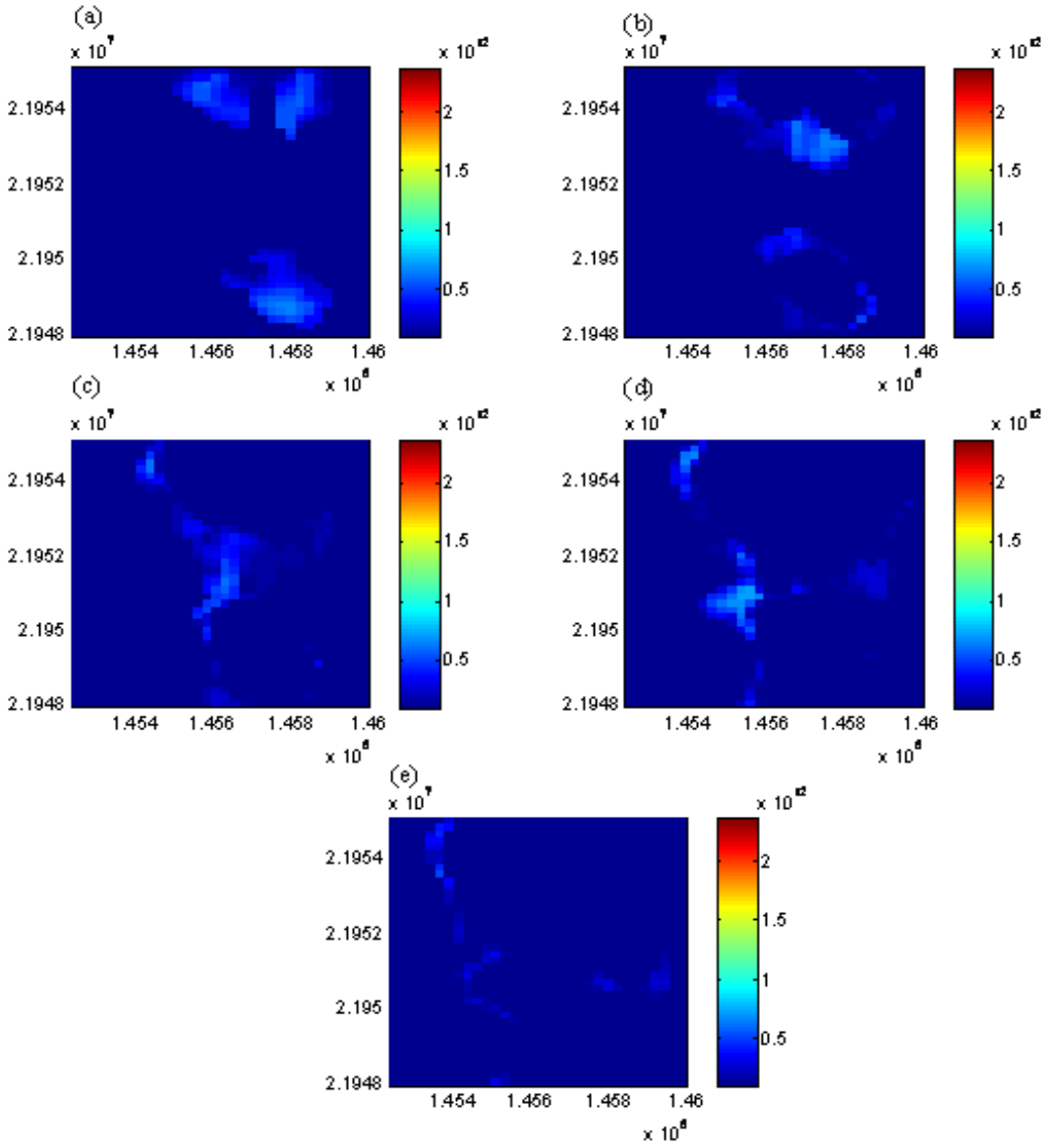

Figure 5.11: *Hydraulic sand connectivity over time: (a) 1998×(1999–1998); (b) 1998× (2000–1999); (c) 1998× (2001–2000); (d) 1998× (2002–2001); and (e) 1998× (2003–2002).*

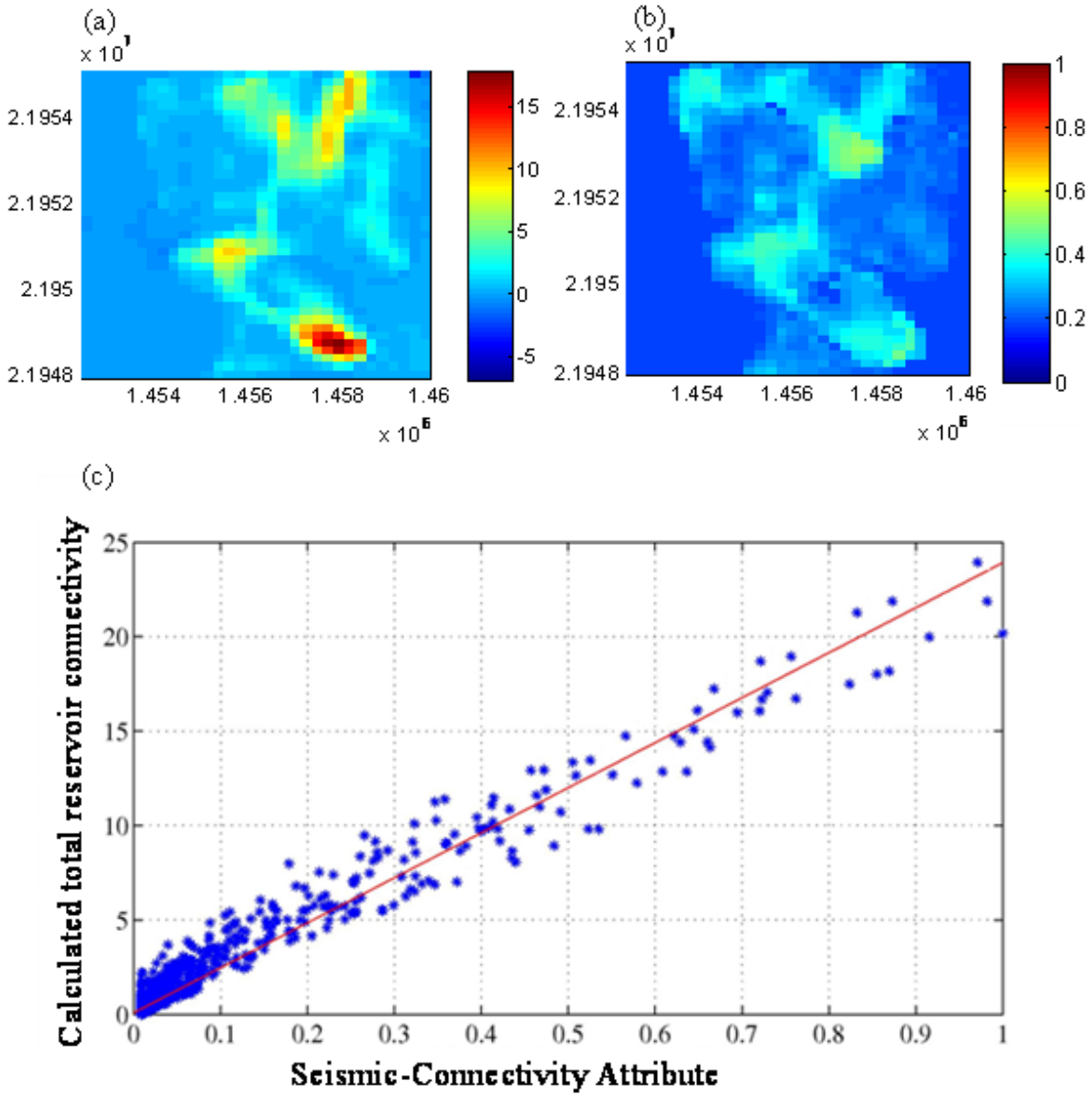

Figure 5.12: *(a) Total reservoir connectivity calculated from Darcy-derived connectivities; (b) the seismic-connectivity attribute calculated from hydraulic sand connectivities; and (c) the seismic-connectivity attribute (SCA) is proportional to the total reservoir connectivity.*

5.7 Barrier connectivity (β)

Time-lapse seismic has been applied for objectives other than monitoring saturation changes, such as pressure monitoring and compaction detection, sometimes with surprising outcomes (Staples *et al.*, 2006). The pressure-up from poorly communicating water injectors, known as 'injection overpressure', can give rise to large signals, as can the 'relaxation' from such overpressures, when the injection rate is reduced (Stammeijer

and Staples, 2003). The large signals caused by pressure-up can in some cases totally dominate and mask the effect of saturation changes.

A pressure-up compartment highlights the faults surrounding the compartments (the compartment boundary). In fact, the pressure profile is a very smooth profile that does not respond to insignificant heterogeneities within the compartment. Therefore, it is more likely to show barrier connectivity around the compartments, in contrast to reservoir-matrix connectivity. The model used previously (SSM) now includes faults, and is used to test this further. Transmissibility multipliers indicating the connectivity of faults are assigned to the model (displayed in Figure 5.13(a)). Also, transmissibility values indicating the static sand connectivity are shown in Figure 5.13(b). Figure 5.13(c) to Figure 5.13(h) show the pressure-change and saturation-change profiles as the result of simulation for a sequence of time-steps (1999–1998, 2000–1998 and 1999–1998). Note that in this time period, injectors CW16 and CW17 are not active. At first glance, it is observed that the pressure profile appears to differ completely from the previous synthetic model profile, since the faults and compartments significantly impacted on the pressure profile in this model. In fact, the introduced compartments are clearly projected to the pressure profile in this reservoir. Each image of pressure at a certain time-step can highlight most of the compartments. Note that, unlike the saturation profile, pressure diffusion is a quick process compared with saturation evolution; hence, it provides a suitable candidate with a full coverage of the reservoir for imaging the connectivity of the reservoir. Saturation change still follows the channel heterogeneity shown in the transmissibility map (Figure 5.13(b)). Therefore, establishing which of these connectivities (hydraulic sand connectivity or barrier connectivity) is the precise candidate to be estimated from 4D seismic, remains dependent on the fact that the 4D-seismic response is more influenced by the saturation- or pressure-signal. This is analysed further below.

Impedances are again calculated from the predicted pressures and saturations, but this time with the pressure compartment included. Figure 5.14 shows the resulting acoustic impedance changes corresponding with the pressure- and saturation-changes in Figure 5.13. Including faults in the model caused pressure-up, so that its effect dominates and controls the 4D-seismic signal. As a result, the 4D-seismic signal can be used for the detection of compartmentalization, rather than the detection of connectivity pathways

previously described for the saturation-controlled 4D signal. The Laplacian attribute described by the β term (decomposed from the Seis2perm transform) is a suitable candidate to evaluate the edges of the compartment highlighted by the pressure signal.

The consistency of the barriers in several seismic surveys acquired at different times adds an additional confidence to the interpretation. The outline of a compartment is fixed from one survey to another. In addition, pressure diffusion is a very rapid process compared with the time-lapse time-scale. The time required for the pressure to diffuse, reach the boundary of the compartment and finally be stabilized, is of the order of weeks, while the time-scale of time-lapse survey is of the order of years. Thus, the pressure signal in time-lapse seismic is usually associated with imaging the outline of the whole compartment. Therefore, the time-lapse anomaly that preserves its shape over time in different surveys is more likely to be a compartment feature due to pressure-up, whereas saturation anomalies evolve over time from the injection well towards the production well. This defines a need for a sequence of surveys that can be utilized as a tool to validate the interpreted compartment boundary. This is studied in Chapter 6. From the reservoir-engineering prospective, barrier connectivity is defined in terms of the fault-transmissibility multiplier. The fault-transmissibility multiplier defines the degree to which the fault is a barrier to flow. A multiplier of zero means that no flow goes through the fault. Therefore, at the fault location, Equation 5.18 can be written as:

$$\Delta\eta_n^{eff} = T_f \times T \times \Delta\lambda_n \tag{5.22}$$

where Δ_n^{eff} is the effective connectivity and involves fault transmissibility (T_f). As described above, the key issue for evaluating barrier connectivity is having a clear pressure-up or pressure-down signal in 4D seismic. This usually happens around an injection or production well surrounded by a reasonably small compartment. However, in some regions, a pressure signal is mixed with a saturation signal. Therefore, to achieve the best result, ideally pressure change has to be separated from saturation prior to connectivity assessment. An alternative solution is to employ a 4D-seismic signal dominated mainly either by pressure or saturation. In this case, the connectivity solution is approximate; however, the implementation is quicker, and indeed more practical. In the next chapter, attempts are made to discriminate between pressure- and saturation-anomalies prior to connectivity evaluation, in order to achieve more accuracy in the result.

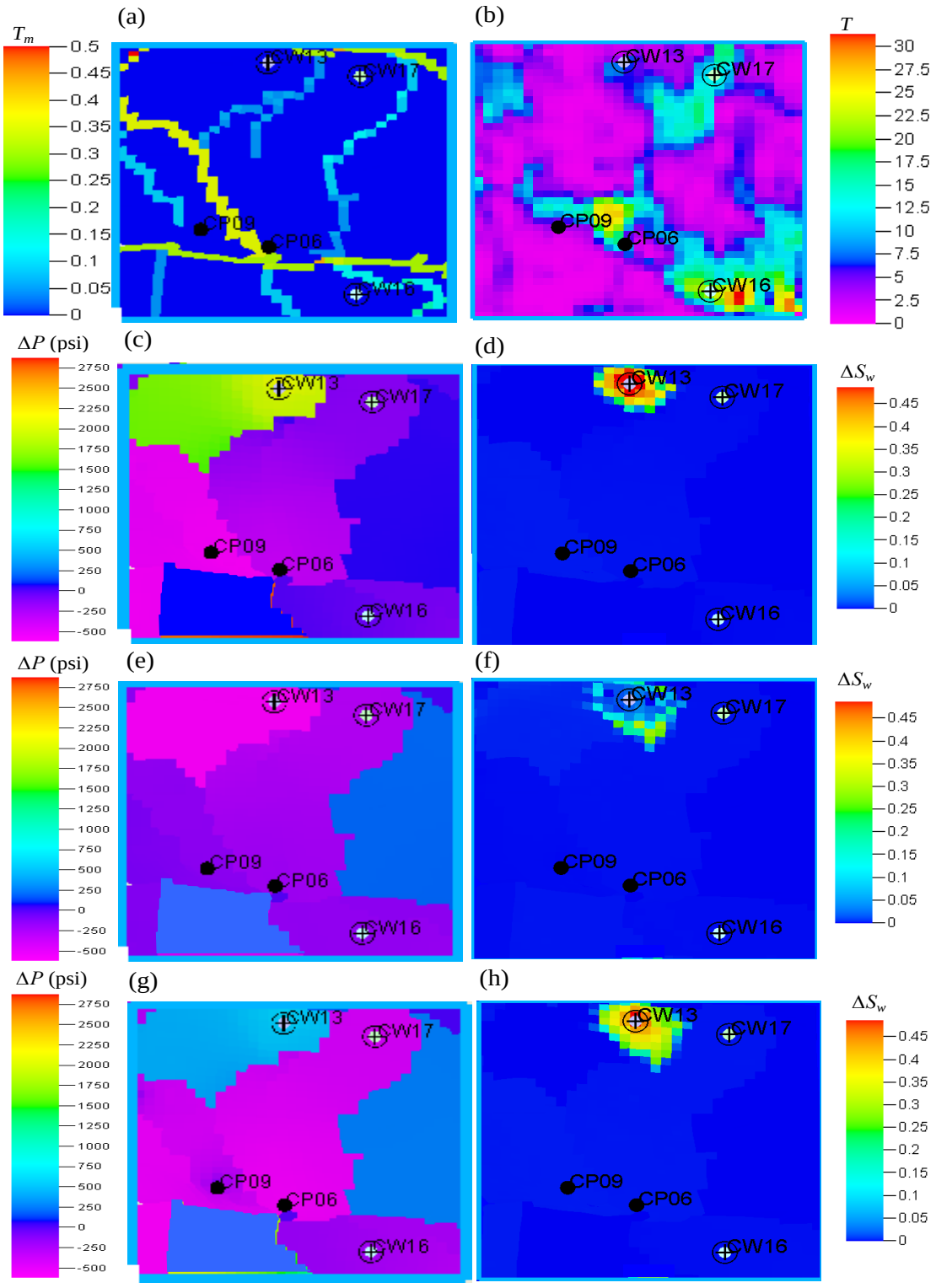

Figure 5.13: *Effect of compartmentalization on the pressure profile: (a) profile of the compartments; (b) transmissibility of the model; (c) and (d) pressure- and saturation-change from simulations between 1998 and 1999; (e) and (f) pressure- and saturation-change between 1999 and 2000; and (g) and (h) pressure- and saturation-change between 1998 and 2000.*

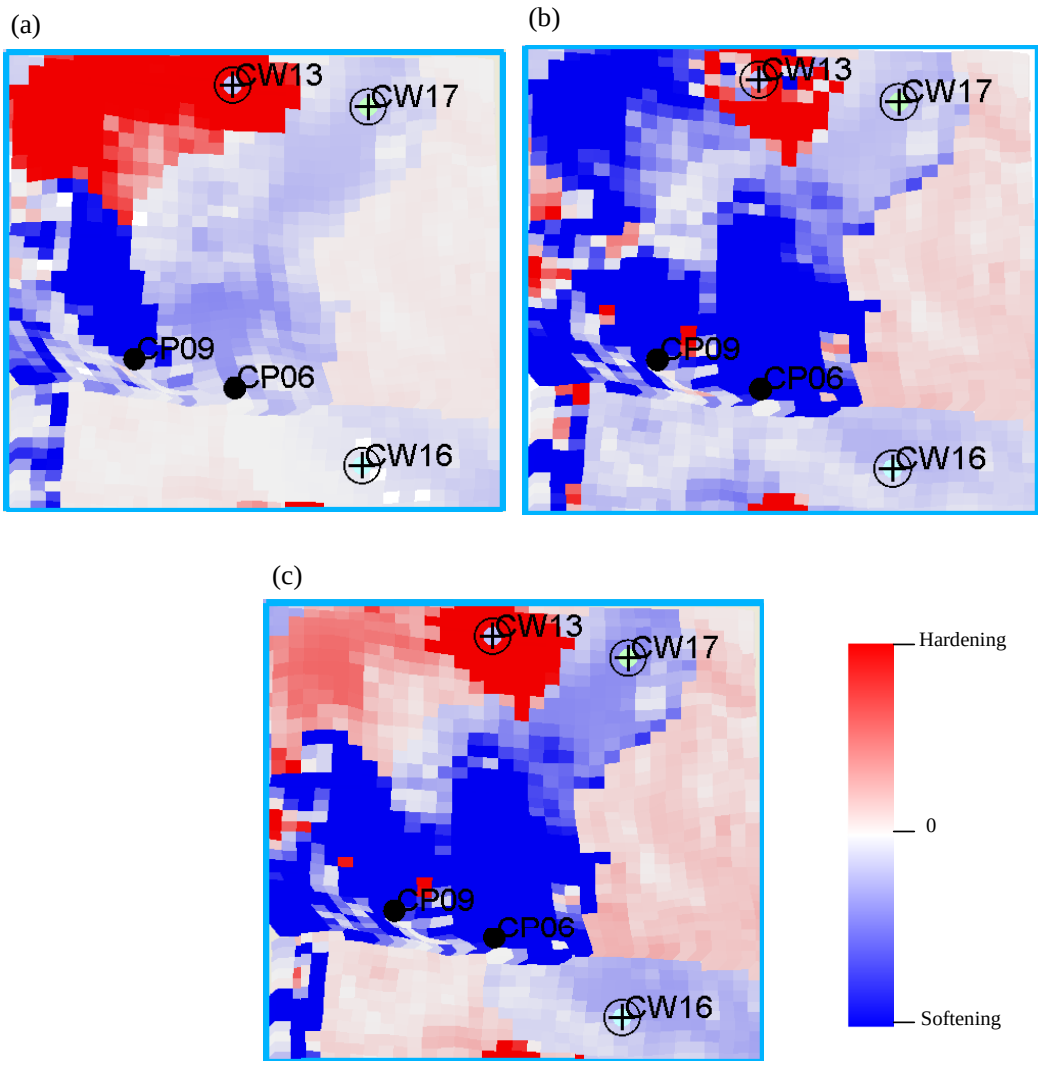

Figure 5.14: *Acoustic impedance change between (a) 1998 and 1999; (b) 1999 and 2000; and (c) 1998 and 2000.*

5.8 Field data and connectivity inversion

Inspection of pressure- and saturation-profiles in the Schiehallion reservoir model (Figure 5.15), in segment 1 from which the SSM properties are derived, shows similar behaviours in the field data to those observed in synthetic tests. In Figure 5.15(c), injection wells CW13, CW16 and CW17 received water injections in 1998, 2002 and 2003 respectively. The flood front follows the areas with high NTG and permeability from wells CW16 and CW13 until it reaches the fault (compartment boundary), where the movement of fluid seems to be slowed down. Therefore, overall, two types of properties in the reservoir model govern the connectivities for fluid advancing within

the reservoir: i.e. transmissibility that impacts hydraulic sand connectivity, and fault transmissibility which is an indication of flow-barrier connectivity. Hydraulic sand connectivity is in turn correlated with the saturation profile, whereas barrier connectivity is correlated to the pressure profile (see Figure 5.16). The route described is confirmed by modelling. On the other hand, in order to invert 4D seismic into the estimation of these connectivitities, there are two systematic stages. The first step is the inversion of 4D seismic to pressure and saturation, since the time-lapse signature is essentially a combination of pressure- and saturation-effects. The second step is inversion of the interpreted pressure/saturation profiles into estimations of transmissibility and transmissibility multipliers (see Figure 5.16). The development of the inversion techniques required for estimating these properties is addressed in Chapter 6.

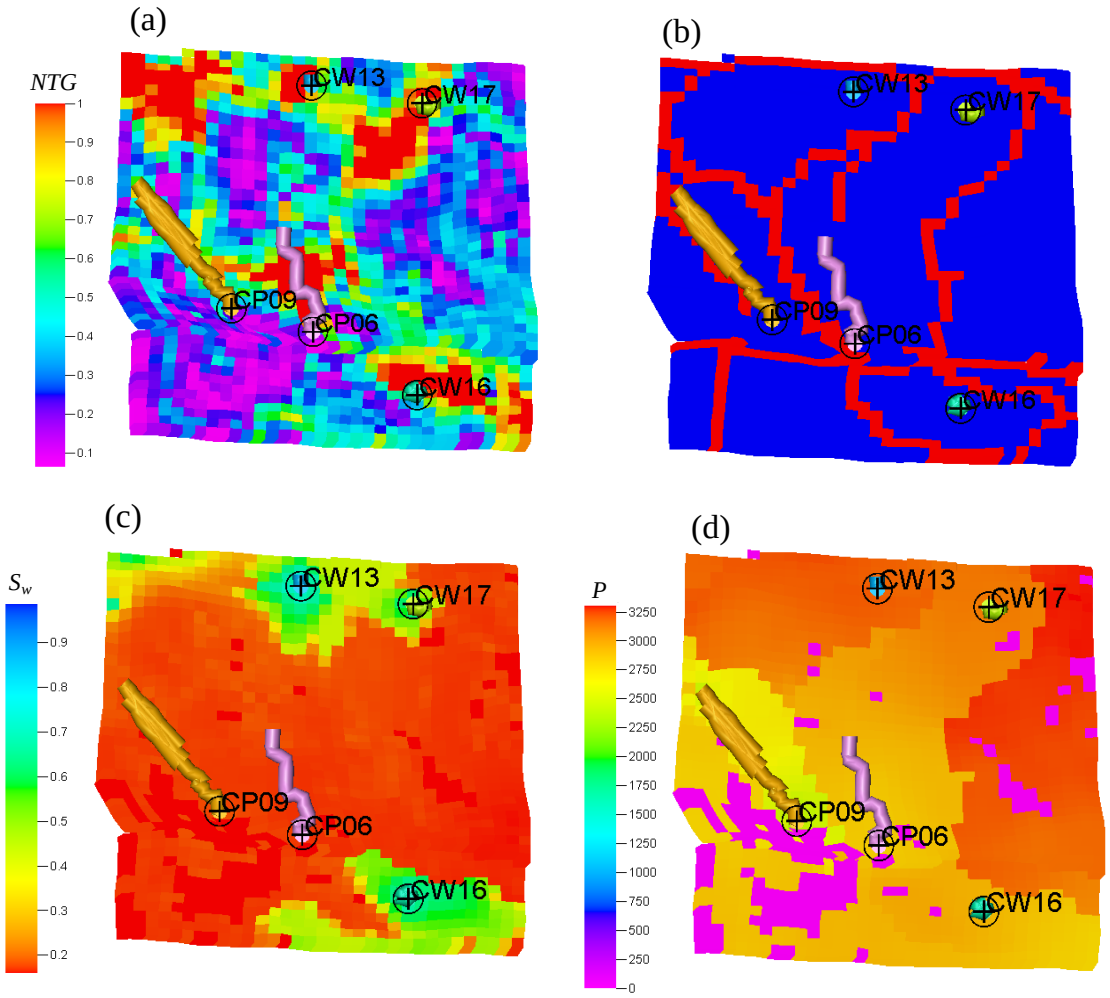

Figure 5.15: *(a) NTG; (b) compartments; (c) the saturation profile on April 2004; and (d) the pressure profile in April 2004 in segment 1 of the Schiehallion field data.*

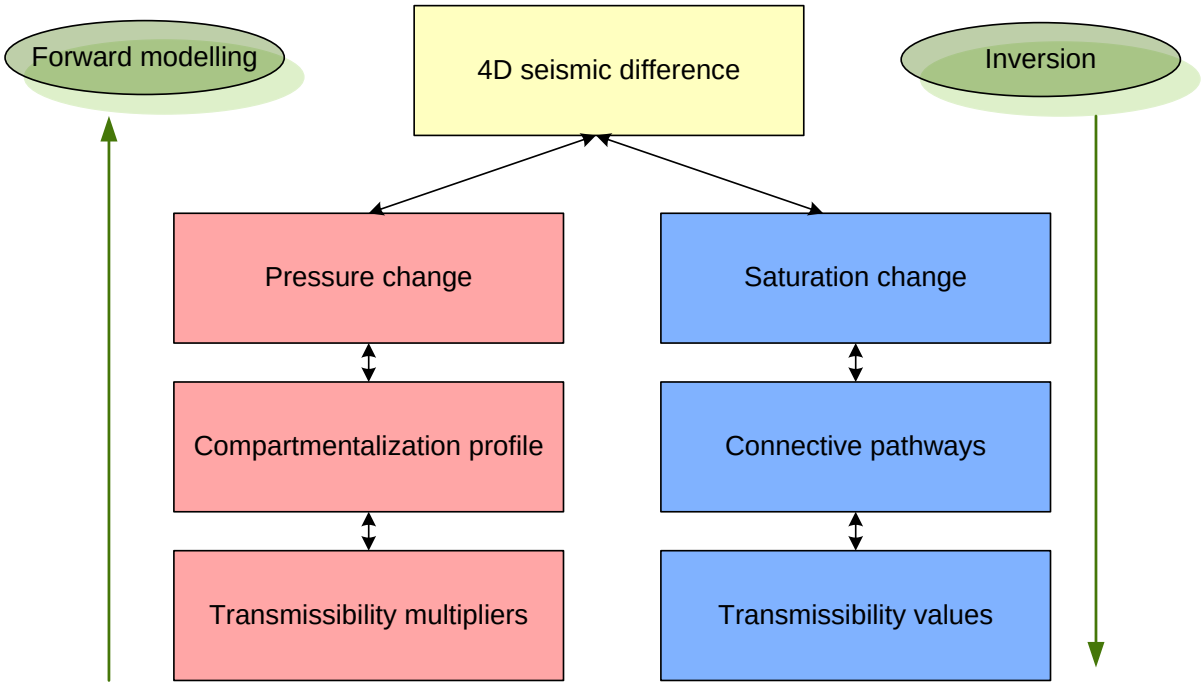

Figure 5.16: *Forward and inverse routes, indicating how transmissibility and transmissibility multipliers are linked to the 4D-seismic response.*

5.9 Discussion

(a) The sequence of time-lapse surveys as a tracking tool for dynamic connectivity assessment: as discussed, the spatial variability of the time-lapse seismic signal can be employed to identify the flow pathways and flow barriers. However, taking into account only one time-lapse survey is not enough to predict all the flow paths over the reservoir. Production activities may highlight different channels in 4D-seismic surveys over time. Besides these, there are certain misinterpretations attached to considering only one survey (Floricich *et al.*, 2008). For example, the front of fluid movement at early production times could be interpreted as a barrier. The continuity of fluid movement can be followed by further 4D-seismic surveys at later times of production. Pressure change can also cause some misinterpretations when it is similar in two compartments and therefore the barrier is seen as a connective pathway. Taking into account more than one 4D-seismic survey helps to validate the pressure discrepancy between compartments over time. Pressure change in compartments is produced by increasing and decreasing the bottom-hole pressure in injection- and production-wells located in the compartment. If, at a certain time, the injection- or production-well is not active within the compartment, then the specified 4D seismic may not be able to capture the compartment

around the well. This is where frequent time-lapse seismic plays a major role in highlighting the captured signal of the compartment in a different time-step. Therefore, integration of all the signals contained in the various time-lapse surveys during the production of the field is of particular importance to overcome such misinterpretations and add additional confidence to the interpretation.

(b) Linearity assumption between total reservoir connectivity and SCA: the linearity assumption may become invalid in some circumstances. Non-linearity may occur due to the tuning effect. In a thin layer, the gravity effect is not dominant, so the flow is piston-wise. As a result, there is less of a tuning effect and the linearity is valid. However, for thicker reservoirs, gravity is dominant and produces coning, which may cause tuning effects in the seismic signal. As a result, the linearity might not be so strong.

(c) How important is saturation/pressure separation for the proposed connectivity evaluation: ideally pressure- and saturation-changes should be separated in order to perform an accurate hydraulic sand-connectivity or barrier-connectivity analysis. However, separating these two effects from 4D seismic is a challenging task, with uncertainty attached to the resulting estimations. However, the dominance of one of these effects in a certain field can provide an approximate assumption of either the pressure- or the saturation-4D signal. Subsequently, one of the pressure- or saturation-approaches can be taken in order to assess the related connectivity.

5.10 Summary and conclusions

The dynamic behaviour of 4D seismic and its unique role in offering high-resolution inter-well information makes it a very promising candidate to assess dynamic local connectivity.

The Seis2perm formula was decomposed into two connectivities, named as hydraulic sand connectivity and barrier connectivity. The hydraulic sand connectivity was compared and contrasted with other connectivity-estimation approaches in the seismic domain and also with the derived connectivity in the reservoir-engineering domain. The reservoir-connectivity derivation was initiated from an analogy between Darcy's law and an electric current, and is extended to the derivation of connectivity for multi-phase

flow in the reservoir. It was found that the definition of hydraulic connectivity is consistent with the reservoir-engineering definition of connectivity when it was tested for a synthesized saturation-controlled 4D seismic. However, the total reservoir connectivity in which the whole connection path within the reservoir is captured can be approximated by stacking all individual hydraulic sand connectivities estimated from the sequence of time-lapse surveys. The final product was termed the seismic connectivity attribute (SCA). Next, a pressure-controlled seismic was modelled, and it was found that pressure-controlled 4D seismic is more suited for compartmentalization identifications (barrier connectivity). In the case of a compartmentalized reservoir, the pressure goes up within a compartment and may eventually mask the saturation effect. Consequently, 4D seismic will show a clear signal from pressure, indicating barrier discontinuities. Application of the Laplacian attribute, which will be discussed in the next chapter, would make it possible to capture the discontinuities in the 4D seismic response along the flow barriers. Since pressure and saturation can image the different connectivity types, they may be used differently for connectivity assessment. Therefore, evaluating the connectivity from 4D seismic depends on the fact that it is dominated by saturation sweep or pressure build-up within compartments.

CHAPTER 6: CONNECTIVITY ASSESSMENT IN THE SCHIEHALLION FIELD

Overview

Further to the analysis in Chapter 5, in this chapter various methodologies are employed for estimating connectivity from 4D seismic, in an application to the Schiehallion field. The choice of the method depends on whether 4D seismic is dominated by pressure- or saturation-changes. The boundaries of the pressure- and saturation-anomalies are interpreted. Following this, inversion techniques are introduced to estimate both transmissibility and transmissibility-multiplier values.

6.1 Introduction

The analysis in the previous chapter provided an insight into connectivity concepts and how connectivity can be estimated from 4D seismic. It is revealed that 4D seismic can provide connectivity estimations based on theoretical investigations and modelling performed on synthetic cases. Two types of connectivity governing the transform phenomena in hydrocarbon reservoirs are presented: hydraulic sand connectivity, and barrier connectivity. Furthermore, it was revealed that using 4D seismic to assess the connectivity of each type depends on the fact that it is dominated by either pressure or saturation. The seismic-connectivity attribute (SCA) and the Laplacian attribute were proposed for a sequence of saturation-dominated 4D-seismic and pressure-dominated 4D-seismic respectively. In this chapter, the connectivity issue in the Schiehallion field is described first. Next, an interpretation approach is employed to distinguish pressure- from saturation-anomalies, using frequent time-lapse seismic. After this, the evaluated pressure- and saturation-anomalies are utilized in two different inversion techniques to estimate the transmissibility and transmissibility-multiplier values for the Schiehallion field. The general workflow pursued in this chapter is illustrated in Figure 6.1.

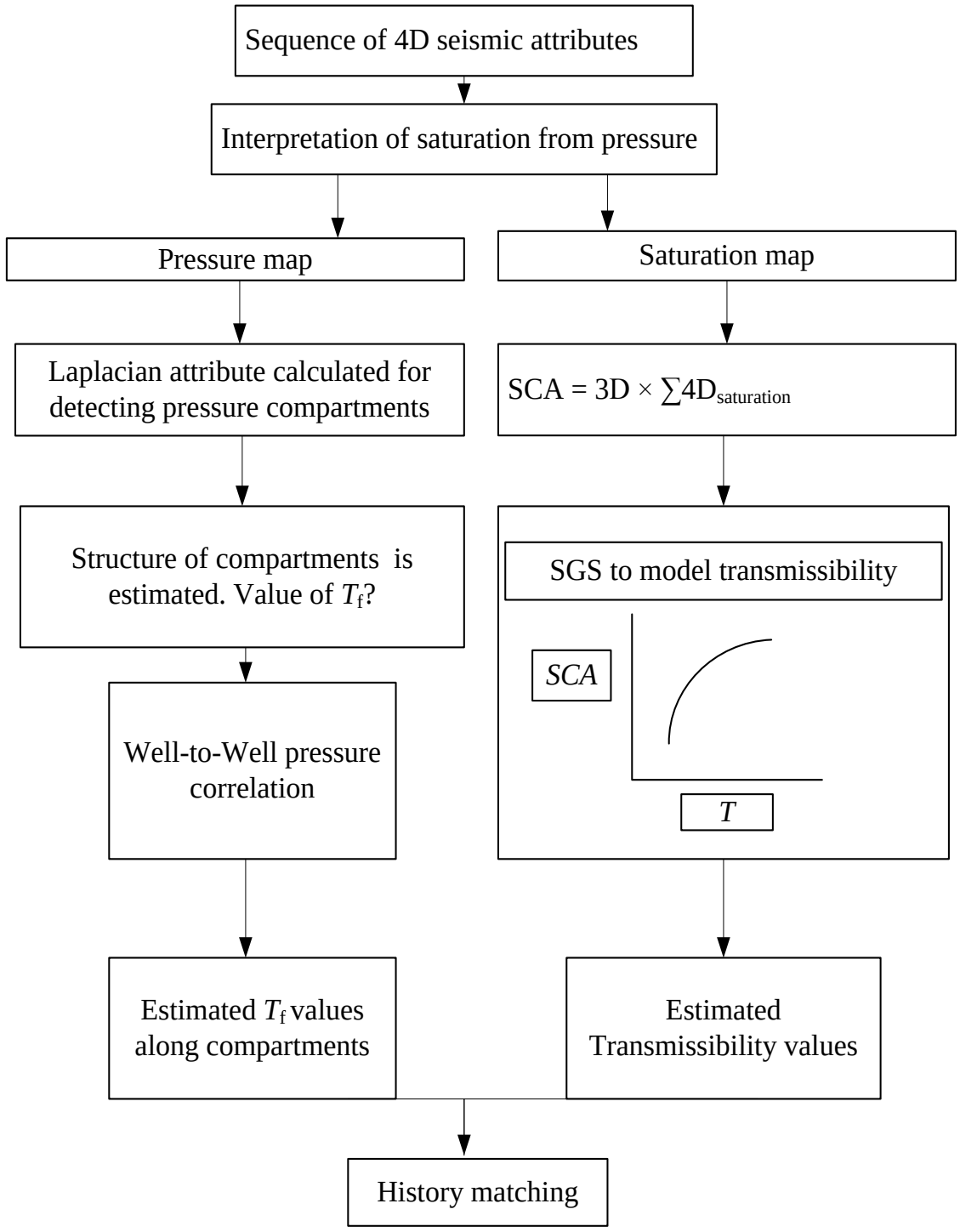

Figure 6.1: *A general workflow in this chapter for transmissibility- and transmissibility-multiplier-estimation in the Schiehallion field.*

6.2 The connectivity issue in the Schiehallion field

There are many examples of enhanced recovery factors in the North Sea and west of Shetland turbidite reservoirs, based on the connectivity interpretation from 4D seismic (see Webber 1990; Øistein *et al.*, 1993; Mijnssen, 1997; Richardson *et al.*, 1997; Leach *et al.*, 1999; Parr and Marsh, 2000; Saxby, 2001). In the Schiehallion field, connectivity has been recognized as a key factor for reservoir management (Govan *et al.*, 2006). The Schiehallion reservoir contains multiple channelized sands segmented by major east–west faults. Prior to development, further probable faults and compartments were identified by 3D-seismic data. The pre-production 1996 base-line seismic clearly showed the main channelized sands dissected by faults revealed by attribute mapping around the T31a reservoir. The mapped attribute is considered to be a reasonable indication of connections in the field at an early stage of production in the Schiehallion field. However, later experience revealed that connectivity in the field is poorer than expected. Consequently, the inaccurate connectivity evaluation caused poor sweep performance, and high levels of gas were produced from solution, due to a decrease in the average reservoir pressure (Dobbyn and Marsh, 2001).

However, the use of frequent time-lapse seismic surveys acquired in the Schiehallion field is a promising tool that can improve the reservoir-connectivity assessment in conjunction with 3D seismic. Continuity- and discontinuity-features are two main targets to be extracted from 3D seismic for further integration with corresponding properties from 4D seismic. The discontinuity features include faults/compartments, and the continuity features include NTG, which is the major factor contributing to static connectivity. The selection of the appropriate attribute for identifying these properties is important. Table 6.1 shows the tested seismic-cube attributes for imaging faults and channels. For the continuity attribute, a pseudo-impedance cube is used (with a 90° phase rotation on amplitude) for the NTG calculation, since it is recognized as a layer-based attribute that is indeed appropriate for identifying sand distributions (see Chopra and Murfurt, 2007; Connolly and Kemper, 2007). The ‘RMS’ (root-mean-square) and the ‘sum of negative values’ attributes are preferred for calculating the map attributes from the pseudo-impedance cube, as they clearly identify the channels. Note that the RMS attribute transforms the energy of the wave, and the ‘sum of negative values’ attribute captures the trough in the time window which is the dominant response

between the top and base of the T31a reservoir. The generated RMS map attribute is further processed to remove the tuning effect and calculate the NTG of the reservoir via the Connolly method (described in Appendix E). The estimated detuned NTG shown in Figure 6.2 is used as the static continuity term for further integration. For discontinuity estimation from 3D seismic, different attributes were generated, and it is found that each attribute of coherency, curvature, Laplacian, instantaneous phase, and ant tracking is useful for representing faults and identifying potential barriers to flow and channel margins (Chopra and Murfurt, 2007). However, the coherency map appeared to highlight most of the possible flow barriers, and it is preferable to use this attribute at this stage (see Figure 6.3).

Table 6.1: *Cube attributes for detecting continuity and discontinuity features in the 3D-seismic response.*

Attributes used for fault detection	Attributes used for NTG
Instantaneous phase: useful for tracking faults and discontinuities (Taner *et al.*, 1979)	Instantaneous frequency: useful in identifying attenuation and thin-bed tuning proportional to permeability
Laplacian attribute	Pseudo-impedance attribute
Coherency attribute	Spectral decomposition attributes
Ant-tracking attribute	Structural smoothing attribute

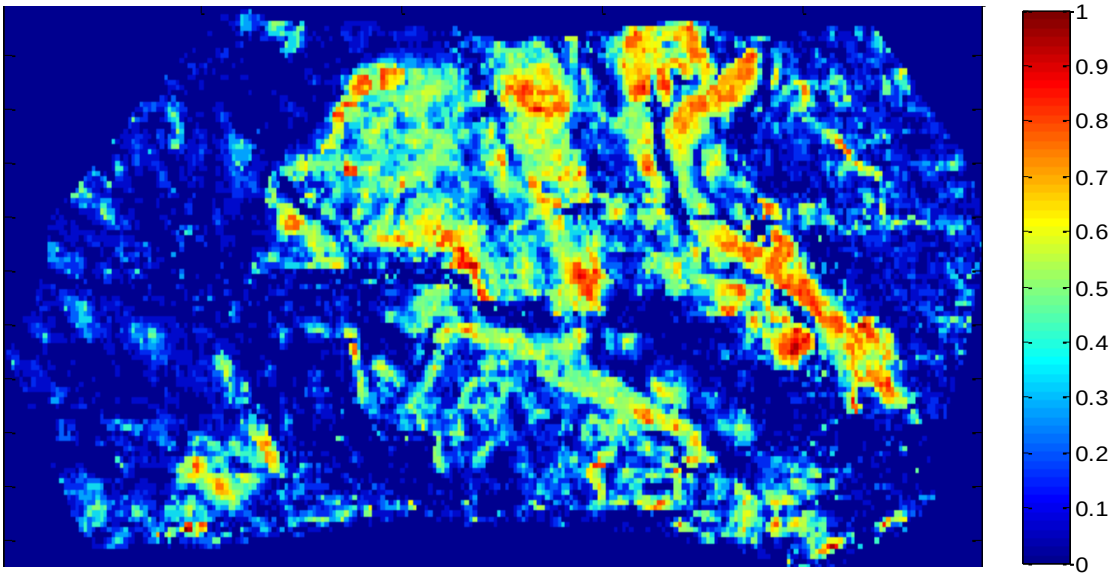

Figure 6.2: *NTG calculated using the Connolly method (2007). Note that the tuning effect is removed by using this method to underline the true response of the channels.*

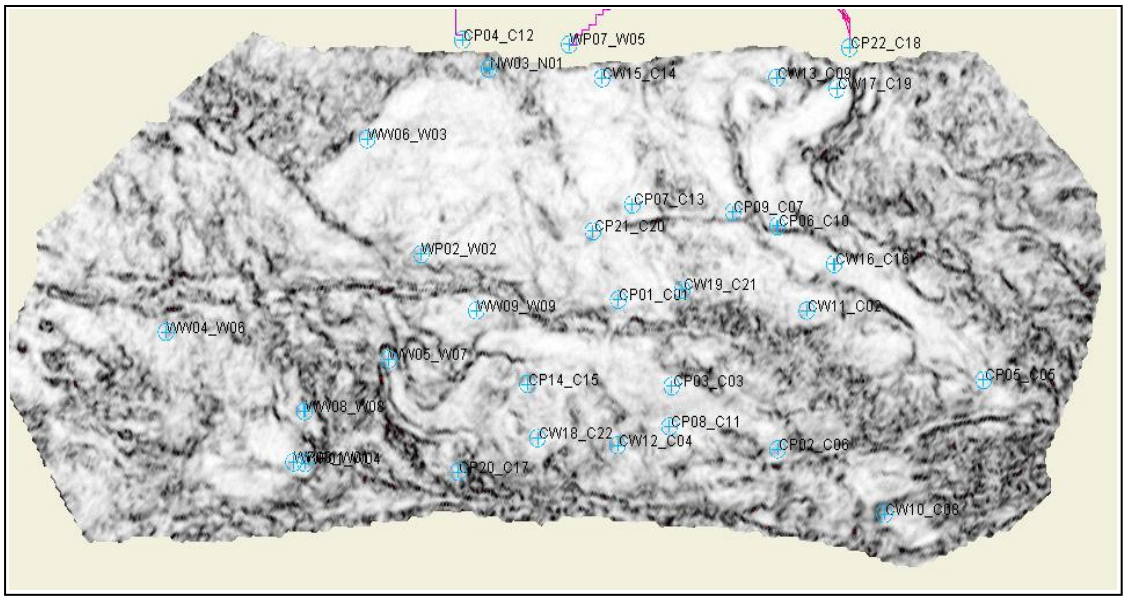

Figure 6.3: *The coherency attribute identifies potential barriers to flow and channel margins. The nature of the boundaries identified by the coherency attribute is likely to be the result of a lithology contrast caused by faulting, facies change, or both.*

6.3 Frequent time-lapse seismic in the Schiehallion field

In order to monitor sweep efficiency for water-flooding in the field and to control the gas coming out of solution, repeat seismic surveys were acquired frequently in 1999, 2000, 2002, 2004, 2006 and 2008. The pseudo-impedance seismic cubes for individual surveys were used to generate map attributes in a pre-defined window for a volume around the T31a reservoir. Before creating the difference map for time-lapse surveys, the base and monitor maps were statistically normalized to balance the amplitudes of each survey prior to subtracting. The attribute maps were then differenced to generate a sequence of time-lapse seismic difference maps. There are 21 possible difference maps between survey times from pre-production base-line (1996) to the last monitored (2008) listed in Table 6.2. All of seismic surveys are processed with 1996 base-line survey except 1999 and 2000 surveys. However, they have been involved in making difference maps here to extend the range of difference map attributes and extract the possible interpreted anomalies in their provided information. The uncertainty attached to this issue is minimized via examination of the consistency of interpretation with the sequence of repeated surveys as well as validation of anomalies with well production data and history-matched simulation prediction as described in the rest of this chapter.

However, the uncertainty of using of 1999 and 2000 surveys may still remain due to discrepancy in non-normalised amplitudes, phase and frequency in mentioned surveys compared to the rest of the surveys.

Table 6.2: *Generated time-lapse-seismic map attributes*

Seismic monitor survey	Number of possible difference maps
2008 survey	Six time-lapse (2008–2006, 2008–2004, 2008–2002, 2008–2000, 2008–1999, 2008–1996)
2006 survey	Five time-lapse (2006–2004, 2006–2002, 2006–2000, 2006–1999, 2006–1996)
2004 survey	Four time-lapse (2004–2002, 2004–2000, 2004–1999, 2004–1996)
2002 survey	Three time-lapse (2002–2000, 2002–1999, 2002–1996)
2000 survey	Two time-lapse (2000–1999, 2000–1996)
1999 survey	One time-lapse (1999–1996)

6.4 An integrated approach to interpreting pressure from saturation-anomaly boundaries in 4D seismic

The 4D seismic in the Schiehallion field is a pressure-dominated signal (Floricich, 2006). Therefore, the Laplacian attribute is employed for assessing barrier connectivity using a pressure compartment anomaly. However, there is always an uncertainty attached to differentiating pressure anomalies from saturation anomalies. Therefore, to achieve an enhanced result, prior to connectivity evaluation, I will attempt to distinguish pressure-anomaly boundaries from saturation-anomaly boundaries within the 4D-seismic signal. Subsequently, the extracted saturation-change anomalies will be utilized in SCA estimation.

6.4.1 The Laplacian attribute

The Laplacian is a second derivative term that identifies the edges (boundaries) of anomalies in the time-lapse seismic maps. The tracing algorithm assigned by the Laplacian detects two categories of boundaries. One is an anomaly limited to well locations, which is surrounded by another type of boundary (Figure 6.4(a), and Figure 6.4(b)). The exterior boundaries correspond with the pressure anomaly (*type-P*), whereas the boundary enclosed by the pressure anomaly seems to be correlated with the

saturation flood front (*type-S*). These features of the Laplacian attribute can be used for distinguishing the pressure anomaly from the saturation anomaly. As demonstrated in Figure 6.4(c), the *type-P/S* anomalies can be observed either in a single 4D survey or between surveys. Figure 6.4(c) shows that the 2008–2004 difference map indicates a *type-P* (pressure) anomaly), and the 2006–2004 difference map shows a *type-S* (saturation) anomaly, whereas the 1999–1996 difference map shows both types, *P* and *S*. The saturation anomaly (*type-S*) is indicated in red in the 2006–2004 and 1999–1996 surveys, and occurs due to the increase in the pseudo-acoustic impedance as the water saturation around the injection well CW13 is increased. Also, the pressure-anomaly feature indicated in blue results from a drop in the pseudo-acoustic impedance as the pressure around injection well CW13 is increased.

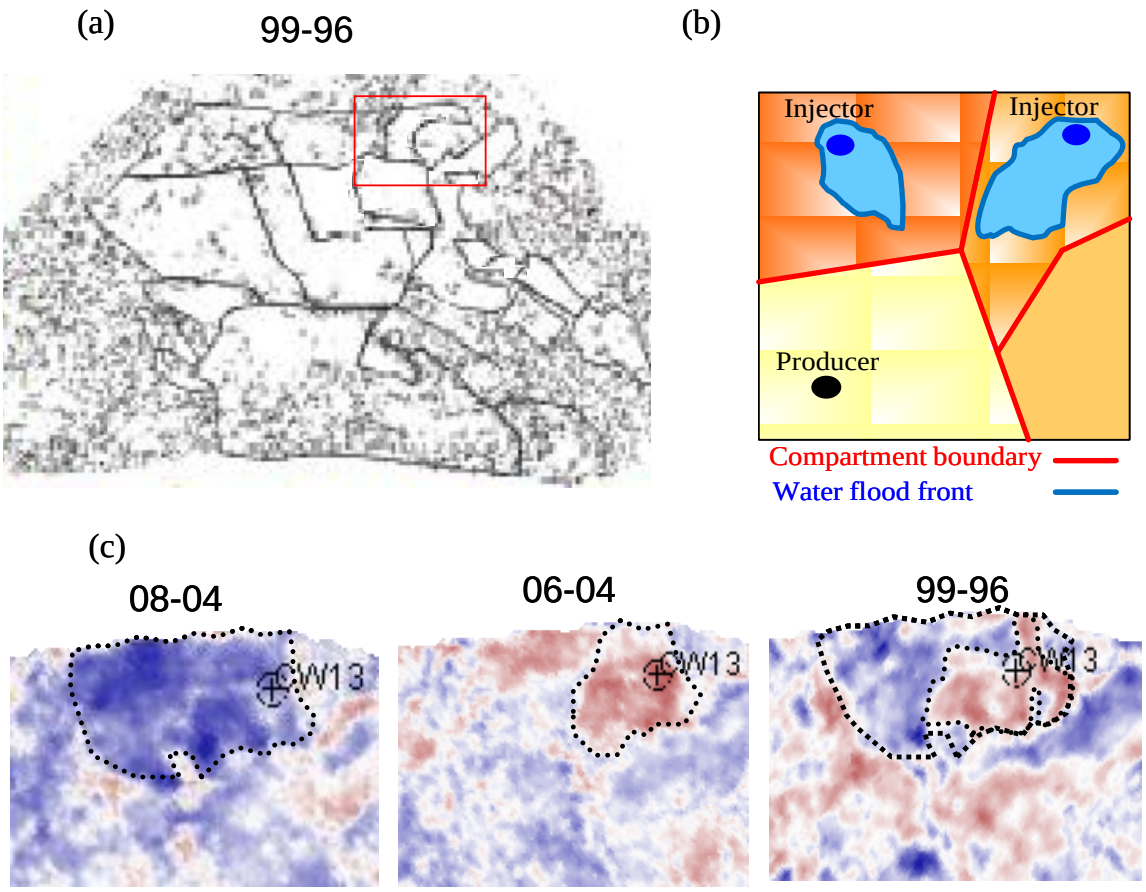

Figure 6.4: *(a) and (b) Laplacian features (type-P and type-S) and an illustration of how they are related to pressure- and saturation-anomalies, and (c) corresponding features observed in 4D seismic, indicating saturation (type-S) and pressure (type-P) anomalies.*

6.4.2 Correlation with seismic NTG and the initial estimate of the 3D-seismic compartments

Integration of the spatial information of 3D seismic with 4D seismic can also be used to discriminate pressure- from saturation-effects. As discussed in Chapter 5, change in saturation and pressure is correlated with NTG and compartment respectively. Therefore, NTG and initial estimate of compartments from 3D seismic can be used to interpret saturation from pressure changes.

As illustrated in Figure 6.5, the compartment around well CW16 seems to be separated by a fault shown in the coherency attribute calculated from 3D seismic. This is further confirmed by the 4D signal change of polarity highlighting the compartment around this well. In addition, the fault appears to be sealing, as the 4D signal shows a distinct highlighted compartment. Therefore, this anomaly is interpreted as a pressure-up compartment, and it seems that the fault is sealing. However, based on the simulation result, the pressure of the compartment is in communication with the neighbouring compartment, suggesting a non-sealing fault. Therefore, the simulation response has to be adjusted to have a consistent response with observed data. Hence, the transmissibility multiplier (T_f) is to be recalculated to address this issue (the details of the T_f calculation are described in section 6.6.1).

Also, the 2004–1996 time-lapse difference map clearly signifies the movement of water-flooding from the injection wells towards the production wells. The flood path is fairly consistent with the detuned NTG pattern, notably from injectors CW15 and CW19 towards producers CP01 and CP21. Similarly, the time-lapse anomalies correlated with the NTG pattern around CW11, WW06 and CW13 appear to be saturation anomalies. Therefore, the 4D anomaly, which is more correlated with the NTG, is assumed to be a saturation anomaly rather than a pressure anomaly.

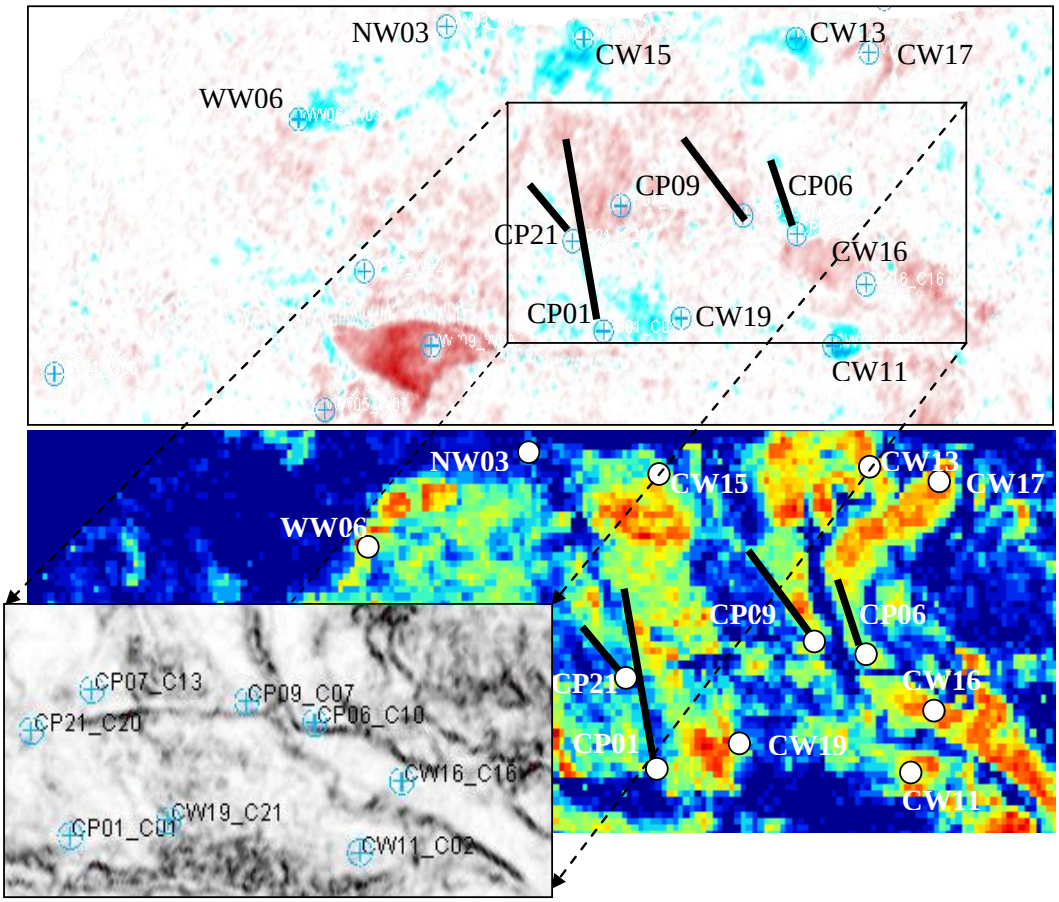

Figure 6.5: *A 2004–1996 RMS difference map extracted with a window defined from 10 ms below the top horizon to 40 ms above it. The difference map shows the movement of water from injectors to producers. Note that hardening around the injectors is indicated in blue, and softening is in red. The hardening effects around the injectors are correlated with high-NTG regions calculated from 3D seismic, indicating that the 4D anomaly is related to changes in saturation. However, softening around CW16 is due to pressure-up in the compartment, as the presence of a sealing fault is confirmed by the comparing the coherency map from 3D seismic with the change in 4D-seismic polarity across the fault.*

6.4.3 Frequent time-lapse surveys used as a tracking tool

After assigning the principle described for the interpretation of pressure from saturation in each 4D-seismic difference map, the validation of these anomalies can be verified effectively using frequent time-lapse surveys.

It is assumed that the pressure compartments are constant over production time; however, the saturation anomaly is evolving over production time from the injection wells towards the production wells. The fact that the pressure compartment is seen to be constant over the sequence of time-lapse seismic maps is due to the relatively small time-scale for pressure stabilization within the compartment as compared with the time-scale of the 4D seismic. This is illustrated in Figure 6.6, in which pressure diffusion is modelled within a trainable compartment. The longest time to reach the boundary of the compartment and obtain a stabilized pressure response is calculated using the following equation (Stewart and Whaballa, 1988):

$$t = \frac{497.6\mu C_t \varphi}{K} r_{inv}^2 \tag{6.1}$$

where μ is viscosity; C_t is compressibility; φ is porosity; K is permeability; and r_{inv} is the distance to the furthest boundary. The longest time taken for pressure to reach the boundary of the compartment is 12 days for the average properties of the Schiehallion field displayed in Figure 6.6. Note that, for 16 mD, this becomes 268 days, which is starting to become significant with regard to frequent 4D seismic (the technique may not work in low-permeability reservoirs). So, generally, the 4D-seismic repeats are at intervals that are larger than the times taken to reach the stable state. Hence, the pressure compartment in 4D seismic is seen to be constant over time. Therefore, the anomaly that preserves its shape in the sequence of 4D survey maps indicates the pressure compartment. Also, the 4D anomaly which is evolving over surveys from injection wells is a saturation anomaly.

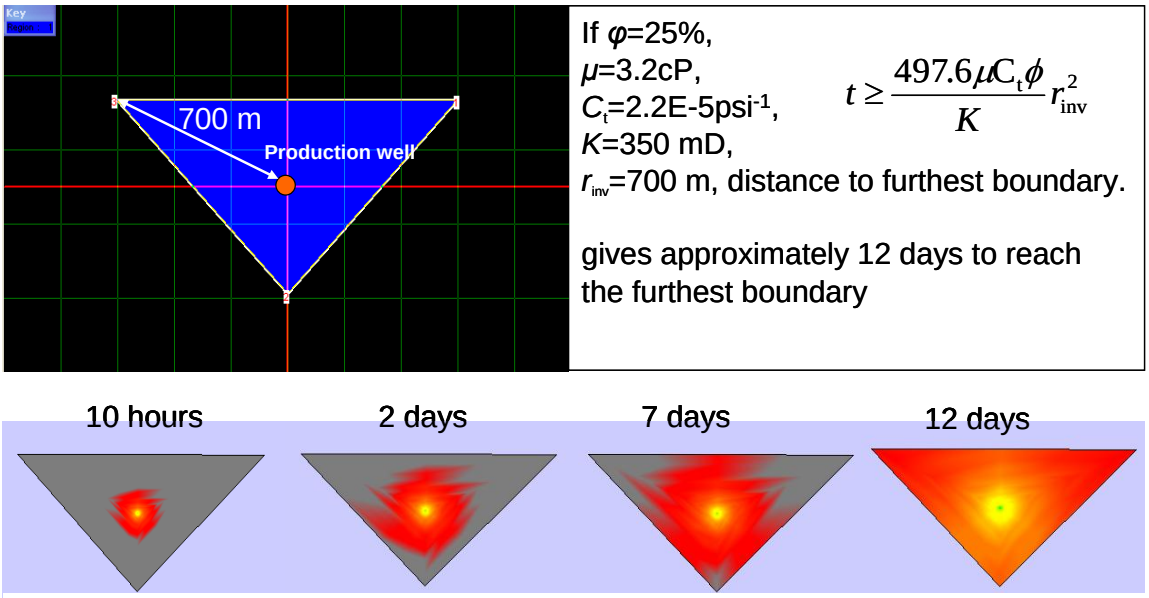

Figure 6.6: *The longest time taken for the pressure to reach the boundary of this triangular compartment is 12 days for the average properties of the Schiehallion field. (The modelling is performed using Pansystem software.)*

Figure 6.7(a) shows how the pressure anomaly around CW13 preserves its shape in different time-steps (note that the polarity is varying between surveys, which is due to the direction change in pressure and is explained by the petro-elastic model), namely, from survey 04-96 to 08-04, whereas the saturation anomaly around CW13 evolves from survey 04-99 to 06-04. Another example is the anomaly around injection well CW16 and production well CP05. Again the pressure anomaly can be identified using the fact that its shape is preserved between surveys 04-02 and 04-96. A water-saturation anomaly around CW16, and a gas-saturation anomaly around CP05, are also observed. Therefore, the consistency of the 4D-seismic anomalies between the surveys during production time adds confidence to the anomaly interpretation. Interpretation can be further extended by comparison with forward-modelling (simulator-to-seismic modelling) results and production data (the analyses are described in Appendix I). Note that the procedure of saturation and pressure separation described here is not an inversion procedure. Instead, it is a qualitative interpretation approach.

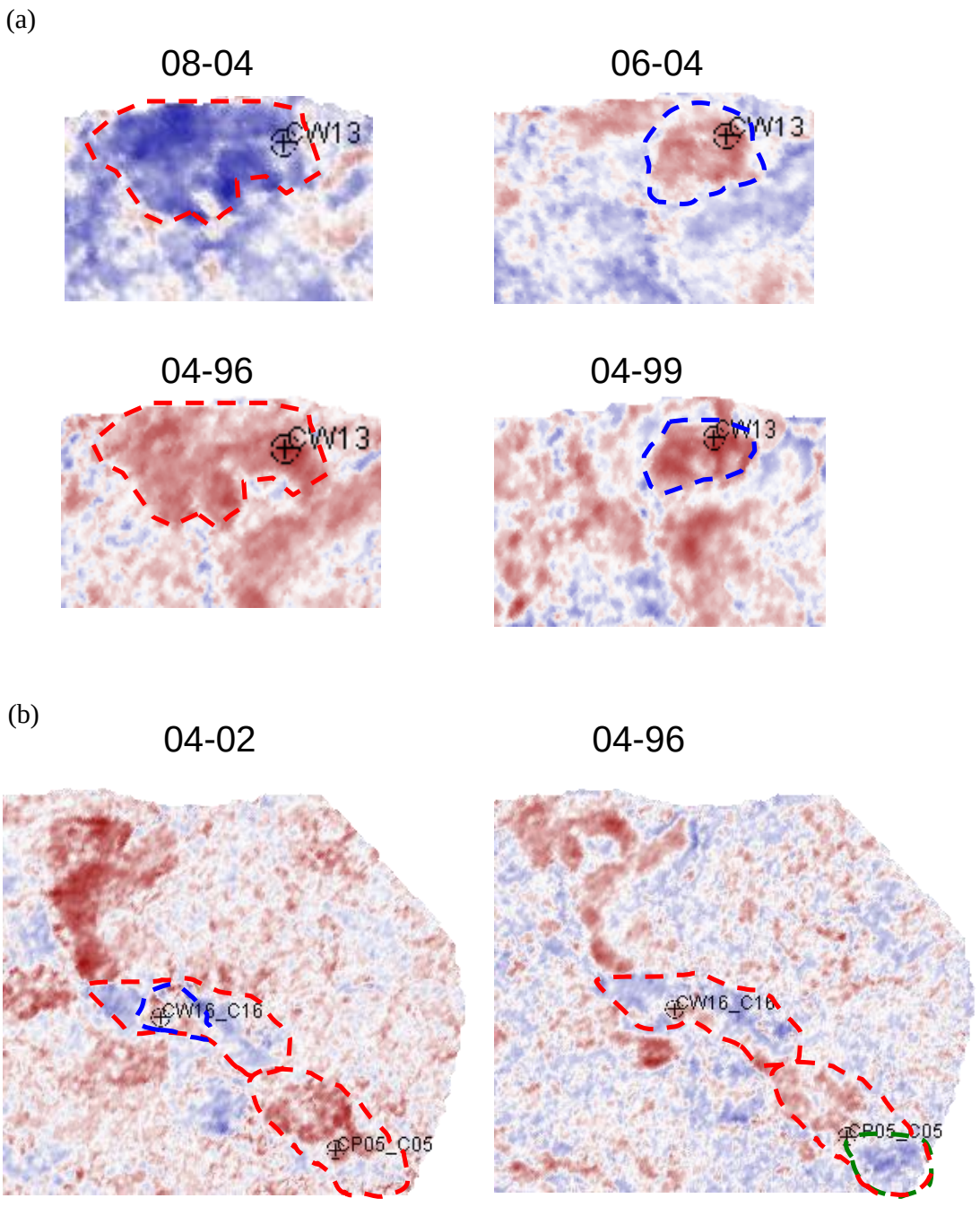

Figure 6.7: *(a) Identification of a pressure anomaly from saturation around well CW13. The shape of the pressure anomaly is preserved between surveys 04-96 and 08-04, whereas the saturation anomaly has evolved from survey 04-99 to survey 06-04, and (b) identification of a pressure compartment around injection well CW16 and production well CP05_C05. Again the shape of the pressure anomaly is preserved between surveys 04-02 and 04-96. A water-saturation anomaly around CW16a, and a gas-saturation anomaly around CP05, are also observed.*

6.5 Resulting pressure- and saturation-maps

The anomalies detected by the Laplacian attribute are interpreted to be either saturation- or pressure-anomalies in each 4D difference map, using the interpretation techniques described. Figure 6.8(a) shows the summation of all saturation anomalies interpreted from each 4D difference map. The anomalies around the injection wells (in blue) indicate hardening due to water injection, while the anomaly around the production well is due to softening resulting from a drop in water saturation (CP23_B is indicated by an opposite response in red). The corresponding simulation-model saturation map is shown in Figure 6.8(b) for comparison purposes. The orientation of the saturation anomalies from the observed data in some regions seems to be different from saturations calculated from flow simulations. The procedure that will be introduced in section 6.7 proposes that the transmissibility values should be adjusted based on this saturation-anomaly map derived from 4D seismic. It is hoped that updated transmissibility in the simulation model will correct the simulation prediction so that it corresponds with the observed 4D-seismic saturation map.

In addition, the boundaries of the pressure compartments detected from different time-lapse surveys overlapped to select the most confirmed compartment over time. The final compartmentalization map is shown in Figure 6.9(a). By comparing the evaluated map with the compartmentalization in the simulation model (Figure 6.9(b)), one may suggest that the simulation model is too compartmentalized. It is important to note that the new estimated compartment map is between the over-compartmentalized new simulation model and the previous simulation model (least compartmentalization) provided by the operator. The procedure that will be described in the next section suggests assigning the estimated compartmentalized model to simulation updating via transmissibility-multiplier values.

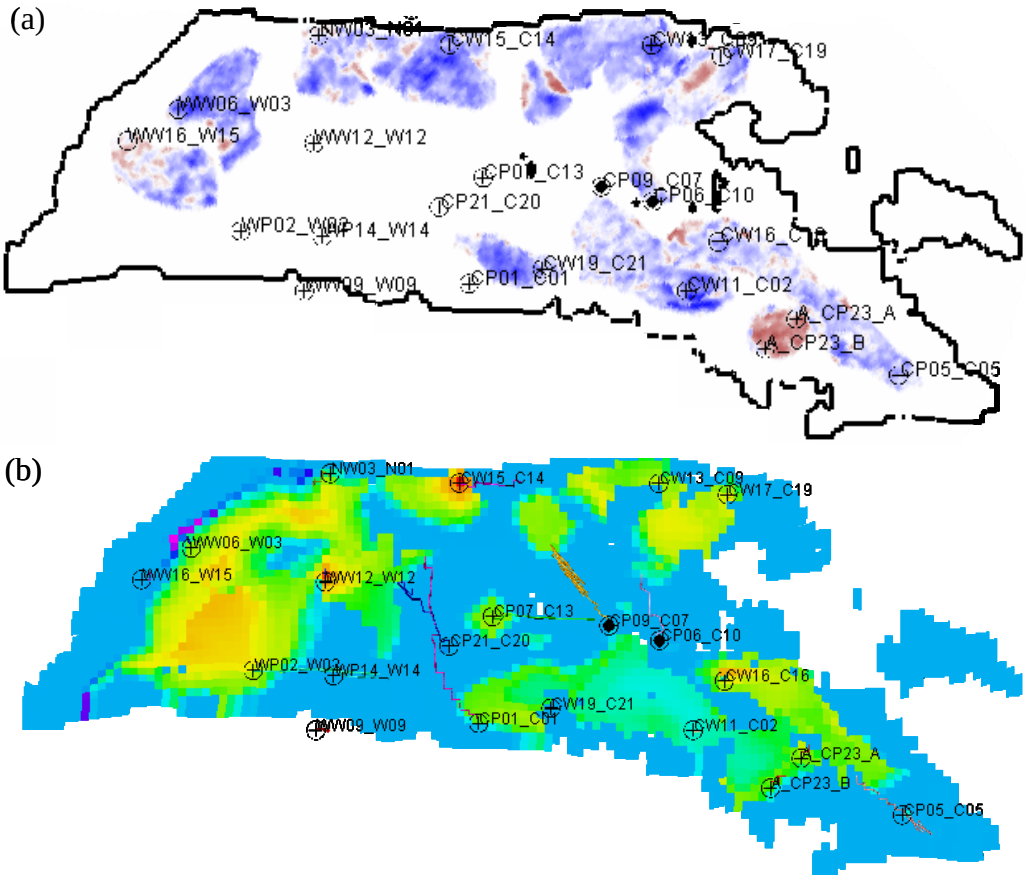

Figure 6.8: *(a) Summation of saturation anomalies from different surveys. The anomalies around the injection wells (in blue) are indicating hardening due to water injection, while the anomaly around the production well (for example, CP23_B is indicated by an opposite response in red) is due to softening; and (b) the corresponding saturation differences are calculated and summed together as predicted from the simulation model.*

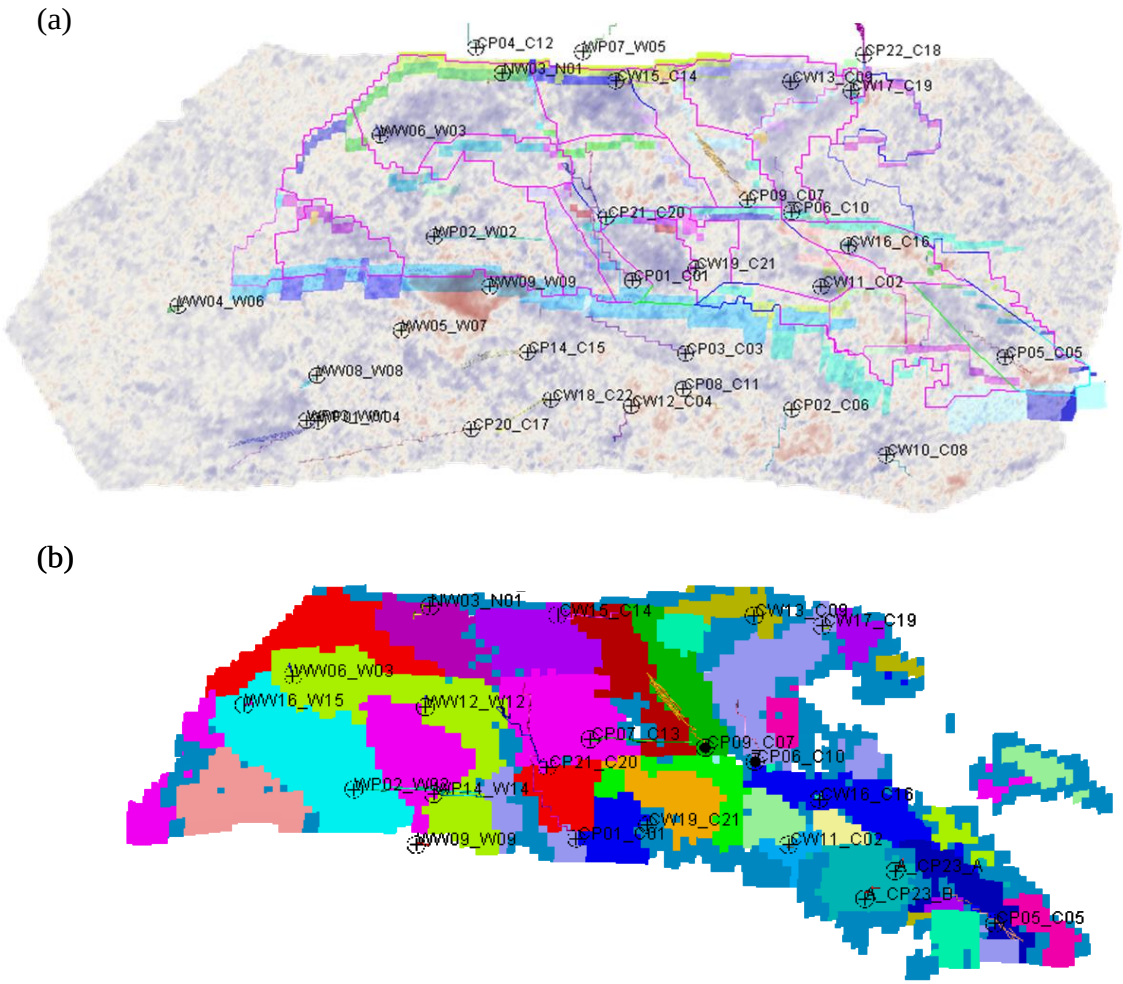

Figure 6.9: *(a) Compartmentalization evaluated from the pressure-anomaly map, and (b) compartmentalization in the simulation model.*

6.6 Integrating historical production data and time-lapse seismic for transmissibility-multiplier estimation (the pressure solution)

Pressure-anomaly boundaries are considered to be the images of compartments, and are employed for identifying the position of flow barriers. In order to utilize the evaluated compartments for updating the simulation-model parameters, the transmissibility-multiplier values for the faults between the compartments must be estimated (Figure 6.10). Well-production performance is often considered to be the most reliable source of information about reservoir compartmentalization. However, there is some degree of uncertainty in the production data, because of commingled production from different intervals and different compartments. Therefore, given the structure of the compartments from the seismic domain, the transmissibility multiplier (T_f) values for

the faults surrounding the compartment are estimated using the available well-production data.

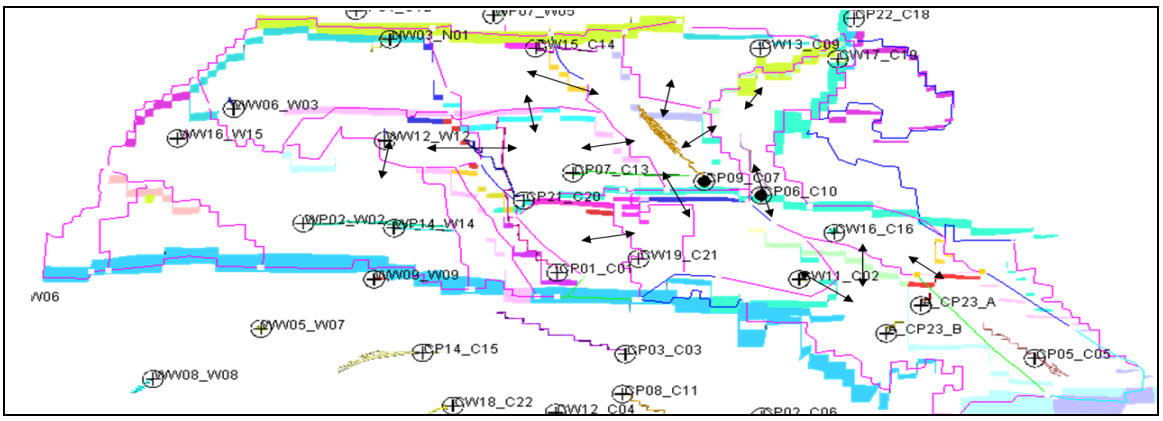

Figure 6.10: *The field is subdivided into regions, using the determined pressure-anomaly map. Transmissibility multipliers for the zone of pressure communication between the polygons obtained is calculated using well-production data. The transmissibility multiplier can represent a barrier without using a cell.*

6.6.1 Transmissibility-multiplier calculation

The field is subdivided into regions, based on the determined pressure-anomaly map. Each area is represented by 'tanks', which can be made to communicate with each other. The intention is to calculate the communication (transmissibility multiplier) between these tanks. The continuous bottom-hole pressure (BHP) data collected from permanently installed gauges are available for the wells in Schiehallion. The BHP of the well located in the compartment is assigned as the compartment pressure. It is essentially accurate if the compartment is small enough to represent the well pressure. Figure 6.11 shows how the pressure fluctuations in the production well in one compartment can be related to an injection well located in an attached compartment. This is illustrated for the well pairs CW16/CP05, CW16/CP06, and CW17/CP06 in Figure 6.11. In Figure 6.11(a), CP05 initially declined due to the lack of pressure support (before 2002), but responded when CW16 was put on injection. After CW16 had raised the pressure sufficiently, the pressure in CP05 responded to a high-pressure impulse from CW16, due to a rapid fall in pressure in the injection well. This shows that there is a volume leakage supporting the fault between CW16 and CP05, which is not completely sealing. In fact the producer is responding mainly to high-pressure impulses

from injector, due to a rapid fall in pressure in the injection. This happens after injector has raised the pressure sufficiently which is not the case in the early time. Also, the communication of CP06 with the injectors (Figure 6.11(b) and Figure 6.11(c)) is indicated by receiving the response in the production well due to the signal of the injection-well fluctuations, although the CW17 fluctuation is the one which is more responsive, and hence more connected. Thus, consistent behaviour in the receiving of pressure impulses between an injection/production pair implies satisfactory communication. On the other hand, it can also be concluded that there is a lack of communication, based on the non-correlated behaviour of the injection/production pairs.

Therefore, given the pressure fluctuations over time in two neighbouring compartments, each having injection and production wells, the extent of the relationship between the pressure fluctuations indicates the linkage of the fault in between. Therefore, the correlation coefficient between the BHP variations of injection–production well pairs can be utilized to classify the set of barriers/baffles from low transmissibility values to higher transmissibility values. This concept is demonstrated in Figure 6.12 (it is very well documented in Heffer *et al.*, 1997; Refunjol and Lake 1999; Soeriasinata and Kelkar, 1999). Thus, the correlation coefficient can be directly transformed into T_f values, using the following formula:

$$T_f = \frac{\rho - \rho_m}{\rho_{max} - \rho_{min}} \tag{6.2}$$

where ρ_{max} and ρ_{min} are the maximum and minimum values of the correlation coefficients, and ρ and T_f are the correlation coefficients and transmissibility multipliers of the desired fault. The maximum correlation is found to be between injection and production located in the same compartment. In Equation 6.2, the calculated T_f for maximum correlation is equal to 1. Accordingly, the rest of the values are scaled between zero and one. The calculated transmissibility values for the faults denoted with arrows in Figure 6.10 are listed in Table 6.3.

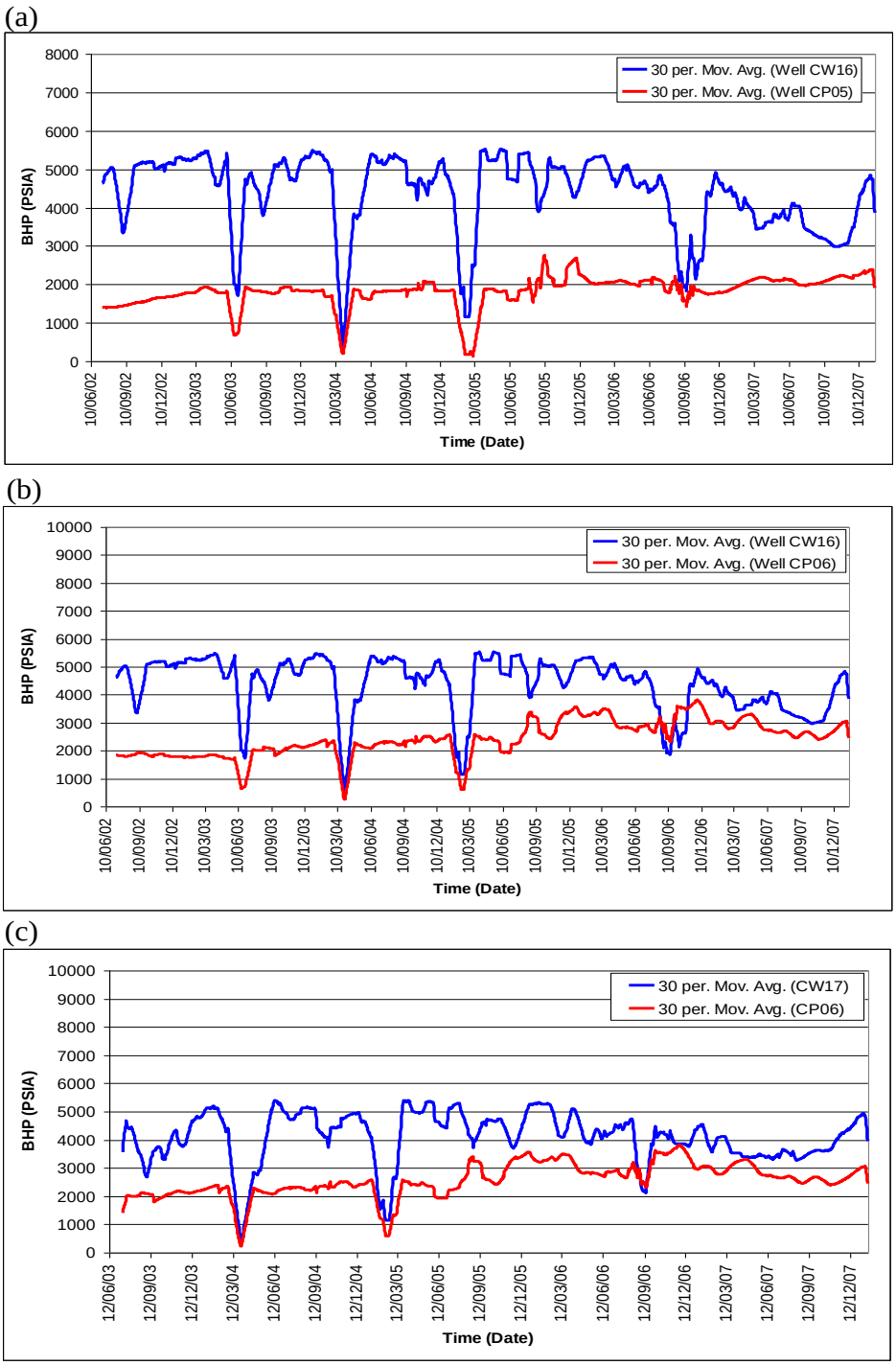

Figure 6.11: *(a) The BHP of injection well CW16 versus production well CP05; (b) the BHP of injection well CW16 versus production well CP06; and (c) the BHP of injection well CW17 versus production well CP06. Consistent behaviour in receiving pressure impulses in a production well from an injection well implies good communication. Data are averaged for every 30 days for visualization purposes.*

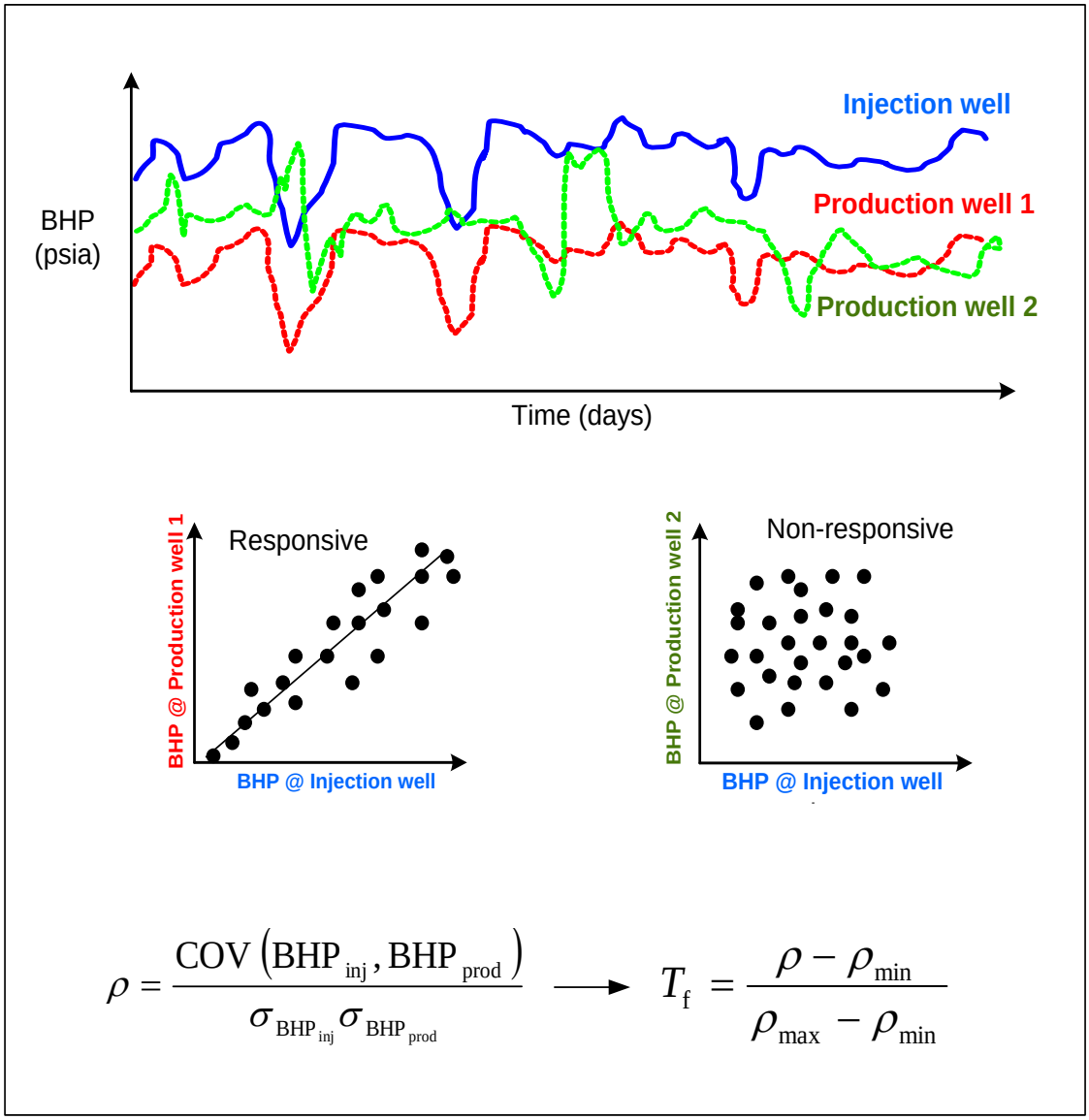

Figure 6.12: *The correlation coefficient measures the degree of linear dependence between two injection and production BHP variations.*

Table 6.3: *Fault transmissibilities calculated from well–well correlations for the faults denoted with arrows in Figure 6.10*

Fault between production well and injection well	Fault transmissibility
CP01 and CW19	1
CP05 and CW16	0.83
CP06 and CW13	0.28
CP06 and CW16	0.69
CP06 and CW17	1
CP09 and CW11	0
CP09 and CW13	0.30
CP09 and CW15	0.55
CP09 and CW19	0.45
CP21 and CW15	1

The final transmissibility-multiplier values can serve as the primary history-matching parameters. Thus, this technique provides a rapid assessment of transmissibility multipliers for updating the simulation model and improving history matching. It is expected that, using this technique, it will be possible to better match the production-, particularly pressure-data in history matching. However, the simple technique used in this work becomes harder as the flow systems between the wells grow more complicated. For example, an injection well may interact with several producers. Also one well may come on stream as the result of production activities or even shut-down from injection or production which influences the spatial balance of field pressure distribution between wells. Therefore, the spatial interactions between the wells in the field need to be taken into account (for more details on this, see Albertoni and Lake, 2003; Yousef et al., 2006; Kaviani et al., 2008).

6.7 The probabilistic approach to integrating well data and SCA for transmissibility estimation (the saturation solution)

Relating the 4D-seismic amplitude type to transmissibility/permeability has been attempted by a few researchers (Oliveira *et al.*, 2007). In Chapter 5 of this thesis, an attribute called the seismic-connectivity attribute (SCA) was defined that contained the stacked frequent time-lapse seismic difference maps dominated by saturation and multiplied by the seismic NTG map. It was shown that this attribute is proportional to

the total reservoir connectivity derived from Darcy's equation. Therefore, the SCA is interrelated to transmissibility term in Darcy reservoir connectivity. Here, the functionality of the connectivity attribute with respect to transmissibility is examined based on linking the hard data (well data) and the soft data (SCA) at the well locations. The relationship between these two factors may not essentially follow a linear trend in practice. Hence, a non-linear relationship is assigned to allow a wider range of possible dependencies. This functionality is translated into a probability function. The uncertainty attached to the relationship is also defined in the probability function. The characteristic probability is then utilized in a stochastic conditional simulation to guide the transmissibility estimation across the reservoir. The general workflow pursued in this section is demonstrated in Figure 6.13.

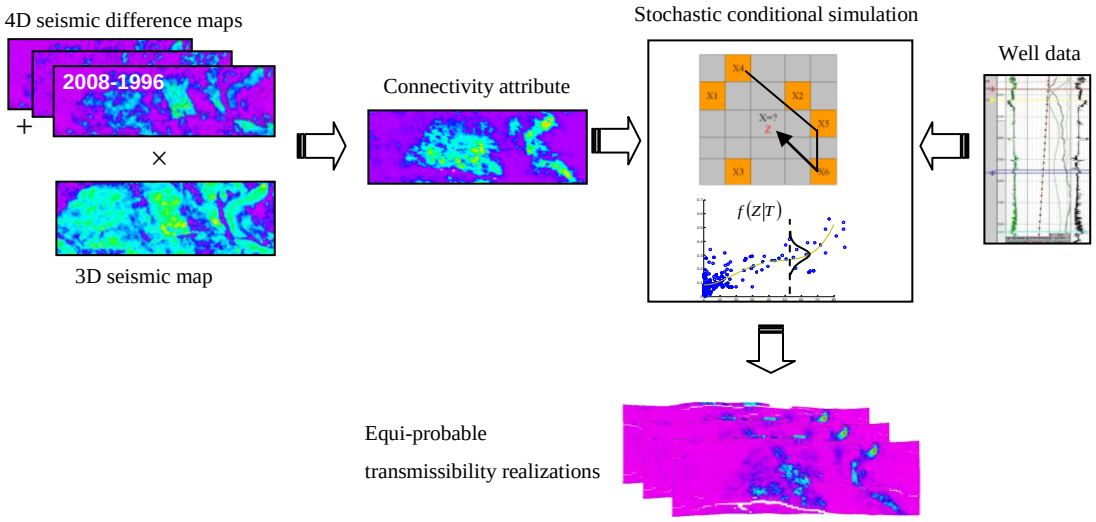

Figure 6.13: *A general workflow for estimating the transmissibility guided by the SCA map. The connectivity attribute is interrelated with transmissibility values which are defined to be average permeabilities at interfaces between two grid blocks in the reservoir-simulation model. A non-linear relationship is assigned between these two properties. The conditional probability is calculated to incorporate the non-linear relationship and the uncertainty attached to this relationship. The assigned probability is then applied in a sequential Gaussian simulation framework to generate equi-probable realizations.*

6.7.1 Calculated SCA

In the Schiehallion field, the individual time-lapse surveys over time provide the sequence of channel illumination. To calculate SCA, selective 4D signals in which the saturation signal is clearly interpreted are chosen (for Schiehallion, the saturation anomalies are observed in the following surveys: 08-04, 08-00, 08-99, 08-96, 06-04, 06-02, 06-00, 04-96, 02-00, 02-96 and 00-96). The SCA is equal to the stacked generated time-lapse seismic difference maps dominated by saturation from individual time-lapse surveys (Figure 6.8), multiplied by the detuned NTG from base-line seismic. The calculated SCA that is scaled between zero and one is shown in Figure 6.14. In fact, the direction of the interpreted water-flood anomalies within the channels carries information on the connectivity of the reservoir. The closer the connectivity factor is to 1.0, the better connected the reservoir. Values closer to 0.0 indicate poor reservoir connectivity. The limited connectivity between CW16 and CP06 in the eastern part of the field is clearly observed in Figure 6.14. This in fact is where there is an uncertainty in the field regarding the connection between these two wells (for more details, see the paper by Govan *et al.*, 2006).

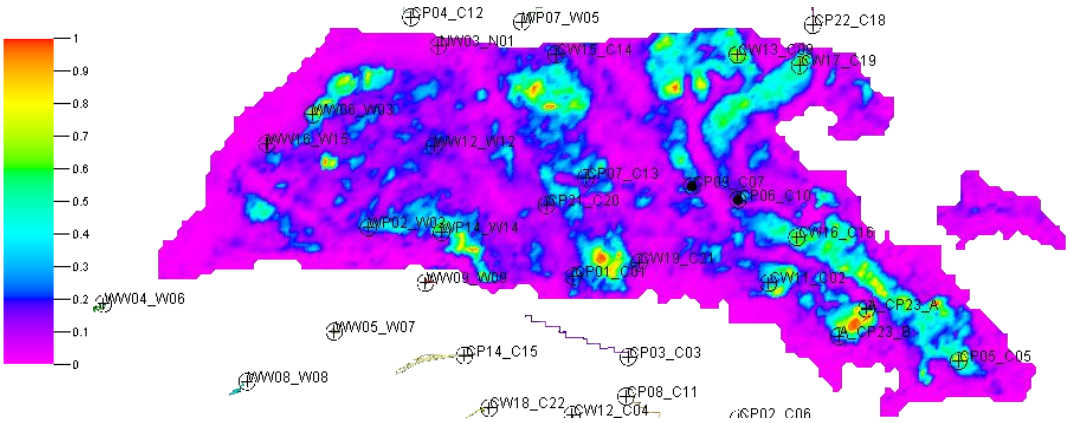

Figure 6.14: *Calculated SCA in segment 1 of the Schiehallion field.*

6.7.2 Well data

The most reliable data in the oil industry are well-log data. In the Schiehallion field, NMR (nuclear magnetic resonance) logs are used to calculate permeability at well locations in the operator's (BP's) geological model. NMR uses hydrogen protons as an indicator of the presence of fluids in the pore space of porous media. This provides an

indication of porosity/saturations, which can then be transformed into permeability values by using empirical relationships. In the operator's reservoir model, permeability log data are resampled from a fine-resolution geological model into the reservoir-simulation grids. This step is performed by identifying the grid cells that intersect the well trajectories, and then averaging the log samples.

Transmissibilities are calculated as a function of permeabilities and NTG in reservoir simulation model grids. Pseudo-logs of transmissibility are created from the simulation model at each well location. Horizontal production wells make it possible to calculate the transmissibility along a number of cells intersecting the well trajectories. The log values are arithmetically averaged in a vertical sense to obtain a 2D map of the well values. The arithmetic averaging is chosen to be consistent with reservoir flow behaviour. In Schiehallion, the reservoir units are separated by shale intervals, so the flow is greater parallel to the layers than through the layers. The general practice for calculating effective permeability in these circumstances is using arithmetic averaging of the permeability in the layers (Cardwell and Parsons, 1945).

6.7.3 Stochastic conditional simulation with SCA constraint

The goal is to predict transmissibility by combining the measurements of this property at well locations with the measurement of SCA correlated to the property. Spatial information offered by SCA is directly utilized to guide transmissibility variation across the reservoir. The evaluated SCA is plotted against transmissibility values at well locations (Figure 6.15). In the cross-plot, the SCA is better correlated with the transmissibility at higher values than at lower ones, which shows deviation from a linear relationship between the two properties. The spread of values for the predicted transmissibility depends on the value of the connectivity attribute. Therefore, a non-linear dependency with varying standard deviation has to be defined. The non-linear relationship can be captured in defining a joint probability-density function, known as the likelihood function, for incorporating the defined relationship and the uncertainty attached. The likelihood function is calculated by extracting the 1D likelihood function from the joint PDF (probability-density-function) For each T value, the likelihood function (see Appendix J) is a Gaussian function with the mean value (Z_m) obtained

from the fitted function and standard deviation (δ_z) as described in the following equation:

$$Z_m = 8.1e^{-8}T^4 - 1.1e^{-5}T^3 + 0.00043T^2 - 0.00082T + 0.086 \quad (6.3)$$

$$\delta_z = \sqrt{\frac{\sum_{i=1}^{n}(Z_i - Z_m)}{n-1}} \quad (6.4)$$

where Z_i represents the connectivity attribute values around the mean (Z_m) corresponding with the specified transmissibility (see Figure 6.15), and n is the number of Z_i values for a specified T value. The fitted function is a fourth-degree polynomial (defined above). Therefore, the Gaussian function for the above-calculated mean and standard deviation is defined as:

$$f(Z|T) = \frac{1}{\sqrt{2\pi}\delta_z}\exp\left\{-\frac{[Z - Z_m]^2}{2\delta_z^2}\right\} \quad (6.5)$$

The local probability-density function for the posterior distribution, $P(T|Z,T_1,...T_n)$, is calculated by multiplying the kriging probability by the likelihood probability (see Appendix J):

$$P(T|Z,T_1,...T_n) \propto f(Z|T) \times P^k(T|T_1,...T_n) \quad (6.6)$$

where $P(T \mid T_1,\ldots T_n)$ is the kriging probability and $f(Z \mid T)$ is the likelihood function.

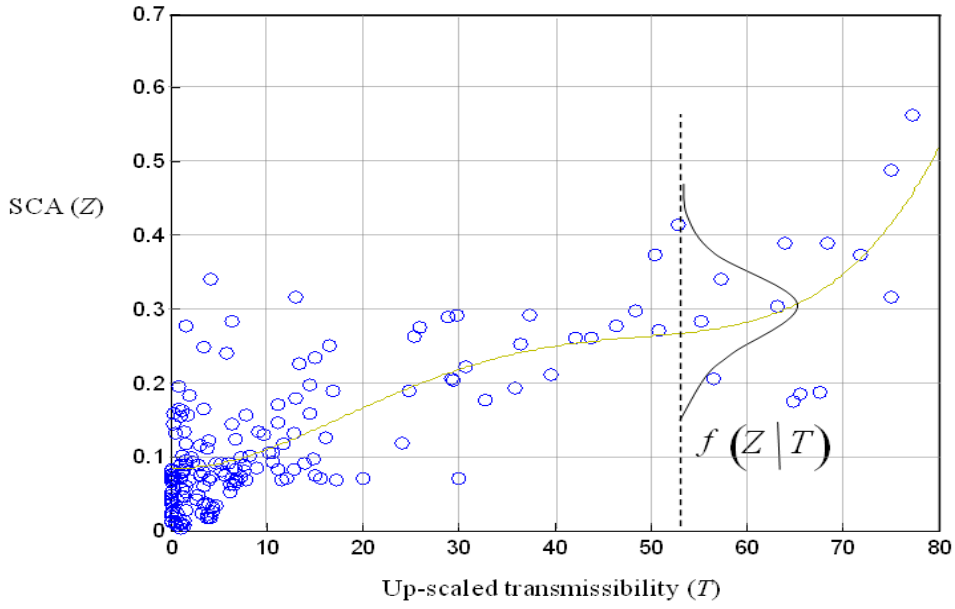

Figure 6.15: *Relationship between the calculated SCA and up-scaled transmissibility values at well locations.*

The local posterior probability function is then employed to estimate the SCA-guided transmissibility in the reservoir model via the sequential Gaussian simulation scheme (see Appendix J). The simulation technique draws a value from the calculated posterior probability in order to simulate the transmissibility value at a certain location in the reservoir. Multiple equi-probable realizations are then generated. The mean value of realizations is shown in Figure 6.16. Figure 6.17 shows the vertically averaged transmissibility values in the reservoir-simulation model. There are some agreements and disagreements between the calculated transmissibilities and the transmissibilities in the model. However, clearly more spatial information is offered between the wells in the seismic product. It is important to note that permeabilities contributing to transmissibility calculation in the reservoir-simulation model provided by the operator are estimated based on empirical equations as a function of the depth and the model facies. However, assuming that both realizations are data-driven transmissibility models, they are not far from the reality. However, the new calculated transmissibility model incorporates the spatial information of connectivity gathered from the sequence of frequent time-lapse surveys, and it is hoped to improve the history-matching result upon reservoir-model updating.

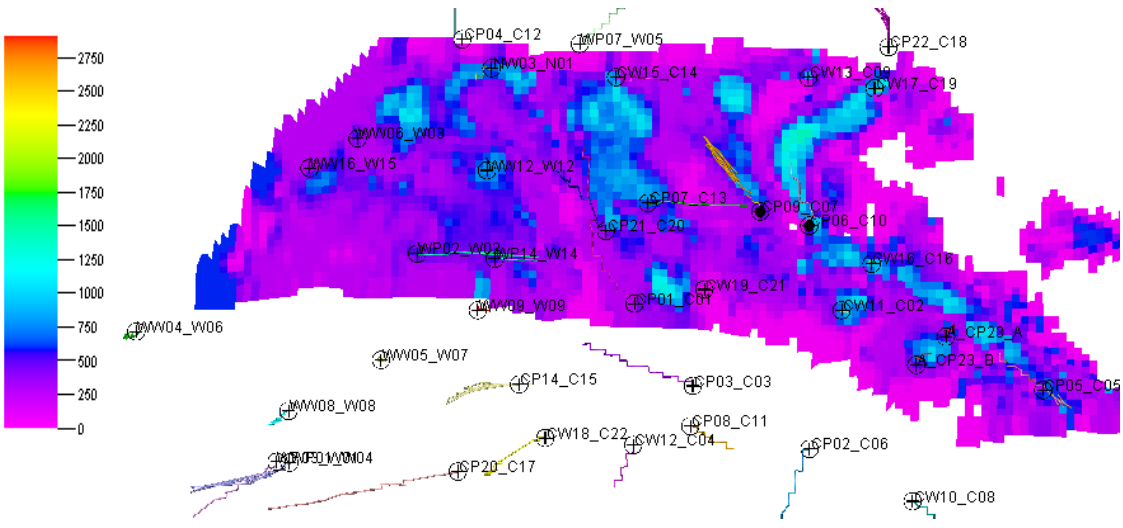

Figure 6.16: *Estimated mean value of transmissibility realization.*

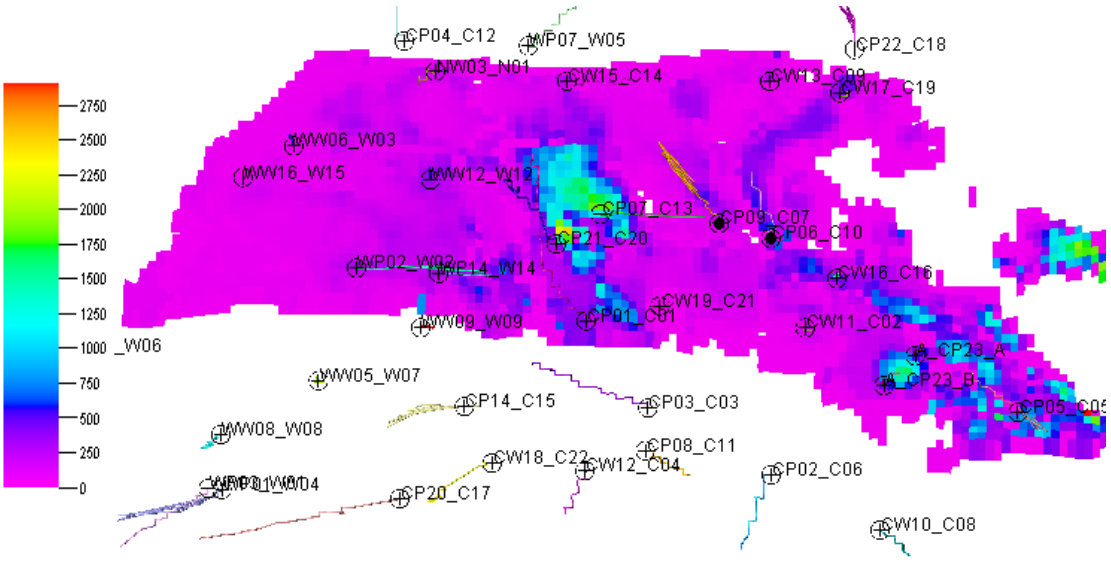

Figure 6.17: *Simulation transmissibility that is vertically averaged over the T31a reservoir.*

6.8 Discussion

The types of approaches introduced here are based on a saturation- or pressure-dominated 4D signal. An integrated interpretation approach for discriminating pressure from saturation is used for this purpose. It is important to note that discriminating pressure from saturation still seems to be a challenging task, and special care has to be dedicated to the interpretation of pressure/saturation changes in 4D-seismic signals. However, the solution to overcome the ambiguity in interpretation of time-lapse seismic data is to compare and validate the data using other available sources of pressure/saturation in the field.

One potential drawback in the saturation-based method applied for estimating transmissibility is that the saturation anomalies are generally limited to well locations, and hence they provide information only in these regions. In fact, this is the limitation of saturation behaviour as an input for this method. However, including frequent time-lapse surveys increases the chance of more coverage of saturation-change regions over time. The resulting transmissibilities can easily be inverted to permeability, providing that the NTG is calculated from 3D seismic. The functionality of transmissibility versus NTG and permeability is derived from the forward model; and, normally, different correlations corresponding with different facies need to be employed (see Figure 6.18).

The resulting transmissibilities/permeabilities can be applied as the input for the simulator for subsequent simulation and history matching.

The Laplacian attribute used in this chapter is very sensitive to noise. Therefore, removing noise or using a low-frequency content of seismic information could be one solution to overcome this problem.

Another possible improvement in the method proposed here is using different attributes that may sense the channel orientation or saturation/pressure in reservoir. Using a multi-attribute signature can provide extra accuracy. Pattern-recognition methods can be employed to integrate different attributes imaging compartments and structures. This is also applicable for possible attributes that are sensitive to fluid changes.

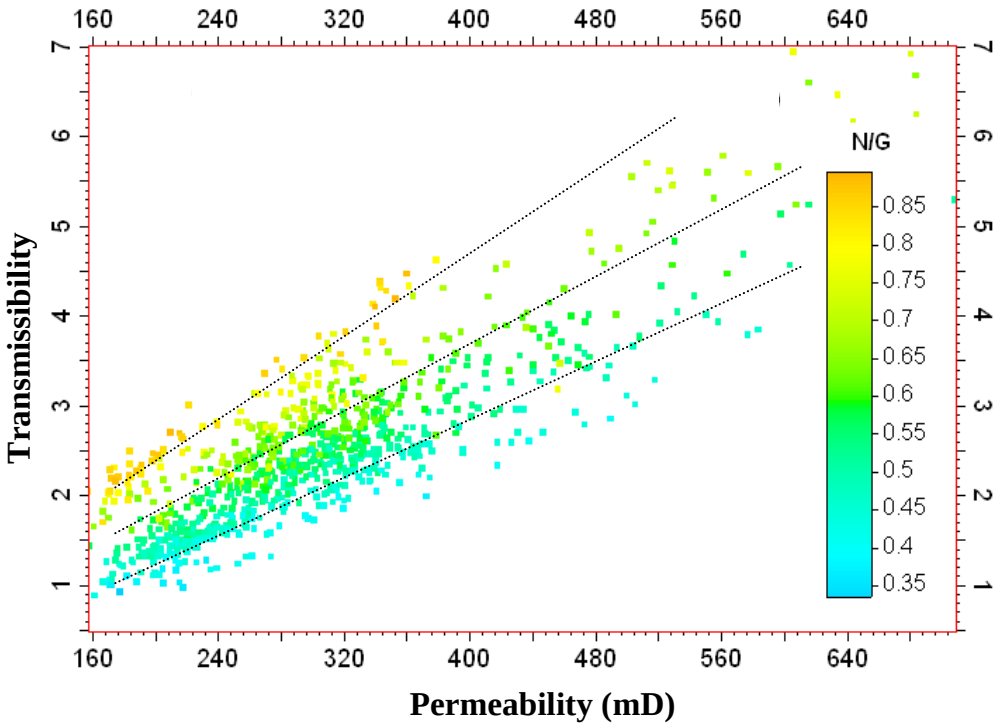

Figure 6.18: *Transmissibility is a function of permeability and NTG in a forward model calculation. For different NTG (sand facies), transmissibility is correlated to permeability with a different relationship.*

6.9 Summary and conclusions

Two types of connectivity assessment were proposed, depending on the fact that 4D-seismic information is pressure- or saturation-dominant. The *pressure solution* is believed to be related to compartmentalization in the reservoir, and the *saturation solution* is believed to be the source of information for the hydraulic sand connectivity illumination. Therefore, an interpretation approach is used to interpret pressure- and saturation-anomalies in frequent time-lapse seismic, using all available sources of data. Then, a pressure-anomaly map is utilized for locating faults and compartments. The resulting map is further integrated with well-pressure data to calculate the transmissibility multipliers for evaluated faults and compartments. Next, the SCA is calculated from repeated time-lapse seismic responses. By linking the well data and the SCA map, a data-driven relationship is established between the connectivity attribute and the transmissibility. A probabilistic approach is then proposed to capture the relationship and the uncertainty attached to that relationship. The resulting probability function is used in a stochastic conditional simulation to perform the transmissibility estimation guided by the SCA in the field.

CHAPTER 7: CONCLUSIONS AND RECOMMENDATIONS FOR FUTURE RESEARCH

Overview

In this thesis, the methodologies for estimating connectivity properties (permeability, transmissibility and transmissibility multipliers) from time-lapse seismic data were developed. In addition, a fast-track history-matching method was introduced. The intention of these approaches was to integrate time-lapse results with reservoir-engineering tools that were successfully tested on synthetic and field data. This chapter presents a summary of the results and the main concluding remarks of this thesis. Recommendations for further improvements and application of this work are also addressed.

7.1 Conclusions

In this thesis, tests performed on synthetic and observed 4D seismic demonstrated the promise of the proposed techniques for the delivery of quantitative information on connectivity properties (permeability, transmissibility and transmissibility multipliers). The 4D-seismic attribute can be directly employed to estimate these properties, and then they can be further incorporated into the reservoir model. In other words, despite the presence of uncertainties due to the following: seismic acquisition and processing artefacts; the difficulty of time-lapse repeatability; differentiating the time-lapse signal from noise; and, finally, non-uniqueness in the inversion methods, it is possible to estimate permeability from time-lapse seismic, feed the simulation model with this estimated permeability, and reduce the production misfit value in an effective way. However, one may argue that the techniques which use time-lapse seismic attributes are only capable of locating large-scale reservoir heterogeneity. Even if one assumes that this is true, the 4D-seismic data would be the only source of permeability information that covers the entire reservoir *between* wells – as compared with most engineering techniques, which are localized and restricted to measurements at wells. *In conclusion, 4D seismic is the only available* in situ *source of information in the inter-well region that has proven its ability to provide information for permeable pathways, at a fairly good areal resolution*. In the following paragraphs, a brief summary is given of the results from each chapter that contributed to the concluding remarks detailed above.

In Chapter 1, a literature survey on the available permeability-estimation methods in the oil industry showed that all of the engineering tools are restricted to measurement *around* the wells. In the seismic domain, although 3D seismic can provide areal coverage, estimating permeability from this sort of data is still ambiguous and controversial. However, two methods (Vasco, 2004; MacBeth and Al-Maskeri, 2006) have reported 4D seismic to be a successfully tested means of imaging permeability.

In Chapter 2, the direct-transform method proposed by MacBeth and Al-Maskeri (2006) was analysed and tested critically on synthetic and real field examples. Several modifications were also proposed – in particular, to control the instability in the Laplacian calculation. The modified formula was termed the Seis2perm method.

In Chapter 3 of this study, the estimated permeability in Chapter 2 was put forward to update the reservoir model. Issues regarding the lack of resolution in the context of permeability estimation using time-lapse were addressed. A solution was proposed to include depth-averaged seismic products (a 2D map of values) in a 3D permeability framework of the simulation model. It was shown that, despite the uncertainties attached to permeability-estimation methods and the uncertainties in transferring properties into the simulation model, this approach could provide a very good method of history matching as compared with traditional techniques. This approach was called the fast-track history-matching (FTHM) approach. As a complement to the FTHM approach, a conventional gradient-based history-matching approach was used on the same dataset. The significance of FTHM versus the conventional method was analysed, and it was concluded that FTHM is an effective and rapid updating method. In addition, FTHM is considered to be a faster approach than full seismic history matching where the prediction of 4D seismic is cumbersome.

In Chapter 4, uncertainties in the Seis2perm method were investigated. A few methods were attempted in order to reduce uncertainties such as the tuning effect, calibration wells and multi-attribute analysis. Eventually, the uncertainty attached to the estimation was quantified.

In Chapter 5, the seismic-connectivity attribute and the Laplacian attribute were decomposed from the Seis2perm method in order to estimate hydraulic sand connectivity and barrier connectivity respectively. This approach was proposed as an alternative to the permeability estimation method in previous chapters in which numerical instabilities in permeability result are experienced. The introduced methods were tested on a number of synthetic models. Synthetic studies showed how employing frequent time-lapse seismic can contribute effectively to the mapping of connectivity.

In Chapter 6, the understanding gathered from theoretical derivations and modelling in Chapter 5 was applied to real field data. Transmissibility and transmissibility multipliers were calculated using integrated approaches.

7.2 Recommendations for further improvements and future applications

This thesis has focused on the integration of the seismic- and reservoir-engineering domains. The broadness of the subject and the fact that time-lapse seismic is a rapidly advancing technology mean that the coverage offered by this thesis cannot be complete, and that the problems and solutions cannot be dealt with in great detail. The integrated approach proposed in this thesis consists of three main stages for tackling problems, listed as:

(a) 4D-seismic-data treatments for property estimation;
(b) integration of 4D seismic with the engineering domain;
(c) updating and history matching.

Below, the recommendations for future work in each category mentioned above are as follows.

7.2.1 4D-seismic-data treatments for property estimation

The methodologies presented in this study are new, and the results of estimating permeability, transmissibility and barrier transmissibility from 4D seismic are encouraging. However, in order to achieve a more robust and accurate outcome, certain challenges have to be carefully addressed in transferring reservoir permeability from the seismic domain to the reservoir-simulation domain, in areas such as the following.

(a) Treatment of seismic noise and tuning: in the methods introduced, the 4D-seismic attribute was transferred directly into estimates of reservoir permeability. However, an attempt was made to eliminate the 4D-related noise outside the sand channel via multiplying by the 3D seismic in the seismic-connectivity attribute. Also, the tuning effect in the 3D-seismic response was removed using the Connolly method. However, the tuning effect also exists in the 4D-seismic response. In addition, distinguishing the noise from the signal in 4D seismic still seems to be a challenging issue. In order to improve the result, the nature of the noise and tuning effect has to be defined properly and removed to enhance the signal generated by permeability. Hence, any enhancement of accuracy in the permeability result is highly dependent on developments related to the removal of the noise associated with the signal.

(b) Pattern recognition and multi-attribute analysis: in this work, different attributes were tested to identify the distributions of the sands and to identify faults. However, the most appropriate attribute that was sensitive to the desired property attribute was selected in most of the analysis (except in Chapter 4, where the attributes were combined together). An enhanced result will be produced from combining attributes (to determine optimum attribute) which are sensitive to relative geological features. Multi-attribute analysis is usually performed using pattern-recognition methods. One example of pattern-recognition techniques is a neural network, where a set of input parameters is related to the output by a transformation that is encoded in the network weightings. Stacking the attributes (employed in Chapter 4) and principal-component analysis (PCA) are also rapid alternatives that can be used. Based on the analysis in this work, it is suggested that multi-attribute analysis should be included as part of the workflow in estimating any reservoir property (including permeability) from seismic attributes.

(c) Seismic cube or seismic map as an input: the methodologies presented here are based on seismic-attribute maps. A natural extension of this work will be the estimation of $K/T/T_f$ in 3D volumes, using the volumes of the seismic attributes. Several key issues in selecting the appropriate reservoir candidate have to be addressed to achieve the best result:

(1) High seismic resolution has to be chosen for the 3D volume estimation of a property.
(2) The less vertical a heterogeneous reservoir, the less uncertainty will be introduced in the 3D volume of the seismically estimated property. Also, a thicker reservoir in which flow can be approximated in 2D areal dimension with a negligible gravity effect is preferred.
(3) The availability of data with a good vertical resolution (such as well logs to constrain the seismic data) is also important.
(4) The use of impedance inversion cubes as basic layer attributes instead of reflectivity attributes is highly recommended.

(d) Frequent time-lapse seismic: the advantage of using frequent time-lapse seismic was successfully applied in this thesis. The increased benefit from time-lapse seismic in interpretation and subsequent integration encourages the use of frequent time-lapse seismic in all 4D seismic analysis.

*(e) Permeability/transmissibility/transmissibility-multiplier (K/T/Tf) estimation: t*he simplicity and practicality of the methods introduced in this thesis for $K/T/T_f$ estimation increases its capability to be applied quickly in different fields and adopted easily for certain situations.

(1) Permeability estimation: in the methods introduced in this thesis, it was preferred to infer permeability either from pressure change or saturation change. An alternative solution to include the trade-off between pressure- and saturation-variation, can be to incorporate both 4D changes to evaluate the permeability in one single formula. The mathematical development is performed for this type of approach in Appendix F.

(2) Transmissibility-multiplier estimation: the correlation of BHP between injection-production pairs is utilized in Chapter 6 to estimate T_f for the faults imaged by time-lapse seismic signatures. This has provided an appropriate initial T_f value for history-matching purposes and can be corrected automatically in an optimization process. However, it is important to account for the spatial correlation between all the wells in the field, in order to achieve more accuracy in the calculations. Applying a type of superposition principle between the wells can address this issue.

(3) Transmissibility estimation: the saturation solution to estimate transmissibility from SCA (introduced in Chapters 5 and 6) is implemented in the Schiehallion field, where the 4D-seismic anomalies are mainly pressure-dominant signal. The saturation-dominant 4D-seismic data in the Heidrun field and the Nelson field (see Figure 7.1) appear to be an appropriate candidate for implementing this method. The application of this method to these field examples is suggested.

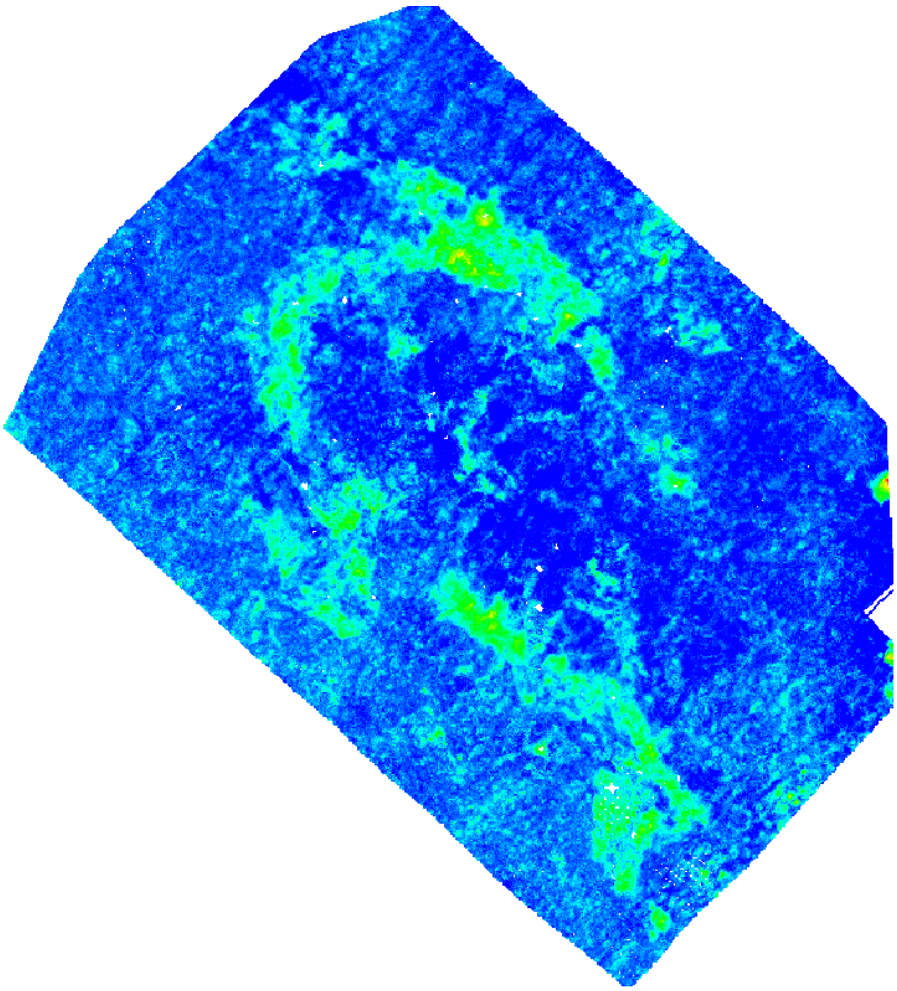

Figure 7.1: *Time-lapse attribute in the Nelson field for the 2000–1990 surveys averaged from the top to the base horizon. Green to red indicates water movement, while blue indicates no change (after Stephen et al., 2007).*

7.2.2 Integration of 4D seismic with the engineering domain

The integration of different disciplines and techniques in order to estimate reservoir properties would increase the reliability of the estimations. Some possible integrations with 4D seismic are described below.

(a) Integration of the 2D map of permeability with the 3D simulation model: if the true permeability variation is vertically very heterogeneous in the reservoir, the derived 2D permeability map will only sample areal variations. Therefore, some means of extracting the appropriate information from the fine-scale areal distribution is necessary. In the method used in Chapter 3, a 2D permeability map was integrated with the vertical heterogeneity of the simulation model. This method can also be adopted to be used in a

geostatistical framework in which the permeability values in a column of a reservoir are conditioned to the averaged permeability value in a 4D-seismic-estimated map. Doyen *et al.* (1997) proposed this type of approach to tackle the resolution problem from the seismic to the simulation domain. The advantage of using geostatistics is that it provides more control over the uncertainty attached to the final permeability map. Hence, one possible extension of the method introduced in this thesis is for it to be adopted in a stochastic framework.

(b) Integration with material balance: material-balance models are developed early in the life of the field, in order to better understand the connectivity within the field and to analyse the simulation behaviour. The distinct regions of compartmentalization in the field are recognized in the material-balance analysis. As a result, material-balance estimates of the compartment can be easily integrated with a 4D-seismic compartment interpretation. This can serve as a possible development for the compartment identification method proposed in this thesis.

(c) Integration with well testing: generally, a well test is a period of time during which the rate/pressure of a well is recorded in order to estimate the well or reservoir properties or to provide the reservoir productivity. Reservoir engineers perform transient pressure tests throughout the life of the field. These tests can ascertain the existence and impact of reservoir heterogeneity, but do not permit the exact location of discontinuities or small-scale heterogeneity features. However, 3D seismic and 4D seismic can provide information about the internal reservoir heterogeneity in order to define the internal geometry of the reservoir. As a result, integration of seismic domain and well-test analysis serves as an effective approach for obtaining the reservoir heterogeneity. This is another type of integration that appears to be promising.

(d) Integration with the well log (calibration): Integration of the well log with seismic attributes is a very common practice in oil industry. However, seismic attributes can be important quantitative predictors of reservoir properties when used correctly in reservoir-characterization studies. When using correlation between seismic attributes and well-logged data, it is crucial to consider: (1) how the seismic data are processed; (2) the physical basis of the correlation; (3) the possibility of false correlations when the number of well data are few, and/or when the number of attributes are many (see

Kalkomey, 1997; Chambers and Yarus, 2002 for details on false correlation); (4) when using multiple attributes, the attributes must provide independent information about the reservoir property; and (5) although, easily applied, linear regression is not recommended because the results will be biased. Geostatistical methods such as collocated cokriging and sequential Gaussian simulation can offer attractive means to integrate seismic attribute and well information, without an estimation bias, and to account for the scale (support) differences between the two data types.

7.2.3 Simulation and history matching

The final aim of estimating the reservoir properties ($K/T/T_f$) from 4D seismic is to feed the simulation model with realistic and geologically constrained information with fairly good spatial resolution. Using such approaches, it is hoped to tackle the non-uniqueness problem in the history-matching process and reduce the misfit function. The techniques introduced in this thesis (FTHM) have proved that 4D seismic has been successful in fulfilling such an intention. However, there are still many improvements that can be pursued to enhance the simulation and history-matching workflow (see below).

(a) Updating simulation using estimated transmissibility and transmissibility multipliers: in Chapter 6 of this thesis, the sequence of time-lapse seismic data is used to estimate transmissibility and transmissibility multipliers for the Schiehallion field. The update of reservoir model with the new dataset of transmissibility of barriers and transmissibility across the reservoir is recommended. It is hoped that this gives a better match between the reservoir simulation and the observed 4D-seismic effects. The integration of the interpreted 4D seismic and the production data in barrier evaluation and sand connectivities can provide the support for possible infill opportunities and reservoir-management decisions**.**

(b) The choice of reservoir update: the models are generally built in a well-defined workflow, illustrated in Figure 7.2. 3D-seismic and well data are used to first identify the structure of the field and then to populate it with facies or rock types. These are further related to the petrophysical properties, again obtained from the wells. The geomodel is up-scaled to be used by the engineer who carries out the history matching. Predictions of well behaviour from simulations are compared with observed data and, in

assisted history matching, a misfit calculation is made. Quantitative or qualitative comparisons can be used to update the simulation model. 4D seismic can contribute to obtaining the facies, to estimating the petrophysical properties in the geological model, and update the reservoir properties in the reservoir-simulation model. Therefore, there are three ways in which 4D seismic can be used to update the reservoir model (i.e. updating the facies and petrophysical properties in the geological model and the reservoir properties in the simulation model).

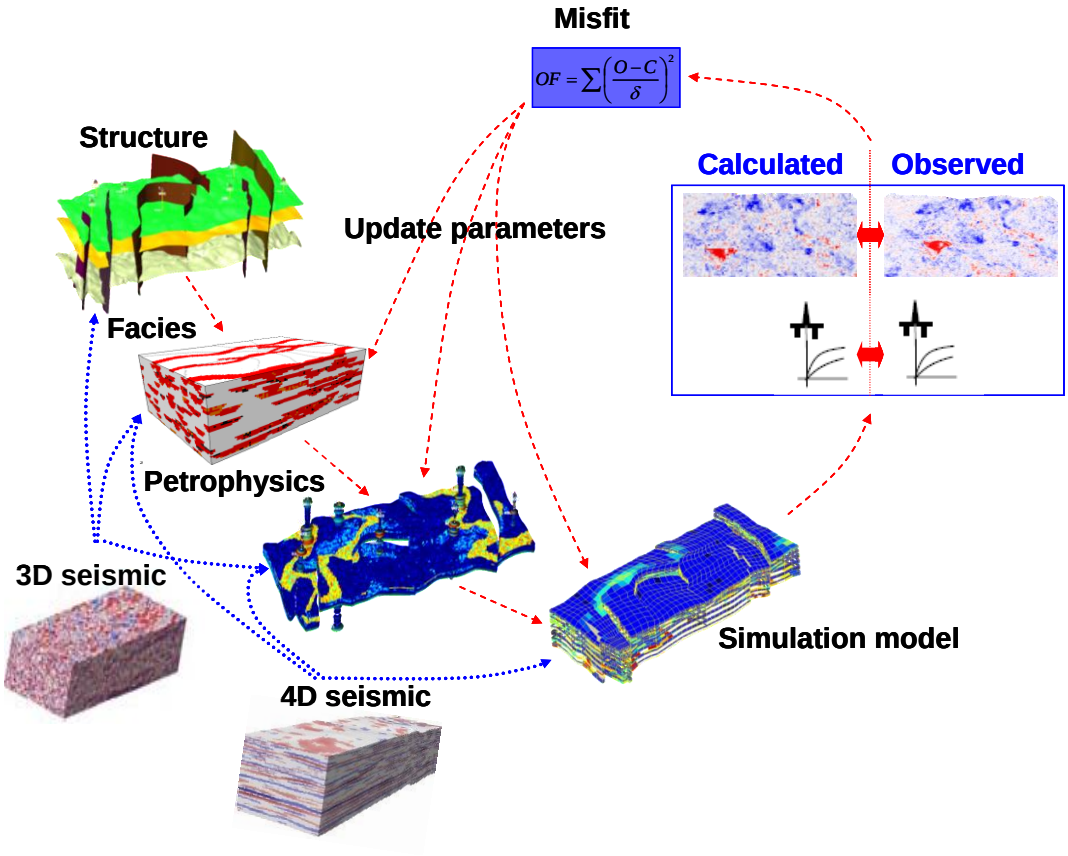

Figure 7.2: *There are three ways in which 4D seismic can be used to update the reservoir model: updating the facies, updating the petrophysical properties in the geological model, and updating the reservoir properties in the simulation model.*

(c) Performing FTHM and SHM simultaneously: the updating technique introduced in Chapter 3 can be used in conjunction with the seismic history-matching method to update the reservoir model. Combining the two methods will reduce the non-uniqueness in the seismic-history inversion, and can quickly provide a reduced misfit between the observed and the predicted data (Figure 7.3).

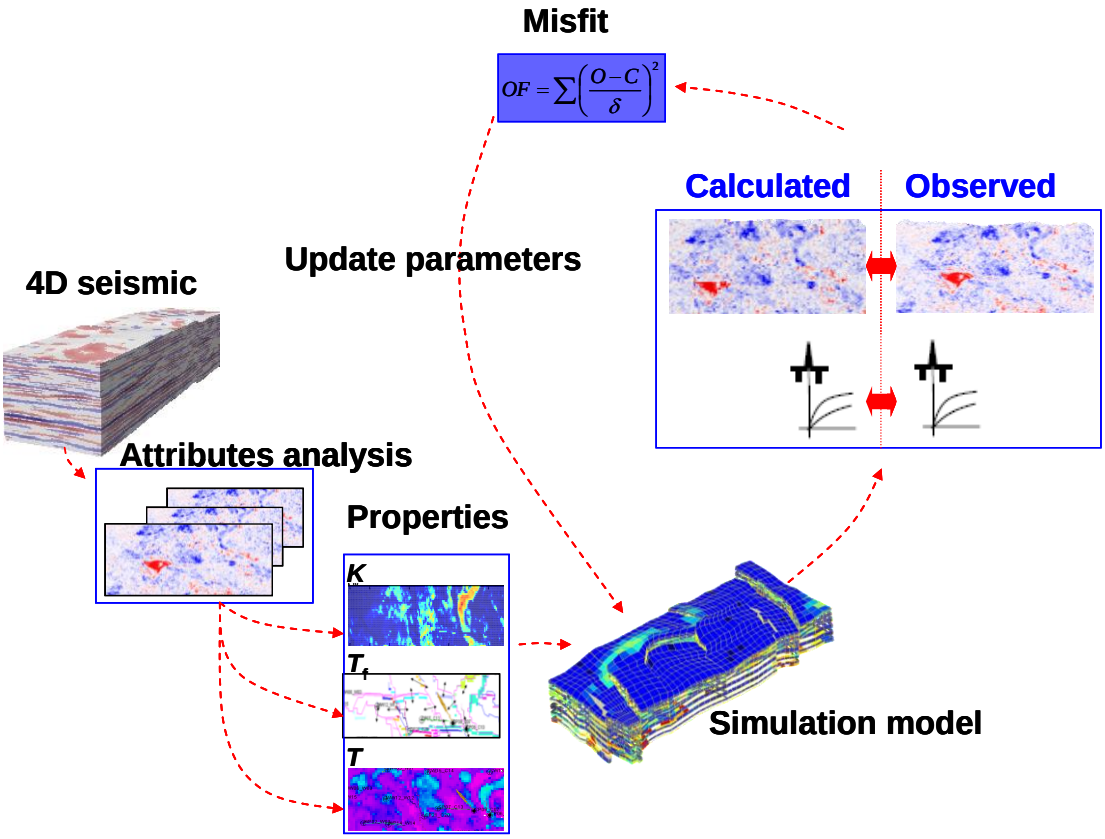

Figure 7.3: *Combining the FTHM and SHM methods will reduce the non-uniqueness in seismic-history inversion, and can quickly provide a reduced misfit between the observed and predicted data.*

(d) Future prediction independent of the simulation model: in an innovative way, 4D-seismic data might be used to directly predict behaviour in the near future or understand current conditions without the use of a simulator. From repeat seismic surveys, it is possible to derive saturation- and pressure-changes for a number of time-steps. With a suitable approximation to the flow equations, one may be able to step forward in time with a prediction of the reservoir behaviour, and then obtain a prediction of the seismic behaviour. A possible choice for modelling the flow in this context is using streamlines that are estimated based on the time-lapse saturation profiles.

(e) Multi-objective optimization: multiple, often conflicting, objectives arise naturally in most real-world optimization scenarios. These also include flow-simulation optimization, in which objective functions are defined not only for different production parameters (GOR, BHP, water-cut, observed 4D seismic, etc.), but also objective functions for these parameters at different wells. As evolutionary algorithms possess

several characteristics that are desirable for this type of problem (i.e. conflicting objectives), this class of search strategies has been used for multi-objective optimization (Collette and Siarry, 2003). This approach to history matching is recommended for any future development in history matching with regard to the current study, particularly when an additional objective function for 4D seismic is defined in the optimization process.

(f) Pressure/saturation separation: it is necessary in all 4D-seismic studies, both for inversion to reservoir properties and also for forward modelling in seismic history-matching, to separate the pressure effects from the saturation effects. Generally, saturation is a high-frequency component of the 4D-seismic signal, whereas pressure is the low-frequency component, unless the field is very compartmentalized. 4D seismic is becoming more quantitative in providing changes in pressure and saturation, and it is a very helpful tool for reservoir engineers to assess the production progress of the field by comparing the result of the simulation model with the time-dependent pressure- and saturation-estimates in the reservoirs. The error bars for the current pressure/saturation inversion methods are still high; however, any advancement in this subject would have a major impact on seismic history-matching and also inversion of 4D seismic to reservoir properties via pressure- and saturation-changes.

7.3 Uncertainty quantification and the role of geostatistics

'Different types of uncertainties, measurement errors and approximations associated with idealistic assumptions of the medium with respect to governing physical laws, make the theoretical equations less reliable. Even if we have to substantially rewrite the book on reservoir simulation and geophysical imaging, we do need to move to stochastic methods' (Aminzadeh and de Groot, 2004).

Interpretation of time-lapse seismic is impeded by acquisition and non-repeatable noise. However, it is not only the data, but also the physical laws, that are uncertain. The inversion methods for reservoir properties are not straightforward, and suffer from the problem of non-uniqueness. Therefore, it is crucial to decide on the risk that is taken, based on the estimated properties. Hence, the impact of measurement and inversion errors on the quality of the reservoir-property estimation has to be analysed.

Deterministic approaches supply simple and rapid means to evaluate reservoir properties. The uncertainty of the input parameters and their influence on the output can be easily quantified. Faster deterministic inversion approaches, with less-quantified uncertainty, are most commonly used when, for practical purposes, we need to have a quick idea of what a reservoir property looks like. However, the level of non-linearity and uncertainty sometimes makes it difficult to generate a single model of heterogeneity. In order to have more control over uncertainty, the preferred method is a stochastic method. Stochastic (or geostatistical) techniques produce multiple equi-probable results that provide an assessment of the uncertainties, and they are ideally suited for integrating non-seismic information in the inversion process.

The general theory has a simple (probabilistic) formulation and applies to any kind of inverse problem, including linear as well as strongly non-linear problems. The theory explains how an a priori probability distribution is transformed into an a posteriori probability distribution, by incorporating a physical theory (relating the model parameters to some observable parameters) and the actual result of the observations (with their uncertainties). The inverse problem is set up based on conditional probabilities and Bayes's theorem. Therefore, in summary, due to the uncertainty associated with seismic and its products, using a probabilistic approach that provides an appropriate basis for quantifying the uncertainty attached to the estimated reservoir property and also is very well suited for integration with other sources of property measurement, is highly recommended.

On the other hand, the appropriate geostatistical method has to be chosen for obtaining certain properties. Traditionally, geostatistical techniques capture geological continuity through a variogram. Since the variogram describes the level of correlation between just two locations, it is not able to model continuous and sinuous patterns such as sand channels or fractures in the reservoir. These features are usually desirable attributes to be estimated from seismic methods. Multiple-point statistics are a suitable method for modelling these geological features (Journel *et al.*, 1993), and come highly recommended.

7.4 Economic evaluation

Apart from the technical aspect, economic evaluation should be considered as part of a 4D-seismic analysis to encourage the acceptance and allow increased benefit from time-lapse seismic data. Economic evaluation is crucial to allow decision-makers in the oil industry to decide on a 4D-seismic acquisition. The success of 4D seismic depends on the value that it offers versus its cost. The relative cost of 4D seismic compared to well work (well work includes recompletion, sidetrack and a new well) in different environments, such as on land, on the marine shelf, and in deep-water fields, has to be analysed and justified before shooting any repeat surveys. The cost ratio of 4D seismic per well ranges from 5 to 35% on land, 10 to 50% in marine-shelf environments, and 5 to 10% in deep water (Lumley and Behrens, 1998).

The value of 4D seismic is also depends on the type of information that it offers for a specific reservoir. 4D seismic does not provide the same reunited value in different reservoirs. Figure 7.4 shows the curve known as an *S-curve*. The success of a 4D project is dependent not only on having a sufficiently large signal to be observed over the 4D noise, but also on the ability to quickly interpret that signal in terms of sweep patterns, fluid pressure, overburden stress, fault transmissibility, stratigraphic reservoir distributions, etc. The maturity *S-curve* is used for different signal types (Staples *et al*., 2006). The position on the maturity curve represents a combination of the signal strength and the complexity of interpreting the signal to make conclusions about reservoir conditions. A reservoir may lie in more than one category – e.g. a reservoir may show an easily interpreted water-flood signal and a more complex depletion signal.

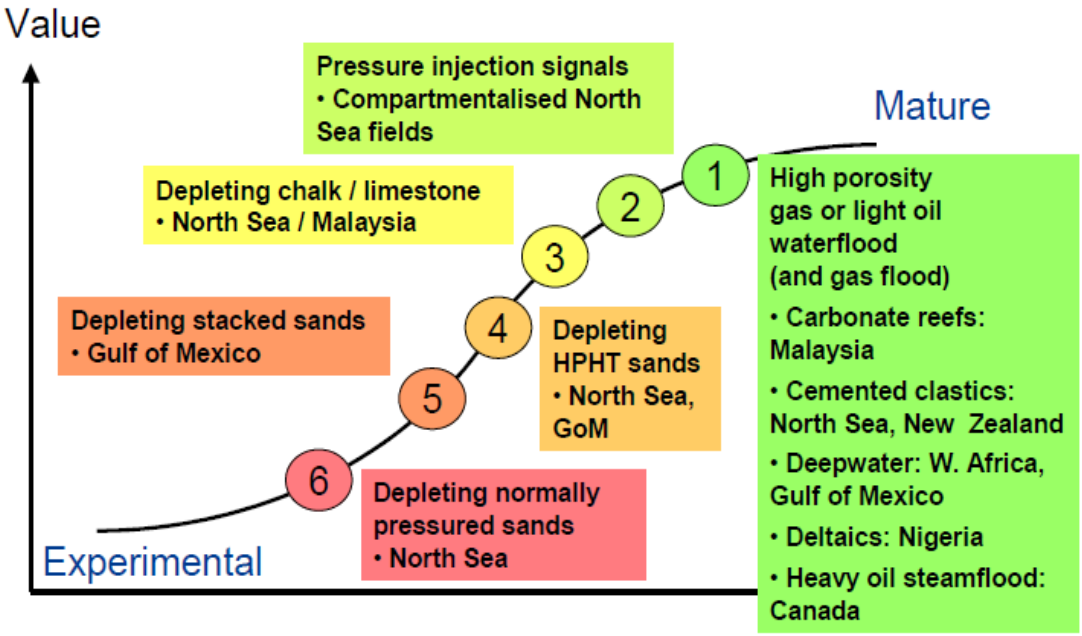

Figure 7.4: *A maturity S-curve for different 4D applications (after Staples et al., 2006).*

Appendix A: Mathematical modelling of porous media (the simulation governing equation)

Permeability-estimation methods from time-lapse pressure data are derived and simplified from the governing equation of fluid flow in reservoir simulation. This equation is considered as the starting point in the derivation of these methods. The governing equation comes from mathematical modelling of the fluid flow in porous media. In order to mathematically model the fluid flow in porous media, three laws are combined:

1. mass balance (the continuity equation);
2. the fluid-flow equation in porous media (Darcy's equation);
3. the equation of state (type of fluid: incompressible, compressible, or a gas).

According to the law of conservation of mass, the mass (m) that flows in a system over time, Δt, must either leave the system or accumulate within the system. Mathematically, the mass balance for a system is written as follows: out

$$m'_{\text{in}} - m'_{\text{out}} = \frac{m\big|_{t+\Delta t} - m\big|_{t}}{\Delta t} \tag{A.1}$$

where m' is the mass flow rate and m is mass at time t and $t + \Delta t$. The m can be written as a function of density (ρ) and the volumetric flow rate (or Q):

$$m' = \rho Q \tag{A.2}$$

and can also be written as the product of the pore volume of the block by density:

$$m = (\varphi V)\rho = \rho\varphi \mathrm{d}x\mathrm{d}yh \tag{A.3}$$

where dx and dy are lengths in the x and y directions, respectively, and h is the thickness of the control volume (see Figure A.1). By substituting Equations A.2 and A.3 in Equation A.1:

$$\left[(Q\rho)_{\text{in}} - (Q\rho)_{\text{out}}\right]_x + \left[(Q\rho)_{\text{in}} - (Q\rho)_{\text{out}}\right]_y = \frac{\left[(\varphi\rho)_{t+\Delta t} - (\varphi\rho)_t\right]\mathrm{d}x.\mathrm{d}y.h}{\mathrm{d}t} \tag{A.4}$$

Dividing through by dx.dy.h gives the following:

$$-\frac{\left[(Q\rho)_{\text{out}} - (Q\rho)_{\text{in}}\right]_x}{\mathrm{d}xA_x} - \frac{\left[(Q\rho)_{\text{out}} - (Q\rho)_{\text{in}}\right]_y}{\mathrm{d}yA_y} = \frac{\left[(\varphi\rho)_{t+\Delta t} - (\varphi\rho)_t\right]}{\mathrm{d}t} \tag{A.5}$$

where we have used the fact that dx.dy.h = dx.A_x and dy.dx.h = dy.A_y. The flow areas, A_x and A_y, divided by the Q's, give the Darcy velocity terms (e.g. $\rho u_x = \left(\frac{Q\rho}{A_x}\right)$), as follows:

$$-\frac{\partial(\rho u_x)}{\partial x} - \frac{\partial(\rho u_y)}{\partial y} = \frac{\partial(\rho\varphi)}{\partial t} \tag{A.6}$$

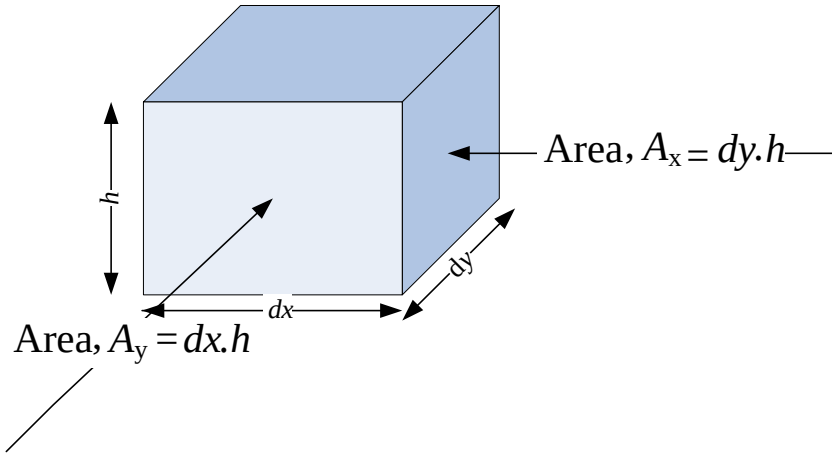

Figure A.1: *The 2D x/y grid, showing the control volume.*

This is the 2D mass-conservation equation. Clearly, this can easily be generalized to 3D by simply adding the z-flow term (for vertical flows, u_y), which is not of interest in this study. Darcy's law for a single phase in each direction of x and y is:

$$u_x = -\frac{K_x}{\mu}\left(\frac{\partial P}{\partial x}\right) \tag{A.7}$$

$$u_y = -\frac{K_y}{\mu}\left(\frac{\partial P}{\partial y}\right) \tag{A.8}$$

Replacing the Darcy velocities in Equation A.6 yields:

$$\frac{\partial}{\partial x}\left[\frac{k_x \rho}{\mu}\frac{\partial P}{\partial x}\right] + \frac{\partial}{\partial y}\left[\frac{k_y \rho}{\mu}\frac{\partial P}{\partial y}\right] = \frac{\partial(\rho\varphi)}{\partial t} \tag{A.9}$$

For a compressible fluid (water and oil), the density is equal to:

$$\rho = \rho_0 e^{C(P-P_0)} \tag{A.10}$$

where C is compressibility; ρ_0 is the initial density; ρ is the density at the desired pressure; P is the desired pressure; and P_0 is the initial pressure. By substituting Equation A.10 in Equation A.9 and simplifying the equation, Equation A.9 becomes:

$$\frac{\partial}{\partial x}\left[k_x \frac{\rho_0}{\mu}\left(\frac{\partial P}{\partial x}\right)\right] + \frac{\partial}{\partial y}\left[k_y \frac{\rho_0}{\mu}\left(\frac{\partial P}{\partial y}\right)\right] = C\varphi\frac{\partial P}{\partial t} \tag{A.11}$$

Equation A.11 is the pressure equation for a single phase. This equation is used in the Seis2perm method to convert the pressure change from 4D seismic to permeability. Neglecting the z term in above equation, the equation is only applicable for sheet-like reservoirs. On the other hand, it is suitable for 2D map attributes extracted from a time-lapse seismic cube. This equation can also be written in Laplacian notation as:

$$\nabla.\left(K\frac{\rho}{\mu}\nabla P\right) = C\varphi\frac{\partial P}{\partial t} \tag{A.12}$$

Conversely, the equation that Vasco (2004) used to invert permeability from pressure change is the two-phase flow equation, including the well term:

$$\frac{\partial}{\partial x}[k_x\lambda\left(\frac{\partial P_\Delta}{\partial x}\right)] + \frac{\partial}{\partial y}[k_y\lambda\left(\frac{\partial P_\Delta}{\partial y}\right) = Q_\Delta \tag{A.13}$$

where λ is the total fluid mobility expressing coexisting fluid phases in porous media, and Q_Δ is the source/sink term indicating how much fluid is injected or produced. Equation A.13 can be written in Laplacian notation as:

$$\nabla.(K\lambda\nabla P) = Q \tag{A.14}$$

Appendix B: Derivation of the Seis2perm method

Strictly speaking, the 2D areal simulation equation discussed in the previous section is valid for reservoirs that have thin oil rims or geological layering resembling sheets, with their thickness being small compared with their areal extent so that gravity terms are unimportant. Areal simulation may also approximate flow in thicker, laterally homogeneous reservoirs if vertical heterogeneity reduces inter-depth communication and prevents gravity slumping, leading to a uniform fluid-saturation profile. In addition if there is vertical equilibrium (vertical effects dominated by gravity segregation and high vertical permeability) 2D areal simulation of horizontal displacement processes can also be used to approximate the 3D solution by the use of pseudo-functions (Coats *et al.*, 1970). Here, the use of 2D simulation equations is considered a necessary approximation for the development of the desired method. However, the applicability of the final results to a particular reservoir must be evaluated on an individual basis in full consideration of the above.

The starting point is the single phase, 2D pressure equation for a compressible fluid with no well terms shown in Equation A.11. Working with the basic underlying assumption that the 4D-seismic signatures at each location in the top reservoir are a direct measure of the natural reservoir pressure, the seismic response can be used to determine the partial derivatives of pressure. By inserting values for φ, C_f and μ (assuming these to be relatively well determined), Equation A.11 provides a way of estimating the unknown permeability value in the coefficient terms. This scheme appears possible, as the spatial variation of effective porosity can be evaluated from the seismic, and the pressure functions $C_f(P)$ and $\mu(P)$ are known to be fairly invariant across the field.

To reformulate Equation A.11 as a transform for effective application of 4D seismic, a few simplifications are made. First, as the main permeability anisotropy is usually between the vertical and horizontal directions, $K_x = K_y$ is assumed. Therefore, information about K_x and K_y in pressure gradients in either the x or the y direction affects the pressure–time derivative in a similar way. By using the chain rule and the definition for compressibility, Equation A.11 can now be rewritten:

$$\varphi.c_{\mathrm{f}}.\mu\frac{\partial P}{\partial t}=K\left[\left\{\frac{\partial^2 P}{\partial x^2}+\frac{\partial^2 P}{\partial y^2}\right\}+c_{\mathrm{f}}.\left\{(\frac{\partial P}{\partial y})^2+(\frac{\partial P}{\partial y})^2\right\}\right] \tag{B.1}$$

The second derivatives in the right-hand side of above equation are much larger than the product of the compressibility and the squared gradient terms (primarily because the compressibility is much smaller in magnitude), and therefore they can be deleted from the equation. The 4D-seismic signature, ΔA, is assumed to be directly proportional to the reservoir pressure change, ΔP, for the pressure-dominated 4D-seismic case. This is a valid assumption for heavily compartmentalized reservoirs, particularly if gas is not coming out of solution, and there is no compaction in the reservoir. Therefore, the pressure change can be expressed by:

$$\Delta P=(\frac{\Delta P_{\max}}{\Delta A_{\max}}).\Delta A \tag{B.2}$$

where $\Delta P_{\max}$ is the maximum pressure change in the reservoir and $\Delta A_{\max}$ is the maximum time-lapse signature. Generally, the scaling constant (the term in brackets) depends on the rock physics, fluid physics and seismic-wave propagation. The desired pressure change corresponding to the difference between the repeat survey (at calendar time T_2), and the baseline survey (at calendar time T_1) is obtained by integrating the product of the pressure–time derivative, compressibility and viscosity on the left-hand side of (B.1) over time. Assuming a weak linear variation of the compressibility–viscosity product with pressure (which may be justified in the estimation of viscosity and compressibility in the case where the pressure fluctuations tend to invalidate assumptions upon which the final equation is derived):

$$\int_{T_1}^{T_2} C_{\mathrm{f}}(P)\mu(P)\frac{\partial P}{\partial t}\,\mathrm{d}t \approx C_{\mathrm{f}}\left(\overline{P}\right)\mu\left(\overline{P}\right)\Delta P \tag{B.3}$$

where $\overline{P}$ is the mean pressure of the two surveys. This in turn links the equation to the 4D signature:

$$C_{\mathrm{f}}\left(\overline{P}\right)\mu\left(\overline{P}\right)\Delta P = C_{\mathrm{f}}\left(\overline{P}\right)\mu\left(\overline{P}\right)\left(\frac{\Delta P_{\max}}{\Delta A_{\max}}\right)\Delta A \tag{B.4}$$

For a constant compressibility and viscosity, the left-hand side of Equation B.1 is directly proportional to the time-lapse signature. Integration of the second derivatives on the right-hand side of Equation B.1 gives the result for each (x,y) location in terms of an average pressure for the two surveys:

$$\int_{T_1}^{T_2}\left(\frac{\partial^2 P}{\partial x^2}+\frac{\partial^2 P}{\partial y^2}\right)\mathrm{d}t=\left(\frac{\partial^2 \overline{P}}{\partial x^2}+\frac{\partial^2 \overline{P}}{\partial y^2}\right)(T_2-T_1) \tag{B.5}$$

P can be written as $P_1+\frac{1}{2}\Delta P$, and the initial (pre-production) pressure, P_1, is assumed to be approximately spatially invariant, hence, P can be substituted by ΔP, and the link with the time-lapse signature can be established. Based on the analysis above, the final approximate expression for permeability can now be written in terms of the 4D-seismic signature:

$$K=\frac{c_f(\overline{p}).\mu(\overline{p})}{T_2-T_1}.\varphi(x,y)\left[\frac{|\Delta A(x,y)|}{\left|\frac{\partial^2(\Delta A(x,y))}{\partial x^2}+\frac{\partial^2(\Delta A(x,y))}{\partial y^2}\right|}\right] \tag{B.6}$$

which is independent of the seismic scaling factor in Equation B.2, due to cancellation in the equation.

Appendix C: Calculation of the Laplacian function

The Laplacian is a 2D isotropic measure of the second spatial derivative of the map values. Laplacian filters are derivative filters used to find areas of rapid change (edges) in images. Therefore, the Laplacian can be calculated using standard convolution methods with pre-specified filters such as the ones that are described below.

(a) Numerical central difference

The approximation of derivatives by finite differences plays a central role in finite-difference methods for the numerical solution of differential equations. Central difference approximation of the second derivative of P in the x direction is:

$$\frac{\partial^2 P(x)}{\partial x^2} \approx \frac{P(x+\Delta x) - 2P(x) + P(x-\Delta x)}{\Delta x^2} \tag{C.1}$$

and the second derivative approximation in the y-direction is:

$$\frac{\partial^2 P(y)}{\partial y^2} \approx \frac{P(y+\Delta y) - 2P(y) + P(y-\Delta y)}{\Delta y^2} \tag{C.2}$$

and finally, the Laplacian is calculated as:

$$\text{Laplacian} = \frac{\partial^2 P}{\partial x^2} + \frac{\partial^2 P}{\partial y^2} \tag{C.3}$$

(b) The Laplacian of the Gaussian (LOG)

As the Laplacian operator may detect edges as well as noise (isolated, out-of-range), it may be desirable to smooth the image first by convolution with a Gaussian kernel of width σ. The 2D LOG function with Gaussian standard deviation σ has the form:

$$\text{LOG}(x, y) = -\frac{1}{\pi\sigma^4}\left[1 - \frac{x^2 + y^2}{2\sigma^2}\right] e^{-\frac{x^2+y^2}{2\sigma^2}} \tag{C.4}$$

(c) Polynomial derivations

A polynomial function is a function that can be defined by evaluating a polynomial. First, a polynomial P of degree n is fitted to each row and column of data in order to approximate the data points in the x and y directions with a function:

$$P(x) = P_1 x^n + P_2 x^{n-1} + ... + P_n x + P_{n+1} \tag{C.5}$$

$$P(y) = P_1 y^n + P_2 y^{n-1} + ... + P_n y + P_{n+1} \tag{C.6}$$

Next, the analytical solutions for the second derivatives in the *x* and *y* directions are computed for the fitted functions:

$$D_x P(x) = P'(x) = \lim_{\Delta x \to 0} \frac{P(x + \Delta x) - P(x)}{\Delta x} \tag{C.7}$$

$$D_x{}^2 P(x) \approx P''(x) = \lim_{\Delta x \to 0} \frac{P'(x + \Delta x) - P'(x)}{\Delta x} \tag{C.8}$$

Similarly, the second derivatives in the *y* direction are calculated, and finally the Laplacian is computed:

$$\text{Laplacian} = D_x{}^2 P(x) + D_y{}^2 P(y) \tag{C.9}$$

(d) Divergence of the gradient

Gradient (or grad) is a vector operation, as follows:

$$\nabla = \frac{\partial}{\partial x} i + \frac{\partial}{\partial y} j \tag{C.10}$$

where *i*, *j* and *k*, are the unit vectors which point in the *x*, *y* and *z* directions, respectively. The gradient operation can be carried out on a scalar field. Divergence (or div), is the dot product of the gradient operator, and acts on a vector to produce a scalar. The operator is denoted as follows:

$$\nabla . = \left(\frac{\partial}{\partial x} i. \quad \frac{\partial}{\partial y} j. \right) \tag{C.11}$$

So, divergence of gradient, known as the Laplacian operator, is given by:

$$\nabla . \nabla P = \left(\frac{\partial}{\partial x} i. \quad \frac{\partial}{\partial y} j. \right) \begin{pmatrix} \frac{\partial}{\partial x} i \\ \frac{\partial}{\partial y} j \end{pmatrix} = \frac{\partial^2}{\partial x^2} i.i + \frac{\partial^2}{\partial y^2} j.j = \frac{\partial^2}{\partial x^2} + \frac{\partial^2}{\partial y^2} \tag{C.12}$$

Appendix D: Permeability averaging techniques

Effective permeability or equivalent permeability is defined as the permeability of a single homogeneous cell which gives rise to the same flow as the fine-scale model when the same pressure gradient is applied (Cardwell, 1945). The resulting permeability accounts for the effects of heterogeneity. It is believed that particular problem of estimating effective permeability needs to be approached from fluid dynamical point of view. As the result, for n cells, each have the thickness, h_i, length, L_i, and permeability, k_i, the following averaging methods are used depending on behaviour of flow system:

a) For the flow parallel to uniform layers, the arithmetic average is used:

$$K_{H\,sim} = \frac{\sum_{i=1}^{n} h_i k_i}{\sum_{i=1}^{n} h_i} \tag{D.1}$$

b) For the flow across uniform layers, the harmonic average is used:

$$K_{H\,sim} = \frac{\sum_{i=1}^{n} L_i}{\sum_{i=1}^{n} \frac{L_i}{K_i}} \tag{D.2}$$

c) For the flow through random permeability distributions, the geometric average is used:

$$K_{H\,sim} = \frac{\sum_{i=1}^{n} h_i Ln(k_i)}{\sum_{i=1}^{n} h_i} \tag{D.3}$$

Appendix E: Removing the tuning effect in the NTG calculation for the Schiehallion field

The tuning effect is a constructive or destructive interference of waves from closely spaced events or reflections. At a spacing of less than one-quarter of the wavelength, reflections undergo constructive interference and produce a single event of high amplitude (see Figure E.1(a)). At a spacing greater than that, the event begins to be resolvable as two separate events. The tuning thickness is the layer thickness at which two events become indistinguishable in time, and knowing this thickness is important in order to interpret thin reservoirs. Apparent thickness is the time separation between zero crossings picked at the top and base of the reservoir. For large intervals, apparent thickness is the same as true thickness, so seismic NTG is equal to true NTG, but, for thin reservoirs, the apparent thickness converges to a minimum value (greater than true thickness) as the reservoir becomes thinner, while the average map attribute, measured between the picks shows a tuning response (see the zoomed-out box in Figure E.1(b)).

To correct this effect, the scheme proposed by Connolly (2007) for net pay estimation is adopted in order to estimate NTG between two seismic picks made on the zero-crossing of coloured inversion seismic data. Band-limited impedance can be obtained from coloured inversion. The detuning procedure of band-limited impedance starts with picking the top and base of reservoir on zero-crossings of band-limited impedance data. Figure E.2 shows a section through the 1996 pre-production seismic in the Schiehallion field for a coloured inversion dataset. The T31a reservoir unit has been picked on the zero-crossings at the top and bottom. The upper reservoir unit is mostly far enough away not to affect the amplitudes of the lower unit, and so it adheres to the requirement that the reservoir must be isolated for this method. Figure E.3(a) shows the RMS average attribute extracted between the top and base of the T31a reservoir. The time-thickness computed between the top and base of the reservoir is also displayed in Figure E.3(b).

Figure E.4 illustrates successive stages of the detuning process. In order to apply detuning correction to an average attribute, it is required to estimate the wavelet prior to

detuning the curve calculation. The wavelet is statistically estimated from the seismic data (Figure E.5).

Based on the estimated wavelet, a trapezoidal filter 5-10-50-60 extracted from the seismic volume, is designed to simulate the wedge and therefore model the tuning response (see Figure E.4). The wedge is assumed to have an NTG equal to unity. The average band-limited impedance for the wedge is calculated. The average band-limited impedance shows a tuning effect, as illustrated in Figure E.4(b); therefore its curve is referred to as the tuning curve. The modelled tuning curve shown in red stars in Figure E.4(b) is superimposed on top of the envelope points for a real data cross-plot (a cross-plot of the average RMS attribute plotted against the apparent thickness). First, this provides a check on the data quality by ensuring that the top of the envelope has a similar shape to the modelled response. Inspection of the data shows that outliers above or to the right of the curve are mostly caused by mis-picks. Second, this presents an initial self-calibration of the data, with the modelled response of wedge having an NTG equal to one. The points in the top ‘cloud’ have a seismic NTG of about one, and lower points have proportionally lower seismic NTG values. The modelled average band-limited impendence is showing a tuning effect; therefore, it cannot be directly transferred to NTG values. However, if the curve is multiplied by its reciprocal, then it will be independent of the apparent thickness and show the correct NTG equal to one; in other words it will be transformed to a horizontal line.

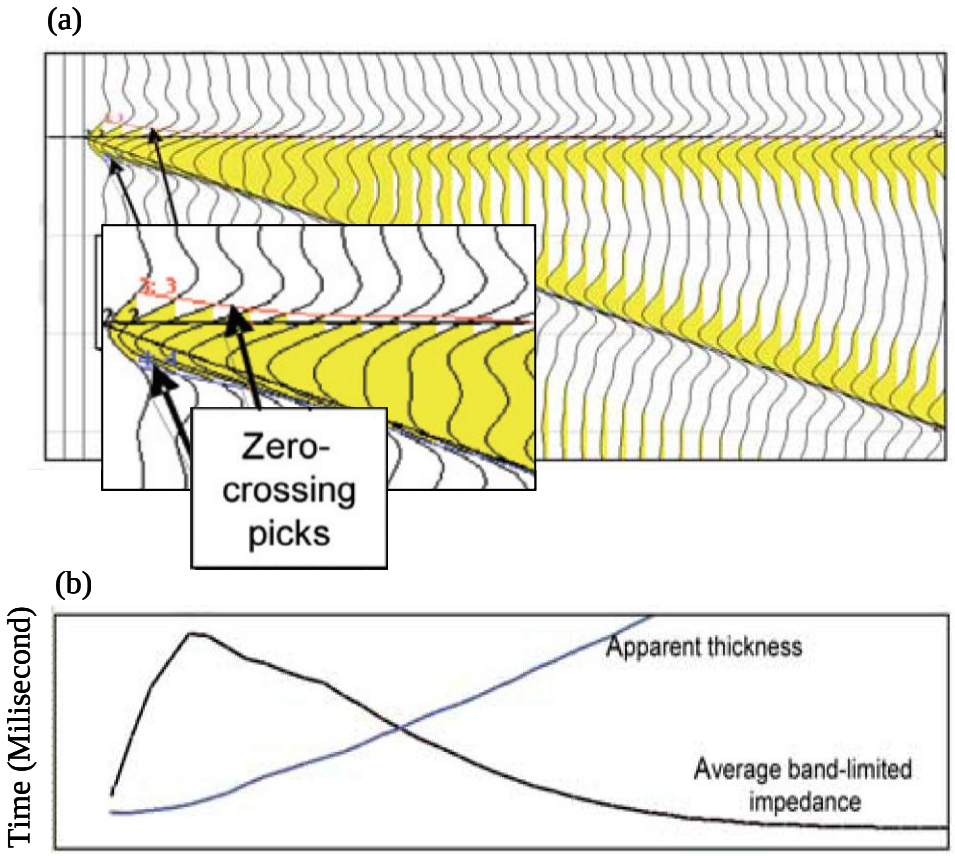

Figure E.1: *(a) Wedge model consisting of a wavelet convolved with a thickening boxcar impedance profile showing the tuning effect, and (b) the apparent time thickness is the time separation between the top and base reservoir horizons picked along zero-crossings of coloured inversion seismic data (after Connolly, 2007).*

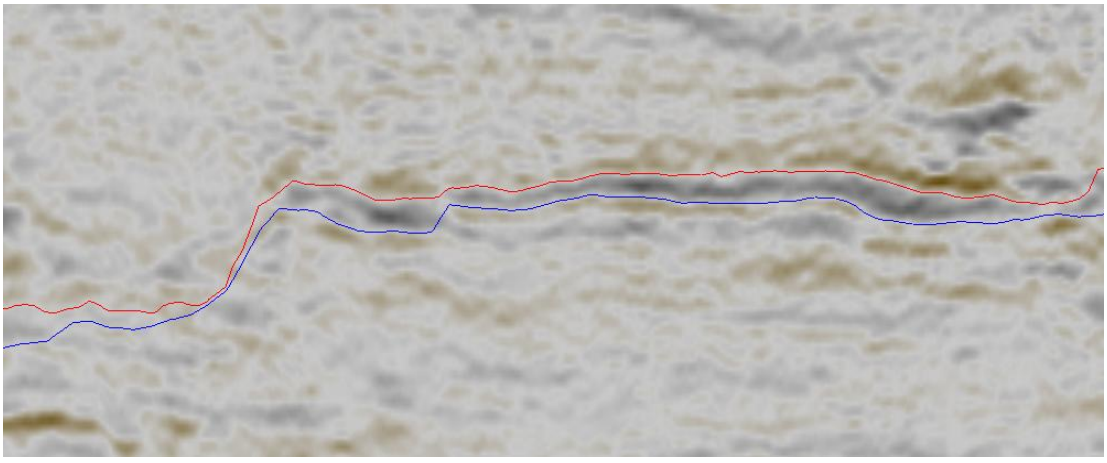

Figure E.2: *Seismic section through the pre-production 1996 base-line volume in the Schiehallion field: band-limited impedance obtained using coloured inversion. The T31a reservoir unit has been picked on the zero-crossings of the tops and bases.*

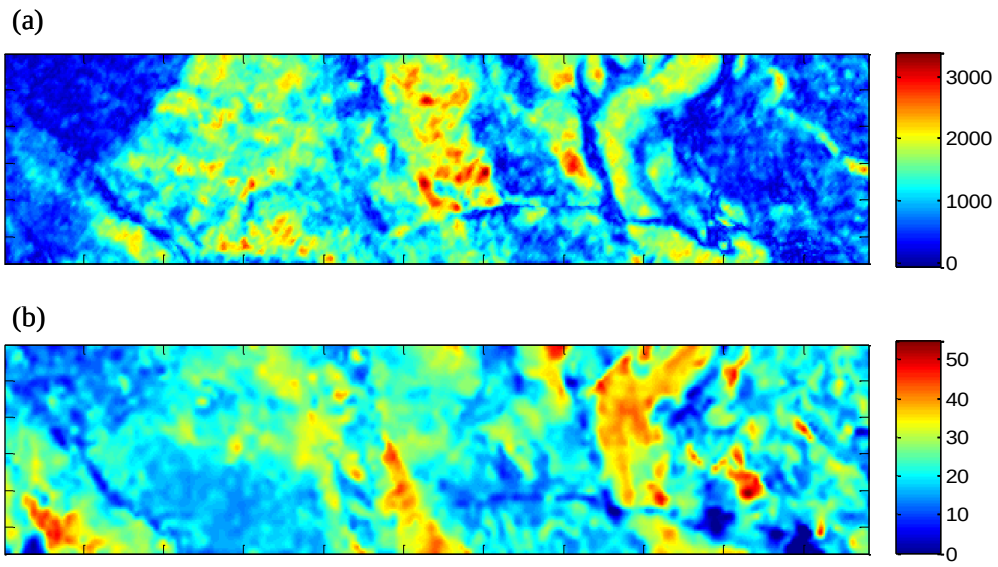

Figure E.3: *(a) Average RMS attribute extracted between the top and base of the T31a reservoir, from 1996 pre-production base-line seismic, and (b) time thickness calculated between the top and the base of reservoir.*

Figure E.4(c) shows the corrected seismic net-to-gross for our 100% true net-to-gross reservoir as a function of apparent thickness. For large gross intervals, seismic net-to-gross will be the same as true net-to-gross, because apparent thickness is equal to true thickness. However, as the gross thickness reduces, the net will reduce but the apparent thickness will approach a minimum value (see Figure E.1(a)); hence the seismic net-to-gross will fall.

Now that the band-limited impedance has been modelled and NTG is corrected for the wedge model (called seismic NTG), it would be possible to back-calculate and derive the correction curve. Dividing the corrected seismic NTG (Figure E.4(c)) by the modelled average band-limited impedance (Figure E.4(b)) can serve as a detuning transform illustrated in Figure E.4(d):

$$\text{Detuning curve} = \frac{\text{Modelled seismic NTG}}{\text{Modelled average attribute}} \tag{E.1}$$

The detuning correction (Figure E.4(d)) increases with apparent thickness, with the slope being dependent upon the low-frequency wavelet parameterization. Hence, for a

large apparent thickness, the detuning factor is very sensitive to the estimation of the low frequencies in the data.

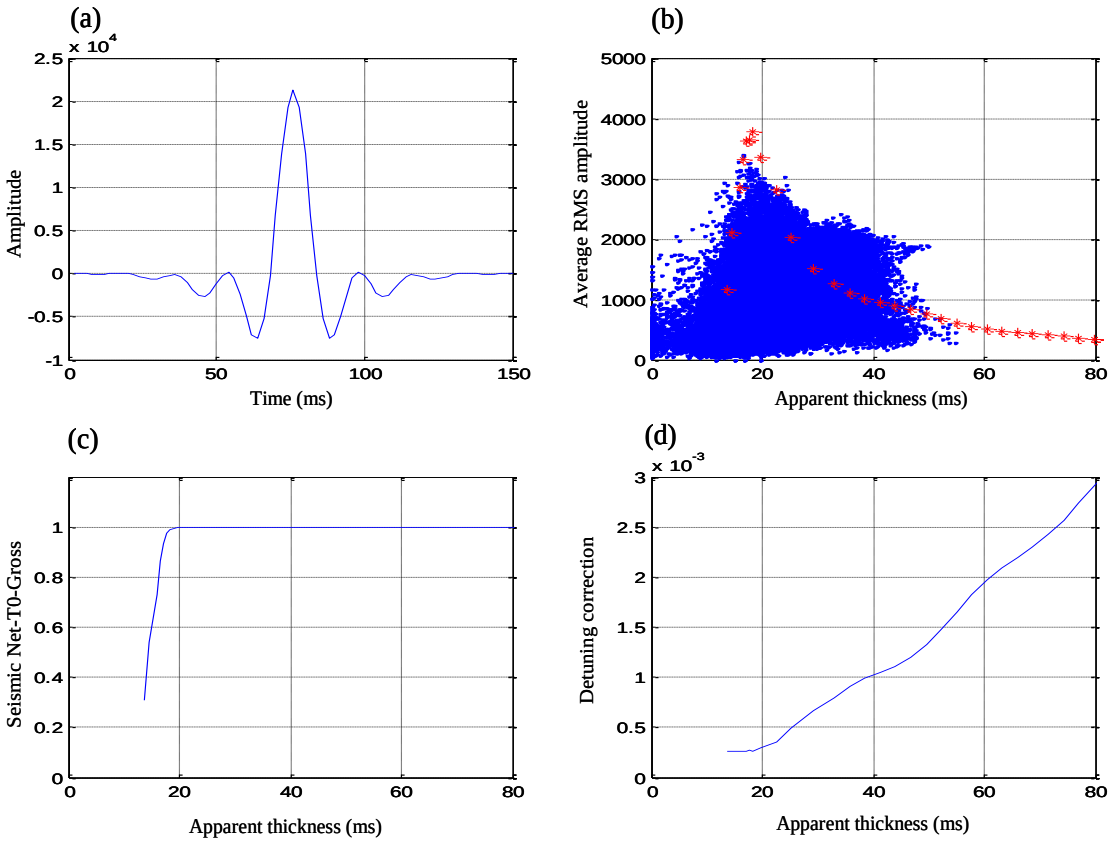

Figure E.4: *Successive stages of the detuning process: (a) extracted wavelet for the data; (b) cross-plot of the average RMS attribute plotted against the apparent thickness for the T31a reservoir unit – superimposed is a modelled tuning curve; (c) modelled seismic net-to-gross; and (d) detuning correction curve.*

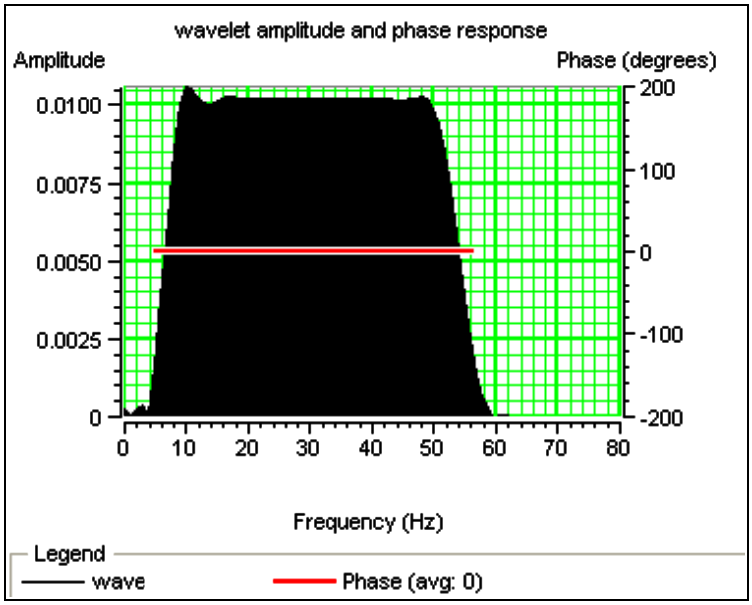

Figure E.5: *Frequency spectrum for the wavelet extracted for the T31a reservoir. Based on the estimated wavelet, a trapezoidal filter 5-10-50-60 is designed to simulate the wedge and therefore model the tuning response.*

The calculated detuning transform is used to correct the average band-limited impedance for seismic NTG calculation. However, NTG is less than unity in the real case. Nevertheless, we may still assume that seismic net-to-gross is proportional to average band-limited impedance. Therefore, the detuning curve is applied to the average band-limited impedance (the seismic map attribute) for removing the apparent thickness effect (the tuning effect).

$$\text{Seismic NTG} = \text{Extracted Average Attribute} \times \text{Modelled Detuning Curve} \tag{E.2}$$

The sensitivity study done by Connolly shows that the seismic NTG calculated here is different from the rue NTG calculated for different gross intervals. Therefore, he assumed that his method can only estimate net:

$$\text{Net} = \text{Seismic NTG} \times \text{Time Thickness} \tag{E.3}$$

Having estimates of the net map, the next stage in this procedure is determining a calibration factor that results in a reasonably sensible range for seismic net map. The first-guess calibration is applied by scaling the seismic net-to-gross map maximum to unity. The resulting map is adjusted by calibration using well data. The calibration factor is determined by minimizing the misfit between the seismic net pay map and the petrophysical net pay values measured at the calibration wells.

Appendix F: A mathematical development to include both saturation and pressure in the permeability-estimation equation

Introduction

In current methods of permeability estimation using 4D seismic, it has been preferred to employ either pressure or saturation to infer permeability, while ignoring the trade-off between them. However, the most appropriate technique would take into account both effects at the same time, in order to infer the permeability. Pressure propagation is a diffusion phenomenon, and therefore the response is a low-frequency smoothed event which cannot detect the effects of small-scale permeability heterogeneity over a long distance, but usually has a full coverage over the field. On the other hand, permeability is usually correlated with saturation (the major application is in well-logging permeability estimation), but the areal coverage of saturation is incomplete most of the time. Therefore, involving both effects would utilize the maximum extracting permeability information concealed in time-lapse seismic attributes. In Vasco's pressure approach (2004), although saturation-dependent variables in the pressure equation do exist, the saturation data are provided from simulation data at distinct times, while in the derivation proposed in this section, I will attempt to replace the saturation estimates directly from the 4D-seismic data. Therefore, saturation change will appear in an explicit form and the finite-difference method can be implemented to solve the problem. This is in contrast to previous saturation methods, which were streamline-based. Using the proposed development, it does not matter whether the field data are pressure- or saturation-dominant, as the method should be able to handle any case. In another note, a robust discretizing method based on the physics of fluid flow in porous media is proposed in order to solve the problem. Also, production data are used to constrain the model.

(a) Derivation

The expressions for the two-phase Darcy's law for the oil- and water-phases are:

$$\nabla.[K\left(\frac{k_{\mathrm{ro}}}{\mu_{\mathrm{o}}}\right)\nabla P] = Q_{\mathrm{o}} + \phi\frac{\partial S_{\mathrm{o}}}{\partial t} \tag{F.1}$$

$$\nabla.[K\left(\frac{k_{\mathrm{rw}}}{\mu_{\mathrm{w}}}\right)\nabla P] = Q_{\mathrm{w}} + \phi\frac{\partial S_{\mathrm{w}}}{\partial t} \tag{F.2}$$

In order to eliminate the saturation derivatives with respect to time in Equations F.1 and F.2, we will proceed as follows:

$$\nabla.[K\left(\sum\frac{k_{ri}}{\mu_i}\right)\nabla P]=Q_o+Q_w+\phi\left(\frac{\partial S_o}{\partial t}+\frac{\partial S_w}{\partial t}\right) \tag{F.3}$$

Since, by definition, $S_w + S_o = 1$, Equation F.3 is simplified to:

$$\nabla.[K\lambda_t\nabla P]=Q_t+\phi\left(\frac{\partial S_o+\partial S_w}{\partial t}\right)=Q_t+0 \tag{F.4}$$

Therefore, at different times (t_0 and t_1):

$$@t_0\longrightarrow\nabla.[K\lambda_0\nabla P_0]=Q_0 \tag{F.5}$$

$$@t_1\longrightarrow\nabla.[K\lambda_1\nabla P_1]=Q_1 \tag{F.6}$$

On the other hand, using the Taylor series, mobility at t_1 is:

$$\lambda_1=\lambda_0+(t_1-t_0)\frac{\partial\lambda}{\partial t} \tag{F.7}$$

and using the chain rule:

$$\frac{\partial\lambda}{\partial t}=\frac{\partial\lambda}{\partial S_w}\times\frac{\partial S_w}{\partial t},\ \alpha=\frac{\partial\lambda}{\partial S_w} \tag{F.8}$$

So, by replacing Equation F.8 in Equation F.7:

$$\lambda_1=\lambda_0+(t_1-t_0)\times\alpha\times\frac{\partial S_w}{\partial t}=\lambda_0+\alpha\times S_{w\Delta} \tag{F.9}$$

where $S_{w\Delta}$ is the change in saturation over time that is estimated from time-lapse seismic. To include P_Δ in the formula, Equation F.6 is subtracted from Equation F.5:

$$\nabla.[K\lambda_1\nabla P_1-K\lambda_0\nabla P_0]=Q_1-Q_0 \tag{F.10}$$

Mobility at t_1 (λ_1) is replaced in this equation:

$$\nabla.[K\left(\lambda_0+\alpha S_{w\Delta}\right)\nabla P_1-K\lambda_0\nabla P_0]=Q_\Delta \tag{F.11}$$

By rearranging:

$$\nabla.[K(\lambda_0 + \alpha Sw_\Delta)\nabla P_1 - K\lambda_0 \nabla P_0] = Q_\Delta \tag{F.12}$$

Using the Taylor-series approximation:

$$\nabla P_1 = \nabla P_0 + \frac{\partial \nabla P}{\partial t}\Delta t = \nabla P_0 + \frac{\nabla \partial P}{\partial t}\Delta = \nabla P_0 + \nabla P_\Delta = \nabla(P_0 + P_\Delta) \tag{F.13}$$

By substituting Equation F.13 in F.12:

$$\nabla.[K(\lambda_0 \nabla(P_0 + P_\Delta) + \alpha S_{w\Delta}\nabla P_1 - \lambda_0 \nabla P_0)] = Q_\Delta \tag{F.14}$$

Therefore, the final equation will be in the form of:

$$\nabla.[K(\lambda_0 \nabla P_\Delta + \alpha S_{w\Delta}\nabla P_1)] = Q_\Delta \tag{F.15}$$

where α can be determined from K_{rw} curves (see Equation F.8); K is the absolute permeability which is the only unknown in this equation; and λ_0 is the total mobility at the base-line survey time:

$$\lambda_0 = \sum_i \frac{k_r(S_i)}{\mu_i}\bigg|_{t=t_0} \tag{F.16}$$

P_Δ and $S_{w\Delta}$ are pressure- and saturation-change estimated from time-lapse seismic and P_1 is the pressure at time t_1. P_1 can be estimated from simulation model or production data if available at this particular time. It is important to note that the weighting function for the saturation term, α, is a function of changing mobility due to saturation change. It would be close to zero if there were no saturation change, for example, in the case of production depletion. In fact, it is a weighing parameter that signifies the trade-off between pressure and saturation.

In addition, Equation F.15 can be used in conjugation with the equation proposed by Floricich (2006):

$$\Delta A = aP_\Delta + bS_{w\Delta} \tag{F.17}$$

(b) Discretization

By discretization of Equation F.15 using the notation in Figure F.1, the following form is obtained:

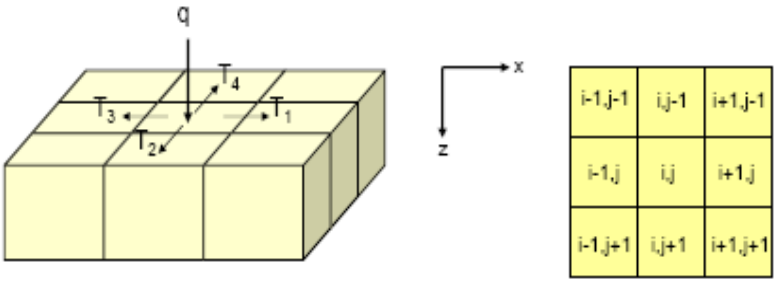

Figure F.1: *Discretization and notation for the 2D equation*

$$
\begin{aligned}
&K_{i+\frac{1}{2},j}\left[\lambda_{0i+\frac{1}{2},j}\left(\frac{P_{\Delta_{i+1,j}}-P_{\Delta_{i,j}}}{\left(x_{i+1,j}-x_{i,j}\right)\left(x_{i+\frac{1}{2},j}-x_{i-\frac{1}{2},j}\right)}\right)+\alpha_{i+\frac{1}{2},j}S_{w\Delta i+\frac{1}{2},j}\left(\frac{P_{1_{i+1,j}}-P_{1_{i,j}}}{\left(x_{i+1,j}-x_{i,j}\right)\left(x_{i+\frac{1}{2},j}-x_{i-\frac{1}{2},j}\right)}\right)\right]\\
&-K_{i-\frac{1}{2},j}\left[\lambda_{0i-\frac{1}{2},j}\left(\frac{P_{\Delta_{i,j}}-P_{\Delta_{i-1,j}}}{\left(x_{i,j}-x_{i-1,j}\right)\left(x_{i+\frac{1}{2},j}-x_{i-\frac{1}{2},j}\right)}\right)+\alpha_{i-\frac{1}{2},j}S_{w\Delta i-\frac{1}{2},j}\left(\frac{P_{1_{i,j}}-P_{1_{i-1,j}}}{\left(x_{i,j}-x_{i-1,j}\right)\left(x_{i+\frac{1}{2},j}-x_{i-\frac{1}{2},j}\right)}\right)\right]\\
&+K_{i,j+\frac{1}{2}}\left[\lambda_{0i,j+\frac{1}{2}}\left(\frac{P_{\Delta_{i,j+1}}-P_{\Delta_{i,j}}}{\left(y_{i+1,j}-y_{i,j}\right)\left(y_{i,j+\frac{1}{2}}-y_{i,j-\frac{1}{2}}\right)}\right)+\alpha_{i,j+\frac{1}{2}}S_{w\Delta i,j+\frac{1}{2}}\left(\frac{P_{1_{i,j+1}}-P_{1_{i,j}}}{\left(y_{i+1,j}-y_{i,j}\right)\left(y_{i,j+\frac{1}{2}}-y_{i,j-\frac{1}{2}}\right)}\right)\right]\\
&-K_{i,j-\frac{1}{2}}\left[\lambda_{0i,j-\frac{1}{2}}\left(\frac{P_{\Delta_{i,j}}-P_{\Delta_{i,j-1}}}{\left(y_{i,j}-y_{i,j-1}\right)\left(y_{i,j+\frac{1}{2}}-y_{i,j-\frac{1}{2}}\right)}\right)+\alpha_{i,j-\frac{1}{2}}S_{w\Delta i,j-\frac{1}{2}}\left(\frac{P_{1_{i,j}}-P_{1_{i,j-1}}}{\left(y_{i,j}-y_{i,j-1}\right)\left(y_{i,j+\frac{1}{2}}-y_{i,j-\frac{1}{2}}\right)}\right)\right]=Q_{i,j}
\end{aligned}
\tag{F.18}
$$

where $K_i + 1/2$, $K_i - 1/2$, $K_j + 1/2$, $K_j - 1/2$ are harmonic average permeabilities between two neighbouring grid blocks similar to transmissibility. However, to obtain the permeabilities at grid blocks, the discretization is shown in Equation F.18 and the system of the equation would be in a non-linear form:

$$A_{i+\frac{1}{2},j}\left(\Delta x_{i+1,j}+\Delta x_{i,j}\right)\left(\frac{1}{\left(\Delta x_{i+1,j}\left(\frac{1}{K_{i+1,j}}\right)+\Delta x_{i,j}\left(\frac{1}{K_{i,j}}\right)\right)}\right)$$

$$-A_{i-\frac{1}{2},j}\left(\Delta x_{i,j}+\Delta x_{i-1,j}\right)\left(\frac{1}{\left(\Delta x_{i,j}\left(\frac{1}{K_{i,j}}\right)+\Delta x_{i-1,j}\left(\frac{1}{K_{i-1,j}}\right)\right)}\right)$$

$$+A_{i,j+\frac{1}{2}}\left(\Delta y_{i,j+1}+\Delta y_{i,j}\right)\left(\frac{1}{\left(\Delta y_{i,j+1}\left(\frac{1}{K_{i,j+1}}\right)+\Delta y_{i,j}\left(\frac{1}{K_{i,j}}\right)\right)}\right)$$

$$-A_{i,j-\frac{1}{2}}\left(\Delta y_{i,j}+\Delta y_{i,j-1}\right)\left(\frac{1}{\left(\Delta y_{i,j}\left(\frac{1}{K_{i,j}}\right)+\Delta y_{i,j-1}\left(\frac{1}{K_{i,j-1}}\right)\right)}\right)-Q_{i,j}=0 \tag{F.19}$$

where $A_i + 1/2$, $A_i - 1/2$, $A_j + 1/2$, and $A_j - 1/2$ are the constant coefficients. Since it is a non-linear discretization, the Newton–Raphson method in combination with a conjugate gradient solver is proposed for solving this numerical problem.

Appendix G: Simulator-to-seismic modelling

G.1 Introduction

In time-lapse seismic studies, it is necessary to have an understanding of the effects of changing pressure and saturation on P- and S-wave velocities and therefore the final seismic response. A feasibility study and the sensitivity analysis of seismic parameters with respect to reservoir-engineering parameters are important practices of time-lapse modelling which are usually performed. The petro-elastic model plays a central role in this type of modelling to recognize how seismic data respond to reservoir properties. A petro-elastic model based on Gassmann's equation and Batzle and Wang's empirical relationship can link the reservoir-engineering domain to the seismic domain.

G.2 Petro-elastic transform

Petro-elastic modelling implies fluid impact on rock seismic properties. This includes:

- Changes in fluid composition (e.g. water replacing oil), which alter both effective density and the bulk modulus of the rock, and therefore the seismic velocities.
- Changes in fluid pressure, which modify the effective stress applied on the rock. Such deformation changes the elastic stiffness and density of the rock, and again changes the seismic wave velocities.

The P- and S-wave velocities (V_P and V_S) for a saturated porous medium are functions of saturated bulk and shear moduli (K_{sat} and G_{sat}) and saturated bulk density (ρ_{sat}):

$$V_P = \sqrt{\frac{K_{sat} + \frac{4}{3}G_{sat}}{\rho_{sat}}} \tag{G.1}$$

$$V_S = \sqrt{\frac{G_{sat}}{\rho_{sat}}} \tag{G.2}$$

Consequently, the saturated moduli and bulk density need to be calculated. It is assumed that fluids do not affect the estimated shear moduli; thus, the shear modulus remains the same regardless of the fluid filling the rock pores:

$$G_{\text{sat}} = G_{\text{dry}} \tag{G.3}$$

Also, the density of saturated rock is given by:

$$\rho_{\text{sat}} = \rho_{\text{m}}(1-\phi) + \rho_{\text{fl}}\phi \tag{G.4}$$

where ρ_{sat} is density of saturated rock, ρ_{m} is the density of the matrix and ρ_{fl} is the fluid mixture density, which is a volume average of the individual fluids:

$$\rho_{\text{fl}} = S_{\text{w}}\rho_{\text{w}} + S_{\text{o}}\rho_{\text{o}} + S_{\text{g}}\rho_{\text{g}} \tag{G.5}$$

where S_{w}, S_{o} and S_{g} are the saturations, and ρ_{w}, ρ_{o} and ρ_{g} are the densities of the water-, oil- and gas-phases respectively. Gas, oil and water density are estimated using the Batzle and Wang empirical correlations expressed in Appendix H.

However, the saturated bulk modulus is calculated from Gassmann's equation as described in section G.3.

G.3 Fluid substitution (K_{sat} calculation)

Gassmann (1951) derived an equation to calculate bulk modulus of a fluid-saturated porous medium. Gassmann's equation combines the dry rock data and effective fluid moduli as a function of pressure, temperature, porosity, and fluid saturation:

$$K_{\text{sat}} = K_{\text{dry}}(\sigma_{\text{eff}}) + \frac{\left(1 - \frac{K_{\text{dry}}(\sigma_{\text{eff}})}{K_{\text{m}}}\right)^2}{\frac{\phi}{K_{\text{fl}}(T, P_{\text{f}}, C)} + \frac{(1-\phi)}{K_{\text{m}}} - \frac{K_{\text{dry}}(\sigma_{\text{eff}})}{K_{\text{m}}^2}} \tag{G.6}$$

where:

K_{sat} : Saturated bulk modulus

K_{dry}: Rock frame bulk modulus

φ: porosity

$\sigma_{\text{eff:}}$ effective stress

K_m: Mineral bulk modulus P_f: average fluid pressure

K_{fl}: Pore-fluid bulk modulus T: reservoir temperature

C: a vector containing fluid-phase-specific parameters, such as API gravity, salinity and solution gas/oil ratio

This formula relates the effective elastic modulus of a dry rock to the effective modulus of the same rock containing fluid at low frequencies. Gassmann expressed the bulk modulus K_{sat} of fluid-saturated sediments as a function of the bulk moduli of the dry frame K_d; of the pore fluid K_{fl}; and of the grains K_m. K_m is characterized with a constant value for the particular type of sand in the reservoir. K_{dry} and K_{fl} are calculated based on the equations expressed in G.3.1 and G.3.2 respectively.

G.3.1 Stress-dependency of the K_{dry}

Gassmann's formulation requires knowledge of the dry bulk. Typically, dry rock properties are measured in the laboratory from core samples as a function of porosity, pressure and temperature. In our study, we did not have laboratory data, so we used the sigmoidal fits proposed by MacBeth (2004). The sigmoidal functions of the bulk modulus, K_{dry}, and the shear modulus, G_{dry}, as a function of pressure are given as:

$$K_{dry} = \frac{K_{inf}}{1 + E_K e^{-\sigma_{eff} / P_K}} \tag{G.7}$$

$$G_{dry} = \frac{G_{inf}}{1 + E_G e^{\sigma_{eff} / P_G}} \tag{G.8}$$

where:

K_{inf}, G_{inf} = the asymptote at high pressures

P_k, P_G = the rate of pressure increase

$$S_K = \frac{K_{inf} - K(0)}{K_{inf}} \text{ and } E_K = \frac{S_K}{1 - S_K} \tag{G.9}$$

$$S_G = \frac{G_{inf} - G(0)}{G_{inf}} \text{ and } E_G = \frac{S_G}{1 - S_G} \tag{G.10}$$

S_K and S_G represent the overall possible pressure change for bulk and shear moduli respectively. Note that the parameters K_{inf}, E_K and P_K control the behaviour of the bulk modulus. Similarly, the shear modulus is controlled by G_{inf}, E_G and P_G. MacBeth (2004) tested these functions on the laboratory measurements that included both outcrop and reservoir rocks from different depositional environments. The equations provided excellent agreement with the real data. The above formulation could be used to predict the pressure dependence for time-lapse feasibility studies by using the parameters listed in Table G.1.

Table G.1: *Stress-sensitivity parameters for the reservoir sandstones used in the study. The table is ordered according to the magnitude of S_K/P_K, with the topmost row corresponding with the maximum pressure sensitivity (MacBeth, 2004).*

Rock	V_P **(km/s)**	V_S **(km/s)**	ρ **(g/cm^3)**	V_P/V_S	φ	S_K	S_G	P_K **(MPa)**	P_G **(MPa)**	K_{inf} **(GPa)**	G_{inf} **(GPa)**
Forties (Nelson)	1.78	1.13	2.02	1.57	25.0	0.66	0.66	6.53	7.08	8.70	7.61
West of Shetland	2.16	1.34	1.91	1.62	26.3	0.56	0.56	6.33	4.23	9.94	7.75
Gulf Coast	2.46	1.84	1.99	1.34	21.7	0.75	0.53	9.55	23.24	12.40	14.30
Rotliegend (North Sea)	2.74	1.67	2.02	1.64	19.8	0.51	0.54	9.69	20.24	15.63	12.28
Cooper Basin	2.98	1.90	2.37	1.56	10.0	0.55	0.59	15.28	12.56	21.23	20.91
North Sea	3.22	2.22	2.41	1.45	9.0	0.61	0.50	25.42	24.48	23.38	23.71
Rotliegend (Germany)	3.60	2.58	2.52	1.40	8.5	0.62	0.36	30.58	36.58	26.81	26.29

G.3.2 Calculating the fluid bulk modulus (K_{fl})

The effective fluid bulk modulus (K_{fl}) of the undrained fluid-mixture porous medium, for partial saturation conditions with homogeneous mixing of gas, oil and water, is given by:

$$\frac{1}{K_{fl}} = \frac{S_w}{K_w} + \frac{S_o}{K_o} + \frac{S_g}{K_g} \qquad \text{(G.11)}$$

where K_w, K_0 and K_g are bulk moduli and S_w, S_o and S_g are saturations for gas, oil and water phases respectively. Gas, oil and water bulk moduli are computed using the Batzle and Wang empirical correlations expressed in Appendix H.

G.4 Mixing of sand and shale

Two options are available for isotropic mixing of sands and shales, Backus averaging (for a layered system) and the Voigt–Reuss–Hill average (i.e. an average of the harmonic and arithmetic means). The equations are set out below.

G.4.1 Backus averaging

For an effective isotropic P-wave velocity of a normal-incidence wave propagation on a stack of horizontal layers (Backus, 1962):

$$V_{\mathrm{P}}^{\mathrm{ave}} = \sqrt{\frac{1}{\rho_{\mathrm{sat}}^{\mathrm{ave}}}\left[\frac{f_{\mathrm{sand}}}{\left(K_{\mathrm{sat}}^{\mathrm{sand}} + \frac{4}{3}G_{\mathrm{sat}}^{\mathrm{sand}}\right)} + \frac{f_{\mathrm{shale}}}{\left(K_{\mathrm{sat}}^{\mathrm{shale}} + \frac{4}{3}G_{\mathrm{sat}}^{\mathrm{shale}}\right)}\right]^{-1}} \tag{G.12}$$

$$V_{\mathrm{S}}^{\mathrm{ave}} = \sqrt{\frac{1}{\rho_{\mathrm{sat}}^{\mathrm{ave}}}\left[\frac{f_{\mathrm{sand}}}{\left(G_{\mathrm{sat}}^{\mathrm{sand}}\right)} + \frac{f_{\mathrm{shale}}}{\left(G_{\mathrm{sat}}^{\mathrm{shale}}\right)}\right]^{-1}} \tag{G.13}$$

where, in both cases

$$\rho_{\mathrm{ave}} = f_{\mathrm{sand}} G_{\mathrm{sat}}^{\mathrm{sand}} + f_{\mathrm{shale}} G_{\mathrm{sat}}^{\mathrm{shale}} \tag{G.14}$$

and f_{sand} and f_{shale} are the fractions of sand and shale which are equal to $1 - V_{\mathrm{shale}}$ and V_{shale} respectively.

G.4.2 VRH average

The VRH (Voit–Reuss–Hill) is the average of the harmonic and arithmetic means. For effective isotropic P-wave velocity:

$$M_{\mathrm{p,Reuss}} = \left[\frac{f_{\mathrm{sand}}}{\left(K_{\mathrm{sat}}^{\mathrm{sand}} + \frac{4}{3}G_{\mathrm{sat}}^{\mathrm{sand}}\right)} + \frac{f_{\mathrm{shale}}}{\left(K_{\mathrm{sat}}^{\mathrm{shale}} + \frac{4}{3}G_{\mathrm{sat}}^{\mathrm{shale}}\right)}\right]^{-1} \tag{G.15}$$

and:

$$M_{\text{P, Voigt}} = \left[f_{\text{sand}} \left(K_{\text{sat}}^{\text{sand}} + \frac{4}{3} G_{\text{sat}}^{\text{sand}} \right) + f_{\text{shale}} \left(K_{\text{sat}}^{\text{shale}} + \frac{4}{3} G_{\text{sat}}^{\text{shale}} \right) \right]^{-1} \tag{G.16}$$

and:

$$M_{\text{P,ave}} = \frac{1}{2} \left[M_{\text{P,Reuss}} + M_{\text{P,Voigt}} \right] \tag{G.17}$$

and finally:

$$V_{\text{P}}^{\text{ave}} = \sqrt{\frac{M_{\text{P,ave}}}{\rho_{\text{ave}}}} \tag{G.18}$$

Similarly, for the effective isotropic S-wave velocity:

$$M_{\text{S,Reuss}} = \left[\frac{f_{\text{sand}}}{\left(G_{\text{sat}}^{\text{sand}} \right)} + \frac{f_{\text{shale}}}{\left(G_{\text{sat}}^{\text{shale}} \right)} \right]^{-1} \tag{G.19}$$

and:

$$M_{\text{S,Voigt}} = \left[f_{\text{sand}} \left(G_{\text{sat}}^{\text{sand}} \right) + f_{\text{shale}} \left(G_{\text{sat}}^{\text{shale}} \right) \right] \tag{G.20}$$

and:

$$M_{\text{S,ave}} = \frac{1}{2} \left[M_{\text{S,Reuss}} + M_{\text{S,Voigt}} \right] \tag{G.21}$$

and finally:

$$V_{\text{S}}^{\text{ave}} = \sqrt{\frac{M_{\text{S,ave}}}{\rho_{\text{ave}}}} \tag{G.22}$$

where ρ_{sat} is calculated using Equation G.14.

Appendix H: The Batzle and Wang empirical correlations

Batzle and Wang (1992) combined thermodynamic relationships and empirical trends from published data in order to predict the effects of pressure, temperature and composition on the seismic properties of fluids. They examined the properties of gases, oils and brines: the three primary types of pore fluid present in most reservoirs. The fluid properties predicted include density and bulk modulus (and therefore velocity) as functions of fluid temperature and pressure, when the pore-fluid composition is known or estimated. The specific equations used are given in this Appendix.

- Brine density

Brine density is a function of temperature (T in °C), pressure (P in MPa) and salinity (S in ppm). The density of pure water is first obtained:

$$\rho_{\mathrm{W}} = 1 + 10^{-6}\begin{pmatrix} -80T - 3.3T^2 + 0.00175T^3 + 489P - 2TP \\ +0.016T^2P - 1.3\times10^{-5}T^3P - 0.333P^2 - 0.002TP^2 \end{pmatrix} \quad \text{(H.1)}$$

Brine density is then deduced from pure water density:

$$\rho_{\mathrm{B}} = \rho_{\mathrm{W}} + S\left(0.668 + 0.44S + 10^{-6}\left(300P - 2400PS + T\left(80 + 3T - 3300S - 13P + 47PS\right)\right)\right) \quad \text{(H.2)}$$

- Brine velocity

Similarly to density, brine velocity is function of T, P and S, and is deduced from the velocity of pure water, which is a polynomial function of temperature and pressure (w_{ij} are given in Table H.1):

$$V_{\mathrm{W}} = \sum_{i=0}^{4}\sum_{j=0}^{3} w_{ij}T^iP^j \quad \text{(H.3)}$$

$$V_{\mathrm{B}} = V_{\mathrm{W}} + S\left(1170 - 9.6T + 0.055T^2 - 8.5\times10^{-5}T^3 + 2.6P - 0.0029TP - 0.0476P^2\right) + S^{1.5}\left(780 - 10P + 0.16P^2\right) - 820S^2 \quad \text{(H.4)}$$

Table H.1: *Polynomial coefficients used to calculate pure water velocity.*

W_{ij}	0	1	2	3
0	1402.85	1.524	3.437E-03	-1.197E-05
1	4.871	-0.0111	1.739E-04	-1.628E-06
2	-0.04783	2.747E-04	-2.135E-06	1.237E-08
3	1.487E-03	-6.503E-07	-1.455E-08	1.327E-10
4	-2.197E-07	7.987E-10	5.230E-11	-4.614E-13

- Oil density

Batzle and Wang (1992) make the distinction between live and dead oil. In our experiment dead oil was chosen in order to simplify the understanding of the production. The density of oil at 15.6 °C under atmospheric pressure is given by:

$$\rho_o = \frac{141.5}{\text{API} + 131.5} \tag{H.5}$$

where API is the oil gravity number. Under different temperature and pressure condition (respectively T and P), the oil density is calculated by:

$$\rho_{\text{oil}} = \frac{\rho_o + \left(0.00277P - 1.71\times10^{-7}P^3\right)\left(\rho_o - 1.15\right)^2 + 3.49\times10^{-4}P}{\left(0.972 + 3.81\times10^{-4}\left(T + 17.78\right)^{1.175}\right)} \tag{H.6}$$

- Oil velocity

The oil velocity under the same conditions is given by the following empirical equation:

$$V_{\text{oil}} = 2096\sqrt{\frac{\rho_{\text{oil}}}{2.6 - \rho_{\text{oil}}}} - 3.7T + 4.64P + 0.0115\left(4.12\sqrt{\frac{1.08}{\rho_{\text{oil}}} - 1} - 1\right)TP \tag{H.7}$$

The oil and brine bulk moduli can be now obtained, using:

$$K = V^2\rho \tag{H.8}$$

- Gas density

$$\rho_g = \frac{28.8gP}{ZRT_a} \tag{H.9}$$

where Z and T_a are calculated using:

$$Z = 0.03 + 0.00527\left(3.5 - T_{pr}\right)^3 P_{pr} + \left(0.642T_{pr} - 0.007T_{pr}^{\ 4} - 0.52 + E\right) \tag{H.10}$$

$$T_a = T\left(^{o}\mathrm{C}\right) + 273.15 \tag{H.11}$$

and T_{pr}, P_{pr} and E are given by:

$$T_{pr} = \frac{T_a}{94.72 + 170.75g},\ P_{pr} = \frac{P}{4.892 - 0.4048g} \tag{H.12}$$

$$E = 0.109\left(3.85 - T_{pr}\right)^2 \exp\left[\frac{-\left(0.45 + 8\left(0.56 - \frac{1}{T_{pr}}\right)^2 P_{pr}^{\ 1.2}\right)}{T_{pr}}\right] \tag{H.13}$$

where G = gas-specific gravity, P = pressure and T = temperature

- Gas bulk modulus

$$K_g = \frac{P}{\left(1 - \frac{P_{pr}}{Z} - \frac{\partial Z}{\partial P_{pr}}\right)_T} r \tag{H.14}$$

$$r = 0.85 + \frac{5.6}{\left(P_{pr} + 2\right)} + \frac{27.1}{\left(P_{pr} + 3.5\right)^2} - 8.7\exp\left(-0.65\left(P_{pr} + 1\right)\right) \tag{H.15}$$

Appendix I: Extension of pressure- and saturation-anomaly interpretation using production data and forward modelling

I.1 Production well data

After computing boundaries of anomalies that are thought to be correlated to pressure/saturation effects using the Laplacian, these anomalies are compared with available production data. Here, production data is referred to those parameters that are routinely measured during the exploitation of the field, i.e. oil rate, water-cut, gas–oil-ratio (GOR) and bottom-hole pressure (BHP). For an injection well, two parameters, namely BHP fluctuations and cumulative water injection data, are utilized, whereas for a production well, BHP and water-cut information are considered in order to differentiate pressure- from saturation–anomalies in the 4D signal. As illustrated in Figure I.1 at well CW13, from 1996 to 1999 the pressure variation was insignificant, whereas the saturation changed significantly; therefore, pseudo-impedance decreases mainly due to the saturation change. However, the 4D signal of 2004–1996 seems to be fairly consistent with pressure drop in the compartment highlighted by the 4D seismic.

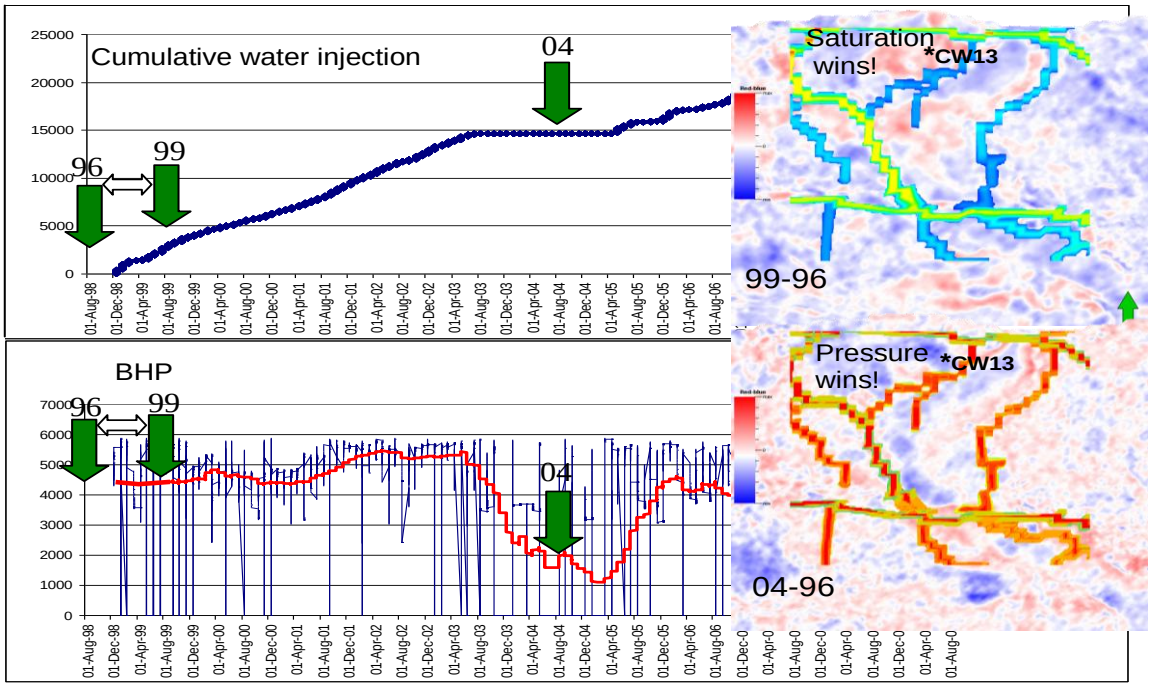

Figure I.1: *Cumulative water injection at well CW13, and BHP (blue represents the daily BHP fluctuations and red represents the moving average over a period of a month) at well CW13. Comparison with the well data identifies the fact that the signal in the 4D seismic is affected by pressure or saturation.*

I.2 Forward-modelling predictions

The accurate discrimination of pressure from the saturation signal in 4D seismic is challenging when the noise level in the data creates the issue of differentiating the signal from noise. To set apart the noise-related regions from the signal-related regions, forward modelling of the 4D-seismic response is a helpful illuminating tool. More importantly, forward modelling examines the pressure/saturation prediction of simulation in relation to the observed 4D signal. In order to calculate the synthetic 4D response, simulator-to-seismic modelling is performed. The procedure consists of flow simulation, a petro-elastic model and convolution. The simulation model of Schiehallion is run to calculate pressure and saturation. Next, the petro-elastic model calibrated with well-log data from the Schiehallion reservoir is utilized to calculate the elastic properties (velocity, density and acoustic impedance). This is followed by 1D convolution of the calculated reflection coefficients with the wavelet for amplitude calculations.

The petro-elastic model is at the heart of simulator-to-seismic modelling. This model governs the change in impedance due to the variation of pressure and saturation (see Figure I.2(a)). According to petro-elastic modelling, an increase in pressure while the saturation variation is insignificant results in a decrease in the acoustic impedance (this is known as softening), whereas an increase in the water saturation when the pressure variation is insignificant results in an increase in the acoustic impedance (this known as hardening). Therefore, the final hardening/softening of the acoustic impedance depends on whether pressure or saturation is the dominant effect in the 4D signal. As demonstrated in Figure I.2, the observed anomalies around the CW13 injection well in 4D-seismic difference maps indicate hardening (red) due to oil replacement by water, and softening (blue) to pressure increase in the compartment surrounding CW13. The consistency of the interpretations of anomalies using simulation responses implies an additional validation of the pressure/situation interpretations made for observed 4D seismic.

Despite the tuning effect inherited in the seismic response, the anomalies in the 4D-seismic attribute maps mainly reflect the areas with amplitude change. To discriminate between hardening and softening, the difference between the RMS maps of monitor and base surveys is calculated (Figure I.3(c)). Blue signals mainly show softening, either

due to pressure increase or gas coming out of solution; and the red anomalies show hardening either due to pressure depletion or replacement of oil by water. The synthetic difference map is compared with the observed response (Figure I.3(d)). There is an overall agreement between the two maps. However, some areas of mismatch are denoted. It is important to note that the simulation prediction of pressure/saturation may not be essentially correct. However, in regions where the simulation response (synthetic seismic) matches the observed time-lapse data, the pressure and saturation prediction are reliable and can be used for calibrating our pressure/saturation interpretation. In the case where they do not match the observed data, several issues have to be examined and corrected: in the synthetic side, the accuracy of the simulation modelling, the rock-physics relationships, the convolution process; and in the observed data, acquisition imprints, the processing artefacts, and the accuracy of the interpreted top and base of the reservoir.

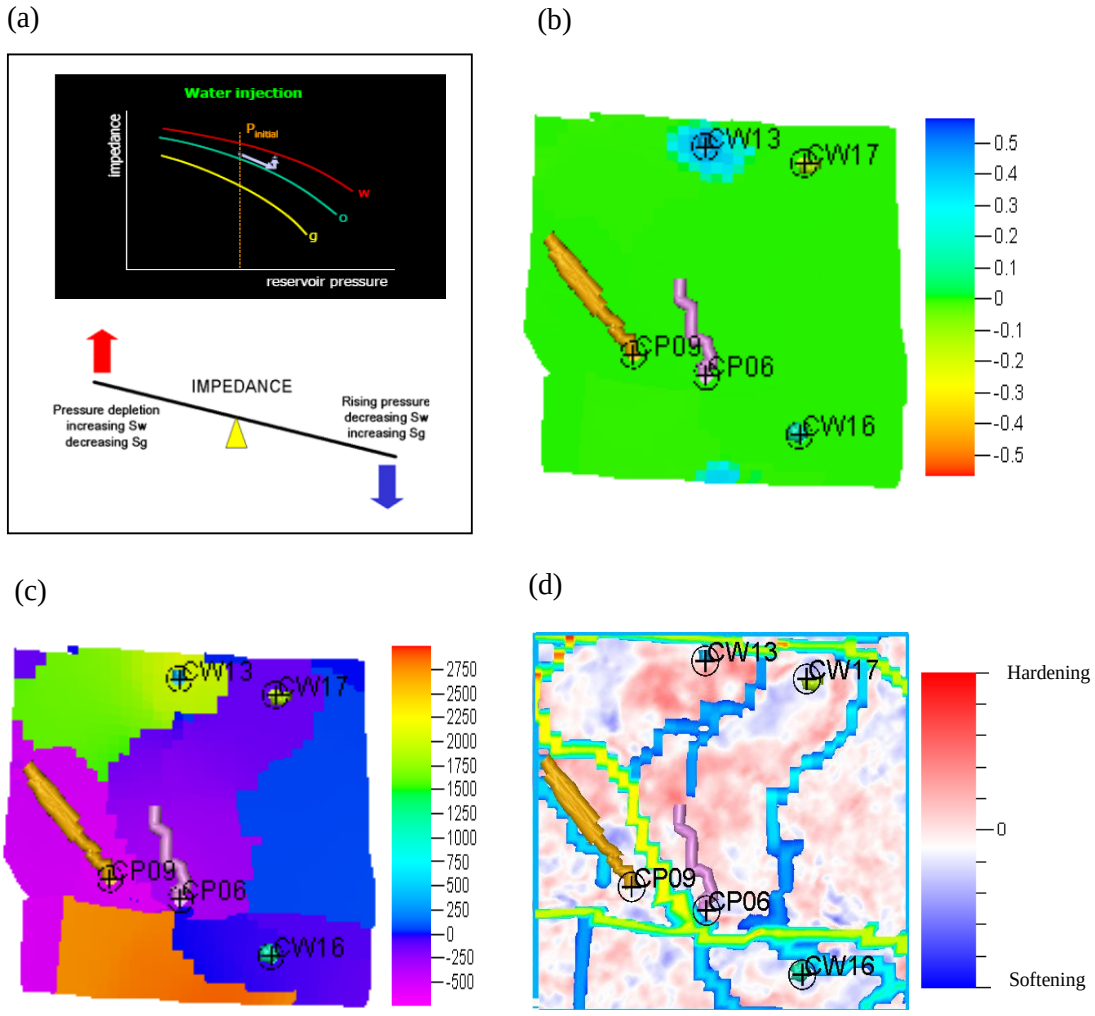

Figure I.2: *(a) Petro-elastic model (after Marsh, 2004); (b) saturation change between 1998 and 1999 from the simulation model; (c) pressure change between 1998 and 1999 from the simulation model; and (d) time-lapse difference map between pre-production 1996 and monitor 1999, interpretable based on the petro-elastic model and consistent with the pressure--saturation predictions of the simulation.*

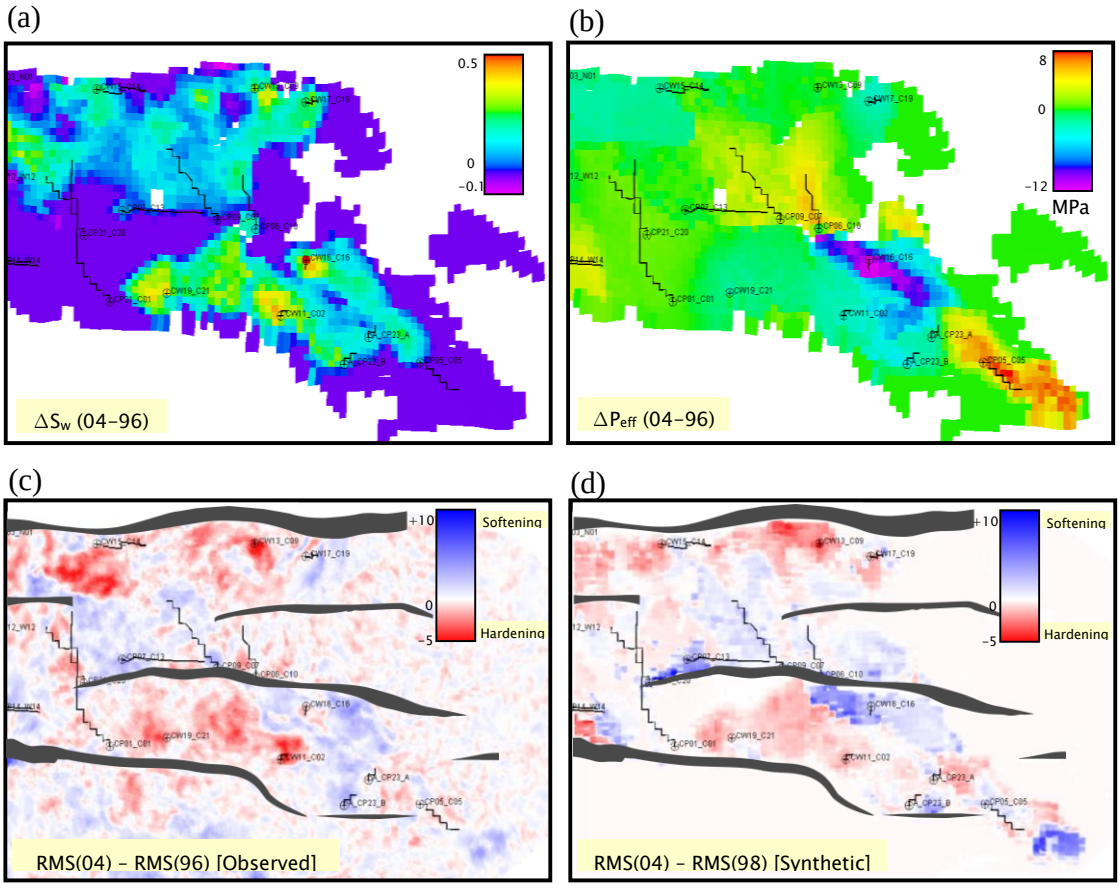

Figure I.3: *(a) Saturation change between 1998 and 2004, from the simulation model; (b) pressure change between 1998 and 2004, from the simulation model; (c) the observed 4D seismic between 1996 and 2004; and (d) the synthetic 4D response between 1996 and 2004 (Amini, 2009).*

Appendix J: The likelihood function and stochastic simulation

A schematic diagram of the likelihood function is shown in Figure J.1. In the cross-plot, the seismic-connectivity attribute is better correlated with the transmissibility at lower values than at higher ones, which shows a deviation from a linear relationship between the two properties. The spread values for the predicted transmissibility depend on the value of the connectivity attribute. Therefore, a non-linear dependency with varying standard deviation has to be defined. The non-linear relationship is captured in a joint probability-density function known as likelihood function, for incorporating the defined relationship and the uncertainty attached. The likelihood function is calculated by extracting the 1D likelihood function from the joint PDF (probability-density function).

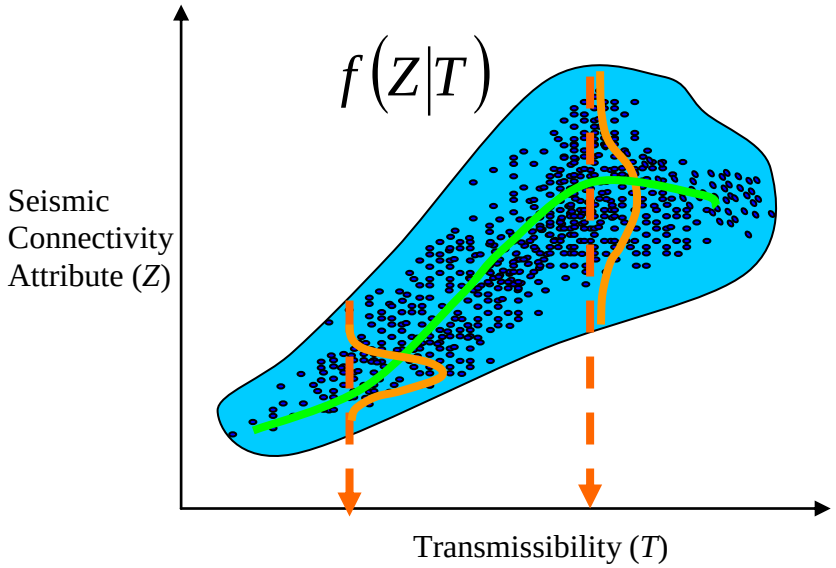

Figure J.1: *The likelihood function is calculated by extracting the 1D likelihood function from the joint PDF.*

The posterior probability is conditioned to this function (f) as described in following. Suppose that T is the transmissibility at certain location u. Z is the calculated connectivity attribute, and $T_1..T_n$ are the averaged transmissibilities at the well locations. The posterior probability at location u between the wells is defined as:

$$P\left(T|Z,T_1,...T_n\right) \propto f\left(Z|T\right) \times P_k\left(T|T_1,...T_n\right) \quad \text{(J.1)}$$

where $P(T \mid T_1,\ldots T_n)$ is the kriging probability and $f(Z \mid T)$ is the likelihood function. The kriging probability (local prior probability from well data) in a Gaussian context is:

$$P(T|T_1,..,T_n)= \frac{1}{\sqrt{2\pi}\delta_k}\exp\left\{-\frac{[T-T_k]^2}{2\delta_k^2}\right\} \quad \text{(J.2)}$$

T_k = the kriging estimate at location u_0

δ^2_k = the kriging variance at location u_0

The calculation of the posterior probability distribution is illustrated in Figure J.2. The procedure described here is a collocated cokriging-type process and the probability defined here has also been addressed as a posterior probability for Bayesian updating of collocated cokriging by a number of researchers (see Doyen *et al.*, 1996).

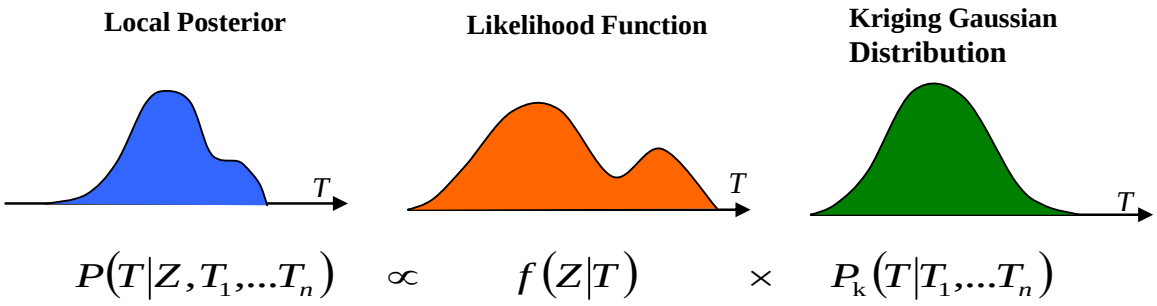

Figure J.2: *Local posterior probability calculation.*

The local posterior probability function is then employed to simulate the transmissibility value at a certain location via the sequential Gaussian simulation scheme. The simulation technique draws a value from the posterior probability calculated here. The workflow is illustrated in Figure J.3, and is described as follows:

1. Select a grid cell to be simulated at random.
2. Apply kriging to calculate the mean T_k and the standard deviation δ_k of the local conditional Gaussian distribution for *T*. Kriging is performed using the well data and previously simulated values as control points.
3. Compute the seismic likelihood function by extracting a 1D slice thorough the joint distribution for a value *Z* corresponding with the collocated attribute. The likelihood function describes the range of possible *T* values consistent with the

observed seismic attribute (Z). The mean and variance are different for each T value.

4. Calculate the local posterior probability by taking the product of the kriging probability and seismic likelihood function.
5. Draw a simulated value for T from posterior distribution and treat this as an extra control point.
6. Repeat steps 1 to 5 until all grid cells have been simulated.

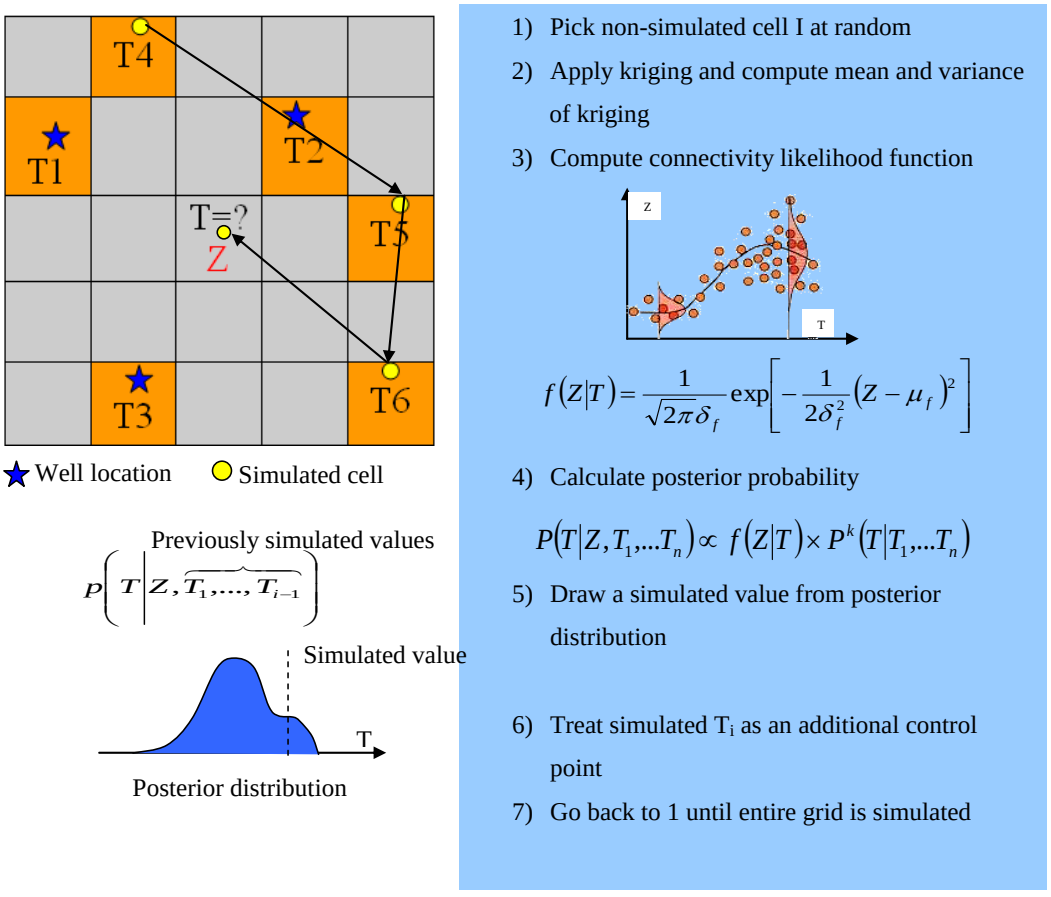

Figure J.3: *Sequential Gaussian simulation with seismic-connectivity attribute conditional probability (adopted from Doyen, 2007).*

REFERENCES

Ahmed, U., Crary, S.F. and Coates, G.R. (1989) Permeability estimation: various sources and their interrelationships (SPE 19604). *SPE Annual Technical Conference and Exhibition*, San Antonio, Texas, USA.

Albertoni, A. and Lake, L.W. (2003) Inferring interwell connectivity only from well-rate fluctuations in waterfloods (SPE 83381). *SPE Reservoir Evaluation and Engineering*, Vol. 6, No. 1, 6–16.

Aminzadeh, F. and de Groot, P. (2004) Soft computing for qualitative and quantitative seismic object and reservoir property prediction. Part 1: Neural network applications. *First Break*, Vol. 22, No. 3, 49–56.

Andersen, T., Zachariassen, E., Høye, T., Meisingset, H.C., Otterlei, C., van Wijngaarden, A.J., Hatland, K., Mangerøy, G., and Liestol, F.M. (2006) Method for Conditioning the Reservoir Model on 3D and 4D Elastic Inversion Data Applied to a Fluvial Reservoir in the North Sea (SPE 100190). *SPE Europec/EAGE Annual Conference and Exhibition*, Vienna, Austria.

Archie, G.E. (1949) The electrical resistivity log as an aid in determining some reservoir characteristics. *Journal of Petroleum Technology*, January issue.

Batzle, M. and Wang, Z. (1992) Seismic properties of pore fluids. *Geophysics*, Vol. 57, No. 11, 1396–1408.

Beggs, S.H. and King, P.R. (1985) Modelling the effects of shales on reservoir performance: calculation of effective vertical permeability. *SPE Reservoir Simulation Symposium*, Dallas, Texas, USA.

Behrens, R.A. and Tran, T.T. (1998) Incorporating seismic data of intermediate vertical resolution into 3D reservoir models (SPE 49143). *SPE Annual Technical Conference and Exhibition*, New Orleans, Louisiana, USA.

Biot, M.A. (1956) Theory of propagation of elastic waves in a fluid-saturated porous solid: low-frequency range; higher-frequency range. *Journal of the Acoustical Society of America*, Vol. 28, 168–191.

Brown, W. (1910) Some experimental results in the correlation of mental abilities. *British Journal of Psychology*, Vol. 3, 296–322.

Brun, B., Gosselin, O. and Barker, J.W. (2004) Use of prior information in gradient-based history matching. *SPE Journal*, Vol. 9, No. 1, 67–78.

Calvert, R. (2005) Insights and methods for 4D reservoir monitoring and characterisation. *SEG Distinguished Instructor Short Course, Distinguished Instructor Series*, No. 8

Cardwell, W.T. and Parsons, R.L. (1945) Average permeabilities of heterogeneous oil sands (SPE 945034-G). *Petroleum Transactions, AIME*, Vol. 160, 34–42.

Chambers, R.L. and Yarus, J.M. (2002) Quantitative use of seismic attributes for reservoir characterization, Houston, Texas, USA. Accessed 20 August 2009. http://132.248.182.189/cursos/geoest/Articulos/Reservoir%20Caracterization/

Chopra, S. and Murfurt, K.J. (2007) Seismic attributes for prospect identification and reservoir characterization. *SEG Geophysical Development Series*, No. 11.

Coates, G.R. and Dumanoir, J.L. (1974) A new approach to improved log-derived permeability. *The Log Analyst*, Vol. 15, No. 1, 17–31.

Coates, G.R., Xiao, L. and Prammer, M.G. (1999) *NMR Logging Principles and Applications*. Gulf Publishing Company, Houston, USA.

Coats, K.H., Dempsey, J.R., Henderson, J.H. (1970) The use of vertical equilibrium in two-dimensional simulation of three-dimensional reservoir performance. *Proceedings of the Second Symposium on Numerical Simulation of Reservoir Performance*, Dallas, USA.

Collette, Y. and Siarry, P. (2003) *Multiobjective Optimization: Principles and Case Studies*, Springer-Verlag, Berlin, ISBN 3-540-40182-2.

Connolly, P. (2007) A simple, robust algorithm for seismic net pay estimation. *The Leading Edge*, Vol. 26, No. 10, 1278–1282.

Connolly, P. and Kemper, M. (2007) Statistical uncertainty of seismic net pay estimations. *The Leading Edge*, Vol. 26, No. 10, 1284–1289.

Corbett, P. (2009) Petroleum geoengineering: integration of static and dynamic models. *SEG Distinguished Instructor Short Course, Distinguished Instructor Series*, No. 12.

Dadashpour, M., Kleppe, J. and Landro, M. (2007) Porosity and permeability estimation by gradient-based history matching using time-lapse seismic data (SPE 104519). *SPE Middle East Oil and Gas Show and Conference*, Bahrain.

de Groot, P., Ligtenberg, H., Oldenziel, T., Connolly, D. and Meldahl, P. (2004) Examples of multi-attribute, neural network-based seismic object detection. *Geological Society, London, Memoirs*, Vol. 29, 335–338.

de Haan, S.C., Oldenziel, T., Berentsen, C.W.J. and Kruijsdijk, C.P.J.W. (2001) Water-cut forecasting and permeability inversion from time-lapse seismic using a stream-line technique (OTC 13165). *OTC Annual Technical Conference*, Houston, USA.

Dobbyn, A. and Marsh, M. (2001) Material balance: a powerful tool for understanding the early performance of the Schiehallion field (SPE 71819). *Offshore Europe Conference*, Aberdeen, UK.

Doyen, P.M. (2007) Seismic reservoir characterization: an Earth modelling perspective. *EAGE Education Tour Series*, EAGE Publications, DB Houten, the Netherlands.

Doyen, P.M., den Boer, L.D. and Pillet, W.R. (1996) Seismic porosity mapping in the Ekofisk Field using a new form of collocated cokriging (SPE 36498). *SPE Annual Technical Conference and Exhibition*, Denver, Colorado, USA.

Doyen, P.M., Psaila, D.E., den Boer, L.D. and Jans, D. (1997) Reconciling data at seismic and well log scales in 3-D earth modelling (SPE 38698). *SPE Annual Technical Conference and Exhibition*, San Antonio, Texas, USA.

Duquerroix, J-P.L., Lemouzy, P., Otinger, B. and Romeu, R.K. (1993) Influence of the permeability–anisotropy ratio on large-scale properties of heterogeneous reservoirs (SPE 26612), *SPE Annual Technical Conference and Exhibition*, Houston, Texas, USA.

Dyer, S., El-Khazinder, Y., Huber, M., Raw, I., Reed, D. (2007). Intelligent completions-A hands-off management style.Accessed on 10 July 2010 on http://www.slb.com/~/media/Files/resources/oilfield_review/ors07/win07/intelligent.ashx

Evensen, G., Hove, J., Meisingset, H.C., Reiso, E., Seim, K.S. and Espelid, O. (2007) Using the EnKF for assisted history matching of a North Sea reservoir model (SPE 106184). *SPE Reservoir Simulation Symposium*, Houston, Texas, USA.

Fasanino, G. and Molinard, J.E. (1986) Inverse modeling of gas reservoirs (SPE 15592). *SPE Annual Technical Conference and Exhibition*, New Orleans, USA.

Floricich, M. (2006) *An engineering-consistent approach for pressure and saturation estimation from time-lapse seismic data*. PhD Thesis, Edinburgh Time-Lapse Project, Heriot-Watt Institute of Petroleum Engineering, Scotland, UK.

Floricich, M., MacBeth, C. and Staples, R. (2005) An engineering-driven approach for separating pressure and saturation using 4D seismic: application to a Jurassic reservoir in the UK North Sea. *SEG Expanded Abstracts*, Vol. 24, No. 1, 2464–2467.

Floricich, M., Evans, A., McCormick, D., Jenkins, G. and Stammeijer, J. (2008) Adding the temporal coherence dimension to 4D seismic data – assessing connectivity in the Schiehallion. *EAGE Conference and Technical Exhibition*, Rome, Italy.

Gassmann, F. (1951) Elastic waves through a packing of spheres, *Geophysics*, Vol. 16, 673-685.

Gentil, P. (2005) *The use of multilinear regression models in patterned waterfloods: physical meaning of the regression coefficients*. MSc Thesis, University of Texas, Austin, Texas, USA.

Goloshubin, G., Slin, D., Vingalov, V., Takkand, G. and Latfullin, M. (2008) Reservoir permeability from seismic attribute analysis. *The Leading Edge*, Vol. 27, No. 3, 376–381.

Goodman, L.A. (1960) The Exact Variance of Products. *Journal of the American Statistical Association*, Vol. 55, No. 292, 708-713.

Gosselin, O., Aanonsen, S.I., Aavatsmark, I., Cominelli, A., Gonard, R., Kolasinski, M., Ferdinandi, F., Kovacic, L. and Neylon, K. (2003) History matching using time-lapse seismic (HUTS) (SPE 84464). *SPE Annual Technical Conference and Exhibition*, Denver, Colorado, USA.

Govan, A., Primmer, T., Douglas, C., Moddie, N., Davies, M. and Nieuwland, F. (2006) Reservoir management in a deepwater subsea field – the Schiehallion experience (SPE 96610). *Offshore Europe Conference*, Aberdeen, Scotland, UK.

Grader, A.S. and Horne, R.N. (1988) Interference testing: detecting a circular impermeable or compressible subregion (SPE 15585). *SPE Annual Technical Conference and Exhibition*, New Orleans, Louisiana, USA.

Grimstad, A.A., Mannseth, T., Aanonsen, S.I., Aavatsmark, I., Cominelli, A. and Mantica, S. (2004) Identification of unknown permeability trends from history matching

of production data (SPE 77485). *SPE Annual Technical Conference and Exhibition*, San Antonio, Texas, USA.

Harpole, K.J. and Hearn, C.L. (1982) The role of numerical simulation in reservoir management of a West Texas carbonate reservoir (SPE 10022). *SPE International Petroleum Exhibition and Technical Symposium*, Beijing, China.

Heffer, K.J., Fox, R.J., McGill, C.A. and Koutsabeloulis, N.C. (1997) Novel techniques show links between reservoir flow directionality, Earth stress, fault structure and geomechanical changes in mature waterfloods (SPE 30711). *SPE Journal*, Vol. 2, No. 2, 91–98.

Huang, X. and Ling, Y. (2006) Water injection optimization using historical production and seismic data (SPE 102499). *SPE Annual Technical Conference and Exhibition*, San Antonio, Texas, USA.

Jian, F.X., Larue, D.K., Castellini, A. and Toldi, J. (2004) Reservoir modelling methods and characterization parameters for a shoreface reservoir: what is important for fluid-flow performance? (SPE 87893). *Annual Technical Conference and Exhibition*, San Antonio, Texas, USA.

Johnson, W.W. (1994) Permeability determination from well logs and core data (SPE 27647). *SPE Permian Basin Oil and Gas Recovery Conference*, Midland, Texas, USA.

Journel, A., Gomez-Hernandez, G. and Jaime, J. (1993) Stochastic imaging of the Wilmington clastic sequence (SPE 19857). *SPE Formation Evaluation*, Vol. 8, No. 1, 33–40.

Kalkomey, C.T. (1997) Potential risks when using seismic attributes as predictors of reservoir properties. *The Leading Edge*, Vol. 16, No. 3, 247–251.

Kaviani, D., Jensen, J.L., Lake, L.W. and Fahes, M. (2008) Estimation of interwell connectivity in the case of fluctuating bottomhole pressures (SPE 117856). *Abu Dhabi International Petroleum Exhibition and Conference*, Abu Dhabi, UAE.

Kenyon, W.E., Day, P.E., Straley, C. and Willemsen, J.F. (1997) Petrophysical principles of applications of NMR logging. *The Log Analyst*, March–April issue.

King, P.R. (1989) The use of renormalization for calculating effective permeability. *Transport in Porous Media*, Vol. 4, 27–28.

Klimentos, T. and McCann, C. (1990) Relationships among compressional wave attenuation, porosity, clay content, and permeability in sandstones. *Geophysics*, Vol. 55, 998–1014.

Koster, K., Gabriels, P., Hartung, M., Verbeek, J., Deinum, G. and Staples, R. (2000) Time-lapse seismic surveys in the North Sea and their business impact. *The Leading Edge*, Vol. 19, No. 3, 286–293.

Kozlov, E., Baransky, N., Motruk, V., Rusalin, A., Persidskaya, L., Kirseleva, O. and Bovykin, A. (2009) Integrating seismic attributes to estimate transport properties of dual porosity reservoir rocks. *First Break*, Vol. 17, No. 5, 43–52.

Kretz, V., Valles, B. and Sonneland, L. (2004) Fluid front history matching using 4D seismic and streamline simulation (SPE 90136). *Annual Technical Conference and Exhibition*, Houston, Texas, USA.

Landa, J.L. and Horne, R.N. (1997) A procedure to integrate well test data, reservoir performance history and 4D seismic information into a reservoir description (SPE 38653), *Annual Technical Conference and Exhibition*, San Antonio, Texas, USA.

Leach, H.M., Herbert, N., Los, A. and Smith, R.L. (1999) The Schiehallion development. In: Fleet, A.J. and Boldy, S.A.R., *Petroleum Geology of Northwest Europe, Proceedings of the 5th Conference*, pp. 683–692.

Lindeberg, T. (1993) Discrete derivative approximations with scale-space properties: a basis for low-level feature extraction. *Journal of Mathematical Imaging and Vision*, Vol. 3, No. 4, 349–376.

Lindeberg, T. (1994) *Scale-Space Theory in Computer Vision*, Kluwer Academic Publishers, Dordrecht, the Netherlands, ISBN 0-7923-9418-6.

Lindeberg, T. (1998) Edge detection and ridge detection with automatic scale selection. *International Journal of Computer Vision*, Vol. 30, No. 2, 117–154.

Lumley, D.E. and Behrens, R.A. (1998) Practical issues of 4D seismic reservoir monitoring: what an engineer needs to know (SPE 53004). *SPE Reservoir Evaluation and Engineering*, Vol. 1, No. 6, 528–538.

McCain, W.D. (1993) *The Properties of Petroleum Fluids*. PennWell Publication, Tulsa, Oklahama, USA

MacBeth, C. (2004) A classification for the pressure-sensitivity properties of a sandstone rock frame. *Geophysics*, Vol. 69, No. 6, 497–510.

MacBeth, C. and Al-Maskeri, Y. (2006) Extraction of permeability from time-lapse seismic data. *Geophysics*, Vol. 54, 333–349.

MacBeth C., Stephen, K.D. and McInally, A., 2005, The 4D signature of oil-water contact movement due to natural production in a stacked turbidite reservoir, *Geophysical Prospecting*, Vol. 53, 183-203

Marsh, M. (2004) 4D in reservoir management - Successes and Challenges. *IOR Views e-Newsletter*, No. 8.

Matthews, C.S. and Russell, D.G. (1967) Pressure buildup and flow tests in wells. *SPE Monograph Series*, Richardson, Texas, USA.

McInally, A., Redondo-Lopez, T., Garnham, J., Kunka, J., Brooks, A., Stenstrup, L., Barclay, F. and Davies, D. (2003) Optimizing 4D fluid imaging. *Petroleum Geoscience*, Vol. 9, No. 1, 91–101.

McLaughlin, D. and Townley, L.R. (1996) A reassessment of the groundwater inverse problem. *Water Resources Research*, Vol. 32, No. 5, 1131–1161.

Mijnssen, F.C.J. (1997) Modelling of sandbody connectivity in the Schooner Field. *Petroleum Geology of the Southern North Sea: Future Potential, Geological Society Special Publication*, No. 123, 169–180.

Naevdal, G., Mannseth, T. and Vefring, E.H. (2002) Near-well reservoir monitoring through ensemble Kalman filter (SPE 75235). S*PE/DOE Improved Oil Recovery Symposium*, Tulsa, Oklahoma, USA.

Nissen, S.E., Marfurt, K.J. and Carr T.R. (2004) Identifying subtle fracture trends in the Mississippian saline aquifer using new 3D seismic attributes: Kansas Geological Survey Open-file report 2004–56. Accessed 26 July 2007, http://www.kgs.ku.edu/PRS?publication/2003/2004-56.

Øistein, H., Kleppe, A. and Nystein, J.P. (1993) Effects of heterogeneities in a braided stream channel sandbody on the simulation of oil recovery: a case study from the Lower Jurassic Statfjord Formation, Snorre Field, North Sea. In: *Advances in Reservoir Geology*, Geological Society Special Publication, No. 69, 105–134.

Oliveira, R.M., Bampi, D., Sansonowski, R.C., Ribeiro Jr, M.S., Schroeder, Johann P.R., dos Santos, M.S. and Ferreira, D.M. (2007) Marlim Field: incorporating 4D seismic in the geological model and application in reservoir management decisions (SPE 108062). *Latin American and Caribbean Petroleum Engineering Conference*, Buenos Aires, Argentina.

Ouenes, A. (1992) *Application of simulated annealing to reservoir characterization and petrophysics inverse problems*. PhD Thesis, New Mexico Institute of Mining and Technology, Socorro, New Mexico.

Parr, R. and Marsh, M. (2000) Development of 4D reservoir management west of Shetland. *World Oil*, Vol. 221, No. 9, 39–47.

Pride, S.R., Harris, J.M., Johnson, D.L., Mateeva, A., Nihel, K.T., Nowack, R.L., Rector, J.W., Spetzler, H., Wu, R., Yamomoto, T., Berryman, J.G. and Fehler, M. (2003) Permeability dependence of seismic amplitudes. *The Leading Edge*, Vol. 22, No. 6, 518–525.

Refunjol, B.T. and Lake, L.W. (1999) Reservoir characterization based on tracer response and rank analysis of production and injection rates. In: *Reservoir Characterization – Recent Advances*, AAPG Monitor, 71, pp. 209–218.

Reynolds, A.C., Li, R. and Oliver, D.S. (2004) Simultaneous estimation of absolute and relative permeability by automatic history matching of three-phase flow production data (SPE 04-03-03). *Journal of Canadian Petroleum Technology*, Vol. 43, No. 3, 37–46.

Richardson, S.M., Herbert, N. and Leach, H.M. (1997) How well connected is the Schiehallion Reservoir? (SPE 38560). *Offshore Europe Conference*, Aberdeen, UK.

Roberts, A. (2001) Curvature attributes and their applications to 3D interpreted horizons. *First Break*, Vol. 19, No. 2, 85–99.

Sabet, M.A. (1991) *Well Test Analysis*. Gulf Publishing Company, Houston, Texas, USA.

Saxby, I. (2001) Impact of 4-D seismic reservoir monitoring in Schiehallion Field. *UKCS: 2001 AAPG Annual Meeting*.

Shams, A., MacBeth, C. and Barens, L. (2007) Local connectivity analysis in a deep water complex turbidite using seismic time lapse and well interference test. *Devex Conference*, Aberdeen, UK.

Shapiro, S.A. and Müller, T.M. (1999) Seismic signatures of permeability in heterogeneous porous media. *Geophysics*, Vol. 64, 99–103.

Soeriasinata, T. and Kelkar, M. (1999) Reservoir management using production data (SPE 52224). *SPE Mid-Continent Operations Symposium*, Oklahoma City, Oklahoma, USA.

Soldo, J.C. (2004) *Quantitative integration of time-lapse seismic information using multiple model history matching and engineering data*. PhD Thesis, Edinburgh Time-Lapse Project, Heriot-Watt Institute of Petroleum Engineering, Edinburgh, Scotland, UK.

Spearman, C.C. (1910) Correlation calculated from faulty data. *British Journal of Psychology*, Vol. 3, 271–295.

Stammeijer, J. and Staples, R. (2003) Putting 4D pressures in perspective. *SEG Expanded Abstracts.*

Staples, R., Hague, P., Weisenborn, T., Ashton, P. and Michalek, B. (2005) 4D seismic for oil-rim monitoring. *Geophysical Prospecting*, Vol. 53, 243–251.

Staples, R., Stammeijer, J., Jones, S., Brain, J. and Smit, F. (2006) Time-lapse (4d) seismic monitoring – expanding applications. *CSEG Convention*.

Stephen, K.D. and MacBeth, C. (2006) Seismic history matching in the UKCS Schiehallion field. *First Break*, Vol. 24, 43–49.

Stephen, K.D., Shams, A. and MacBeth, C. (2007) Faster seismic history matching in a UKCS reservoir (SPE 107147). *EUROPEC/EAGE Conference and Exhibition*, London, UK.

Stewart, G. and Whaballa, A.E. (1988) Pressure behavior of compartmentalized reservoir, (SPE 19779). *SPE Annual Technical Conference and Exhibition*, San Antonio, Texas, USA.

Taner, M.T., Koehler, F. and Sheriff, R.E. (1979) Complex seismic trace analysis. *Geophysics*, Vol. 44, No. 6, 1041–1063.

Tang, H. and Wang, F. (2007) Using production data to mitigate reservoir connectivity uncertainty (SPE 2007-026-EA). *Canadian International Petroleum Conference, Calgary*, Alberta, Canada.

Tarantola, A. (2005) *Inverse Problem Theory and Model Parameter Estimation*. SIAM (Society of Industrial and Applied Mathematics) Publication, Paris, France.

Timur, A. (1969) Pulsed NMR studies of porosity, movable fluids and permeability of sandstones. *Journal of Petroleum Technology*, Vol. 21, 775–786.

Tran, T.T., Xian-Huan, W., Behrens, R.A., 1999, Efficient Conditioning of 3D Fine-Scale Reservoir Model To Multiphase Production Data Using Streamline-Based Coarse-Scale Inversion and Geostatistical Downscaling (SPE 56518), *SPE Annual Technical Conference and Exhibition*, Houston, Texas, U.S.A.

Valstar, J.R. (2001) *Inverse modelling of groundwater flow and transport*, PhD Thesis, Delft University of Technology, the Netherlands.

Vasco, D.W. (2004) Seismic imaging of reservoir fluid flow properties: time-lapse pressure changes. *Geophysics*, Vol. 69, 511–521.

Vasco, D.W., Datta-Gupta, A., Behrens, R., Condon, P. and Rickett, J. (2004) Seismic imaging of reservoir flow properties: time-lapse amplitude changes. *Geophysics*, Vol. 69, 1425–1442.

Vega, N.A.R. (1995) *Estimating effective permeability of porous media with stochastic permeability distributions*. MSc Thesis, University of Texas at Austin, Texas, USA.

Webber, K.J. and van Geuns, L.C. (1990) Framework for constructing clastic reservoir simulation models (SPE 19582). *Journal of Petroleum Technology*, Vol. 42, No. 10, 1248–1253, 1296–1297.

Wyllie, M.R.J. and Rose, W.D. (1950) Some theoretical considerations related to the quantitative evaluation of the physical characteristics of reservoir rock from electrical log data. *Petroleum Transactions*, Vol. 189.

Yoon, S., Malallah, A.H., Datta-Gupta, A., Vasco, D.W. and Behrens, R.A. (1999) A multiscale approach to production data integration using streamline models (SPE 56653). *SPE Annual Technical Conference and Exhibition*, Houston, Texas, USA.

Yousef, A.A., Gentil, P., Jensen, J.L. and Lake, L.W. (2006) A capacitance model to infer interwell connectivity from production- and injection-rate fluctuations (SPE 95322). *SPE Reservoir Evaluation and Engineering*, Vol. 9, No. 6, 630–646.

Zhang, F., Skjervheim, J.A., Reynolds, A.C. and Oliver, D.S. (2005) Automatic history matching in a Bayesian framework (SPE 84461). *SPE Reservoir Evaluation and Engineering*, Vol. 8, No. 3, 214–223.

Ziou, D. and Tabbone, S. (1998) Edge detection techniques: an overview. *International Journal of Pattern Recognition and Image Analysis*, Vol. 8, No. 4, 537–559.